

# Investigating the intracellular delivery of non-viral gene therapeutics

## A focus on the endosomal barrier

**Lotte Vermeulen**

Pharmacist

Master of Science in Drug Development

**2018**

Thesis submitted to obtain the degree of  
Doctor in Pharmaceutical Sciences

Proefschrift voorgedragen tot het bekomen van de graad van  
Doctor in de Farmaceutische Wetenschappen

Dean

Prof.dr.apr. Jan Van Bocxlaer

Promoters

Prof.dr. Kevin Braeckmans

Prof.dr.apr. Katrien Remaut



**Members of the Exam Committee:**

Prof.dr.apr. **Filip Van Nieuwerburgh** (Chairman)

Ghent University

Prof.dr.apr. **Christophe Stove** (Secretary)

Ghent University

Prof.dr.apr. **Niek Sanders**

Ghent University

Prof.dr.ir. **Herman Favoreel**

Ghent University

Prof.dr. **Manfred Ogris**

University of Vienna

Prof.dr. **Rabah Boukherroub**

French National  
Centre for Scientific  
Research



The authors and the promoters give the authorization to consult and to copy parts of this thesis for personal use only. Any other use is limited by the Laws of Copyright, especially the obligation to refer to the source whenever results from this thesis are cited.

De auteur en de promotoren geven de toelating dit proefschrift voor consultering beschikbaar te stellen en delen ervan te kopiëren voor persoonlijk gebruik. Elk ander gebruik valt onder de beperkingen van het auteursrecht, in het bijzonder met betrekking tot de verplichting uitdrukkelijk de bron te vermelden bij het aanhalen van resultaten uit dit proefschrift.

Ghent, May 9<sup>th</sup> 2018

**The promoters**

Prof.dr. Kevin Braeckmans

Prof.dr.apr. Katrien Remaut

**The author**

Apr. Lotte Vermeulen



## TABLE OF CONTENTS

List of abbreviations		9
Aim and outline		13
<b>Chapter 1</b>	Methodologies to Investigate Intracellular Barriers for Nucleic Acid Delivery in Non-viral Gene Therapy	15
<b>Chapter 2</b>	The Proton Sponge Hypothesis: Fable or Fact?	69
<b>Chapter 3</b>	Endosomal Size and Membrane Leakiness Influence Proton Sponge-Based Rupture of Endosomal Vesicles	87
<b>Chapter 4</b>	Photothermally Triggered Endosomal Escape and Its Influence on Transfection Efficiency of Gold-functionalized JetPEI/pDNA Nanoparticles	133
<b>Chapter 5</b>	Broader International Context, Relevance and Future Perspectives	163
<b>Addendum A</b>	Synthesis and Evaluation of Chitosan-disulfide-conjugated LMW-PEI as a Non-viral Vector for Gene Delivery	179
Summary and conclusions		201
Samenvatting en conclusies		205
Curriculum Vitae		209



## LIST OF ABBREVIATIONS

<b>AAV</b>	Adeno-associated virus
<b>AF</b>	Alexa fluor
<b>AgNP</b>	Silver NP
<b>ANOVA</b>	Analysis of variance
<b>AOTF</b>	Acousto-optical tunable filter
<b>ATPase</b>	Adenosine triphosphatase
<b>ATR-FTIR</b>	Attenuated total reflectance Fourier transform IR
<b>AuNP</b>	Gold NP
<b>BS</b>	Beam splitter
<b>ccRICS</b>	Cross-correlation raster image correlation spectroscopy
<b>CD</b>	Cluster of differentiation
<b>CLSM</b>	Confocal laser scanning microscopy
<b>CTB</b>	Cholera toxin subunit B
<b>DAB</b>	3,3'-diaminobenzidine
<b>DAPI</b>	4',6-diamidino-2-phenylindole
<b>ddiH<sub>2</sub>O</b>	Distilled deionized water
<b>DDT</b>	Dithiothreitol
<b>DLS</b>	Dynamic light scattering
<b>DMEM/F-12</b>	Dulbecco's modified eagle medium: nutrient mixture F-12
<b>DMSO</b>	Dimethylsulfoxide
<b>DNA</b>	Deoxyribonucleic acid
<b>DOPA</b>	Dioleylphosphatidic acid
<b>DPBS</b>	Dulbecco's phosphate-buffered saline
<b>DTNB</b>	5,5-dithio-bis-(2-nitrobenzoic acid)
<b>EC</b>	Extracellular
<b>EDTA</b>	Ethylenediaminetetraacetic acid
<b>EEA1</b>	Early endosome antigen 1
<b>eGFP</b>	Enhanced GFP
<b>ELISA</b>	Enzyme-linked immunosorbent assay
<b>EM</b>	Electron microscopy
<b>EMA</b>	European medicines agency
<b>ESEM</b>	Environmental scanning EM
<b>FBS</b>	Fetal bovine serum

<b>FCCS</b>	Fluorescence cross-correlation spectroscopy
<b>FCS</b>	Fluorescence correlation spectroscopy
<b>FDA</b>	Food and drug administration
<b>FFS</b>	Fluorescence fluctuation spectroscopy
<b>FIB-SEM</b>	Focused Ion Beam - Scanning EM
<b>FIP</b>	Fluorescent internalization probe
<b>FISH</b>	Fluorescence in situ hybridization
<b>FITC</b>	Fluorescein isothiocyanate
<b>FRET</b>	Förster resonance energy transfer
<b>GFP</b>	Green fluorescent protein
<b>GTPase</b>	Guanosine triphosphatase
<b>HA</b>	Hyaluronic acid
<b>HCF</b>	Hexacyanoferrate
<b>HEPES</b>	4-(2-hydroxyethyl)-1-piperazineethanesulfonic acid
<b>HMW</b>	High molecular weight
<b>HRP</b>	Horseradish peroxidase
<b>IC</b>	Intracellular
<b>ICP-AES</b>	Inductively coupled plasma - Optical emission spectrometry
<b>ICP-MS</b>	Inductively coupled plasma MS
<b>ICP-OES</b>	Inductively coupled plasma - Atomic emission spectrometry
<b>IFP</b>	Intracellular fluorescence pattern
<b>IPS</b>	Image processing software
<b>IR</b>	Infrared
<b>LacCer</b>	Lactosylceramide
<b>LAMP</b>	Lysosomal-associated membrane protein
<b>LC3</b>	Microtubule-associated protein 1A/1B light chain 3
<b>LMW</b>	Low molecular weight
<b>LNP</b>	Lipid NP
<b>LSPR</b>	Localized surface plasmon resonance
<b>MFI</b>	Median fluorescence intensity
<b>miRNA</b>	MicroRNA
<b>MPS</b>	Mononuclear phagocyte system
<b>MRI</b>	Magnetic resonance imaging
<b>mRNA</b>	Messenger RNA
<b>MS</b>	Mass spectrometry

<b>MSD</b>	Mean square displacement
<b>mTOR</b>	Mammalian target of rapamycin
<b>MTT</b>	3-(4,5-dimethyl-2-thiazolyl)-2,5-diphenyl-2H-tetrazolium bromide
<b>MVB</b>	Multivesicular body
<b>NA</b>	Nucleic acid
<b>NA</b>	Numerical aperture
<b>NLS</b>	Nuclear localization sequence
<b>NM</b>	Nanomedicine
<b>NMR</b>	Nuclear magnetic resonance
<b>NP</b>	Nanoparticle
<b>NPC</b>	Nuclear pore complex
<b>NPC1</b>	Niemann Pick type C1
<b>ON</b>	Oligonucleotide
<b>OPO</b>	Optical parametric oscillator
<b>p(CBA-ABOL)</b>	Poly(amido amine) poly(N,N0-cystaminebisa- crylamide 4 aminobutanol)
<b>P/S</b>	Penicillin-streptomycin solution
<b>PALM</b>	Photoactivated localization microscopy
<b>PCR</b>	Polymerase chain reaction
<b>PdI</b>	Polydispersity index
<b>pDMAEMA</b>	Poly(2-dimethylamino ethyl)-methacrylate
<b>pDNA</b>	Plasmid DNA
<b>PEG</b>	Polyethylene glycol
<b>PEI</b>	Polyethylenimine
<b>PLL</b>	Poly-L-lysine
<b>ppm</b>	Parts per million
<b>ppt</b>	Parts per trillion
<b>QD</b>	Quantum dot
<b>QP</b>	Quenching probe
<b>qPCR</b>	Quantitative PCR
<b>qRAS</b>	Quantitative redox-activatable sensor
<b>RISC</b>	RNA-induced silencing complex
<b>RNA</b>	Ribonucleic acid
<b>rpm</b>	Revolutions per minute

<b>RPMI</b>	Roswell Park memorial institute
<b>SDC</b>	Spinning disk confocal
<b>SEM</b>	Scanning EM
<b>SEM</b>	Standard error of the mean
<b>SERS</b>	Surface enhanced Raman scattering
<b>SFC</b>	Swept field confocal
<b>SHIP</b>	Specific hybridization internalization probe
<b>siRNA</b>	Small interfering RNA
<b>SPT</b>	Single particle tracking
<b>SSC</b>	Side scatter
<b>Stdev</b>	Standard deviation
<b>STED</b>	Stimulated emission depletion microscopy
<b>STEM</b>	Scanning transmission EM
<b>STORM</b>	Stochastic reconstruction microscopy
<b>TBE</b>	Tris/Borate/EDTA
<b>TEM</b>	Transmission EM
<b>TIRM</b>	Total internal reflection microscopy
<b>TS</b>	Thiosulphate
<b>USPIO</b>	Ultrasmall superparamagnetic iron oxide
<b>UV</b>	Ultraviolet
<b>VNB</b>	Vapour nanobubble

# Aim and Outline

Gene therapy has attracted the interest of scientists worldwide as it offers the potential to treat diseases at their genetic roots. To do so, it needs to deliver therapeutic genes to target cells in order to replace or counteract a malfunctioning gene. In order to deliver these therapeutic genes, nanomedicines have emerged as a promising strategy due to their increased safety profile, low costs, ease of production and their ability to package large payloads. However, in order to deliver their therapeutic cargo to the final target destination, nanomedicines have to cross a variety of biological barriers, installed by nature to defend tissues and cells against external influences. It is, therefore, of crucial importance to study and characterize on a fundamental level the interaction between nanomedicines and these biological barriers. This fundamental knowledge is needed for the development of a second generation of rationally designed nanomedicines that are capable of conquering these many barriers and efficiently deliver therapeutic genes to their desired target site in the body. Of the many barriers that exist, in this thesis we focus specifically on barriers inside target cells, and in particular the endosomal barrier.

In **Chapter 1**, we provide an overview of the intracellular barriers that need to be overcome in order to efficiently deliver the therapeutic cargo of nanomedicines to their intracellular target. After discussing barrier-specific physiology, we elaborate on the role that these barriers play during the process of transfection with nucleic acids delivered by nanomaterials. In particular we provide an overview of both well-known and state-of-the-art methodologies that are developed in order to visualize and reliably quantify the interaction of nanomedicines with intracellular barriers.

Of the many intracellular barriers, endosomal escape is thought to be one of the major bottlenecks for gene therapy on the intracellular level. Indeed, as nanomedicines are taken up in cells by endocytosis, they mostly reside in endosomal compartments. It is a matter of fact that the majority of internalized nanomedicines remain entrapped inside these endosomal vesicles, making them prone to lysosomal degradation and preventing the therapeutic nucleic acids from reaching the cytosol or nucleus. While this is a common problem to many types of drug delivery nanoparticles, in **Chapter 2** we focus specifically on commonly used cationic polymers which are designed to rupture the endosomes *via* the so-called 'proton sponge hypothesis'. Even though the proton sponge hypothesis is a common tenet in the gene therapy field, there remains much debate over its exact mechanism. After discussing the discovery and the principle of the proton sponge hypothesis, we will reflect on the – often

conflicting – reports that have been published on this subject over the years. By taking the influence of membrane destabilization and polymer swelling into account, we try to reach a conclusion on the role of the proton sponge hypothesis in endosomal escape that incorporates the various insights that have emerged over 20 years of research on this topic.

In **Chapter 3** we aim to get a more fundamental understanding of the factors that contribute to effective proton sponge-based endosomal escape. We start from a comparative study on the endosomal escape capacity of JetPEI/pDNA nanoparticles in HeLa cells and ARPE-19 cells. Finding that endosomal escape is markedly different in both cell types, we take this as a starting point to find out more on the intrinsic properties that determine whether proton-sponge based endosomal escape is successful or not. We investigate several intrinsic endosomal properties such as endosomal mobility, pH, size and membrane leakiness that all could affect endosomal escape efficiency and cause intercellular variation in the efficacy of proton sponge-based endosomal rupture.

In **Chapter 4** we explore the use of gold nanoparticles in combination with laser irradiation to induce endosomal escape of pDNA. Gold nanoparticles are plasmonic nanoparticles that cause photothermal effects such as heating or the formation of explosive vapour nanobubbles upon laser irradiation. Besides its potential to be an efficient endosomal escape mechanism for pDNA, the spatio-temporal control that comes with light-triggered delivery would also be a valuable tool to perform fundamental investigations regarding the influence of time and place of endosomal escape on transfection efficiency. We evaluate the effect of heating and vapour nanobubble formation on endosomal escape efficiency, pDNA integrity and final transfection efficiency.

**Chapter 5** discusses the broader international context of the work in this thesis and its relevance to the field. We first discuss the current advancements in gene therapy, along with its key challenges. Next, we provide a critical note to highlight the difficulties that are currently limiting nanomedicines for gene therapy to reach their full potential. We will discuss how the work performed in this thesis contributes to the field and give some advice on how we could progress from here on.

# Chapter 1

## Methodologies to Investigate Intracellular Barriers for Nucleic Acid Delivery in Non-viral Gene Therapy

**A manuscript of this chapter is reviewed with minor revisions requested:**

Vermeulen, L.M.P.<sup>1,2</sup>, Brans, T.<sup>1,2</sup>, De Smedt, S.C.<sup>1</sup>, Remaut, K.<sup>1</sup>, Braeckmans, K.<sup>1,2</sup>  
Methodologies to Investigate Intracellular Barriers for Nucleic Acid Delivery in Non-  
viral Gene Therapy. *Nano Today* **2018**

<sup>1</sup>Lab. General Biochemistry & Physical Pharmacy, Ghent University, Ottergemsesteenweg 460,  
Ghent, Belgium

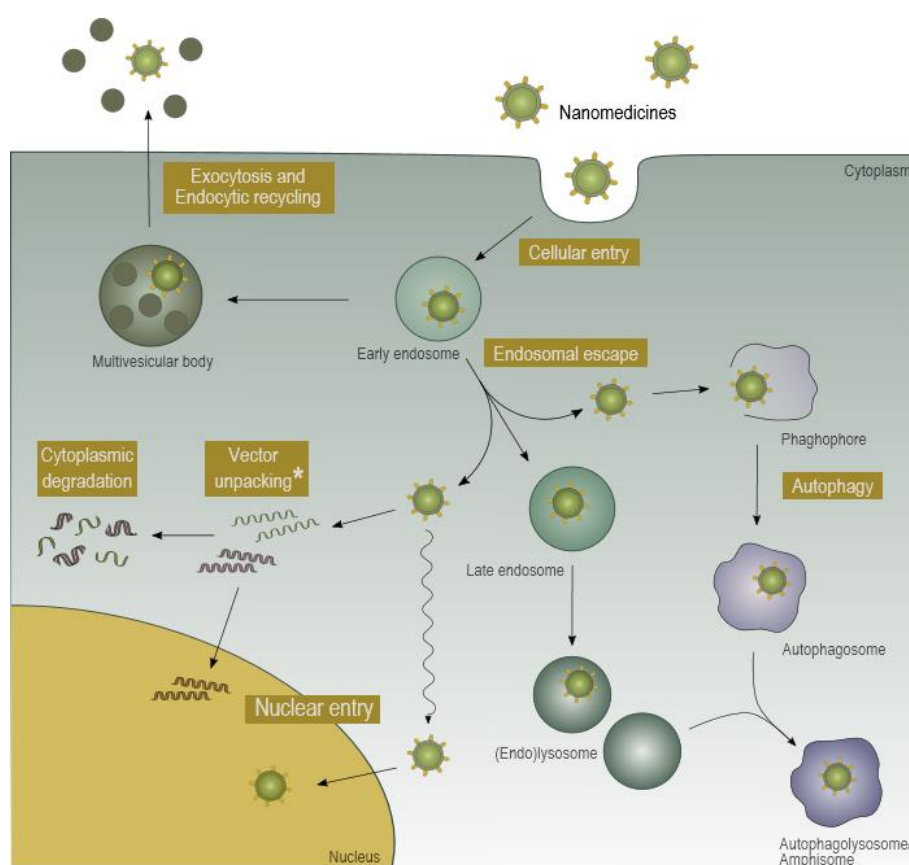
<sup>2</sup>Centre for Nano- and Biophotonics, Ghent University, Ottergemsesteenweg 460, Ghent,  
Belgium

## TABLE OF CONTENTS

1	INTRODUCTION .....	18
2	INVESTIGATING SPECIFIC INTRACELLULAR BARRIERS .....	21
2.1	Cellular uptake .....	21
2.1.1	Evaluation and quantification of cellular uptake efficiency .....	21
2.1.2	Elucidating cellular uptake pathways and intracellular trafficking.....	29
2.2	Exocytosis.....	35
2.3	Endosomal escape.....	37
2.4	Autophagy .....	42
2.5	Vector unpacking .....	45
2.6	Cytoplasmic degradation.....	47
2.7	Nuclear entry .....	49
3	CONCLUSIONS .....	51

## ABSTRACT

A plethora of biological barriers, intended to defend tissues and cells against external influences, stand in the way of efficient gene delivery by nanomedicines (NMs). Even when NMs successfully evade extracellular barriers and reach their target cell, many intracellular barriers remain to be conquered. These include overcoming the plasma membrane, evading endosomal compartmentalization, and in some cases crossing the nuclear envelope. At the same time, exocytosis, autophagy and cytoplasmic degradation of the cargo should be avoided. Currently, there is a growing appreciation that the interaction of NMs with these barriers should be understood in detail in order to rationally design NMs that are capable of overcoming these many hurdles. Studying intracellular biobarriers is, however, quite challenging and specialized methods are constantly being developed. In this review, we present an overview of established as well as emerging techniques and assays that are currently available to the experimentalist to study NM-barrier interaction, with a focus on quantitative methods.



\* Vector unpacking is not limited to the cytosol but could also happen in the nucleus or endosomes

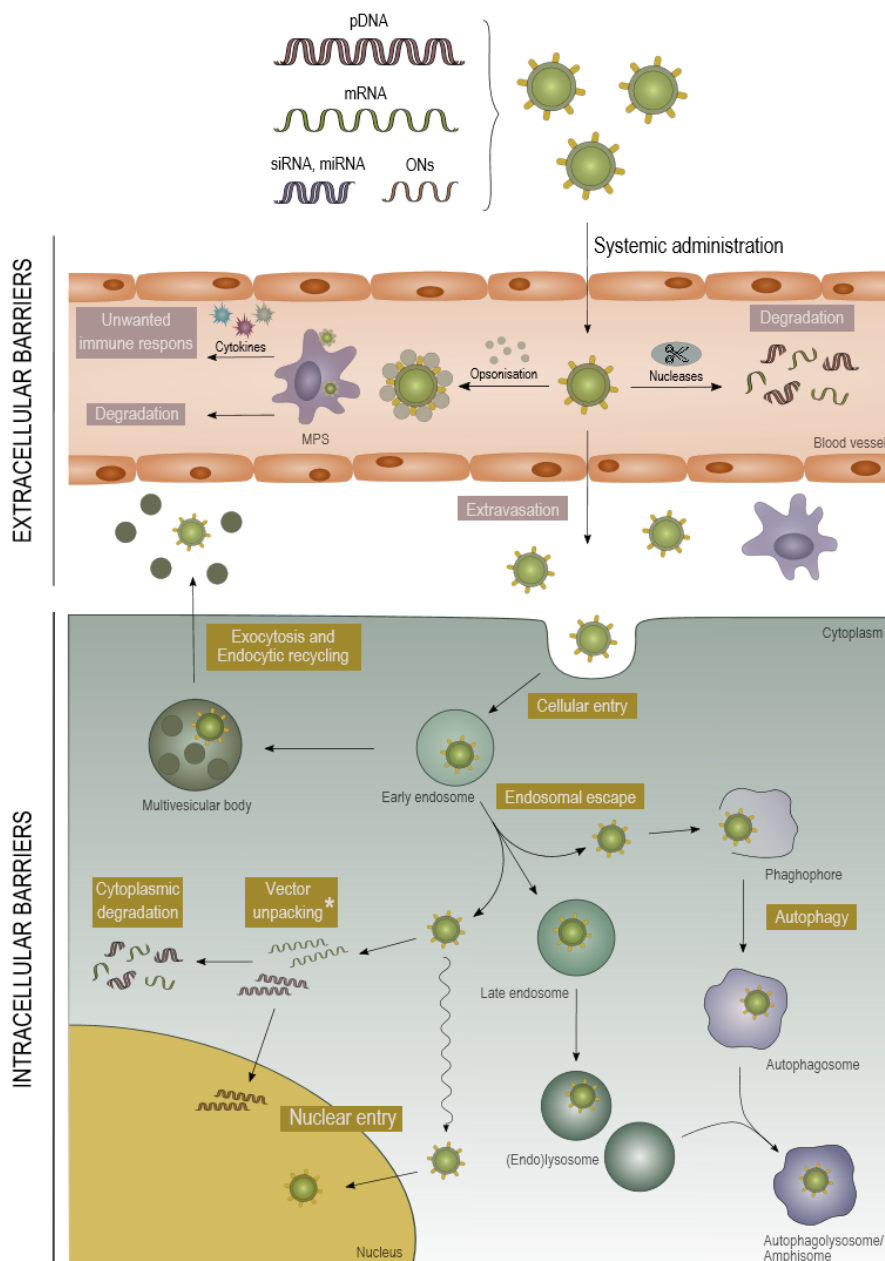
# 1 INTRODUCTION

Gene therapy is defined as the delivery of therapeutic genes to target cells in order to replace or counteract a malfunctioning gene and has emerged as a promising strategy to cure a wide variety of inherited or acquired diseases at their genetic roots.<sup>1-3</sup> Besides the delivery of pDNA, several other nucleic acids (NAs), such as mRNA, siRNA and miRNA, have emerged as promising tools to modulate protein expression levels.<sup>4</sup> A fundamental challenge for successful delivery of these NAs lies within the engineering of delivery vectors that are both safe and effective.<sup>5</sup> On the one hand, viral vectors offer great efficiency in transfecting host cells, but unfortunately they suffer from several safety concerns including immunogenicity, cytotoxicity and the possibility for insertional mutagenesis. On the other hand, non-viral vectors have attracted substantial attention due to their advantages in terms of safety (reduced immunogenicity and no risk for insertional mutagenesis), lower costs, ease of production and ability to carry larger payloads.<sup>5-7</sup> Non-viral or synthetic vectors are typically based on cationic lipids and/or polymers that complex negatively charged NAs to form nanoparticles (NPs).<sup>1</sup> However, despite decades of research, the success of non-viral vectors in clinical trials remains limited due to their poor efficiency in navigating through various biological barriers.<sup>5-7</sup>

Biological barriers for non-viral gene therapy are typically divided into two categories: extracellular (EC) and intracellular (IC) barriers, schematically depicted in **Figure 1.1**. In short, EC barriers need to be overcome prior to reaching the target cell. These include endo- and exonuclease activity in the blood circulation, interaction with blood components, activation of the immune system, surpassing endothelial barriers and migration through the extracellular space. These EC obstacles can lead to cargo degradation, rapid clearance of NMs or NM immobilization, thereby rendering them ineffective.<sup>1,2</sup> Once past the EC barriers, several IC barriers obstruct the way to efficient gene delivery. First, in order to reach the IC environment, NMs need to cross the plasma membrane.<sup>2,8,9</sup> Although physical methods, such as photoporation, electroporation or sonoporation, are sometimes used to provide direct access to the cell cytoplasm<sup>6,10-12</sup>, non-viral vectors usually gain entrance to the cell by endocytosis.<sup>4,13</sup> Following endocytic uptake, NMs are localized in early endosomes which mature *via* late endosomes into endolysosomes. This maturation is accompanied by intraluminal acidification and activation of various degradative enzymes.<sup>4</sup> Hence, using endocytosis as a way to enter the cell gives rise to an additional barrier: escaping endosomal confinement before enzymatic degradation of NAs in the endolysosomes. Moreover, NM excretion from the cell via exocytosis may happen, further reducing gene delivery efficiency.<sup>14</sup> Even if endosomal escape happens, the NAs (whether still

complexed to the vector or not) reside in the cytosol where they have to avoid being cleared from the cell by autophagy or being degraded by cytoplasmic nucleases. Furthermore, the kinetics of cargo release from the carrier is an important consideration, since vector unpacking has been reported as another bottleneck for efficient transfection. Finally, while NAs such as siRNA, mRNA and miRNA have their site of action in the cytosol, pDNA needs to be delivered to the nucleus in order to be effective, thereby making the nuclear envelope a major barrier as well. <sup>2,8,9,15</sup>

There is a growing appreciation that understanding how NMs behave at each of these IC barriers is necessary to rationally design more efficient vectors.<sup>16-18</sup> Hence, the ability to visualize and reliably quantify the interaction of NMs with these biological barriers is crucial.<sup>18</sup> However, studying IC barriers has been proven quite challenging, not in the least because of the small size and low quantity of NMs in the cell. In this review, it is our aim to provide an overview of the entire toolbox that is available to study the different IC barriers in an *in vitro* setting. In this regard, we will discuss several well-established techniques, as well as emerging state-of-the-art techniques that provide exciting new possibilities. We first provide information on barrier-specific physiology and elaborate on the role these barriers play during the process of transfection with nanomaterials. Next, we will present assays and techniques that are available to evaluate interaction of NMs with these barriers, including a discussion on their advantages and drawbacks. Finally, we will elaborate on the gaps that remain present up to date and discuss the implementation of available techniques to boost the field in the future.



\*Vector unpacking could also occur inside nucleus or endosomes.

**Figure 1.1 Extracellular (EC) and intracellular (IC) barriers for non-viral gene therapy.** Several nucleic acids (e.g. pDNA, mRNA, siRNA, miRNA) can be incorporated in nanoparticles in order to modulate protein expression levels. Upon systemic administration, several EC barriers are encountered: nucleases can lead to degradation of the NA, opsonization of nanomedicines (NMs) can cause activation of the mononuclear phagocyte system (MPS) which can lead to degradation of the NMs and their cargo or to unwanted immune responses as a consequence of cytokine release. Also, extravasation poses an additional barrier for NMs to reach their target cells. Once the target cell is reached, there are several IC barriers that hinder transfection. First, the plasma membrane must be overcome to ensure cellular entry, which for NMs is usually accomplished by endocytic uptake. After endocytosis, NMs are separated from the cytosol as they reside in endosomal vesicles. In order to gain access to the cytosol, they must escape the endosomal pathway before the cargo is degraded in the lysosomes. Endocytosed NMs should avoid recycling back to the EC environment via exocytosis or endocytic recycling. Several other barriers are to be avoided including autophagy and cytoplasmic degradation. Finally, pDNA should be delivered into the nucleus, requiring passage across the nuclear envelope. Overall, vector unpacking represents an extra barrier since the cargo must be free from its vector to interact with its IC target. Figure was based on <sup>5</sup>.

## **2 INVESTIGATING SPECIFIC INTRACELLULAR BARRIERS**

### **2.1 Cellular uptake**

Once nanomedicines reach their target site, they have to ensure cellular uptake by traversing the plasma membrane. The amphiphilic properties of this lipid bilayer make it an efficient barrier and gatekeeper. It provides protection to the IC components from the surrounding environment, allows to maintain homeostasis and is involved in controlling the entry and exit of nutrients and charged small molecules.<sup>19</sup> Although several methods have been reported for cellular uptake, the dominant mechanism for NM cell entry is endocytosis<sup>4,13</sup>, which can be subdivided in many different endocytic pathways (as discussed in several excellent reviews<sup>20-22</sup>). After endocytic vesicles pinch off from the plasma membrane, they fuse with early endosomes from where the cargo is trafficked to different IC locations.<sup>18,19</sup> The understanding and quantification of cellular entry is of crucial importance, not only because efficient cellular entry is a prerequisite for effective gene delivery but also because the various endocytic pathways and subsequent vesicle trafficking have been shown to strongly affect NA delivery efficiency.<sup>23,24</sup> As there may be a link between the endocytic pathway and the final transfection efficiency, it is not only important to study the total amount of uptake, but also the way they are internalized. Both will be discussed in detail in the following paragraphs.

#### **2.1.1 Evaluation and quantification of cellular uptake efficiency**

Investigating cellular uptake can be carried out qualitatively (yes or no) or quantitatively (amount of uptake). Even though in some cases qualitative determination of uptake might be sufficient, quantitative determination clearly is more informative and allows to compare uptake efficiencies between cell lines or between different particles. However, before one can quantify cellular uptake, one has to think about how to characterize and quantify NMs: by mass, surface area or particle number. All three metrics have been employed in the past, depending on experimental conditions and the method used. While mass concentration is convenient and frequently used in environmental risk assessment, surface area is considered a more suitable metric when studying interaction with biological interfaces, since these interactions are proportional to the surface area. However, quantification by particle number better reflects the particulate nature of NMs and would, if combined with size distribution information, be the metric of choice for quantification of NMs in biological systems.<sup>25-27</sup> Cellular uptake of NMs has been studied extensively over the last decades, resulting in a large amount of methods available for evaluation of NM internalization.

**Flow cytometry** allows (semi)quantification of cellular uptake in a large number of individual cells at high throughput and is therefore the most frequently used method to study NM uptake in cells.<sup>28,29</sup> In this technique, size, granularity and multicolor fluorescent features of single cells passing through a light source in a fluid stream are measured.<sup>30,31</sup> In a typical experiment, cells are incubated with fluorescently labeled NMs for a certain amount of time, after which the total fluorescence per cell is determined, which is assumed to be proportional to the number of internalized particles. However, several limitations should be considered when using this technique.

First of all, being a non-confocal technique, flow cytometry cannot distinguish between fluorescence coming from inside the cells or fluorescence arising from NMs that are merely attached to the outer cell surface. Yet, for NM uptake studies, one is interested specifically in the fluorescence coming from actually internalized particles.<sup>32</sup> In order to aid in the differentiation of internalized vs membrane-attached NMs, various tricks have been developed. The most widely used technique is the addition of fluorescence quenchers, such as Trypan Blue, that can be added to the flow medium to quench extracellular fluorescence.<sup>33</sup> As a more specific alternative, Liu *et al.* developed a specific hybridization internalization probe (SHIP) assay where a fluorescent internalization probe (FIP) is incorporated into the NP. Once the incubation time with the NPs is completed, a quenching probe (QP) is added. The QP hybridizes to the FIP and quenches its fluorescence on the cell surface. As the QP is unable to quench internalized FIP (no access) or other surface markers (no hybridization), fluorescence from internalized NMs and surface markers remains unaltered (**Figure 1.2 A-B**).<sup>34</sup> Another approach is to try to remove cell-bound particles by interfering with NM-cell interactions or *via* the actual destruction of membrane-bound particles. In this regard, Braun *et al.* used a NP probe that comprises a fluorescently labeled polyethylene glycol (PEG) around a fluorescence-enhancing silver NP (AgNP) core. After incubation of the cells with these NPs, an etching solution is added to the cells consisting of a mixture of hexacyanoferrate (HCF) and thiosulphate (TS). HCF is used to oxidize  $\text{Ag}^0$  to  $\text{Ag}^+$ , while TS clears away the newly formed  $\text{Ag}^+$  ions. In this way, the core of the NP dissolves and the labeled components are released from etched AgNPs, thereby losing their fluorescence enhancement. Since both HCF and TS are charged molecules, they do not readily diffuse through cell membranes, thus protecting internalized AgNPs from being etched (**Figure 1.2 C-D**).<sup>35</sup> This etching technique was also reported in order to determine the cellular internalization of gold NPs (AuNPs) and should be applicable for a myriad of materials, as long as there is a suitable etching solution available that does not induce high levels of cellular toxicity.<sup>36</sup> Complete destabilization of the interaction between the NM and the cell can be realized by

extensive washing with NaOH<sup>37</sup> or an acidic buffer<sup>38</sup>. Alternatively, when evaluating cellular uptake based on labeled cargo, polyanions (e.g. heparin) are frequently used to competitively displace the labeled NA from the carrier, followed by removal through washing.<sup>39</sup> Another possibility is to estimate the amount of membrane-attached NMs *via* inhibition of active uptake of NMs at 4°C.<sup>40</sup> The fluorescence measured from those cells can be used to correct the total measured fluorescence of the cells incubated at 37°C (having membrane-bound + internalized NMs) in order to correctly estimate the fraction of internalized NMs. One could also use non-cell penetrating reagents to achieve a double-labeling of the membrane-bound particles *vs* single-labeling of internalized particles. Ogris *et al.* labeled pDNA with YOYO-1 prior to complexation and added TOTO-3 after the addition of complexes to the cells. Since TOTO-3 is unable to penetrate the plasma membrane, only EC pDNA is double-stained. Cells are measured *via* flow cytometry and data were analyzed to render a ratio of fluorescence intensities on a single-cell level, which is indicative of the binding and internalization kinetics of the NMs.<sup>41</sup> On the same note, Smirnov *et al.* incubated cells with fluorescent particles and afterwards exposed the cells to an antibody, labeled with a different fluorophore and targeted to the particles (**Figure 1.2 E**). Next, using imaging flow cytometry, they quantified the number of EC (double fluorescent) and IC (single fluorescent) particles per cell, from which internalization was determined. Even though the authors applied this protocol to examine the binding and internalization of a pathogenic bacterium into neutrophils, it should be applicable to evaluate any cell type and particle of interest that can be recognized using antibodies or alternatives such as streptavidin-biotin complexes.<sup>32</sup>

As a second issue, flow cytometry uptake measurements are usually reported in arbitrary fluorescence units. However, ideally one would like to convert these values to particle numbers. To this purpose, various calibration methods have been reported.<sup>25,26</sup> For instance, Summers *et al.* were able to quantify the number of quantum dots (QDs) internalized per cell through calibration of flow cytometry measurements to electron microscopy data.<sup>42</sup> Also fluorimetry has been used to relate fluorescence intensities to particle numbers, but in this case particles with a narrow size distribution and fixed amount of labels are needed.<sup>43</sup> For the quantification of internalized fluorescently labeled plasmids, flow cytometry can be calibrated with qPCR.<sup>44</sup> Bishop *et al.* transfected human primary glioblastoma cells with poly(beta-amino ester) NMs containing Cy3 labeled eGFP pDNA. Thanks to the qPCR *vs* fluorescence calibration curve, the amount of Cy3 fluorescence could be converted to number of plasmid copies per cell.<sup>17</sup> A third important issue with flow cytometry has to do with the use of fluorophores to label NMs which may alter the way in which NMs interact with cells.<sup>17,45</sup> As such it may be prudent to compare results obtained with

labeled and non-labeled NMs to estimate to which extent the label may influence the transfection process. Furthermore, it must be noted that the measured fluorescence intensities are not always proportionate to cellular uptake since several particles are able to quench fluorescence, which could potentially lead to the loss of fluorescence.<sup>46,47</sup> Also, the intensity might be dependent on environmental properties, such as the pH-dependent fluorescence of FITC fluorophores. The pros and cons of several fluorescent labeling strategies available for NAs are nicely reviewed by Rombouts *et al.*<sup>48</sup> There are of course particular types of NPs, such as AuNPs, AgNPs or TiO<sub>2</sub> NPs, whose uptake could be determined to some extent without the need to use fluorescent labels. Due to their strong light scattering properties uptake measurements can be based on the change in side-scattered light (SSC).<sup>49</sup>

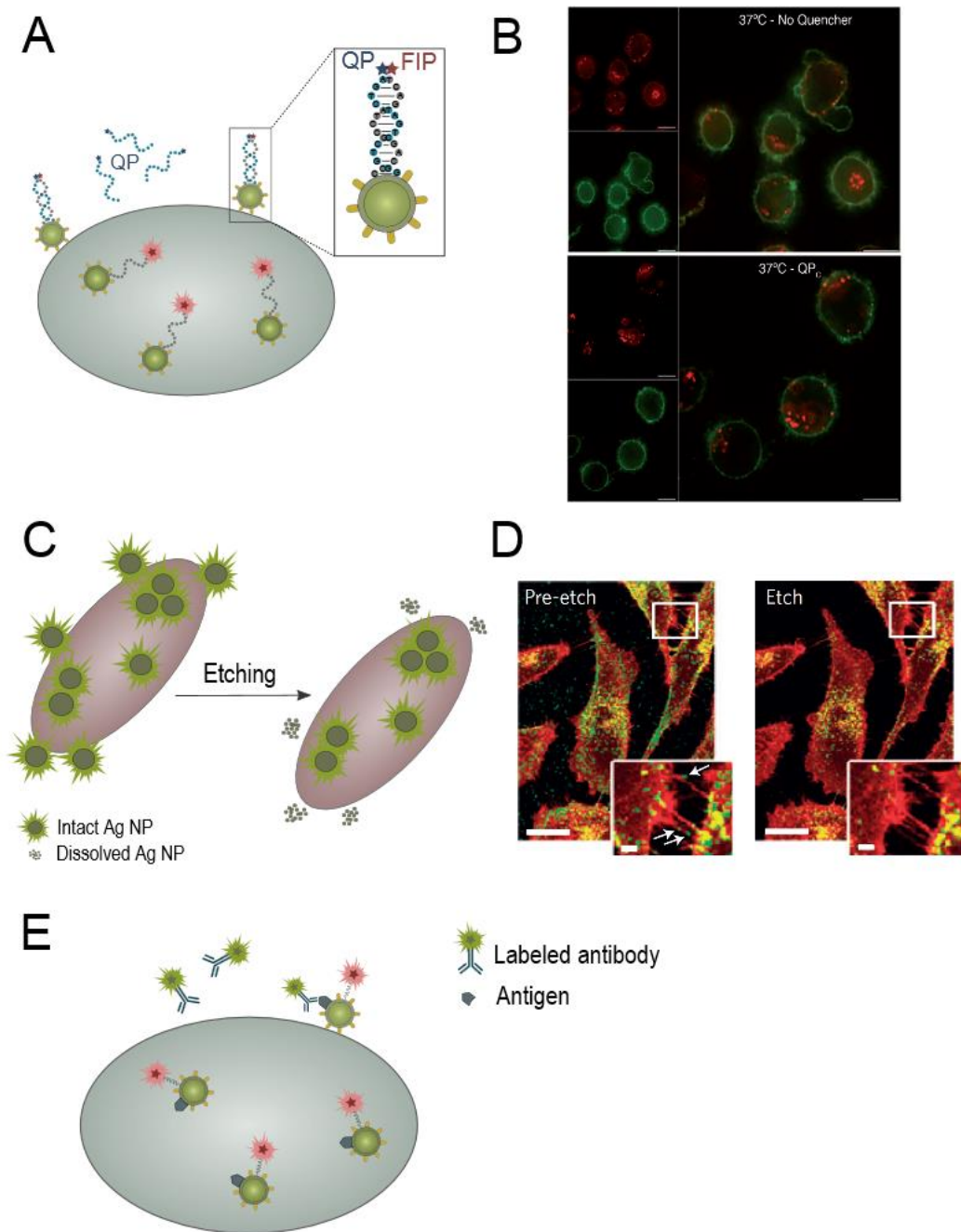


**Figure 1.2 Tricks to distinguish between membrane-bound and internalized NMs during classical uptake studies using flow cytometry. (A)** Liu and coworkers developed a specific hybridization internalization probe (SHIP) to differentiate between membrane-attached and internalized NMs. The NM is labeled with a fluorescent internalization probe (FIP), which consists of a DNA strand with a fluorophore attached. Once the cells have been incubated with the NM, a quenching probe (QP) is added to the transfection medium. The QP is complementary to the sequence of the FIP, which enables it to hybridize to the FIP. Once the hybridization with the QP is completed, the fluorescence of the FIP is quenched by the QP. Since the QP is unable to migrate through the cellular membrane, internalized FIP remain fluorescent. **(B)** Confocal images showing the efficiency of the SHIP assay. NMs are added at 37°C to allow active uptake of NMs, with (upper images) or without (lower images) the addition of the QP. Images adapted with permission from <sup>34</sup> © 2013 WILEY-VCH Verlag GmbH & Co. KGaA, Weinheim. **(C)** Schematic representation of fluorescently labeled AgNPs that are attached to the membrane and internalized into the cell. The brightness of the dye is enhanced by the local plasmonic field of

intact AgNPs. After incubation, an etching solution is added to the cells which dissolves the Ag core of membrane-bound particles. Upon dissolution of the core, the plasmonic enhancement is lost. Internalized particles remain intact since the etching solution is unable to diffuse through the cell membrane. **(D)** Confocal microscopy images of cells incubated with AgNPs (green) and membrane stain (red) show how AgNPs are selectively retained in the cells after etching (right). Extracellular particles appear as green dots in the pre-etched image on the left (indicated by the white arrows) and are selectively removed after etching (right). Scalebar represents 15  $\mu\text{m}$  in the main images and 2  $\mu\text{m}$  in the insets. Images adapted with permission from Springer Nature Nature Materials <sup>35</sup> © 2014. **(E)** This figure depicts the general mechanism, developed by Smirnov *et al.* with *N. gonorrhoeae* as a particle on neutrophils. The protocol includes the addition of labeled antibodies to non-permeabilized cells that have been previously exposed to fluorescently labeled particles. Since the antibodies are unable to penetrate into the intracellular environment, the internalized particles will be single fluorescent, while external (membrane-bound) particles will have a double-fluorescent labeling.

A second well-established technique to evaluate cellular uptake that is often used in conjunction to flow cytometry is **light and fluorescence microscopy**. This technique has proven to be extremely useful to study distribution and qualitative uptake<sup>50-53</sup> and is also – to a minor extent – used to quantify cellular uptake of NMs<sup>54,55</sup>. Quantification of NM uptake via light microscopy is, however, not that straightforward. While the total fluorescence per cell could be quantified if cells can be segmented reliably in the images, optical microscopy does not possess the necessary resolving power to detect single NPs, a key requirement for the quantification of particle numbers.<sup>25,56</sup> Recently, so-called “super-resolution” microscopy techniques have emerged that go beyond the diffraction limit and reach a resolution of <100 nm. Van der Zwaag *et al.* reported on the use of stochastic reconstruction microscopy (STORM) to extract quantitative information about the size, number and positioning of polystyrene NPs inside HeLa cells, while Peuschel *et al.* used stimulated emission depletion microscopy (STED) to quantify the uptake of silica NPs in A549 cells.<sup>23,57</sup> These promising results confirm that super-resolution microscopy can be used successfully in the quantification of cellular uptake on a single particle level.

Due to the small de Broglie wavelength of accelerated electrons, **electron microscopy (EM)** provides superior spatial resolution (<0.2 nm for TEM;  $\pm 1$  nm for SEM) and is the technique of choice when it comes to resolving structures that are below the optical resolution limit.<sup>19,58,59</sup> Thus, EM is frequently used as a third technique to evaluate<sup>60-64</sup> or quantify<sup>65-67</sup> cellular uptake. Rothen-Rutishauser *et al.* compared uptake of AuNPs in A549 cells via CLSM and TEM. AuNPs can be easily detected by TEM because of their high electron density and by CLSM due to the addition of the red fluorescent marker ATTO 590. Quantification *via* TEM resulted in the total number of internalized NPs since TEM, in contrast to CLSM, provides enough spatial resolution for detection of single NPs.<sup>68</sup> In order to downsize the complicated and time-consuming sample preparation that accompanies EM, liquid EM is regarded as an emerging field

since it can eliminate some of the steps that are required for sample preparation in classic EM.<sup>69</sup> Peckys and de Jonge used a liquid-STEM approach to study live fibroblast cells with AuNPs using a microfluidic chamber. Since their approach can be used to study whole cells with a thickness up to  $\pm 10 \mu\text{m}$ , the need for sectioning is excluded and only minimal sample preparation is required.<sup>70</sup> In 2014, Peckys and de Jonge performed imaging of whole cells in a fully hydrated state using environmental scanning electron microscopy (ESEM), resulting in a sample preparation time that is comparable to that for light microscopy. As a result, 145 whole cells could be imaged in 80h – a very limited amount of time for EM.<sup>71</sup> Alternatively, volume restrictions may be eliminated by the use of focused ion beam scanning electron microscopy (FIB-SEM), which continuously sections matrix-embedded cells using an ion beam, thereby making 3D SEM images possible.<sup>49,67</sup> Apart from volume restrictions and time-consuming sample preparation, another issue that is often encountered in EM imaging is low contrast. Indeed, the NP of interest can only be seen if it has sufficient contrast compared to the biological material. Inorganic NPs like AuNPs and superparamagnetic iron oxide NPs can be distinguished easily, but organic NPs usually need contrast enhancing agents in order to be visualized.<sup>72</sup>

**Analytical techniques**, for instance inductively coupled plasma mass spectrometry (ICP-MS), are also frequently used to quantify cellular uptake of NMs.<sup>73-76</sup> In ICP-MS the sample is ionized and its elemental composition is analyzed via MS. Alternatively, the ionized sample can be analyzed by atomic emission spectrometry (ICP-AES), also referred to as optical emission spectrometry (ICP-OES).<sup>26,77,78</sup> Both methods can be used for high-throughput analysis of a wide range of NMs such as NMs based on metals, (metal)oxides and quantum dots. The main benefits of ICP-MS over ICP-OES/AES is the higher sensitivity of ICP-MS (ppt range) compared to ICP-OES/AES (ppm range) and that ICP-MS is capable of providing isotope information.<sup>25,26,56</sup> An important limitation of these techniques is that they do not allow quantification of uptake on a single cell level as the analysis is performed on the cell population as a whole. It is however possible to extrapolate this data to calculate the average uptake per cell after determination of the total number of cells per sample. Nevertheless, one must take into account that this average is expressed as the average mass of the element per cell instead of the average number of particles per cell, although a conversion is possible if the mass and size of the NMs is known.<sup>26,79</sup> Modifications of ICP-MS have become available that allow single cell ICP-MS<sup>80</sup> or single particle ICP-MS<sup>81</sup>. In both cases, highly diluted samples are used so that each signal corresponds to a single particle or cell. Single particle ICP-MS allows quantification of mass concentration, particle size and particle number in complex environmental and biological matrices, while single cell ICP-MS allows quantification of NM content in

individual cells.<sup>79,81,82</sup> A second issue that needs to be overcome is, similar to flow cytometry, the differentiation between cell-associated and internalized particles. As these methods are often used on metallic/metal oxide NMs, chemical etching is typically used as discussed above and schematically presented in **Figure 1.2C**.<sup>36</sup> As a possible alternative, Hou *et al.* described a rapid laser-based method to selectively desorb and ionize extracellular AuNPs.<sup>83</sup>

**Other techniques** to study NM uptake – often less frequently used – include Raman spectroscopy and labeling of particles with radioisotopes. In Raman spectroscopy, a Raman fingerprint is obtained based on inelastic scattering of laser light due to the interaction of photons with molecular vibrations. Inelastic scattering of photons is a very inefficient process, but Raman band intensities can be enhanced several orders of magnitude by adsorbing a molecule on a metallic surface, typically composed of Au or Ag.<sup>84,85</sup> Surface enhanced Raman scattering (SERS) offers high sensitivity, minimal sample preparation and resistance to photobleaching and was successfully applied for the quantification of AuNPs taken up by macrophage cells.<sup>56,86</sup> Huang *et al.* used SERS to investigate the cellular internalization of graphene oxide loaded with AuNPs. By combining SERS with light microscopy and TEM, they concluded that cell entry happened mainly via energy-dependent, clathrin-mediated endocytosis.<sup>87</sup> Furthermore, it should be mentioned that labeling of particles with radioisotopes has also been used to quantify NM uptake in cells. This approach allows quantitative evaluation with high sensitivity both *in vitro* and *in vivo*.<sup>88,89</sup> However, many drawbacks are related to working with radioisotopes such as difficult particle preparation and restricted use by regulations involving disposal of materials.<sup>25</sup> On a side note, it is worth mentioning that PCR is frequently used to quantify the amount of NA molecules delivered to the IC environment. Colombo *et al.* quantified IC siRNA concentrations using reverse transcription and stem-loop qPCR after administration of siRNA-loaded lipid-polymer hybrid NMs to H1299 cells that stably expressed eGFP.<sup>90</sup> The technique has a wide range of quantification but lysing cells, isolating and purifying DNA and running PCR is considered a time-consuming process. However, some researchers state that it should be amenable to high-throughput formats and automation.<sup>16,17,91,92</sup>

### **2.1.2 Elucidating cellular uptake pathways and intracellular trafficking**

NMs commonly find their way into cells through distinct endocytic pathways, as reviewed elsewhere.<sup>20-22</sup> A common methodology to find out which pathways are involved is via **exclusion studies** where pharmacological or biological agents that can shut down a particular pathway are used and any remaining NM uptake is quantified. The decrease in NM uptake relative to untreated cells is a measure for the importance of that particular pathway.<sup>22,93</sup> While any of the above-mentioned techniques to measure NM uptake can be used for this, in practice flow cytometry is used the most. A plethora of pharmacological inhibitors is available<sup>20,94</sup> and their use is quite widespread<sup>93,95-97</sup>. Yet, one should bear in mind that such inhibitor experiments should be interpreted with care. It has been shown that chemical inhibitors of endocytosis, such as chlorpromazine or genistein, show poor specificity and that their effect is highly cell line-dependent.<sup>97</sup> To avoid the problem of non-specificity, biological strategies such as RNA interference or the introduction of dominant-negative mutants can be used to inhibit specific endocytic pathways.<sup>94,98,99</sup> The main drawback here is that these compounds could affect cell viability and are frequently observed to influence other endocytic pathways.<sup>94,97</sup>

**Fluorescence colocalization microscopy** is another very popular technique to study not only internalization pathways but especially the subsequent IC trafficking of NMs. Here, colocalization analysis methods are applied to microscopy images of fluorescent NMs that may or may not coincide with fluorescently labeled subcellular structures or compounds.<sup>100,101</sup> Labeling of specific endocytic proteins is frequently performed either by immunostaining of fixed cells or, in live cells, by transfecting cells with fluorescent protein constructs (**Figure 1.3 A**). Specific proteins related to uptake and trafficking include caveolin-1, flotillin-1, Rab5, Rab7 and LAMP-1, markers for caveolae-mediated endocytosis, flotillin-mediated endocytosis, early endosomes, late endosomes and lysosomes respectively. However, one should be mindful of potential artifacts due to protein overexpression, such as interactions that do not occur under normal circumstances due to low affinity, mislocalization of the fusion protein or aggregation and fusion of organelles.<sup>93</sup> One notorious example is the mistaken discovery of the so-called "caveosome", which was later declared to correspond to late endosomal compartments modified by the accumulation of overexpressed caveolin-1 awaiting degradation instead of a distinct endosomal compartment.<sup>102,103</sup>

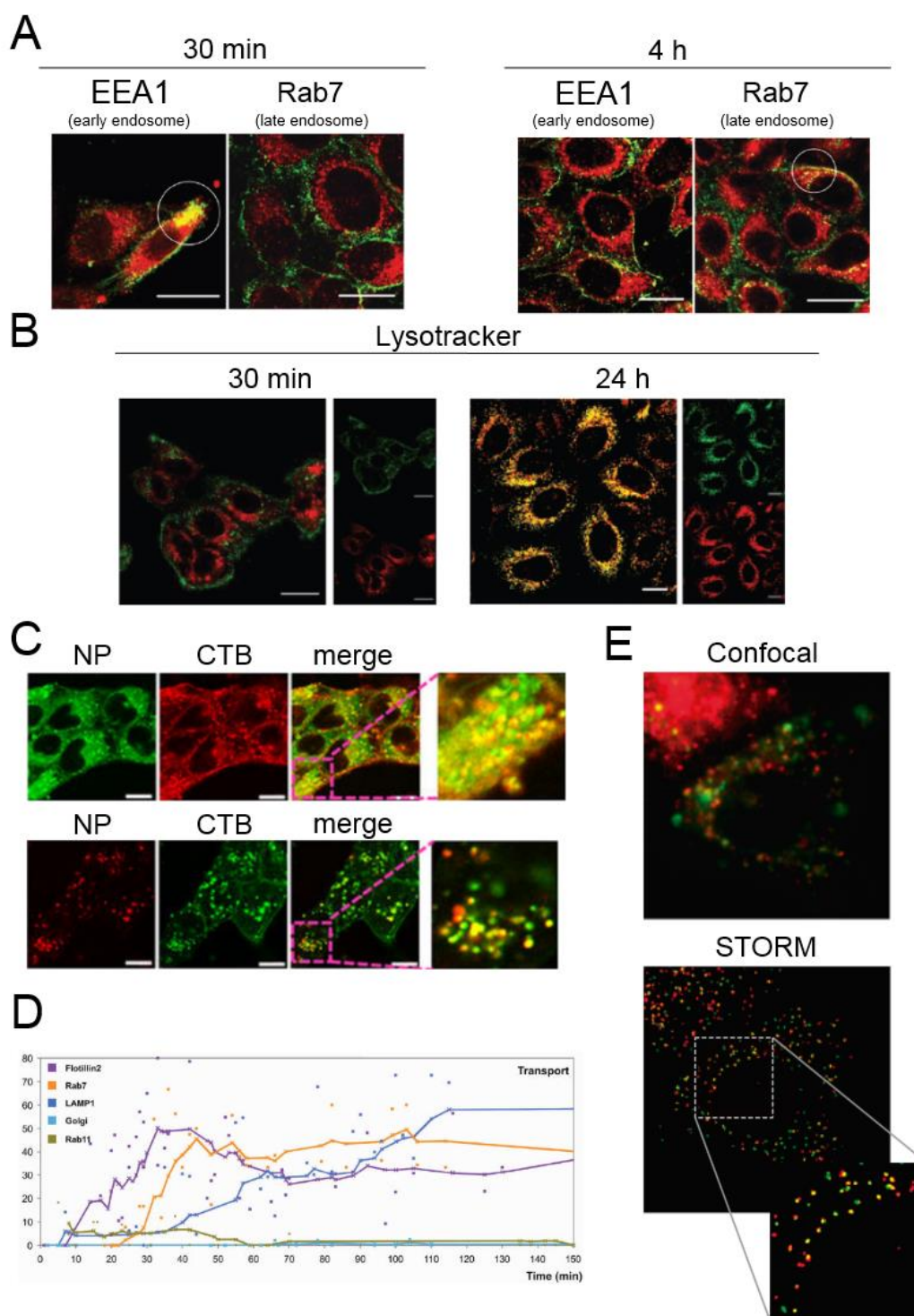


**Fig. 1.3 Evaluation of NM colocalization with IC structures. (A)** NMs are labeled in green and are incubated with the cells for 30 min or 4 h before staining of specific endocytic proteins using AF568-labeled antibodies (red). Antibodies were used to label the early endocytic marker EEA1 and the late endocytic marker Rab7. Scale bar represents 20  $\mu$ m. Images adjusted with permission from <sup>110</sup> with permission of The Royal Society of Chemistry. **(B)** NMs are labeled in green and are incubated with cells for 30 min or 24 h before staining the lysosomes with Lysotracker Red. Scale bar represents 20  $\mu$ m. Images adjusted with permission from <sup>110</sup> with permission of The Royal Society of Chemistry. **(C)** Upper images: cells were incubated for 4h with C6 labeled-NMs (green) and AF594-Cholera toxin subunit B (CTB; red), a known endocytic

marker of caveolae-mediated internalization. Lower images: cells are incubated for 4h with Cy5 labeled-NMs (red) and AF488-CTB (green). Scalebar represents 10  $\mu\text{m}$ . Images adapted with permission from <sup>111</sup> © 2017 Public License. **(D)** Spatiotemporal trafficking profile of p(CBA-ABOL) polyplexes in ARPE-19 cells. Graph shows the percentage of polyplexes that colocalize with late endosomal markers (LAMP1, Rab7, Golgi, Flotilin2 and Rab11), obtained with the dynamic colocalization algorithm based on trajectories. Image reprinted with permission of <sup>101</sup> © 2011 Americal Chemical Society. **(E)** Upper image: cell incubated with polystyrene NPs (red) and macropinosome-labeling (green); imaged via conventional confocal microscopy. Lower image: same cell imaged via stochastic optical reconstruction microscopy (STORM), demonstrating the vast improvement in resolution over traditional confocal microscopy. Image size is 40  $\mu\text{m}$  and inset size is 5  $\mu\text{m}$ . image adapted with permission from <sup>23</sup> © 2016 Americal Chemical Society.

Apart from labeling specific proteins, a diverse array of organelle probes is available such as LysoTracker (lysosomes) or Mitotracker (mitochondria) that are designed to accumulate in specific IC structures (**Figure 1.3 B**).<sup>104,105</sup> Using LysoSensor yellow/blue, Wang *et al.* performed ratiometric imaging to study the effect of cell-penetrating peptides on the IC distribution of NMs in live cells. The  $I_{\text{blue}}/I_{\text{green}}$  ratio of LysoSensor in every pixel was measured and assigned a pH value based on a calibration curve. These pH values were then categorized into endosomes (pH 5-6) or lysosomes (pH <5) and distribution of NMs in endolysosomal compartments was quantified by correlating the pH value with the fluorescence intensity of the particle at each pixel.<sup>106</sup> It should be noted however that combining acidotropic dyes (e.g. LysoTracker), which preferentially accumulate in acidic vesicles such as late endosomes and lysosomes, with proton sponge-based NMs could influence the outcome of colocalization assays. Since proton sponge-based NMs exert a buffering effect on endosomes, they could potentially inhibit staining with these acidotropic dyes. However, it is not clear if successful staining of endosomes in combination with proton sponge-based NMs indicate a lack of buffering effect since an increased flux of protons into the endosome would allow acidification and thus staining of the endosomes.<sup>107-109</sup> It is also possible to use fluorescently labeled ligands (e.g. LacCer and CTB) with known internalization pathway (**Figure 1.3 C**). However, it should be noted that even though these markers may exploit distinct uptake mechanisms, further intracellular trafficking of these markers is rarely differentiated and they frequently end up colocalized.<sup>93</sup> In this regards they are more suited for studying internalization pathways rather than intracellular trafficking.

It is of note that some types of highly scattering or reflective NPs, such as AuNPs, can be visualized by microscopy in reflectance mode so that they do not have to be labeled with a fluorophore. This only works well using a microscope with optical sectioning ability, such as confocal microscopy or total internal reflection microscopy (TIRM). For instance, TIRM was used to study the colocalization of GFP-clathrin with 500 nm colloidal particles. Unfortunately, since the penetration depth of the

evanescent field is limited to approximately 200 nm, TIRM can only be used to study events close to the plasma membrane at the coverslip interface, i.e. the initial stages of NM internalization.<sup>112</sup> For trafficking in live cells it is important to use a microscope that combines speed with sensitivity. For instance, a disadvantage of CLSM is the relatively low rate at which images can be recorded, especially when visualizing small and/or dim objects which need slow scan speeds to collect enough photons. A solution is provided by spinning disk confocal microscopy, where a disk with a series of pinhole apertures is used so that several pixels are illuminated simultaneously and light can be collected from all of them at the same time. In this way, fast confocal acquisition in live cells can be performed, albeit at a somewhat reduced confocality (i.e. lower contrast) due to pinhole crosstalk.<sup>113</sup>

In static colocalization, the overlap of two objects is analyzed based on static images and color merges are frequently used to provide qualitative information (e.g. green + red = yellow). However, a proper understanding of these experiments requires quantitative analysis of colocalization. Strategies for static colocalization quantification can be categorized into object-based or pixel-based, the latter being subdivided into co-occurrence and correlation measures. In co-occurrence methods, the Manders coefficients are well-established and calculate the percentage of total signal from one channel that overlaps with signal from the other channel, based only on the presence or absence of signal. In correlation measures, the Pearson coefficient measures linear correlation, i.e. the extent of a relationship between signals in both channels.<sup>114-116</sup> Besides static colocalization, dynamic colocalization, where a colocalization algorithm looks for correlated movements of two objects, can be used as well. In dynamic colocalization, photobleaching is increased because of longer acquisition times but chances for false positives are highly reduced. Moreover, dynamic colocalization allows spatiotemporal characterization of NM internalization. Vercauteren *et al.* first performed quantitative live-cell fluorescence microscopy to study the IC processing of poly(amido amine) poly(N,N0-cystaminebisa- crylamide 4-aminobutanol) (p(CBA-ABOL)) NMs in retinal pigment epithelium cells. They found that polyplexes were specifically delivered to Rab5- and flotillin-2-positive vesicles and were subsequently trafficked to Rab7 and LAMP-1-labeled endolysosomes, where the major fraction remained entrapped (**Figure 1.3 D**).<sup>101</sup> When objects are closer to one another than the optical resolution limit, they always appear to be colocalized in static microscopy images. This is resolved in dynamic colocalization experiments where it is the correlated motion of two objects (NM and endosome) that is taken as a measure of true colocalization. While being more reliable, it is, however, more demanding in terms of experiments and analysis. Also super-resolution techniques are proving useful to enhance the reliability of colocalization experiments. Shang *et al.* prepared NPs for

super-resolution imaging and imaged their internalization in living cells with STED nanoscopy.<sup>95</sup> Van der Zwaag *et al.* evaluated colocalization of 80 nm PS NPs with the plasma membrane, macropinosomes (**Figure 1.3 E**), nuclear membrane and actin using STORM, thereby allowing to resolve subdiffraction endocytic vesicles.<sup>23</sup> Li and coworkers used dynamic colocalization via PALM to visualize clathrin-dependent internalization of polystyrene NPs with different sizes by COS-7 cells.<sup>117</sup> However, the true competence of super-resolution microscopy in the intracellular trafficking of NMs remains to be demonstrated.

Due to the limitations associated with both exclusion and colocalization assays, it is worth mentioning that these assays are often performed simultaneously to confirm or further investigate observations. A nice example is provided by Sahay *et al.* who identified the internalization pathway required for cationic lipid nanoparticle (LNP) entry into HeLa cells. Downregulation of Cdc42 and Rac1 (regulators of macropinocytosis) led to an 80% decrease in uptake, whereas inhibition of caveolin-1 and clathrin heavy chain-1 (regulators of caveolae- and clathrin-mediated endocytosis respectively) had little impact on NP internalization. Cellular entry through macropinocytosis was then further confirmed through strong colocalization with Cdc42-GFP and ovalbumin-positive vesicles (both markers for macropinocytosis).<sup>14</sup> Another example is supplied by Zhou *et al.* who studied the influence of oligoarginine modifications on the internalization of polymeric NMs. The authors performed flow cytometry experiments after treatment with chemical endocytic inhibitors, colocalization assays using immunostaining of specific endocytic proteins (e.g. Rab 7) and colocalization with organelle-specific fluorescent markers (e.g. LysoTracker).<sup>110</sup>

Another method to study the distribution of NMs in endocytic vesicles is **subcellular fractionation**, where organelles such as early endosomes, late endosomes and lysosomes are separated through density-gradient centrifugation.<sup>118,119</sup> Although fractionation allows evaluation of a large number of cells, the method has proven to be experimentally challenging. The main drawbacks are the difficulty of identifying endocytic vesicles after centrifugation since they have many marker proteins in common and do not vary greatly in density. Furthermore, the requirement of breaking the cells before separating the intact organelles can induce damage or rupture of internal vesicles. Therefore, Lazebnik and coworkers developed an approach based on the polymerization of 3,3'-diaminobenzidine (DAB), a membrane-permeable molecule, by endocytosed horseradish peroxidase (HRP), a marker for fluid phase pinocytosis, in the presence of H<sub>2</sub>O<sub>2</sub>. In this way, only vesicles containing HRP were crosslinked, the vesicles' density was increased and the vesicles were made resistant to detergents. As a consequence, insoluble crosslinked vesicles

(early endosomes, late endosomes or lysosomes – determined by localization and thus incubation time of HRP) were easily separated from non-crosslinked vesicles using a detergent. Next, the relative fractions of PEI/AF647-siRNA polyplexes in early endosomes, late endosomes and lysosomes were quantified by measuring the fluorescence of the supernatant and comparing it to the fluorescence of the supernatant of matching samples where H<sub>2</sub>O<sub>2</sub> was omitted and thus crosslinking was inhibited.<sup>24</sup> Alternatively, Bertoli and coworkers used the magnetic properties of NPs to isolate NP-containing endosomes from A549 cells at different times. Recovered fractions were tested against different markers of the endolysosomal pathway by Western Blot to evaluate the distribution of NMs.<sup>120</sup>

Although used less frequently, **analytical methods** can be employed to study endocytosis, provided that the NM meets the rather specific requirements related to the selected method. In 2014, Hofmann *et al.* introduced a mass spectrometry method to study IC trafficking. Intracellular vesicles containing superparamagnetic iron oxide polystyrene NPs were magnetically isolated and their protein composition was analyzed by label-free quantitative MS. Proteomics identified relevant proteins involved in a macropinocytic-like internalization pathway, guiding the NPs *via* macropinosome-like vesicles towards the final destination inside multilamellar lysosomes.<sup>121</sup> Huefner *et al.* successfully applied a reporter-free SERS method to generate a color-coded distribution of 'principal component analysis – linear discriminant analysis'-derived spectral features in SERS maps of cells, allowing detailed hyperspectral characterization of endosomes and lysosomes in SH-SY5Y human neuroblastoma cells. Furthermore, this method allowed determination of vesicular localization of AuNPs and revealed the molecular environment throughout the cellular uptake pathway.<sup>122</sup>

## 2.2 Exocytosis

Cells use the process of exocytosis to remove membrane proteins such as transporters and ion channels, to excrete essential molecules, to communicate with other cells or to repair the plasma membrane.<sup>123</sup> However, this natural cellular process can interfere with the delivery of NMs for gene therapy. During endocytic confinement, NMs can be exocytosed *via* three different routes. First, early endosomes can fuse with recycling endosomes that direct the cargo towards the plasma membrane for recycling. Second, following early endosome maturation into late endosomes, multivesicular bodies (MVBs) can arise that fuse with the plasma membrane, thereby releasing their content outside the cell, for instance in the form of exosomes. Contrary to the lumen of these MVBs that can inherit NMs from late endosomes, exosomes can contain NMs only when MVBs pick them up from the cytoplasm after successful endosomal escape upon formation of the exosomes. A similar type of EC vesicles, named ectosomes, originate directly from budding at the plasma membrane and could also contain NMs, picked up from the cytoplasm, if endosomal escape was realized.<sup>19,124–126</sup> Thirdly, the ER-Golgi secretory pathway, active after IC sorting of the NMs, is defined as “conventional exocytosis”.<sup>19</sup> In contrast to the extensive study of cellular uptake mechanisms of NMs in the last decades, little is known to date about NM excretion from cells. Understanding the involvement of exocytosis is relevant because exocytosis of NMs may cause a change in protein corona, leading to unwanted toxicity or unpredicted biological effects.<sup>123</sup> Additionally and most importantly, efficiency of gene delivery is effectively reduced when NMs are directed back out of the cells.<sup>14,123,127</sup>

The most straightforward method to quantify exocytosis of NMs is to measure the amount of **expelled NMs** in fresh medium or the decrease of internalized NMs in function of time. One way to do this is by measuring the fluorescence of labeled NMs.<sup>14</sup> Shukla *et al.* estimated exocytosis of AF647-labeled siRNA from HSC-T6 cells by evaluating the fluorescence in freshly added medium after several time points.<sup>128</sup> Alternatively, Yanes *et al.* measured the decrease in IC fluorescence after administration of FITC-labeled mesoporous silica NPs to A549 cells as an indication of the amount of exocytosis.<sup>129</sup> Likewise, Jiang *et al.* studied exocytosis of QDs using spinning disk confocal microscopy to calculate the fraction of exocytosed QDs based on the decrease in IC fluorescence after applying fresh cell medium.<sup>55</sup> However, it should be noted that evaluating exocytosis based on a decrease in IC fluorescence is tricky since there are other mechanism that can lower IC fluorescence (*e.g.* degradation). When working with AuNPs, fluorescent measurements can be replaced by dark-field microscopy to estimate exocytosis as AuNPs are strong light scatterers.<sup>130</sup> Alternatively, ICP-coupled spectrometry methods can be used for quantitative

assessment of exocytosis of NMs based on metallic and inorganic NPs.<sup>131,132</sup> Strobel *et al.* used ICP-MS to measure the concentration of Ce (related to amount of CeO<sub>2</sub> NPs) in cell culture medium supernatants of HMEC-1 cells with or without the addition of exocytosis inhibitors.<sup>133</sup> However, with this approach it is not possible to differentiate between intact NMs and their breakdown products.<sup>123,134</sup>

**Fluorescence microscopy** can be used as well to study NM exocytosis. Besides live-cell imaging to observe exocytosis in real-time<sup>135</sup>, colocalization with relevant subcellular structures is frequently used as well. To evaluate exocytosis in the form of exosomes, colocalization with CD9, an established protein marker of exosomes, can be studied.<sup>98</sup> However, the most studied protein involved in endocytic recycling is Rab11, a protein that is primarily associated with recycling endosomes and regulates recycling of endocytosed material.<sup>136,137</sup> An example is again provided by Sahay *et al.*, who found that LNP showed colocalization with Rab11-positive recycling endosomes. Surprisingly, however, Rab11 depletion did not improve LNP retention. Depletion of Rab8a (which blocks secretion from the Golgi/ER after material exchange with late endosomes) and Rab27b (which blocks exosome secretion and/or fusion with the plasma membrane) did increase LNP retention, leading to enhanced silencing. This phenotype of increased retention was also observed when LNPs were applied to mouse embryonic fibroblasts devoid of Niemann Pick type C1 (NPC1). NPC1 is a 13 transmembrane glycoprotein that is located on the surface of late endosomes. Subcellular trafficking of lipids from late endosomes and lysosomes towards the EC environment has been reported to utilize NPC1 and the absence of this protein causes late endosomal and lysosomal dysfunction. Combining all this information led the authors to conclude that LNPs are exocytosed through NPC1-mediated recycling, independent of Rab11 function. This result was consistent with previous reports that indicated that NPC1-mediated recycling was independent of Rab11 function even though some colocalization with Rab11-positive vesicles was shown.<sup>14</sup> Besides colocalization assays, single particle tracking (SPT) can be used to study exocytosis. Jin *et al.* used SPT to study the movement of single-walled carbon nanotubes as they were expelled from NIH-3T3 cells. Comparable to dynamic colocalization, photobleaching is the major limitation for SPT measurements, since the photobleaching time constrains the total observation time.<sup>138</sup>

## 2.3 Endosomal escape

Cellular uptake through the process of endocytosis results in the cargo residing in endosomes, thus being physically separated from the cytoplasm by the endosomal limiting membrane. Escape out of the endosomes is generally required since endosomal sequestration potentially causes enzymatic degradation in lysosomes, recycling out of the cell or may prevent the particle or its therapeutic cargo from reaching the intended intracellular target. NMs are, therefore, often designed to have some form of endosomal escape mechanism.<sup>9,107,139</sup> Several approaches have been developed to promote endosomal escape of NMs including the use of cell penetrating peptides, the flip-flop phenomenon, the proton sponge mechanism, pore formation and membrane fusion. A detailed description of these mechanisms has been subject of numerous reviews.<sup>140,141</sup> However, despite extensive research performed in the last decades, endosomal escape remains a highly inefficient process as, typically, less than 10% of NM-containing vesicles show efficient endosomal release.<sup>142</sup> Even though it has been proven difficult, quantifying endosomal escape efficiency and elucidating release mechanisms of NMs could improve our understanding of this formidable IC barrier, which in turn may lead to the design of new and improved NMs.<sup>143</sup> Besides quantification, qualitative information about the mechanism of endosomal escape can be useful since enhancing endosomal escape efficiency requires prior knowledge about the mechanism of endosomal release. Therefore several assays that provide information about endosomal escape mechanisms are available, as discussed in more detail in a recent review by our group.<sup>107</sup>

In the context of NA delivery, endosomal escape efficiency is often related to the extent of reporter **protein expression** (mRNA and pDNA) or silencing of the reporter protein expression (siRNA).<sup>107,144,145</sup> Although endosomal escape is related to the final level of protein expression, one should be careful interpreting these results since several other barriers could influence the therapeutic effect of NAs after successful endosomal escape. As such there is a need for more specific assays to quantify endosomal escape specifically without the influence of subsequent barriers.

The most well-established method to evaluate endosomal escape efficiency is **fluorescence microscopy**. The transition from a punctate (endosomal confinement) to a diffuse (cytosolic release) intracellular fluorescence pattern (IFP) is frequently used as a qualitative confirmation of endosomal escape.<sup>107</sup> Since out of focus light can falsely give the impression of diffuse staining, confocal microscopy is recommended to evaluate the IFP.<sup>107,143</sup> A first way to do this is by co-incubation with small fluorescent molecules such as labeled dextrans or calcein, as shown in **Figure 1.4 A**.<sup>146-149</sup> Calcein has the specific advantage that it can be loaded in self-quenching concentrations,

making the diffuse cytoplasmic staining brighter due to dequenching of the fluorescence upon dilution of calcein into the cytoplasm. However, one should remain cautious when drawing conclusions from these experiments, since the release of a small molecule such as calcein doesn't necessarily guarantee the release of the cargo of interest. Calcein release can be evaluated after co-incubation with a wide array of NMs but also after incorporation into the lumen of liposomes. When present in the liposomal lumen, calcein will reach the cytosol due to endosomal membrane fusion, the preferential mechanism of endosomal release for liposomes.<sup>150,151</sup> Loading calcein inside the liposome has the benefit of visualizing the NM itself and avoiding interactions between the NM and the co-incubation solution. A related methodology to determine the endosomal escape capacity of a variety of NMs was provided by Rehman *et al.* who co-incorporated a high concentration of fluorescently labeled oligonucleotides (ONs) in NMs. When the NM resides in the endosome, the ON fluorescence is mostly quenched. Upon endosomal escape, the labeled ONs are released, resulting in a local burst of fluorescence due to dequenching and eventual accumulation into the nucleus, as illustrated in **Figure 1.4 B**. With this method it is not only possible to count the number of endosomal escape events within a cell, it also allows to visualize endosomal escape in real-time, pinpointing endosomal escape events in time and place. Additionally, by evaluating the rate of ON accumulation into the nucleus, the authors showed that the polymeric carrier PEI induces a sudden burst (proton-sponge effect) whereas a more gradual leaking occurred with a lipid based carrier.<sup>152</sup>

The transition of a punctate to a diffuse pattern to evaluate endosomal escape can also be used if the cargo itself is labeled. Clearly, this would only work for cargo that is small enough (*e.g.* siRNA) to diffuse through the cytoplasm upon endosomal release. Basha *et al.* used this strategy to examine the effect of different lipids on the cytoplasmic delivery of cy5-labeled siRNA.<sup>153</sup> However, the dose needed to visualize cytosolic siRNA with most microscopes is far above the therapeutic range.<sup>154</sup> To extend the dynamic range, Wittrup *et al.* used a spinning disk confocal microscope with two different exposure settings. Most of the cellular volume was imaged with short exposure times so as to visualize the brightest structures within the cells (*e.g.* intact lipoplexes and vesicles). Next, they focused on a particular plane in the cells and recorded an image with a long exposure time, intentionally overexposing bright areas to detect weakly fluorescent siRNA signal in the cytosol. Using this method, they could observe the sudden cytosolic release of AF647-siRNA from lipoplex-containing vesicles in HeLa cells, as depicted in **Figure 1.4 C**. Furthermore, they found that galectin-8 recruitment can be used to identify the siRNA-releasing endosomes as it recruits to the damaged endosome within 5-10 s after cytosolic siRNA detection.<sup>142</sup>

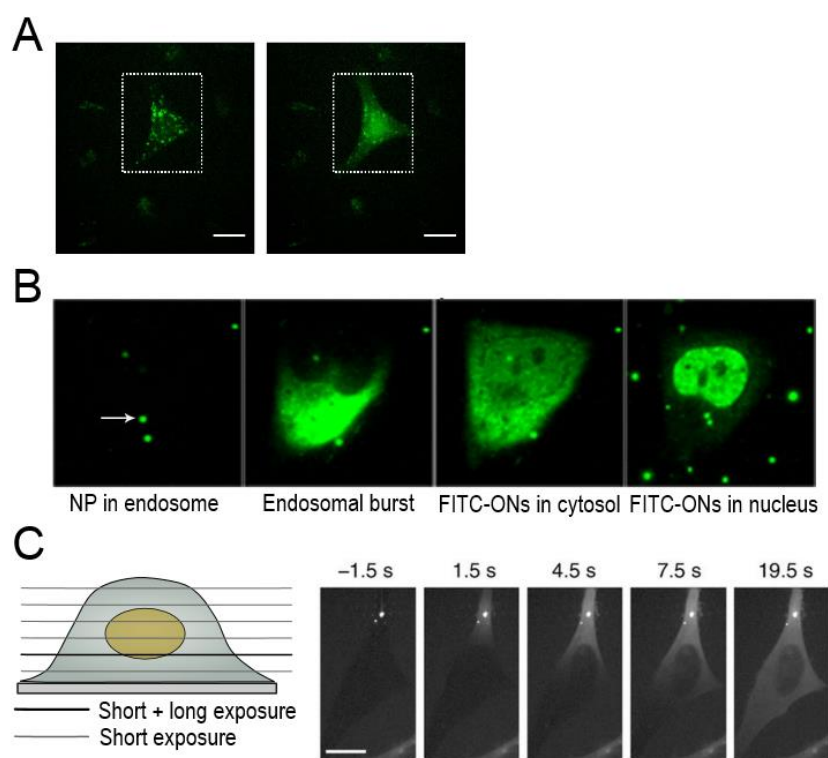


**Figure 1.4 Microscopic evaluation of endosomal escape. (A)** Visualization of calcein uptake and release after co-incubation with AuNPs conjugated to cell-penetrating peptides for 4h. Left: the cell in the dotted box shows a clear punctate intracellular fluorescence pattern (IFP) due to endosomal uptake of calcein. Right: calcein has spread as a diffuse staining towards the entire cytoplasm, indicative of endosomal escape. Scalebars represent 20  $\mu\text{m}$ . Images reprinted with the permission of <sup>149</sup> © 2016 Public License. **(B)** Upon endocytosis of the NM with co-incorporated FITC-labeled ONs, the fluorescence of these ONs is efficiently quenched. The NM can be seen as a fluorescent dot (white arrow in frame 1). Upon endosomal escape, the fluorescence of these ONs is dequenched (frame 2) and spreads throughout the entire cytoplasm (frame 3). Eventually, FITC-ONs will readily accumulate inside the nucleus (frame 4). Images reprinted with permission of <sup>152</sup> © 2013 American Chemical Society **(C)** Left: protocol used by Wittrup *et al.* to visualize sudden cytosolic release of AF647-siRNA. Short exposure times, adjusted to the brightest structures in the cell, were used to image the cell at several z-positions (grey lines). Next, a single plane was captured with longer exposure time to detect the weakly fluorescent siRNA signal in the cytosol. Right: single-plane images at long exposure times reveal that the released siRNA rapidly diffuses throughout the entire cytoplasm upon endosomal escape. Scale bar represents 10  $\mu\text{m}$ . Images reprinted with permission of Springer Nature Nature Biotechnology <sup>142</sup> © 2015.

In order to distinguish cytosolic NMs from those still sequestered in endolysosomal compartments, colocalization analysis can be employed. When NMs are situated in the cytoplasm, they are no longer colocalized with endosomes. Therefore, the lack of colocalization with endosomal compartments is an indirect measure for endosomal escape.<sup>155-157</sup> Of course this method essentially relies on being able to see all types of endosomes. Non-specific endosomal markers such as dextrans or transferrins or markers that will end up in most endocytic vesicles like plasma-membrane specific dyes are best suited for this.

**Changes in the microenvironment of the NP** can also be useful to evaluate endosomal escape efficiency. For instance, Deng *et al.* developed a ratiometric pH-sensing nanoprobe that was used for quantitative, high-throughput evaluation of endosomal escape. The nanoprobe was co-incubated with several polymeric NMs in order to examine endosomal escape efficiency of the polymeric particles. This IC pH-sensing probe is able to estimate the efficacy of endosomal escape since it senses a change in pH when going from the acidic endosomal environment to the cytosol, thereby altering its fluorescence.<sup>158</sup> Alternatively, Wang *et al.* designed a quantitative redox-activatable sensor (qRAS) for the real-time monitoring of cytosolic delivery of macromolecules, again *via* co-incubation. The qRAS-labeled macromolecules are silent inside the endosomal compartment but are switched on by redox activation upon delivery into the cytosol after endosomal escape.<sup>159</sup> The main benefit of these methods lies within the fact that they can be used as a high-throughput technique to evaluate endosomal escape. However, the use of high-throughput measurements does not allow for direct visualization of the processes, in contrast to confocal microscopy, a largely qualitative and low-throughput technique.<sup>158,159</sup>

Due to its unparalleled resolution, **electron microscopy (EM)** allows to visually distinguish between NMs that are sequestered in endolysosomal vesicles or located freely in the cytoplasm.<sup>155,160</sup> However, excessive sample preparation and complex image analysis limit the amount of cells that can be evaluated, thereby making it difficult to extract quantitative information. Furthermore, fixation artefacts can make visual assessment of endosomal escape challenging.<sup>107</sup> Gilleron *et al.* developed a semi-automatic quantification of EM images where automatic detection of LNP-siRNA-AuNPs was followed by manually assigning the particles to either endosomal compartments or the cytoplasm in order to quantify endosomal escape. This way, they estimated that siRNA escape from endosomes into the cytosol occurred at low efficiency and during a limited window of time.<sup>154</sup>

**Subcellular fractionation** can be used as well to physically separate endosomal vesicles from the cytosol. The amount of NP or cargo present in the vesicle or cytosol fractions can then be measured by classic analytical techniques, such as PCR, fluorimetry, ICP-MS etc. However, considering the uncertainty of perfect separation of both fractions it is advised to seek further confirmation with other assays.<sup>107</sup> Finally, two additional tests are discussed with the sole aim to **obtain more information on the mechanism** of endosomal escape. In order to examine the influence of pH on endosomal escape, the pH-responsiveness of the NM or the pH of the endosomal compartment itself could be altered. To this end, V-type proton-pump ATPase inhibitors such as bafilomycins or concanamycins are frequently used since

they block the acidification process altogether. The use of buffering agents such as chloroquine, monensin or ammonium chloride is not recommended since they might enhance endosomal escape due to the proton sponge effect rather than block it. Finally, to study endosomal escape via membrane fusion, the fusion of lipids is usually assayed by dye dilution, where fluorescent markers consisting of a donor and acceptor pair are diluted over an increased surface area so that Förster resonance energy transfer (FRET) efficiency goes down. Dilution can then be monitored *via* spectrofluorimetry or fluorescence microscopy. The major limitation of this assay is that it cannot distinguish between lipid fusion and lipid mixing, which is important since lipid mixing does not result in cytosolic release of the therapeutic cargo. To this end, a fluorescent content marker can be incorporated into the NM since the loss of its fluorescence will indicate fusion instead of mixing.<sup>107</sup>

## 2.4 Autophagy

Distinct from the endocytic pathway, autophagy is mediated by autophagosomes that have engulfed a portion of the cytoplasm for non-selective degradation. As depicted in **Figure 1.1**, during the process of autophagy a phagophore is created and evolves into a double-membraned autophagosome upon sequestration of cytoplasmic material. Next, this autophagosome can fuse with a lysosome, generating an autophagolysosome in a process typically referred to as “autophagy flux”. Alternatively, an amphisome can be created when an autophagosome merges with an endosome.<sup>161</sup> Autophagy is an evolutionary conserved process that supports cell preservation through degradation of cytosolic material. Recently, it has been discovered that autophagy has a greater variety of physiological roles than initially expected including cell cycle regulation, tumor suppression, development, anti-aging, etc. However, autophagy poses an additional barrier to efficient gene delivery since it can recapture NMs after their initial escape to the cytoplasm and can redirect them towards lysosomal degradation.<sup>19,162,163</sup> Roberts *et al.* reported that inhibition of autophagy by knockdown of autophagy-related protein 5 led to an 8-fold increase in gene expression efficiency, thereby confirming that autophagy can act as a substantial barrier in gene therapy.<sup>164</sup> In order to examine the extent of autophagic activity for a particular NM and cell type combination, a variety of established methods are already available. In 2016, Klionsky *et al.* published the third version of a guideline paper to standardize the use and interpretation of autophagy assays.<sup>165,166</sup>

**TEM** was the first method used to evaluate autophagy and still remains important today as it provides highly detailed information. Assuming sufficient expertise, TEM allows detection of the distinct steps of autophagy since autophagy organelles show a specific morphology.<sup>167,168</sup> Duan *et al.* used ultrastructural analysis on TEM images, which indicated that SiO<sub>2</sub> NPs induced autophagy in primary human umbilical vein endothelial cells (HUVECs), as shown in **Figure 1.5 A-H**.<sup>169</sup> Likewise, Lopes *et al.* found a dose-dependent increase in the autophagic effect of TiO<sub>2</sub> NPs on human keratinocytes (HaCaTs).<sup>170</sup> Furthermore, recent technology breakthroughs in methods used to characterize cellular ultrastructure such as cryo-EM FIB-SEM, have only just begun to contribute to autophagy research but promise to increase our understanding of autophagy processes.<sup>171</sup>

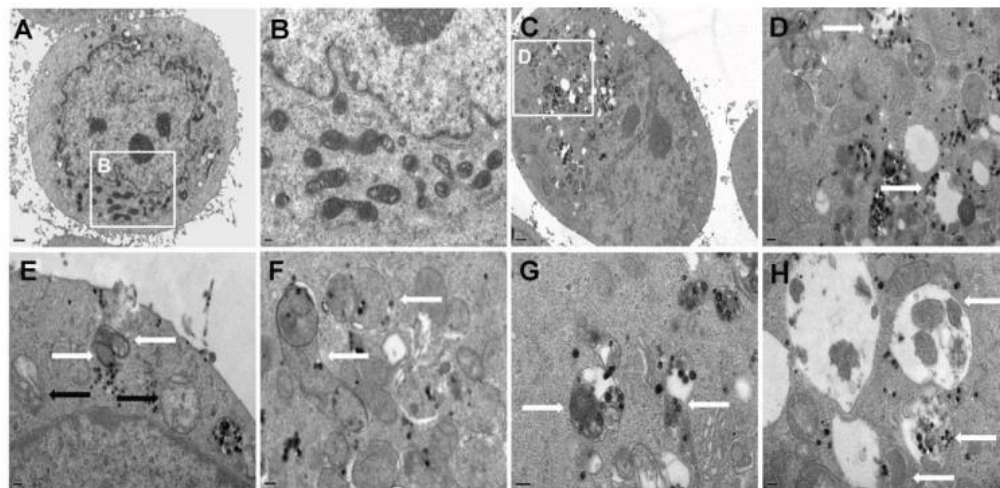


**Figure 1.5 Evaluation of NM-induced autophagy via TEM. (A-B)** Untreated human umbilical vein endothelial cells (HUVECs) with normally shaped organelles. **(C-D)** HUVECs treated with SiO<sub>2</sub> NPs show cytoplasmic vacuoles that contain electron-dense NPs (arrows). **(E)** Double-membraned phagophores evolving into autophagosomes (white arrows). **(F)** Autophagosomes (arrows). **(G)** Autolysosomes/amphisomes containing cytoplasmic material (arrows). **(H)** Autolysosomes/ amphisomes containing mitochondria and SiO<sub>2</sub> NPs (arrows). Image reprinted with permission from <sup>169</sup>.

Using **fluorescence microscopy**, autophagy is often evaluated by quantifying the number of autophagy-related vesicles. This can be performed using the autophagic dye monodansylcadaverine, which selectively accumulates in autophagic vacuoles presumably because of ion-trapping and/or interaction with membrane lipids.<sup>172,173</sup> However, the specificity of this dye remains a matter of debate. Therefore, the more specific microtubule-associated protein 1A/1B light chain 3 (LC3), a major structural protein of autophagosomes, is the most frequently used marker for autophagy. Under normal conditions, fluorescently labeled LC3 is diffusely spread throughout the cytoplasm. However, when the number of autophagosomes increases, they can be identified as distinct puncta.<sup>161,167,174</sup> Alternatively, colocalization assays of NMs with autophagy markers such as LC3 are frequently used to evaluate the role of autophagy in NM-mediated gene delivery.<sup>14</sup> However, upon fusion with lysosomes, the autophagosomal membrane is degraded and LC3 expression is lost. Furthermore, LC3 has been observed on other vesicles such as phagosomes and macropinosomes, so it is advised to remain cautious when interpreting results.<sup>101,161,163</sup> It must be noted however that above-mentioned assays do not allow differentiation between upregulation of autophagy or an impaired clearance of autophagosomes (inhibition of autophagic flux), since they both result in an increased number of autophagosomes.<sup>161</sup> Co-treatment with lysosomal inhibitors to block lysosomal degradation can be used as an additional test to differentiate between an inhibited autophagic flux or a general induction of autophagy.<sup>166</sup> The distribution of several other proteins related to autophagy, such as p62 (also called sequestosome 1), can be evaluated as well.

However, the validity of p62 as a marker for autophagy is being questioned since p62 is also involved in other cellular processes.<sup>164,172,175</sup>

Alternatively, **Western blotting** can be used to evaluate autophagy flux or signaling events involved in autophagy. An impaired autophagy flux can be detected by evaluating the ratio of LC3-II/LC3-I (membrane-bound/cytosolic form of LC3) in the presence of lysosomal protease inhibitors (e.g. pepstatin A) or buffers (e.g. chloroquine) that inhibit LC3-II degradation. When LC3-II remains constant in the presence or absence of the inhibitor, autophagy flux is likely to be blocked. GFP-LC3 cleavage can also be determined by Western blotting in order to evaluate autophagy flux. Since GFP is resistant to lysosomal hydrolysis, the amount of free GFP is correlated to autophagosome degradation. Additionally, an increase in undegraded p62 can indicate an autophagy flux blockage. Also actively studied is the activity of the mammalian target of rapamycin (mTOR) and its interacting proteins via Western blotting by means of phospho-specific antibodies.<sup>161,167,176</sup> Song *et al.* postulated that it is important to assess involvement of mTOR-dependent autophagy in NM degradation since they described distinct results for mTOR-dependent and mTOR-independent autophagy regulators. For instance, induction of mTOR-dependent autophagy by rapamycin increased siRNA knockdown whereas induction of mTOR-independent autophagy by LiBr diminished siRNA silencing tremendously.<sup>177</sup>

Finally, **enzyme-linked immunosorbent assay (ELISA)** can be used to evaluate autophagy and several kits are already available on the market (e.g. p62, Atg5). These assays allow high-throughput quantification of autophagic activity.<sup>178,179</sup> Recently, Oh *et al.* reported on an assay to evaluate autophagy flux using ELISA with two LC3 antibodies. Using this technique, changes in membrane-associated LC3-II levels and the ratio of LC3-II to LC3-I levels were evaluated. The authors demonstrated that this ELISA technique was more sensitive and reliable for the detection of a blocked autophagy flux compared to the most commonly used LC3 turnover assay via Western blot. However, since ELISA is unable to quantify LC3-I and LC3-II levels simultaneously in a single well, detection should be preceded by separation of subcellular compartments.<sup>175</sup>

It should be noted that in order to draw correct conclusions it is advised to combine several techniques. Song *et al.* evaluated the role of autophagy after administration of lipofectamine 2000 or chitosan-based NMs in H1299 cells by showing an increased number of monodansylcadaverine-stained vesicles, a significant increase in LC3-II expression via Western blotting and colocalization of siRNA with LC3-labeled autophagosomes.<sup>177</sup> Another example is provided by Zhong *et al.* who evaluated autophagy in mouse fibroblasts after transfection with PEI/DNA polyplexes. Polyplex-

induced autophagy was confirmed by visualization of autophagosomes via TEM, light microscopic detection of IC LC3-aggregation into distinctive puncta and elevated expression of LC3-II protein, measured by Western blotting.<sup>180</sup>

## 2.5 Vector unpacking

Another issue that should be considered is the kinetics of cargo release from the carrier. The stability of the interaction between carrier and cargo must be optimized since both premature dissociation and overly stable binding can be disadvantageous to the overall transfection efficiency. On the one hand, the vector needs to protect the cargo from enzymatic degradation through efficient complexation. On the other hand, the cargo needs to be dissociated from the vector prior to interaction with the final IC target (*e.g.* RISC for siRNA, translation machinery for mRNA and transcription machinery for pDNA).<sup>8,15,181</sup> It has been stated before that there might be a difference in the best unpacking moment between lipoplexes and polyplexes. This is based on the observation that nuclear microinjection of liposome-pDNA complexes inhibited gene expression while PEI complexes did not. This suggests that polymers may still dissociate from the cargo inside the nucleus while lipid carriers should dissociate from their cargo before entering the nucleus.<sup>182,183</sup> Modulation of vector unpacking properties can be achieved by changing its chemical features, using stimuli-responsive strategies or by inclusion of enzymes, proteins or chemicals.<sup>184</sup>

In order to study cargo association with or dissociation from a certain vector, **gel electrophoresis** is frequently used. When dissociation has happened, the cargo is free to migrate through the gel and form a detectable band. However, while this method allows to study vector unpacking under controlled lab conditions (*e.g.* in buffers with different pH), it cannot be used to study the stability of complexes in the actual cellular environment.<sup>185</sup> This is again where **fluorescence microscopy** comes in. In order to examine vector unpacking, the fluorescence intensity of the DNA intercalating dye YOYO-1 can be evaluated. When YOYO-1 labeled pDNA is complexed, its fluorescence is largely quenched. Consequently, when pDNA is released from the carrier, the YOYO-1 signal increases substantially, which can be visualized in cells with fluorescence microscopy. Another approach is based on colocalization of cargo and carrier, each labeled with a different fluorophore.<sup>184</sup> Using this method, Schaffer *et al.* demonstrated that vector unpacking can indeed be a limiting step for gene expression in large polymer constructs.<sup>186</sup> However, since components must diffuse far away from each other (further than the microscope's resolution) to be detected as separate, colocalization methods do not provide sufficient sensitivity to detect the onset of dissociation. FRET imaging may be used instead, which probes interactions on the sub 10 nm length scale. When the complex is intact there will be high FRET efficiency,

which reduces upon vector unpacking.<sup>184,187</sup> One should however be careful when using traditional organic fluorophores since they are susceptible to photobleaching and spectral cross-talk due to broad emission bands. A proposed solution is the use of QDs as efficient FRET-donors since they have a broad absorption, narrow emission spectrum and are highly photostable.<sup>181,184,188</sup> Ho *et al.* used QD-mediated FRET to study the distribution and unpacking of individual chitosan nanocomplexes within HEK293 cells. The use of QD-FRET permitted an immediate detection of changes in the nanocomplex state intracellularly. Another fluorescence based technique to study unpacking of complexes is dual color fluorescence fluctuation spectroscopy (dual color FFS). Here, fluctuations in fluorescence intensities are measured that originate from molecules that move in and out of a confocal detection volume. When cargo and carrier are associated, each labeled with its own fluorophore, the fluorescently labeled molecules move simultaneously, causing similar fluorescence time traces in both spectral channels. When dissociated, the molecules will move independently, resulting in a loss of similarity between both signals.<sup>184</sup> Lucas *et al.* successfully used dual color FFS on rhodamine green-labeled ONs complexed with Cy5-labeled polymers in order to characterize IC vector unpacking in Vero cells. On the downside, it should be noted that the number of particles that can be analyzed is limited since the detection volume is very small (femtoliters) and particles are highly diluted in the cytosol.<sup>189</sup>

**Magnetic resonance imaging (MRI)** was also reported for the evaluation of vector unpacking. Park *et al.* conjugated ultrasmall superparamagnetic iron oxide (USPIO) to PEI polymers. This conjugate was capable of complexing pDNA and the T<sub>2</sub> relaxation time of water enhanced by USPIO was shown to be a function of the packaging state of the vector. This technique can be used to study vector unpacking in *in vivo* situations since USPIO NPs itself are used as a contrast agents for MRI imaging with high resolution. Furthermore, NM unpacking is studied while avoiding fluorescent labeling of NMs, thereby eliminating the issue of *in vivo* tissue autofluorescence and the issue of possible alteration of vector unpacking of unlabeled vs fluorescently labeled NMs.<sup>190</sup>

## 2.6 Cytoplasmic degradation

Following successful endosomal escape and vector unpacking another significant barrier to gene delivery arises: nucleases present in the cytoplasm can degrade released NAs. For instance, several studies have demonstrated that the half-life of pDNA in the cytoplasm is in the range of 50-90 min.<sup>2,4,163</sup> Surprisingly, research on NA degradation in the cytosol remains rather limited to date, presumably because only few techniques are available to investigate this experimentally.

In order to investigate the integrity of NAs, **gel electrophoresis** can be used.<sup>191</sup> However, specificity of this technique is limited to lab conditions since free NAs and other biomolecules will generate a high background in complex biologic environments. Alternatively, **PCR** can be used to investigate NAs because of the method's high specificity and sensitivity. Recent advances in qPCR have made measurements in undiluted biological samples possible by using a PCR buffer with a higher pH, eliminating the need for DNA isolation.<sup>192</sup> However, besides detecting intact plasmids, PCR also quantifies partially degraded plasmids that contain the amplified region, which is of course undesirable when evaluating NA degradation. A more suitable method to evaluate degradation would be **Southern blotting**, where only intact plasmids are detected and quantified.<sup>193</sup>

The above mentioned methods in any case do not allow to study NA degradation in real-time within the cell. An advanced **fluorescence microscopy** method in this regard is fluorescence correlation spectroscopy (FCS). From the fluctuations measured by this technique, arising from labeled NAs moving through the confocal detection volume, the diffusion coefficient of those molecules in the cell can be obtained from fitting a theoretical model to the experimental autocorrelation function. Using FCS, degradation can be monitored by an increase in diffusional rate of the NA.<sup>194</sup> Sasaki and Kinjo monitored the size and structure of double-labeled DNA by FCS and fluorescence cross-correlation spectroscopy (FCCS) after introduction of the DNA into the cytoplasm of COS7 cells by bead-loading. In FCCS, the fluorescence fluctuation patterns of the two labels are recorded and cross-correlated in order to evaluate if the two labels move simultaneously or not. The authors employed FCS to evaluate the diffusion properties of pDNA and FCCS to monitor the degradation of pDNA at the single molecule level.<sup>195</sup> As FCS and FCCS only obtain information from within a single focal point, Sasaki *et al.* also used cross-correlation raster image correlation spectroscopy (ccRICS) to visualize the spatial distribution of nuclease degradation in live cells. ccRICS was employed to visualize when and where exogenous DNA, injected into the cytosol, is degraded. Their results indicated that nuclease activity in the cytoplasm differs between cell lines, leading to the proposition that nuclease activity impacts the

cell's resistance to exogenous DNA incorporation.<sup>196</sup> More accessible than FCS or RICS is confocal FRET imaging, which can be used to determine NA degradation in the cytosol. In this case the NA should be labeled with strategically placed FRET pairs. Upon NA degradation, the FRET pair will dissociate, resulting in lower FRET intensities.<sup>197,198</sup> Chen *et al.* developed a two-step QD-FRET approach to monitor vector unpacking and cytoplasmic degradation at the same time. pDNA, double-labeled with QD and a NA dye was complexed with Cy5-labeled polymer. The QD donor drives energy transfer through the intermediate nucleic acid dye to the Cy5-labeled polymer. This way, three states of DNA condensation and integrity could be distinguished (complexed and intact, unpacked and intact, unpacked and degraded).<sup>199</sup> Remaut *et al.* used FRET-FCS to study the IC degradation of single-stranded ONs. ONs were labeled on the 3' end with rhodamine green and on the 5' end with Cy5, resulting in high FRET efficiency as long as the ONs are intact and loss of FRET signal when the ON are degraded.<sup>200</sup> Finally, Lechardeur *et al.* used fluorescence in situ hybridization (FISH) in combination with quantitative single-cell fluorescence video-image analysis to determine for the first time the half-life of single- and double-stranded circular pDNA delivered by microinjection in HeLa and COS cells.<sup>201</sup>

## 2.7 Nuclear entry

Nuclear entry is the final barrier that needs to be overcome for successful pDNA delivery.<sup>202</sup> The nuclear envelope consists of an inner and outer nuclear membrane, joined in nuclear pore complexes (NPCs), and the underlying nuclear lamina. NPCs tightly regulate entry into the nucleus as they are the sole channels through which exchange of (macro)molecules happens. Passive entry through the NPCs is limited to molecules less than 10 nm in diameter, thereby excluding passive pDNA entry.<sup>139,203,204</sup> In dividing cells, nuclear entry can occur during mitosis, when the nuclear membrane breaks down.<sup>205</sup> However, in non-dividing cells, genetic cargo must cross the nuclear envelope through the NPCs. In order to promote transnuclear transport through the NPCs, the attachment of nuclear localization sequences (NLS) is a traditional strategy. Other methods to enhance nuclear translocation include linking of nuclear proteins or small molecule ligands. One example is the binding of the glucocorticoid receptor ligand dexamethasone to the plasmid. When dexamethasone binds to the glucocorticoid receptor, its NLS is exposed and the entire DNA-ligand-receptor complex can be translocated into the nucleus.<sup>206,207</sup> Unfortunately, nuclear entry remains rather poorly studied and requires more extensive research to investigate potential improvements.<sup>4</sup>

Nuclear uptake efficacy is indirectly evaluated in most studies simply by measuring the efficiency of **gene expression**. However, it is necessary to not only measure the final effect of the loaded therapeutic agent but also the amount of delivered cargo to the nucleus.<sup>182</sup> Qualitative evaluation of nuclear uptake can be provided by CLSM<sup>208,209</sup> and other forms of microscopy such as EM<sup>210</sup>. Although these methods give an idea about the presence or absence of nuclear delivery, it is very difficult to relate this information to the actual percentage of cargo (from the total amount administered) that has been efficiently delivered to the nucleus.<sup>204</sup>

When quantifying the total amount administered to the nucleus, it is often difficult to differentiate between particles residing in the cytoplasm and particles residing in the nucleus. Therefore, in order to correctly measure nuclear uptake, the nucleus needs to be separated from other cellular components before the measurement. Here, it is important to make a distinction between nuclear-membrane associated particles and particles that are effectively internalized into the nucleus.<sup>204</sup> Cohen *et al.* compared a density gradient technique to a detergent-based method to isolate the nuclei of transfected cells and found that the density gradient procedure yielded nuclei with substantially less plasmid attached on the outside of the nuclear membrane. Next, they determined the number of plasmids that reach the nucleus after transfection with PEI- or Lipofectamine-based NMs using an internally standardized **qPCR** assay. This method accurately measures the ratio of plasmids to a single-copy

gene and thus the number of nuclei, thereby directly revealing the amount of plasmids per nucleus.<sup>211</sup> In the quantification of nuclear uptake, PCR is the most widely used method since it is able to quantify plasmid numbers, has good sensitivity and avoids the need to fluorescently label the cargo upon transfection.<sup>193,211,212</sup> Besides PCR, **Southern blotting** was also used to quantify nuclear uptake without the need of using fluorophores.<sup>193</sup> However, efforts are being made to introduce techniques that allow a higher throughput. One example is provided by Bishop *et al.*, who developed a flow cytometry-based assay to quantify the number of plasmids within the nucleus after nuclei isolation. Conversion from fluorescence intensities, measured by flow cytometry, to plasmid numbers was performed through calibration via qPCR and fluorimetry. Fluorimetry was used to measure the fluorescence of several calibration solutions with a known amount of NAs (determined by qPCR). Flow cytometric analysis can provide important information since it is able to quantify nuclear uptake on the single cell level.<sup>17</sup> Alternatively, the amount of metallic NMs present in the nucleus can be measured by ICP-MS. Huo *et al.* determined the number of Au-TIOP NMs in MCF-7 cells via ICP-MS after cell nuclei were extracted.<sup>210</sup>

It should be noted however that cellular fractionation and nuclear isolation usually involve centrifugation which could lead to inaccurate conclusions due to precipitation of cell-surface bound and cytoplasmic NMs within the nuclei pellet.<sup>204</sup> An elegant solution to avoid errors generated by cell fractionation and nuclear isolation protocols was proposed by Tammam *et al.* who assessed nuclear delivery in intact cells using FRET fluorometry and microscopy. The authors used Hoechst (nuclear staining) as the donor and fluorescein (present on cargo – in this case albumin) as the acceptor of the FRET pair and corrected the measurements for cross talk. When the cargo is successfully delivered to the nucleus, the dyes are located in close proximity from each other and a FRET signal can be measured.<sup>213</sup> However, this assay might be less ideal when using NAs as cargo since Hoechst is commonly used to stain DNA and will highly likely interact with NA-cargo outside the nucleus.

### **3 CONCLUSIONS**

NMs need to overcome several IC barriers before they can exert their therapeutic function. Detection and quantification of the interaction between NMs and these IC barriers is crucial to gain a better understanding of these events, which could lead to the rational development of improved NMs, equipped to conquer the many IC hurdles. In this review, we have given an overview of the methods and assays that are currently available to study the different IC barriers. Although there is often a preferred method to study a given barrier, the most reliable and in-depth information is gathered by combining complementary assays. In the future, it might be interesting to gain more detailed information on the interaction between NPs and their barriers through the use of super-resolution microscopy. However, despite the successful use of super-resolution techniques in biological sciences to image cellular structures<sup>214</sup>, their application to probe NM-cell interactions remains rather limited.<sup>95</sup> Furthermore, efforts should be made in the future to allow investigation of NM-barrier interactions without the need of labeling, since labeling strategies might alter the behavior of NMs.<sup>215</sup> Therefore, it is again very important to compare results provided by several assays and to think carefully about the advantages and limitation of the methods selected to study the interaction of NMs and their IC barriers.

### **ACKNOWLEDGEMENTS**

Financial support of the Agency for Innovation by Science and Technology in Belgium (IWT Flanders) and by the Ghent University Special Research Fund and the Fund for Scientific Research Flanders (FWO, Belgium) is acknowledged with gratitude. The authors have no other relevant affiliations or financial involvement with any organization or entity with a financial interest in or financial conflict with the subject matter or materials discussed in the manuscript apart from those disclosed.

## REFERENCES

- (1) Guo, X.; Huang, L. Recent Advances in Non-Viral Vectors for Gene Delivery. *Acc Chem Res* **2012**, *45*, 971–979.
- (2) Gottfried, L. F.; Dean, D. a. Extracellular and Intracellular Barriers to Non-Viral Gene Transfer. *Nov. Gene Ther. Approaches* **2013**, 75–88.
- (3) Naldini, L. Gene Therapy Returns to Centre Stage. *Nature* **2015**, *526*, 351–360.
- (4) Jones, C. H.; Chen, C.-K.; Ravikrishnan, A.; Rane, S.; Pfeifer, B. A. Overcoming Nonviral Gene Delivery Barriers: Perspective and Future. *Mol. Pharm.* **2013**, *10*, 4082–4098.
- (5) Yin, H.; Kanasty, R. L.; Eltoukhy, A. A.; Vegas, A. J.; Dorkin, J. R.; Anderson, D. G. Non-Viral Vectors for Gene-Based Therapy. *Nat. Rev. Genet.* **2014**, *15*, 541–555.
- (6) Ramamoorth, M. Non Viral Vectors in Gene Therapy- An Overview. *J. Clin. Diagnostic Res.* **2015**, *9*, 1–6.
- (7) Riley, M.; Vermerris, W. Recent Advances in Nanomaterials for Gene Delivery— A Review. *Nanomaterials* **2017**, *7*, 94.
- (8) Li, L.; Wei, Y.; Gong, C. Polymeric Nanocarriers for Non-Viral Gene Delivery. *J. Biomed. Nanotechnol.* **2015**, *11*, 739–770.
- (9) Kozielski, K. L.; Rui, Y.; Green, J. J. Non-Viral Nucleic Acid Containing Nanoparticles as Cancer Therapeutics. *Expert Opin. Drug Deliv.* **2016**, *5247*, 1–13.
- (10) Mellott, A. J.; Forrest, M. L.; Detamore, M. S. Physical Non-Viral Gene Delivery Methods for Tissue Engineering. *Annals of Biomedical Engineering*, **2013**, *41*, 446–468.
- (11) Ibraheem, D.; Elaissari, A.; Fessi, H. Gene Therapy and DNA Delivery Systems. *Int. J. Pharm.* **2014**, *459*, 70–83.
- (12) Xiong, R.; Samal, S. K.; Demeester, J.; Skirtach, A. G.; De Smedt, S. C.; Braeckmans, K. Laser-Assisted Photoporation: Fundamentals, Technological Advances and Applications. *Adv. Phys. X* **2016**, *1*, 596–620.
- (13) Khalil, I. a; Kogure, K.; Akita, H.; Harashima, H. Uptake Pathways and Subsequent Intracellular Trafficking in Nonviral Gene Delivery. *Pharmacol. Rev.* **2006**, *58*, 32–45.
- (14) Sahay, G.; Querbes, W.; Alabi, C.; Eltoukhy, A.; Sarkar, S.; Zurenko, C.; Karagiannis, E.; Love, K.; Chen, D.; Zoncu, R.; *et al.* Efficiency of SiRNA Delivery by Lipid Nanoparticles Is Limited by Endocytic Recycling. *Nat. Biotechnol.* **2013**, *31*, 653–658.
- (15) Stewart, M. P.; Sharei, A.; Ding, X.; Sahay, G.; Langer, R.; Jensen, K. F. In Vitro and Ex Vivo Strategies for Intracellular Delivery. *Nature* **2016**, *538*, 183–192.
- (16) Zhou, J.; Yockman, J. W.; Kim, S. W.; Kern, S. E. Intracellular Kinetics of Non-

- Viral Gene Delivery Using Polyethylenimine Carriers. *Pharm. Res.* **2007**, *24*, 1079–1087.
- (17) Bishop, C. J.; Majewski, R. L.; Guiriba, T. R. M.; Wilson, D. R.; Bhise, N. S.; Quinones-Hinojosa, A.; Green, J. J. Quantification of Cellular and Nuclear Uptake Rates of Polymeric Gene Delivery Nanoparticles and DNA Plasmids via Flow Cytometry. *Acta Biomater.* **2016**, *37*, 120–130.
  - (18) Chou, L. Y. T.; Ming, K.; Chan, W. C. W. Strategies for the Intracellular Delivery of Nanoparticles. *Chem. Soc. Rev.* **2011**, *40*, 233–245.
  - (19) Behzadi, S.; Serpooshan, V.; Tao, W.; Hamaly, M. A.; Alkawareek, M. Y.; Dreaden, E. C.; Brown, D.; Alkilany, A. M.; Farokhzad, O. C.; Mahmoudi, M.; *et al.* Cellular Uptake of Nanoparticles: Journey inside the Cell. *Chem. Soc. Rev.* **2017**, *10*, 1.
  - (20) Zaki, N. M.; Tirelli, N. Gateways for the Intracellular Access of Nanocarriers: A Review of Receptor-Mediated Endocytosis Mechanisms and of Strategies in Receptor Targeting. *Expert Opin. Drug Deliv.* **2010**, *7*, 895–913.
  - (21) Doherty, G. J.; McMahon, H. T. Mechanisms of Endocytosis. *Annu. Rev. Biochem.* **2009**, *78*, 857–902.
  - (22) Sahay, G.; Alakhova, D. Y.; Kabanov, A. V. Endocytosis of Nanomedicines. *J. Control. Release* **2010**, *145*, 182–195.
  - (23) Van Der Zwaag, D.; Vanparijs, N.; Wijnands, S.; De Rycke, R.; De Geest, B. G.; Albertazzi, L. Super Resolution Imaging of Nanoparticles Cellular Uptake and Trafficking. *ACS Appl. Mater. Interfaces* **2016**, *8*, 6391–6399.
  - (24) Lazebnik, M.; Pack, D. W. Rapid and Facile Quantitation of Polyplex Endocytic Trafficking. *J. Control. Release* **2017**, *247*, 19–27.
  - (25) Elsaesser, A.; Taylor, A.; de Yanés, G. S.; McKerr, G.; Kim, E.-M.; O’Hare, E.; Howard, C. V. Quantification of Nanoparticle Uptake by Cells Using Microscopical and Analytical Techniques. *Nanomedicine* **2010**, *5*, 1447–1457.
  - (26) Drasler, B.; Vanhecke, D.; Rodriguez-Lorenzo, L.; Petri-Fink, A.; Rothen-Rutishauser, B. Quantifying Nanoparticle Cellular Uptake: Which Method Is Best? *Nanomedicine (Lond.)* **2017**, *12*, 1095–1099.
  - (27) Palchoudhury, S.; Baalousha, M.; Lead, J. R. *Methods for Measuring Concentration (Mass, Surface Area and Number) of Nanomaterials*; Elsevier, **2015**; Vol. 8.
  - (28) Guedj, A.; Kell, A. J.; Barnes, M.; Stals, S.; Gonçalves, D.; Girard, D.; Lavigne, C. Preparation, Characterization, and Safety Evaluation of Poly ( Lactide- Co - Glycolide ) Nanoparticles for Protein Delivery into Macrophages. *Int. J. Nanomedicine* **2015**, 5965–5979.
  - (29) Bai, Y.; Xing, H.; Wu, P.; Feng, X.; Hwang, K.; Lee, J. M.; Phang, X. Y.; Lu, Y.; Zimmerman, S. C. Chemical Control over Cellular Uptake of Organic Nanoparticles by Fine Tuning Surface Functional Groups. *ACS Nano* **2015**, *9*, 10227–10236.
  - (30) Jaroszeski, M.; Radcliff, G. Fundamentals of Flow Cytometry. *Mol. Biotechnol.*

**1999**, *11*, 37–53.

- (31) Adan, A.; Alizada, G.; Kiraz, Y.; Baran, Y.; Nalbant, A. Flow Cytometry: Basic Principles and Applications. *Crit. Rev. Biotechnol.* **2016**, *37*, 163–176.
- (32) Smirnov, A.; Solga, M. D.; Lannigan, J.; Criss, A. K. An Improved Method for Differentiating Cell-Bound from Internalized Particles by Imaging Flow Cytometry. *J Immunol Methods* **2015**, *423*, 60–69.
- (33) Torrano, A. a; Blechinger, J.; Osseforth, C.; Argyo, C.; Reller, A.; Bein, T.; Michaelis, J.; Bräuchle, C. A Fast Analysis Method to Quantify Nanoparticle Uptake on a Single Cell Level. *Nanomedicine* **2013**, *8*, 1815–1828.
- (34) Liu, H.; Johnston, A. P. R. A Programmable Sensor to Probe the Internalization of Proteins and Nanoparticles in Live Cells. *Angew. Chemie - Int. Ed.* **2013**, *52*, 5744–5748.
- (35) Braun, G. B.; Friman, T.; Pang, H.-B.; Pallaoro, A.; de Mendoza, T. H.; Willmore, A.-M. a; Kotamraju, V. R.; Mann, A. P.; She, Z.-G.; Sugahara, K. N.; *et al.* Etchable Plasmonic Nanoparticle Probes to Image and Quantify Cellular Internalization. *Nat. Mater.* **2014**, *13*, 1–19.
- (36) Cho, E. C.; Xie, J.; Wurm, P. A.; Xia, Y. Understanding the Role of Surface Charges in Cellular Adsorption versus Internalization by Selectively Removing Gold Nanoparticles on the Cell Surface with a I 2/KI Etchant. *Nano Lett.* **2009**, *9*, 1080–1084.
- (37) Manunta, M.; Tan, P. H.; Sagoo, P.; Kashefi, K.; George, A. J. T. Gene Delivery by Dendrimers Operates via a Cholesterol Dependent Pathway. *Nucleic Acids Res.* **2004**, *32*, 2730–2739.
- (38) Grosse, S.; Aron, Y.; Thévenot, G.; François, D.; Monsigny, M.; Fajac, I. Potocytosis and Cellular Exit of Complexes as Cellular Pathways for Gene Delivery by Polycations. *J. Gene Med.* **2005**, *7*, 1275–1286.
- (39) McLendon, P. M.; Buckwalter, D. J.; Davis, E. M.; Reineke, T. M. Interaction of Poly(Glycoamidoamine) DNA Delivery Vehicles with Cell-Surface Glycosaminoglycans Leads to Polyplex Internalization in a Manner Not Solely Dependent on Charge. *Mol. Pharm.* **2010**, *7*, 1757–1768.
- (40) dos Santos, T.; Varela, J.; Lynch, I.; Salvati, A.; Dawson, K. A. Effects of Transport Inhibitors on the Cellular Uptake of Carboxylated Polystyrene Nanoparticles in Different Cell Lines. *PLoS One* **2011**, *6*.
- (41) Ogris, M.; Wagner, E.; Steinlein, P. A Versatile Assay to Study Cellular Uptake of Gene Transfer Complexes by Flow Cytometry. *Biochim. Biophys. Acta* **2000**, *1474*, 237–243.
- (42) Summers, H. D.; Brown, M. R.; Holton, M. D.; Tonkin, J. A.; Hondow, N.; Brown, A. P.; Brydson, R.; Rees, P. Quantification of Nanoparticle Dose and Vesicular Inheritance in Proliferating Cells. *ACS Nano* **2013**, *7*, 6129–6137.
- (43) Ferrari, R.; Lupi, M.; Falcetta, F.; Bigini, P.; Paoletta, K.; Fiordaliso, F.; Bisighini, C.; Salmona, M.; D’Incalci, M.; Morbidelli, M.; *et al.* Integrated Multiplatform Method for in Vitro Quantitative Assessment of Cellular Uptake for Fluorescent

- Polymer Nanoparticles. *Nanotechnology* **2014**, *25*.
- (44) James, M. Nuclear-Associated Plasmid, but Not Cell-Associated Plasmid, Is Correlated with Transgene Expression in Cultured Mammalian Cells. *Mol. Ther.* **2000**, *1*, 339–346.
  - (45) Gottstein, C.; Wu, G.; Wong, B. J.; Zasadzinski, J. A. Precise Quantification of Nanoparticle Internalization. *ACS Nano* **2013**, *7*, 4933–4945.
  - (46) Remaut, K.; Lucas, B.; Raemdonck, K.; Braeckmans, K.; Demeester, J.; De Smedt, S. C. Protection of Oligonucleotides against Enzymatic Degradation by Pegylated and Nonpegylated Branched Polyethyleneimine. *Biomacromolecules* **2007**, *8*, 1333–1340.
  - (47) Kang, K. A.; Wang, J.; Jasinski, J. B.; Achilefu, S. Fluorescence Manipulation by Gold Nanoparticles: From Complete Quenching to Extensive Enhancement. *J. Nanobiotechnology* **2011**, *9* (11), 16.
  - (48) Rombouts, K.; Braeckmans, K.; Remaut, K. Fluorescent Labeling of Plasmid DNA and mRNA: Gains and Losses of Current Labeling Strategies. *Bioconjug. Chem.* **2016**, *27*, 280–297.
  - (49) Klingberg, H.; B. Oddershede, L.; Loeschner, K.; Larsen, E. H.; Loft, S.; Møller, P. Uptake of Gold Nanoparticles in Primary Human Endothelial Cells. *Toxicol. Res.* **2015**, *4*, 655–666.
  - (50) Costanzo, M.; Carton, F.; Marengo, A.; Berlier, G.; Stella, B.; Arpicco, S.; Malatesta, M. Fluorescence and Electron Microscopy to Visualize the Intracellular Fate of Nanoparticles for Drug Delivery. *Eur. J. Histochem.* **2016**, *60*, 107–115.
  - (51) Jiang, L.; Li, X.; Liu, L.; Zhang, Q. Cellular Uptake Mechanism and Intracellular Fate of Hydrophobically Modified Pullulan Nanoparticles. *Int. J. Nanomedicine* **2013**, *8*, 1825–1834.
  - (52) Abbad, S.; Wang, C.; Waddad, A. Y.; Huixia Lv, J. Z. Preparation , in Vitro and in Vivo Evaluation of Polymeric Nanoparticles Based on Hyaluronic Acid- Poly (Butyl Cyanoacrylate) and D-Alpha-Tocopheryl Polyethylene Glycol 1000 Succinate for Tumor- Targeted Delivery of Morin Hydrate. *Int. J. Nanomedicine* **2015**, 305–320.
  - (53) Barthel, A. K.; Dass, M.; Dröge, M.; Cramer, J. M.; Baumann, D.; Urban, M.; Landfester, K.; Mailänder, V.; Lieberwirth, I. Imaging the Intracellular Degradation of Biodegradable Polymer Nanoparticles. *Beilstein J. Nanotechnol.* **2014**, *5*, 1905–1917.
  - (54) Kim, C. S.; Li, X.; Jiang, Y.; Yan, B.; Tonga, G. Y.; Ray, M.; Solfiell, D. J.; Rotello, V. M. Cellular Imaging of Endosome Entrapped Small Gold Nanoparticles. *MethodsX* **2015**, *2*, 306–315.
  - (55) Jiang, X.; Rocker, C.; Hafner, M.; Brandholt, S.; Dorlich, R. M.; Nienhaus, G. U. Endo- and Exocytosis of Zwitterionic Quantum Dot Nanoparticles by Live HeLa Cells. *ACS Nano* **2010**, *4*, 6787–6797.
  - (56) Vanhecke, D.; Rodriguez-Lorenzo, L.; Clift, M. J. D.; Blank, F.; Petri-Fink, A.; Rothen-Rutishauser, B. Quantification of Nanoparticles at the Single-Cell Level:

- An Overview about State-of-the-Art Techniques and Their Limitations. *Nanomedicine* **2014**, *9*, 1885–1900.
- (57) Peuschel, H.; Ruckelshausen, T.; Cavellius, C.; Kraegeloh, A. Quantification of Internalized Silica Nanoparticles via STED Microscopy. *Biomed Res. Int.* **2015**, *2015*.
- (58) Bozzola, J. J.; Russell, L. D. *Electron Microscopy - Second Edition*; 1999.
- (59) Egerton, R. F. *Physical Principles of Electron Microscopy*; 2nd ed.; 2016.
- (60) Baiu, D.; Artz, N.; McElreath, M.; Menapace, B. D.; Reeder, S. B.; Grüttner, C. High Specificity Targeting and Detection of Human Neuroblastoma Using Nanoparticles. *Nanomedicine* **2015**, *10*, 2973–2988.
- (61) Havrdova, M.; Polakova, K.; Skopalik, J.; Vujtek, M.; Mokdad, A.; Homolkova, M.; Tucek, J.; Nebesarova, J.; Zboril, R. Field Emission Scanning Electron Microscopy (FE-SEM) as an Approach for Nanoparticle Detection inside Cells. *Micron* **2014**, *67*, 149–154.
- (62) George, I.; Naudin, G.; Boland, S.; Mornet, S.; Contremoulins, V.; Beugnon, K.; Martinon, L.; Lambert, O.; Baeza-Squiban, A. Metallic Oxide Nanoparticle Translocation across Human Bronchial Epithelial Barrier. *Nanoscale* **2015**, *7*, 4529–4544
- (63) Kucki, M.; Diener, L.; Bohmer, N.; Hirsch, C.; Krug, H. F.; Palermo, V.; Wick, P. Uptake of Label-Free Graphene Oxide by Caco-2 Cells Is Dependent on the Cell Differentiation Status. *J. Nanobiotechnology* **2017**, *15*, 1–18.
- (64) Brown, A. P.; Brydson, R. M. D.; Hondow, N. S. Measuring *in Vitro* Cellular Uptake of Nanoparticles by Transmission Electron Microscopy. *J. Phys. Conf. Ser.* **2014**, *522*, 012058.
- (65) Hondow, N.; Brydson, R.; Brown, A. The Use of Transmission Electron Microscopy in the Quantification of Nanoparticle Dose. *J. Phys. Conf. Ser.* **2014**, *522*, 12055.
- (66) Hondow, N.; Brown, M. R.; Starborg, T.; Monteith, A. G.; Brydson, R.; Summers, H. D.; Rees, P.; Brown, A. Quantifying the Cellular Uptake of Semiconductor Quantum Dot Nanoparticles by Analytical Electron Microscopy. *J. Microsc.* **2016**, *261*, 167–176.
- (67) Guehrs, E.; Schneider, M.; Günther, C. M.; Hessing, P.; Heitz, K.; Wittke, D.; López-Serrano Oliver, A.; Jakubowski, N.; Plendl, J.; Eisebitt, S.; *et al.* Quantification of Silver Nanoparticle Uptake and Distribution within Individual Human Macrophages by FIB/SEM Slice and View. *J. Nanobiotechnology* **2017**, *15*, 21.
- (68) Rothen-Rutishauser, B.; Kuhn, D. a; Ali, Z.; Gasser, M.; Amin, F.; Parak, W. J.; Vanhecke, D.; Fink, A.; Gehr, P.; Brandenberger, C. Quantification of Gold Nanoparticle Cell Uptake under Controlled Biological Conditions and Adequate Resolution. *Nanomedicine* **2014**, *9*, 607–621.
- (69) Ross, F. M. Opportunities and Challenges in Liquid Cell Electron Microscopy. *Science (80-. )*. **2015**, *350*, 9886-1-9886–9889.

- (70) Peckys, D. B.; de Jonge, N. Visualizing Gold Nanoparticle Uptake in Live Cells with Liquid Scanning Transmission Electron Microscopy. *Nano Lett.* **2011**, *11*, 1733–1738.
- (71) Peckys, D. B.; de Jonge, N. Gold Nanoparticle Uptake in Whole Cells in Liquid Examined by Environmental Scanning Electron Microscopy. *Microsc. Microanal.* **2014**, *20*, 189–197.
- (72) Chlanda, P.; Krijnse Locker, J. The Sleeping Beauty Kissed Awake: New Methods in Electron Microscopy to Study Cellular Membranes. *Biochem. J.* **2017**, *474*, 1041–1053.
- (73) Chinen, A. B.; Guan, C. M.; Ko, C. H.; Mirkin, C. A. The Impact of Protein Corona Formation on the Macrophage Cellular Uptake and Biodistribution of Spherical Nucleic Acids. *Small* **2017**, *13*, 1–8.
- (74) Ng, C. T.; Tang, F. M. A.; Li, J. J.; Ong, C.; Yung, L. L. Y.; Bay, B. H. Clathrin-Mediated Endocytosis of Gold Nanoparticles *In Vitro*. *Anat. Rec.* **2015**, *298*, 418–427.
- (75) Schneider, T.; Westermann, M.; Gleib, M. In Vitro Uptake and Toxicity Studies of Metal Nanoparticles and Metal Oxide Nanoparticles in Human HT29 Cells. *Arch. Toxicol.* **2017**, *91*, 3517–3527.
- (76) Saikia, J.; Yazdimamaghani, M.; Hadipour Moghaddam, S. P.; Ghandehari, H. Differential Protein Adsorption and Cellular Uptake of Silica Nanoparticles Based on Size and Porosity. *ACS Appl. Mater. Interfaces* **2016**, *8*, 34820–34832.
- (77) Krpetic, Z.; Saleemi, S.; Prior, I. A.; See, V.; Qureshi, R.; Brust, M. Negotiation of Intracellular Membrane Barriers by TAT-Modified Gold. *ACS Nano* **2011**, *5*, 5195–5201.
- (78) Orlando, A.; Colombo, M.; Prosperi, D.; Gregori, M.; Panariti, A.; Rivolta, I.; Masserini, M.; Cazzaniga, E. Iron Oxide Nanoparticles Surface Coating and Cell Uptake Affect Biocompatibility and Inflammatory Responses of Endothelial Cells and Macrophages. *J. Nanoparticle Res.* **2015**, *17*, 1–13.
- (79) Hsiao, I.-L.; Bierkandt, F. S.; Reichardt, P.; Luch, A.; Huang, Y.-J.; Jakubowski, N.; Tentschert, J.; Haase, A. Quantification and Visualization of Cellular Uptake of TiO<sub>2</sub> and Ag Nanoparticles: Comparison of Different ICP-MS Techniques. *J. Nanobiotechnology* **2016**, *14*, 1–13.
- (80) Zheng, L.-N.; Wang, M.; Wang, B.; Chen, H.-Q.; Ouyang, H.; Zhao, Y.-L.; Chai, Z.-F.; Feng, W.-Y. Determination of Quantum Dots in Single Cells by Inductively Coupled Plasma Mass Spectrometry. *Talanta* **2013**, *116*, 782–787.
- (81) Laborda, F.; Bolea, E.; Jimenez-Lamana, J. Single Particle Inductively Coupled Plasma Mass Spectrometry Powerful Tool for Nanoanalysis. *Anal. Chem.* **2014**, *86*, 2270–2278.
- (82) Amable, L.; Stephan, C.; Smith, S.; Merrifield, R. An Introduction to Single Cell ICP-MS Analysis. *PerkinElmer* **2017**.
- (83) Hou, S.; Sikora, K. N.; Tang, R.; Liu, Y.; Lee, Y. W.; Kim, S. T.; Jiang, Z.; Vachet, R. W.; Rotello, V. M. Quantitative Differentiation of Cell Surface-Bound and

- Internalized Cationic Gold Nanoparticles Using Mass Spectrometry. *ACS Nano* **2016**, *10*, 6731–6736.
- (84) Lane, L. A.; Qian, X.; Nie, S. SERS Nanoparticles in Medicine: From Label-Free Detection to Spectroscopic Tagging. *Chem. Rev.* **2015**, *115*, 10489–10529.
- (85) Stremersch, S.; Marro, M.; Pinchasik, B.-E.; Baatsen, P.; Hendrix, A.; De Smedt, S. C.; Loza-Alvarez, P.; Skirtach, A. G.; Raemdonck, K.; Braeckmans, K. Identification of Individual Exosome-Like Vesicles by Surface Enhanced Raman Spectroscopy. *Small* **2016**, *12*, 3292–3301.
- (86) Amendola, V.; Meneghetti, M.; Fiameni, S.; Polizzi, S.; Fracasso, G.; Boscaini, A.; Colombatti, M. SERS Labels for Quantitative Assays: Application to the Quantification of Gold Nanoparticles Uptaken by Macrophage Cells. *Anal. Methods* **2011**, *3*, 849–856.
- (87) Huang, J.; Zong, C.; Shen, H.; Liu, M.; Chen, B.; Ren, B.; Zhang, Z. Mechanism of Cellular Uptake of Graphene Oxide Studied by Surface-Enhanced Raman Spectroscopy. *Small* **2012**, *8*, 2577–2584.
- (88) Shao, X.; Schnau, P.; Qian, W.; Wang, X. Quantitatively Understanding Cellular Uptake of Gold Nanoparticles via Radioactivity Analysis. *J Nanosci Nanotechnol.* **2015**, *15*, 3834–3838.
- (89) Jani, P.; Halbert, G. W.; Langridge, J.; Florence, A. T. Nanoparticle Uptake by the Rat Gastrointestinal Mucosa: Quantitation and Particle Size Dependency. *J. Pharm. Pharmacol.* **1990**, *42*, 821–826.
- (90) Colombo, S.; Cun, D.; Remaut, K.; Bunker, M.; Zhang, J.; Martin-bertelsen, B.; Yagmur, A.; Braeckmans, K.; Nielsen, H. M.; Foged, C. Mechanistic Profiling of the siRNA Delivery Dynamics of Lipid – Polymer Hybrid Nanoparticles. *J. Control. Release* **2015**, *201*, 22–31.
- (91) Carapuça, E.; Azzoni, A. R.; Prazeres, D. M. F.; Monteiro, G. A.; Mergulhão, F. J. M. Time-Course Determination of Plasmid Content in Eukaryotic and Prokaryotic Cells Using Real-Time PCR. *Mol. Biotechnol.* **2007**, *37*, 120–126.
- (92) Ragelle, H.; Colombo, S.; Pourcelle, V.; Vanvarenberg, K.; Vandermeulen, G.; Bouzin, C.; Marchand-Brynaert, J.; Feron, O.; Foged, C.; Preat, V. Intracellular siRNA Delivery Dynamics of Integrin-Targeted, PEGylated Chitosan-Poly(Ethylene Imine) Hybrid Nanoparticles: A Mechanistic Insight. *J. Control. Release* **2015**, *211*, 1–9.
- (93) Vercauteren, D.; Rejman, J.; Martens, T. F.; Demeester, J.; De Smedt, S. C.; Braeckmans, K. On the Cellular Processing of Non-Viral Nanomedicines for Nucleic Acid Delivery: Mechanisms and Methods. *J. Control. Release* **2012**, *161*, 566–581.
- (94) Dutta, D.; Donaldson, J. G. Intended Specificity and Unintended Consequences. *Cell. Logist.* **2012**, *2*, 203–208.
- (95) Shang, L.; Gao, P.; Wang, H.; Popescu, R.; Gerthsen, D.; Nienhaus, G. U. Protein-Based Fluorescent Nanoparticles for Super-Resolution STED Imaging of Live Cells. *Chem. Sci.* **2017**, *8*, 2396–2400.

- (96) Herd, H.; Daum, N.; Jones, A. T.; Huwer, H.; Ghandehari, H.; Lehr, C. M. Nanoparticle Geometry and Surface Orientation Influence Mode of Cellular Uptake. *ACS Nano* **2013**, *7*, 1961–1973.
- (97) Vercauteren, D.; Vandenbroucke, R. E.; Jones, A. T.; Rejman, J.; Demeester, J.; De Smedt, S. C.; Sanders, N. N.; Braeckmans, K. The Use of Inhibitors to Study Endocytic Pathways of Gene Carriers: Optimization and Pitfalls. *Mol. Ther.* **2010**, *18*, 561–569.
- (98) Wang, T.; Wang, L.; Li, X.; Hu, X.; Han, Y.; Luo, Y.; Wang, Z.; Li, Q.; Aldalbahi, A.; Wang, L.; *et al.* Size-Dependent Regulation of Intracellular Trafficking of Polystyrene Nanoparticle-Based Drug Delivery Carriers. *ACS Appl. Mater. Interfaces* **2017**, *9*, 18619–18625.
- (99) Benmerah, A.; Bayrou, M.; Cerf-Bensussan, N.; Dautry-Varsat, A. Inhibition of Clathrin-Coated Pit Assembly by an Eps15 Mutant. *J. Cell Sci.* **1999**, *112*, 1303–1311.
- (100) Rosazza, C.; Deschout, H.; Buntz, A.; Braeckmans, K.; Rols, M.-P.; Zumbusch, A. Endocytosis and Endosomal Trafficking of DNA After Gene Electrotransfer In Vitro. *Mol. Ther. - Nucleic Acids* **2016**, *5*, e286.
- (101) Vercauteren, D.; Deschout, H.; Remaut, K.; Engbersen, J. F. J.; Jones, A. T.; Demeester, J.; De Smedt, S. C.; Braeckmans, K. Dynamic Colocalization Microscopy to Characterize Intracellular Trafficking of Nanomedicines. *ACS Nano* **2011**, *5*, 7874–7884.
- (102) Pelkmans, L.; Kartenbeck, J.; Helenius, a. Caveolar Endocytosis of Simian Virus 40 Reveals a New Two-Step Vesicular-Transport Pathway to the ER. *Nat. Cell Biol.* **2001**, *3*, 473–483.
- (103) Hayer, A.; Stoeber, M.; Ritz, D.; Engel, S.; Meyer, H. H.; Helenius, A. Caveolin-1 Is Ubiquitinated and Targeted to Intraluminal Vesicles in Endolysosomes for Degradation. *J. Cell Biol.* **2010**, *191*, 615–629.
- (104) Bassøe, C.-F.; Li, N.; Ragheb, K.; Lawler, G.; Sturgis, J.; Robinson, J. P. Investigations of Phagosomes, Mitochondria, and Acidic Granules in Human Neutrophils Using Fluorescent Probes. *Cytom. Part B Clin. Cytom.* **2003**, *51B*, 21–29.
- (105) Ragg, R.; Natalio, F.; Tahir, M. N.; Janssen, H.; Kashyap, A.; Strand, D.; Strand, S.; Tremel, W.; Chemie, A.; Duesbergweg, À.; *et al.* Molybdenum Trioxide Nanoparticles with Intrinsic Sulfite Oxidase Activity. *ACS Nano* **2014**, *8*, 5182–5189.
- (106) Wang, J.; Macewan, S. R.; Chilkoti, A. Quantitative Mapping of the Spatial Distribution of Nanoparticles in Endo-Lysosomes by Local PH. *Nano Lett.* **2017**, *17*, 1226–1232.
- (107) Martens, T. F.; Remaut, K.; Demeester, J.; De Smedt, S. C.; Braeckmans, K. Intracellular Delivery of Nanomaterials: How to Catch Endosomal Escape in the Act. *Nano Today*, **2014**, *9*, 344–364.
- (108) Richard, I.; Thibault, M.; De Crescenzo, G.; Buschmann, M. D.; Lavertu, M. Ionization Behavior of Chitosan and Chitosan-DNA Polyplexes Indicate That

- Chitosan Has a Similar Capability to Induce a Proton-Sponge Effect as PEI. *Biomacromolecules* **2013**, *14*, 1732–1740.
- (109) Benjaminsen, R. V.; Matthebjerg, M. A.; Henriksen, J. R.; Moghimi, S. M.; Andresen, T. L. The Possible “Proton Sponge ” Effect of Polyethylenimine (PEI) Does Not Include Change in Lysosomal PH. *Mol. Ther.* **2013**, *21*, 149–157.
- (110) Zhou, J.; Chau, Y. Different Oligoarginine Modifications Alter Endocytic Pathways and Subcellular Trafficking of Polymeric Nanoparticles. *Biomater. Sci.* **2016**, *4*, 1462–1472.
- (111) Zhang, L.; Yang, X.; Lv, Y.; Xin, X.; Qin, C.; Han, X.; Yang, L.; He, W.; Yin, L. Cytosolic Co-Delivery of MiRNA-34a and Docetaxel with Core-Shell Nanocarriers via Caveolae-Mediated Pathway for the Treatment of Metastatic Breast Cancer. *Sci. Rep.* **2017**, *7*, 46186.
- (112) Byrne, G. D.; Vllasaliu, D.; Falcone, F. H.; Somekh, M. G.; Stolnik, S. Live Imaging of Cellular Internalization of Single Colloidal Particle by Combined Label-Free and Fluorescence Total Internal Reflection Microscopy. *Mol. Pharm.* **2015**, *12*, 3862–3870.
- (113) Conchello, J.-A.; Lichtman, J. W. Optical Sectioning Microscopy. *Nat. Methods* **2005**, *2*, 920–931.
- (114) Pike, J. A.; Styles, I. B.; Rappoport, J. Z.; Heath, J. K. Quantifying Receptor Trafficking and Colocalization with Confocal Microscopy. *Methods* **2017**, *115*, 42–54.
- (115) Dunn, K. W.; Kamocka, M. M.; McDonald, J. H. A Practical Guide to Evaluating Colocalization in Biological Microscopy. *Am J Physiol Cell Physiol* **2011**, *300*, 723–742.
- (116) Bolte, S.; Cordelieres, F. P. A Guided Tour into Subcellular Colocalisation Analysis in Light Microscopy. *J. Microsc.* **2006**, *224*, 13–232.
- (117) Li, Y.; Shang, L.; Nienhaus, G. U. Super-Resolution Imaging-Based Single Particle Tracking Reveals Dynamics of Nanoparticle Internalization by Live Cells. *Nanoscale* **2016**, *8*, 7423–7429.
- (118) Shi, J.; Chou, B.; Choi, J. L.; Ta, A. L.; Pun, S. H. Investigation of Polyethylenimine/DNA Polyplex Transfection to Cultured Cells Using Radiolabeling and Subcellular Fractionation Methods. *Mol. Pharm.* **2013**, *10*, 2145–2156.
- (119) Manunta, M.; Izzo, L.; Duncan, R.; Jones, A. T. Establishment of Subcellular Fractionation Techniques to Monitor the Intracellular Fate of Polymer Therapeutics II. Identification of Endosomal and Lysosomal Compartments in HepG2 Cells Combining Single-Step Subcellular Fractionation with Fluorescent Imag. *J. Drug Target.* **2007**, *15*, 37–50.
- (120) Bertoli, F.; Davies, G. L.; Monopoli, M. P.; Moloney, M.; Gun’Ko, Y. K.; Salvati, A.; Dawson, K. A. Magnetic Nanoparticles to Recover Cellular Organelles and Study the Time Resolved Nanoparticle-Cell Interactome throughout Uptake. *Small* **2014**, *10*, 3307–3315.

- (121) Hofmann, D.; Tenzer, S.; Bannwarth, M. B.; Messerschmidt, C. Mass Spectrometry and Imaging Analysis of Nanoparticle-Containing Vesicles Provide a Mechanistic Insight into Cellular Trafficking. *ACS Nano* **2014**, *8*, 10077–10088.
- (122) Huefner, A.; Kuan, W. L.; Müller, K. H.; Skepper, J. N.; Barker, R. A.; Mahajan, S. Characterization and Visualization of Vesicles in the Endo-Lysosomal Pathway with Surface-Enhanced Raman Spectroscopy and Chemometrics. *ACS Nano* **2016**, *10*, 307–316.
- (123) Sakhtianchi, R.; Minchin, R. F.; Lee, K. B.; Alkilany, A. M.; Serpooshan, V.; Mahmoudi, M. Exocytosis of Nanoparticles from Cells: Role in Cellular Retention and Toxicity. *Adv. Colloid Interface Sci.* **2013**, *201–202*, 18–29.
- (124) Stremersch, S.; De Smedt, S. C.; Raemdonck, K. Therapeutic and Diagnostic Applications of Extracellular Vesicles. *J. Control. Release* **2016**, *244*, 167–183.
- (125) Busato, A.; Bonafede, R.; Bontempi, P.; Scambi, I.; Schiaffino, L.; Benati, D.; Malatesta, M.; Sbarbati, A.; Marzola, P.; Mariotti, R. Magnetic Resonance Imaging of Ultrasmall Superparamagnetic Iron Oxide-Labeled Exosomes from Stem Cells: A New Method to Obtain Labeled Exosomes. *Int. J. Nanomedicine* **2016**, *11*, 2481–2490.
- (126) Ma, D. Enhancing Endosomal Escape for Nanoparticle Mediated siRNA Delivery. *Nanoscale* **2014**, *6*, 6415.
- (127) Oh, N.; Park, J. H. Endocytosis and Exocytosis of Nanoparticles in Mammalian Cells. *Int. J. Nanomedicine* **2014**, *9*, 51–63.
- (128) Shukla, R. S.; Jain, A.; Zhao, Z.; Cheng, K. Intracellular Trafficking and Exocytosis of a Multi-Component siRNA Nanocomplex. *Nanomedicine Nanotechnology, Biol. Med.* **2016**, *12*, 1323–1334.
- (129) Yanes, R. E.; Tarn, D.; Hwang, A. A.; Ferris, D. P.; Sherman, S.; Thomas, C. R.; Lu, J.; Pyle, A. D.; Zink, J. .; Tamanoi, F. Involvement of Lysosomal Exocytosis in the Excretion of Mesoporous Silica Nanoparticles and Enhancement of Drug Delivery Effect by Exocytosis Inhibition. *Small* **2013**, *9*, 697–704.
- (130) Tlotleng, N.; Vetten, M. A.; Keter, F. K.; Skepu, A.; Tshikhudo, R.; Gulumian, M. Cytotoxicity, Intracellular Localization and Exocytosis of Citrate Capped and PEG Functionalized Gold Nanoparticles in Human Hepatocyte and Kidney Cells. *Cell Biol. Toxicol.* **2016**, *32*, 305–321.
- (131) Cui, Y.; Song, X.; Li, S.; He, B.; Yuan, L.; Dai, W.; Zhang, H.; Wang, X.; Yang, B.; Zhang, Q. The Impact of Receptor Recycling on the Exocytosis of Avβ3 Integrin Targeted Gold Nanoparticles. *Oncotarget* **2017**, *8*, 38618–38630.
- (132) Kim, C. S.; Le, N. D. B.; Xing, Y.; Yan, B.; Tonga, G. Y.; Kim, C.; Vachet, R. W.; Rotello, V. M. The Role of Surface Functionality in Nanoparticle Exocytosis. *Adv. Healthc. Mater.* **2014**, *3*, 1200–1202.
- (133) Strobel, C.; Oehring, H.; Herrmann, R.; Förster, M.; Reller, A.; Hilger, I. Fate of Cerium Dioxide Nanoparticles in Endothelial Cells: Exocytosis. *J. Nanoparticle Res.* **2015**, *17*.

- (134) Frohlich, E. Cellular Elimination of Nanoparticles. *Environ. Toxicol. Pharmacol.* **2016**, *46*, 90–94.
- (135) Slowing, I. I.; Vivero-Escoto, J. L.; Zhao, Y.; Kandel, K.; Peeraphatdit, C.; Trewyn, B. G.; Lin, V. S. Y. Exocytosis of Mesoporous Silica Nanoparticles from Mammalian Cells: From Asymmetric Cell-to-Cell Transfer to Protein Harvesting. *Small* **2011**, *7*, 1526–1532.
- (136) Takahashi, S.; Kubo, K.; Waguri, S.; Yabashi, A.; Shin, H.-W.; Katoh, Y.; Nakayama, K. Rab11 Regulates Exocytosis of Recycling Vesicles at the Plasma Membrane. *J. Cell Sci.* **2012**, *125*, 4049–4057.
- (137) Sandin, P.; Fitzpatrick, L. W.; Simpson, J. C.; Dawson, K. A. High-Speed Imaging of Rab Family Small GTPases Reveals Rare Events in Nanoparticle Trafficking in Living Cells. *ACS Nano* **2012**, *6*, 1513–1521.
- (138) Jin, H.; Heller, D. A.; Strano, M. S. Single-Particle Tracking of Endocytosis and Exocytosis of Single-Walled Carbon Nanotubes in NIH-3T3 Cells. *Nano Lett.* **2008**, *8*, 1577–1585.
- (139) McErlean, E. M.; McCrudden, C. M.; McCarthy, H. O. Delivery of Nucleic Acids for Cancer Gene Therapy: Overcoming Extra- and Intra- Cellular Barriers. *Ther. Deliv.* **2016**, *7*, 619–637.
- (140) Shete, H. K.; Prabhu, R. H.; Patravale, V. B. Endosomal Escape: A Bottleneck in Intracellular Delivery. *J. Nanosci. Nanotechnol.* **2014**, *14*, 460–474.
- (141) Varkouhi, A. K.; Scholte, M.; Storm, G.; Haisma, H. J. Endosomal Escape Pathways for Delivery of Biologicals. *J. Control. Release* **2011**, *151*, 220–228.
- (142) Wittrup, A.; Ai, A.; Liu, X.; Hamar, P.; Trifonova, R.; Charisse, K.; Manoharan, M.; Kirchhausen, T.; Lieberman, J. Visualizing Lipid-Formulated siRNA Release from Endosomes and Target Gene Knockdown. *Nat. Biotechnol.* **2015**, *33*, 870–876.
- (143) Selby, L. I.; Cortez-Jugo, C. M.; Such, G. K.; Johnston, A. P. R. Nanoescapology: Progress toward Understanding the Endosomal Escape of Polymeric Nanoparticles. *Wiley Interdiscip. Rev. Nanomedicine Nanobiotechnology* **2017**, *9*, 1–23.
- (144) Habrant, D.; Peuziat, P.; Colombani, T.; Dallet, L.; Gehin, J.; Goudeau, E.; Evrard, B.; Lambert, O.; Haudebourg, T.; Pitard, B. Design of Ionizable Lipids to Overcome the Limiting Step of Endosomal Escape: Application in the Intracellular Delivery of mRNA, DNA, and siRNA. *J. Med. Chem.* **2016**, *59*, 3046–3062.
- (145) Funhoff, A. M.; van Nostrum, C. F.; Koning, G. A.; Schuurmans-Nieuwenbroek, N. M. E.; Crommelin, D. J. A.; Hennink, W. E. Endosomal Escape of Polymeric Gene Delivery Complexes Is Not Always Enhanced by Polymers Buffering at Low pH. *Biomacromolecules* **2004**, *5*, 32–39.
- (146) Kongkatigumjorn, N.; Cortez-Jugo, C.; Czuba, E.; Wong, A. S. M.; Hodgetts, R. Y.; Johnston, A. P. R.; Such, G. K. Probing Endosomal Escape Using PHlexi Nanoparticles. *Macromol. Biosci.* **2017**, *17*, 1–11.

- (147) Salomone, F.; Cardarelli, F.; Di Luca, M.; Boccardi, C.; Nifosì, R.; Bardi, G.; Di Bari, L.; Serresi, M.; Beltram, F. A Novel Chimeric Cell-Penetrating Peptide with Membrane-Disruptive Properties for Efficient Endosomal Escape. *J. Control. Release* **2012**, *163*, 293–303.
- (148) Hornung, V.; Bauernfeind, F.; Halle, A.; Samstad, E. O.; Kono, H.; Rock, K. L.; Fitzgerald, K. A.; Latz, E. Silica Crystals and Aluminum Salts Activate the NALP3 Inflammasome through Phagosomal Destabilization. *Nat. Immunol.* **2008**, *9*, 847–856.
- (149) Krawinkel, J.; Richter, U.; Torres-Mapa, M. L.; Westermann, M.; Gamrad, L.; Rehbock, C.; Barcikowski, S.; Heisterkamp, A. Optical and Electron Microscopy Study of Laser-Based Intracellular Molecule Delivery Using Peptide-Conjugated Photodispersible Gold Nanoparticle Agglomerates. *J. Nanobiotechnology* **2016**, *14*, 2.
- (150) Kono, K.; Igawa, T.; Takagishi, T. Cytoplasmic Delivery of Calcein Mediated by Liposomes Modified with a PH-Sensitive Poly(Ethylene Glycol) Derivative. *Biochim. Biophys. Acta - Biomembr.* **1997**, *1325*, 143–154.
- (151) Itakura, S.; Hama, S.; Ohgita, T.; Kogure, K. Development of Nanoparticles Incorporating a Novel Liposomal Membrane Destabilization Peptide for Efficient Release of Cargos into Cancer Cells. *PLoS One* **2014**, *9*, 1–11.
- (152) Rehman, Z. U.; Hoekstra, D.; Zuhorn, I. S. Mechanism of Polyplex- and Lipoplex-Mediated Delivery of Nucleic Acids: Real-Time Visualization of Transient Membrane Destabilization without Endosomal Lysis. *ACS Nano* **2013**, *7*, 3767–3777.
- (153) Basha, G.; Novobrantseva, T. I.; Rosin, N.; Tam, Y. Y. C.; Hafez, I. M.; Wong, M. K.; Sugo, T.; Ruda, V. M.; Qin, J.; Klebanov, B.; *et al.* Influence of Cationic Lipid Composition on Gene Silencing Properties of Lipid Nanoparticle Formulations of siRNA in Antigen-Presenting Cells. *Mol. Ther.* **2011**, *19*, 2186–2200.
- (154) Gilleron, J.; Querbes, W.; Zeigerer, A.; Borodovsky, A.; Marsico, G.; Schubert, U.; Manygoats, K.; Seifert, S.; Andree, C.; Stöter, M.; *et al.* Image-Based Analysis of Lipid Nanoparticle-mediated siRNA Delivery, Intracellular Trafficking and Endosomal Escape. *Nat. Biotechnol.* **2013**, *31*, 638–646.
- (155) Chu, Z.; Miu, K.; Lung, P.; Zhang, S.; Zhao, S.; Chang, H.-C.; Lin, G.; Li, Q. Rapid Endosomal Escape of Prickly Nanodiamonds: Implications for Gene Delivery. *Sci. Rep.* **2015**, *5*, 11661.
- (156) Sakurai, Y.; Hatakeyama, H.; Sato, Y.; Akita, H.; Takayama, K.; Kobayashi, S.; Futaki, S.; Harashima, H. Endosomal Escape and the Knockdown Efficiency of Liposomal-siRNA by the Fusogenic Peptide ShGALA. *Biomaterials* **2011**, *32*, 5733–5742.
- (157) Akita, H.; Kogure, K.; Moriguchi, R.; Nakamura, Y.; Higashi, T.; Nakamura, T.; Serada, S.; Fujimoto, M.; Naka, T.; Futaki, S.; *et al.* Nanoparticles for Ex Vivo siRNA Delivery to Dendritic Cells for Cancer Vaccines: Programmed Endosomal Escape and Dissociation. *J. Control. Release* **2011**, *149*, 58–64.

- (158) Deng, Z. J.; Morton, S. W.; Bonner, D. K.; Gu, L.; Ow, H.; Hammond, P. T. A Plug-and-Play Ratiometric PH-Sensing Nanoprobe for High-Throughput Investigation of Endosomal Escape. *Biomaterials* **2015**, *51*, 250–256.
- (159) Wang, Z.; Luo, M.; Mao, C.; Wei, Q.; Zhao, T.; Li, Y.; Huang, G.; Gao, J. A Redox-Activatable Fluorescent Sensor for the High-Throughput Quantification of Cytosolic Delivery of Macromolecules. *Angew. Chemie - Int. Ed.* **2017**, *56*, 1319–1323.
- (160) Boeneman, K.; Delehanty, J. B.; Blanco-Canosa, J. B.; Susumu, K.; Stewart, M. H.; Oh, E.; Huston, A. L.; Dawson, G.; Ingale, S.; Walters, R.; *et al.* Selecting Improved Peptidyl Motifs for Cytosolic Delivery of Disparate Protein and Nanoparticle Materials. *ACS Nano* **2013**, *7*, 3778–3796.
- (161) Peynshaert, K.; Manshian, B. B.; Joris, F.; Braeckmans, K.; De Smedt, S. C.; Demeester, J.; Soenen, S. J. Exploiting Intrinsic Nanoparticle Toxicity: The Pros and Cons of Nanoparticle-Induced Autophagy in Biomedical Research. *Chem. Rev.* **2014**, *114*, 7581–7609.
- (162) Mizushima, N. Autophagy: Process and Function. *Genes Dev.* **2007**, *21*, 2861–2873.
- (163) Remaut, K.; Oorschot, V.; Braeckmans, K.; Klumperman, J.; De Smedt, S. C. Lysosomal Capturing of Cytoplasmic Injected Nanoparticles by Autophagy: An Additional Barrier to Non Viral Gene Delivery. *J. Control. Release* **2014**, *195*, 29–36.
- (164) Roberts, R.; Al-Jamal, W. T.; Whelband, M.; Thomas, P.; Jefferson, M.; Van Den Bossche, J.; Powell, P. P.; Kostarelos, K.; Wileman, T. Autophagy and Formation of Tubulovesicular Autophagosomes Provide a Barrier against Nonviral Gene Delivery. *Autophagy* **2013**, *9*, 667–682.
- (165) Klionsky, D. J.; Abdelmohsen, K.; Abe, A.; Abedin, M. J.; Abeliovich, H.; Arozana, A. A.; Adachi, H.; Adams, C. M.; Adams, P. D.; Adeli, K.; *et al.* Guidelines for the Use and Interpretation of Assays for Monitoring Autophagy (3rd Edition). *Autophagy* **2016**, *12*, 1–222.
- (166) Geng, J.; Klionsky, D. J. Direct Quantification of Autophagic Flux by a Single Molecule-Based Probe. *Autophagy* **2017**, *13*, 639–641.
- (167) Wu, Q.; Jin, R.; Feng, T.; Liu, L.; Yang, L.; Tao, Y.; Anderson, J. M.; Ai, H.; Li, H. Iron Oxide Nanoparticles and Induced Autophagy in Human Monocytes. *Int. J. Nanomedicine* **2017**, *12*, 3993–4005.
- (168) Ylä-Anttila, P.; Vihinen, H.; Jokitalo, E.; Eskelinen, E. L. *Monitoring Autophagy by Electron Microscopy in Mammalian Cells*; 1st ed.; Elsevier Inc., **2009**; Vol. 451.
- (169) Duan, J.; Yu, Y.; Yu, Y.; Li, Y.; Wang, J.; Geng, W.; Jiang, L.; Li, Q.; Zhou, X.; Sun, Z. Silica Nanoparticles Induce Autophagy and Endothelial Dysfunction via the PI3K/Akt/MTOR Signaling Pathway. *Int. J. Nanomedicine* **2014**, *9*, 5131–5141.
- (170) Lopes, V. R.; Loitto, V.; Audinot, J.-N.; Bayat, N.; Gutleb, A. C.; Cristobal, S. Dose-Dependent Autophagic Effect of Titanium Dioxide Nanoparticles in Human

- HaCaT Cells at Non-Cytotoxic Levels. *J. Nanobiotechnology* **2016**, *14*, 22.
- (171) Hurley, J. H.; Nogales, E. Next-Generation Electron Microscopy in Autophagy Research. *Curr. Opin. Struct. Biol.* **2016**, *41*, 211–216.
- (172) Man, N.; Chen, Y.; Zheng, F.; Zhou, W.; Wen, L. P. Induction of Genuine Autophagy by Cationic Lipids in Mammalian Cells. *Autophagy* **2010**, *6*, 449–454.
- (173) Biederbick, A.; Kern, H. .; Elsasser, H. . Monodansylcadaverine Is a Specific in Vivo Marker for Autophagic Vacuoles. *Eur. J. Cell Biol.* **1995**, *66*, 3–14.
- (174) Bravo-San Pedro, J. M.; Pietrocola, F.; Sica, V.; Izzo, V.; Sauvat, A.; Kepp, O.; Maiuri, M. C.; Kroemer, G.; Galluzzi, L. High-Throughput Quantification of GFP-LC3+ Dots by Automated Fluorescence Microscopy. *Methods Enzymol.* **2017**, *587*, 71–86.
- (175) Oh, S. hee; Choi, Y. bok; Kim, J. hyun; Weihl, C. C.; Ju, J. sun. Quantification of Autophagy Flux Using LC3 ELISA. *Anal. Biochem.* **2017**, *530*, 57–67.
- (176) Huang, D.; Zhou, H.; Gao, J. Nanoparticles Modulate Autophagic Effect in a Dispersion-Dependent Manner. *Sci. Rep.* **2015**, *5*, 14361.
- (177) Song, W.; Ma, Z.; Zhang, Y.; Yang, C. Autophagy Plays a Dual Role during Intracellular SiRNA Delivery by Lipoplex and Polyplex Nanoparticles. *Acta Biomater.* **2017**, *58*, 196–204.
- (178) Enzolifesciences. p62 ELISA kit <http://www.enzolifesciences.com/ADI-900-212/p62-elisa-kit/> (accessed Aug 24, 2017).
- (179) Cusabio. Mouse Atg5 ELISA kit <http://www.cusabio.com/ELISA-Kit/Mouse-Autophagy-protein-5ATG5-ELISA-kit-65804.html> (accessed Aug 24, 2017).
- (180) Zhong, X.; Panus, D.; Ji, W.; Wang, C. Modulating Polyplex-Mediated Gene Transfection by Small-Molecule Regulators of Autophagy. *Mol. Pharm.* **2015**, *12*, 932–940.
- (181) Ho, Y. P.; Chen, H. H.; Leong, K. W.; Wang, T. H. Evaluating the Intracellular Stability and Unpacking of DNA Nanocomplexes by Quantum Dots-FRET. *J. Control. Release* **2006**, *116*, 83–89.
- (182) Tachibana, R.; Harashima, H.; Shinohara, Y.; Kiwada, H. Quantitative Studies on the Nuclear Transport of Plasmid DNA and Gene Expression Employing Nonviral Vectors. *Adv. Drug Deliv. Rev.* **2001**, *52*, 219–226.
- (183) Pollard, H.; Remy, J. S.; Loussouarn, G.; Demolombe, S.; Behr, J. P.; Escande, D. Polyethylenimine but Not Cationic Lipids Promotes Transgene Delivery to the Nucleus in Mammalian Cells. *J. Biol. Chem.* **1998**, *273*, 7507–7511.
- (184) Grigsby, C. L.; Leong, K. W. Balancing Protection and Release of DNA : Tools to Address a Bottleneck of Non-Viral Gene Delivery Balancing Protection and Release of DNA : Tools to Address a Bottleneck of Non-Viral Gene Delivery. *J. R. Soc. Interface* **2010**, *7*, S67–S82.
- (185) Buyens, K.; Lucas, B.; Raemdonck, K.; Braeckmans, K.; Vercammen, J.; Hendrix, J.; Engelborghs, Y.; De Smedt, S. C.; Sanders, N. N. A Fast and Sensitive Method for Measuring the Integrity of SiRNA-Carrier Complexes in Full

- Human Serum. *J. Control. Release* **2008**, *126*, 67–76.
- (186) Schaffer, D. V.; Fidelman, N. A.; Dan, N.; Lauffenburger, D. A. Vector Unpacking as a Potential Barrier for Receptor-Mediated Polyplex Gene Delivery. *Biotechnol. Bioeng.* **2000**, *67*, 598–606.
- (187) Trusov, G. A.; Ulasov, A. V; Beletkaia, E. A.; Khramtsov, Y. V; Durymanov, M. O.; Rosenkranz, A. A.; Sverdlov, E. D.; Sobolev, A. S. Investigation of Transport and Unpacking Mechanisms of Polyplexes for Transfection Efficacy on Different Cell Lines. *Biochem. Biophys.* **2011**, *437*, 77–79.
- (188) Chen, H. H.; Ho, Y.-P.; Jiang, X.; Mao, H.-Q.; Wang, T.-H.; Leong, K. W. Quantitative Comparison of Intracellular Unpacking Kinetics of Polyplexes by a Model Constructed From Quantum Dot-FRET. *Mol. Ther.* **2008**, *16*, 324–332.
- (189) Lucas, B.; Remaut, K.; Sanders, N. N.; Braeckmans, K.; De Smedt, S. C.; Demeester, J. Studying the Intracellular Dissociation of Polymer-Oligonucleotide Complexes by Dual Color Fluorescence Fluctuation Spectroscopy and Confocal Imaging. *Biochemistry* **2005**, *44*, 9905–9912.
- (190) Park, I. K.; Ng, C. P.; Wang, J.; Chu, B.; Yuan, C.; Zhang, S.; Pun, S. H. Determination of Nanoparticle Vehicle Unpackaging by MR Imaging of a T2 Magnetic Relaxation Switch. *Biomaterials* **2008**, *29*, 724–732.
- (191) Magadala, P.; Amiji, M. Epidermal Growth Factor Receptor-Targeted Gelatin-Based Engineered Nanocarriers for DNA Delivery and Transfection in Human Pancreatic Cancer Cells. *AAPS J.* **2008**, *10*, 565–576.
- (192) Bu, Y.; Huang, H.; Zhou, G. Direct Polymerase Chain Reaction (PCR) from Human Whole Blood and Filter-Paper-Dried Blood by Using a PCR Buffer with a Higher PH. *Anal. Biochem.* **2008**, *375*, 370–372.
- (193) Tachibana, R.; Harashima, H.; Ide, N.; Ukitsu, S.; Ohta, Y.; Suzuki, N.; Kikuchi, H.; Shinohara, Y.; Kiwada, H. Quantitative Analysis of Correlation between Number of Nuclear Plasmids and Gene Expression Activity after Transfection with Cationic Liposomes. *Pharm. Res.* **2002**, *19*, 377–381.
- (194) Thompson, N. L. Fluorescence Correlation Spectroscopy. In *Topics of fluorescence spectroscopy*; **2002**; pp. 337–378.
- (195) Sasaki, A.; Kinjo, M. Monitoring Intracellular Degradation of Exogenous DNA Using Diffusion Properties. *J. Control. Release* **2010**, *143*, 104–111.
- (196) Sasaki, A.; Yamamoto, J.; Jin, T.; Kinjo, M. Raster Image Cross-Correlation Analysis for Spatiotemporal Visualization of Intracellular Degradation Activities against Exogenous DNAs. *Sci. Rep.* **2015**, *5*, 14428.
- (197) Hirsch, M.; Helm, M. Live Cell Imaging of Duplex siRNA Intracellular Trafficking. *Nucleic Acids Res.* **2015**, *43*, 4650–4660.
- (198) Uchiyama, H.; Hirano, K.; Kashiwasake-Jibu, M.; Taira, K. Detection of Undegraded Oligonucleotides in Vivo by Fluorescence Resonance Energy Transfer. *J. Biol. Chem.* **1996**, *271*, 380–384.
- (199) Chen, H. H.; Ho, Y.-P.; Jiang, X.; Mao, H.-Q.; Wang, T.-H.; Leong, K. W. Simultaneous Non-Invasive Analysis of DNA Condensation and Stability by Two-

- Step QD-FRET. *Nano T* **2009**, *4*, 125–134.
- (200) Remaut, K.; Lucas, B.; Braeckmans, K.; Sanders, N. N.; De Smedt, S. C.; Demeester, J. FRET-FCS as a Tool to Evaluate the Stability of Oligonucleotide Drugs after Intracellular Delivery. *J. Control. Release* **2005**, *103*, 259–271.
- (201) Lechardeur, D.; Sohn, K. J.; Haardt, M.; Joshi, P. B.; Monck, M.; Graham, R. W.; Beatty, B.; Squire, J.; O’Brodoovich, H.; Lukacs, G. L. Metabolic Instability of Plasmid DNA in the Cytosol: A Potential Barrier to Gene Transfer. *Gene Ther.* **1999**, *6*, 482–497.
- (202) Nguyen, J.; Szoka, F. C. Nucleic Acid Delivery: The Missing Pieces of the Puzzle? *Acc. Chem. Res.* **2012**, *45*, 1153–1162.
- (203) Vaughan, E. E.; DeGiulio, J. V; Dean, D. a. Intracellular Trafficking of Plasmids for Gene Therapy: Mechanisms of Cytoplasmic Movement and Nuclear Import. *Curr. Gene Ther.* **2006**, *6*, 671–681.
- (204) Tammam, S. N.; Azzazy, H. M. E.; Lamprecht, A. How Successful Is Nuclear Targeting by Nanocarriers? *J. Control. Release* **2016**, *229*, 140–153.
- (205) Symens, N.; Soenen, S. J.; Rejman, J.; Braeckmans, K.; De Smedt, S. C.; Remaut, K. Intracellular Partitioning of Cell Organelles and Extraneous Nanoparticles during Mitosis. *Adv. Drug Deliv. Rev.* **2012**, *64*, 78–94.
- (206) Dean, D.; Strong, D.; Zimmer, W. Nuclear Entry of Nonviral Vectors. *Gene Ther.* **2005**, *12*, 881–890.
- (207) Lam, A.; DA, D. Progress and Prospects: Nuclear Import of Nonviral Vectors. *Gene Ther.* **2010**, *17*, 439–447.
- (208) Xu, Y.; Liang, W.; Qiu, Y.; Cespi, M.; Palmieri, G. F.; Mason, A. J.; Lam, J. K. W. Incorporation of a Nuclear Localization Signal in PH Responsive LAH4-L1 Peptide Enhances Transfection and Nuclear Uptake of Plasmid DNA. *Mol. Pharm.* **2016**, *13*, 3141–3152.
- (209) Chen, K.; Guo, L.; Zhang, J.; Chen, Q.; Wang, K.; Li, C.; Li, W.; Qiao, M.; Zhao, X.; Hu, H.; *et al.* A Gene Delivery System Containing Nuclear Localization Signal: Increased Nucleus Import and Transfection Efficiency with the Assistance of RanGAP1. *Acta Biomater.* **2017**, *48*, 215–226.
- (210) Huo, S.; Jin, S.; Ma, X.; Xue, X.; Yang, K.; Kumar, A.; Wang, P. C.; Zhang, J.; Hu, Z.; Liang, X. J. Ultrasmall Gold Nanoparticles as Carriers for Nucleus-Based Gene Therapy Due to Size-Dependent Nuclear Entry. *ACS Nano* **2014**, *8*, 5852–5862.
- (211) Cohen, R. N.; van der Aa, M. A. E. M.; Macaraeg, N.; Lee, A. P.; Szoka, F. C. Quantification of Plasmid DNA Copies in the Nucleus after Lipoplex and Polyplex Transfection. *J. Control. Release* **2009**, *135*, 166–174.
- (212) Moriguchi, R.; Kogure, K.; Iwasa, A.; Akita, H.; Harashima, H. Non-Linear Pharmacodynamics in a Non-Viral Gene Delivery System: Positive Non-Linear Relationship between Dose and Transfection Efficiency. *J. Control. Release* **2006**, *110*, 605–609.
- (213) Tammam, S. N.; Azzazy, H. M. E.; Breitinger, H. G.; Lamprecht, A. Chitosan

- Nanoparticles for Nuclear Targeting: The Effect of Nanoparticle Size and Nuclear Localization Sequence Density. *Mol. Pharm.* **2015**, *12*, 4277–4289.
- (214) Sahl, S. J.; Hell, S. W.; Jakobs, S. Fluorescence Nanoscopy in Cell Biology. *Nat. Rev. Mol. Cell Biol.* **2017**.
- (215) Rombouts, K.; Martens, T. F.; Zagato, E.; Demeester, J.; De Smedt, S. C.; Braeckmans, K.; Remaut, K. Effect of Covalent Fluorescence Labeling of Plasmid DNA on Its Intracellular Processing and Transfection with Lipid-Based Carriers. *Mol. Pharm.* **2014**, *11*, 1359–1368.

# Chapter 2

## The Proton Sponge Hypothesis: Fable or Fact?

**A manuscript of this chapter is under review:**

Vermeulen, L.M.P.<sup>1,2</sup>, De Smedt, S.C.<sup>1,3</sup>, Remaut, K.<sup>1,3</sup>, Braeckmans, K.<sup>1,2</sup> The Proton Sponge Hypothesis: Fable or Fact? *Eur. J. Pharm. Biopharm.* **2018**

<sup>1</sup>Lab. General Biochemistry & Physical Pharmacy, Ghent University, Ottergemsesteenweg 460, Ghent, Belgium

<sup>2</sup>Centre for Nano- and Biophotonics, Ghent University, Ottergemsesteenweg 460, Ghent, Belgium

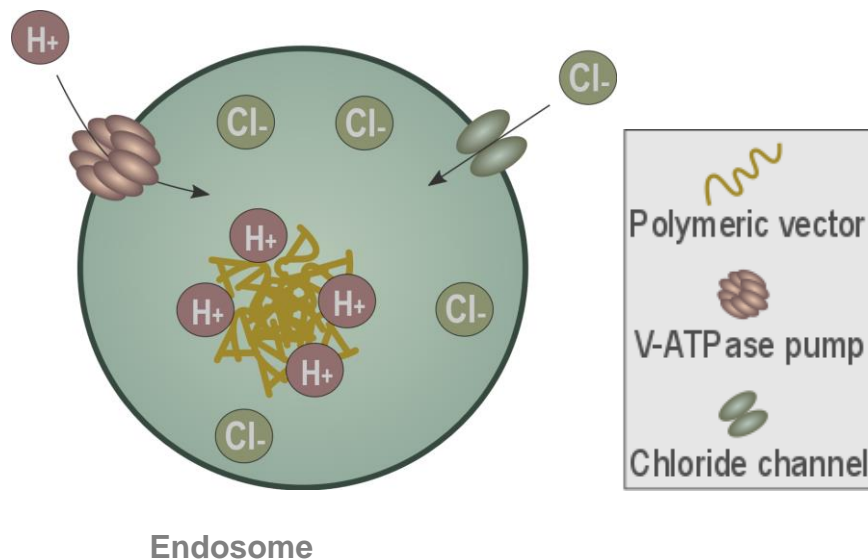
<sup>3</sup>Cancer Research Institute Ghent (CRIG)

## TABLE OF CONTENTS

1	INTRODUCTION .....	72
2	THE DISCOVERY OF THE PROTON SPONGE HYPOTHESIS .....	73
3	EVIDENCE PRO AND CON THE PROTON SPONGE EFFECT.....	75
3.1	Buffering effect of polymers .....	75
3.2	Acidification of endosomes .....	76
3.3	Chloride accumulation and endosomal swelling .....	77
4	BEYOND POLYMER BUFFER CAPACITY: ADDITIONAL FACTORS THAT INFLUENCE THE PROTON SPONGE HYPOTHESIS .....	79
4.1	Polymer swelling .....	79
4.2	Membrane destabilization.....	80
5	CONCLUSION .....	82

## ABSTRACT

In non-viral gene therapy, cationic polymers and lipids are frequently used to encapsulate macromolecular therapeutics into nanomedicines. During their journey to deliver the cargo to the intended intracellular target, many biological barriers need to be overcome. One of the major bottlenecks for efficient transfection is the endosomal barrier since nanomedicines often remain entrapped inside endosomes and are trafficked towards the lysosomes where the cargo is degraded. For cationic polymers, the proton sponge hypothesis was introduced in the late '90s as a way to explain their endosomal escape properties. However, to date, no consensus has been reached in the scientific community about the validity of this hypothesis due to many contradictory reports. Here we review the sometimes conflicting reports that have been published on the proton sponge hypothesis. We also discuss membrane destabilization and polymer swelling as additional factors that might influence endosomal escape of polyplexes. Based on the key publications on this subject, we aim to launch a consensus on the role of the proton sponge hypothesis in endosomal escape.



## 1 INTRODUCTION

Non-viral gene therapy vectors, that are used to deliver therapeutic macromolecules to their desired intracellular (IC) target, are typically subdivided into liposomes (using a lipid carrier) and polyplexes (using a polymeric carrier).<sup>1</sup> Unfortunately, non-viral vectors still lack the capacity of transfecting host cells as efficiently as their viral counterparts. This can be explained by the fact that viruses have evolved over millions of years to become highly efficient in evading the cellular barriers.<sup>2,3</sup> This becomes evident when comparing the relatively high amount of viral vectors that go into clinical trials as opposed to the few non-viral ones that have reached this stage (>70% of clinical trials concerns viral vectors).<sup>4</sup> To become as efficient as their viral competitors, non-viral vectors should improve their ability to conquer the many cellular barriers that are currently preventing them from reaching their full potential.<sup>5</sup>

In **Chapter 1**, we gave an extensive overview of the intracellular barriers that are encountered by nanomedicines (NMs) after reaching their target cell. Even though each barrier represents a critical step towards achieving effective delivery of nucleic acids, the release of genetic cargo from endosomes, referred to as endosomal escape, appears to be a major bottleneck for gene therapy.<sup>6-8</sup> Indeed, after gaining entrance to the intracellular milieu through endocytosis, the vast majority of NMs remains entrapped inside the endosomes, thereby inhibiting the cargo to interact with its target.<sup>9</sup> Furthermore, these NMs will be trafficked towards the lysosomes during endosomal entrapment, where lysosomal digestive enzymes may cause degradation of the macromolecular therapeutic cargo.<sup>10,11</sup> Several strategies have been explored to promote endosomal escape of non-viral nanoparticles.<sup>12,13</sup> The most well-known and intensively studied strategy for endosomal escape of NMs based on cationic polymers is the so-called 'proton sponge effect'.<sup>14</sup> First discovered by Behr in the '90s,<sup>15</sup> the proton sponge hypothesis has ruffled a few feathers over the years with both supporters and opponents. We will discuss the discovery and the principle of the proton sponge hypothesis and we will reflect on the often conflicting reports that have been published on this subject over the years. Based on this reflection, we will conclude on the role of the proton sponge hypothesis related to endosomal escape of NMs based on buffering polymers.

## 2 THE DISCOVERY OF THE PROTON SPONGE HYPOTHESIS

Cationic polymers are able to form polyplexes with nucleic acids through electrostatic interactions and are being explored for many years to transfer nucleic acids to the cell's interior.<sup>16,17</sup> One of the first cationic polymers explored for nucleic acid delivery was poly-L-lysine (PLL) (**Figure 2.1 A**). However, since it failed to transfect cells on its own, it was quickly realized that the addition of other compounds would be required to induce endosomal release (e.g. chloroquine or fusogenic peptides that cause endosome disruption).<sup>14,18</sup> During the early '90s, it was discovered that several cationic polymers with substantial buffering capacity below physiological pH (e.g. lipopolyamines (**Figure 2.1 B**) and polyamidoamines) were able to mediate high transfection efficiencies without the need of adding such membrane-disruptive agents.<sup>19,20</sup> This observation inspired Bousif *et al.* in 1995 to test the gene delivery potential of polyethylenimine (PEI; structure shown in **Figure 2.1 C-D**), a synthetic cationic polymer with high amine density and high buffer capacity. Although the cellular mechanisms underlying this relationship were not understood, several hypotheses were proposed as possible explanations: endosome buffering could i) protect DNA from lysosomal nucleases; ii) alter endosomal trafficking and iii) alter osmolarity, which could lead to osmotic swelling and subsequent endosome disruption.<sup>21</sup> The latter hypothesis is currently known to be an essential part of the proton sponge hypothesis.

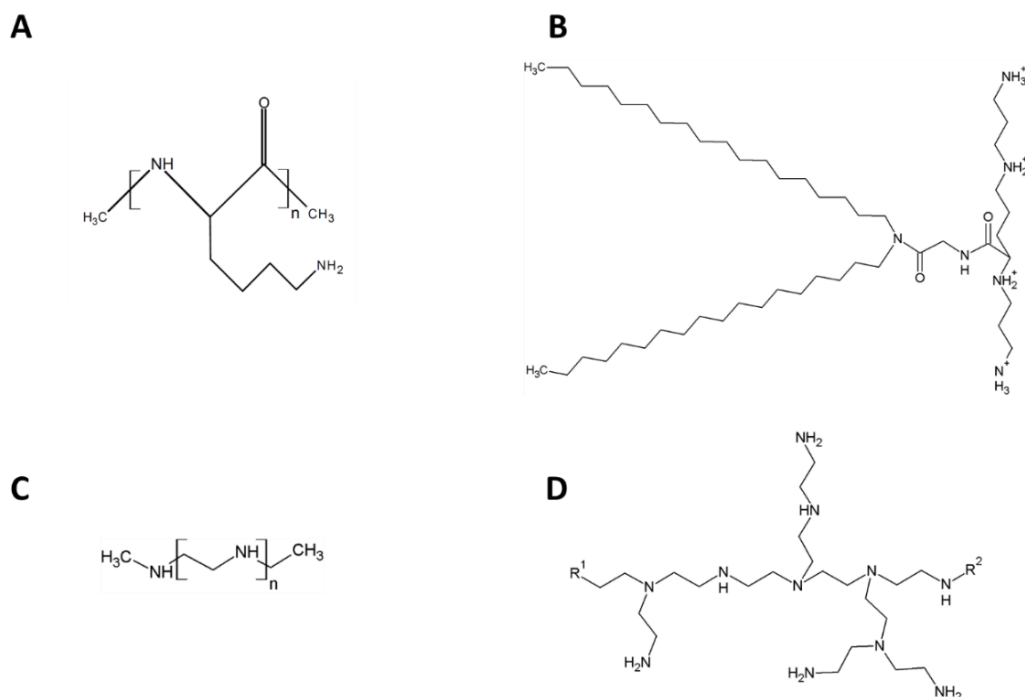


**Figure 2.1 Chemical structures of cationic polymers used for mediating transfection efficiency.** (A) Poly-L-lysine (PLL) (B) the lipopolyamine DOGS (C) linear polyethylenimine (PEI) (D) branched PEI

Indeed, some years later, in 1997, Behr and colleagues summarized the essence of the proton sponge hypothesis as follows: “*The accumulation of protons brought in by the endosomal ATPase is coupled to an influx of chloride anions. In the presence of PEI there will be a large increase in the ionic concentration within the endosome resulting in osmotic swelling of the endosome. Moreover, PEI protonation will also expand its polymeric network by internal charge repulsion. With the two phenomena occurring simultaneously, it is likely that endosomal life expectancy is sorely reduced! Taking into account the protonation profile of PEI we can expect that about a third of the N-atoms in the molecule participate in the swelling action, making the molecule a virtual proton sponge.*”<sup>15</sup> A schematic representation of the proton sponge hypothesis, as proposed by Behr, is depicted in **Figure 2.2**. Over the years, several cationic polymers (usually containing protonable secondary and/or tertiary amine groups with a pKa close to endosomal/lysosomal pH) were found to exhibit high transfection efficiencies, a quality that was generally attributed to the proton sponge phenomenon.<sup>14</sup>

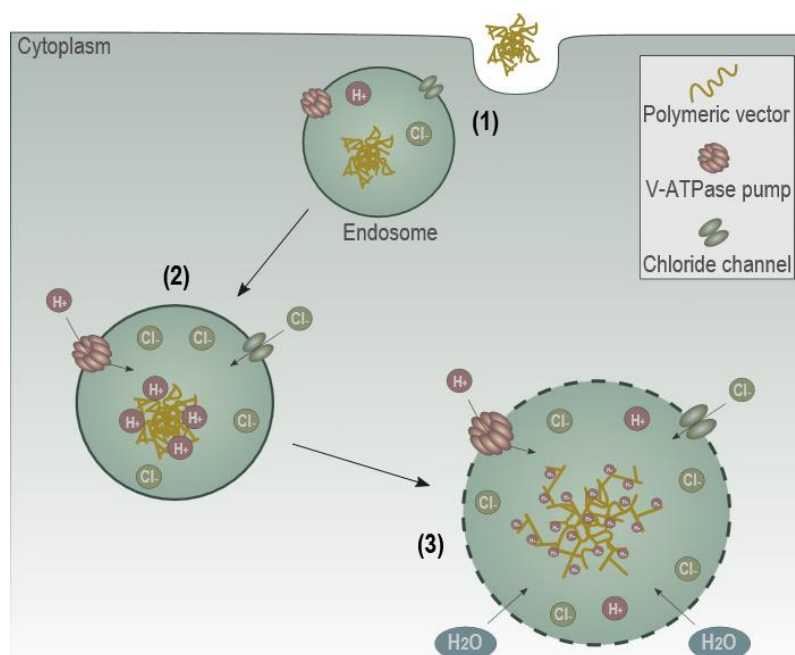


**Figure 2.2 The proton sponge hypothesis according to Behr and colleagues.**<sup>15</sup> **(1)** When polyplexes enter the cells through endocytosis, they reside inside endosomal vesicles. **(2)** Upon maturation, the membrane-bound V-ATPase proton pumps actively translocate protons into the endosomal lumen. Since the polymers used in the proton sponge hypothesis have a high buffer capacity, they are able to bind these protons, thereby limiting the acidification of the endosome. **(3)** As a result, the proton pumps will translocate even more protons to the endosomal compartment in an attempt to lower the pH. The translocation of protons is accompanied by entry of chloride ions (to maintain the charge balance) which will lead to an increase in ionic concentration and influx of water to maintain osmolarity. The influx of water molecules generates an osmotic pressure that makes the endosome swell and, combined with swelling of the polymer due to internal charge repulsion, eventually causes endosomal rupture with release of the endosomal content into the cytosol.

### 3 EVIDENCE PRO AND CON THE PROTON SPONGE EFFECT

Ever since the proposition of the proton sponge effect as a gene transfer mechanism there have been supporters of the hypothesis on the one side and critics on the other side. Indeed, there is a substantial amount of evidence to support both parties. Although the proton sponge effect used to be linked predominantly to the buffering capacity of the polymer, recent findings indicate that membrane destabilization might play a substantial role in this process as well. In this section, we will comment on the data that has been collected over the years regarding the essential components that govern the proton sponge hypothesis. These components include the buffering effect of polymers, the acidification of endosomes and endosomal swelling. In the next section, we will contemplate on the added value of polymer swelling and membrane destabilization to the osmotic forces that are at the basis of the proton sponge hypothesis.

#### 3.1 Buffering effect of polymers

Since the buffer capacity of polymers is at the basis of the proton sponge hypothesis, it seems reasonable to test its validity by investigating the relation between buffer capacity of the polymer and the amount of transfection efficiency it can induce. The most well-known example is the comparison between PLL and PEI. PLL, with low buffer capacity at endo-lysosomal pH, was unable to induce cell transfection, whereas PEI, with high buffer capacity at endo-lysosomal pH, produced high transfection efficiency.<sup>22</sup> Singh *et al.* synthesized glycerol-crosslinked PEIs in order to produce polymers with different buffer capacities but similar uptake, DNA binding and unpacking. They confirmed that decreasing the buffer capacity in the endolysosomal pH range also decreased transfection efficiency.<sup>23</sup> The importance of the buffering moieties was further confirmed by removing the buffer capacity of PEI through N-quaternization, a manipulation which again resulted in a substantial reduction of transfection efficiency.<sup>24,25</sup> Pack *et al.* developed complexes of pDNA with transferrin-conjugated PLL and gluconic acid-modified polyhistidine. Transferrin-conjugated PLL was used to maximize DNA condensation and to provide a ligand for endocytosis. Gluconic acid-modified polyhistidine, containing imidazole groups with pKa of 6.15, was added to the complex to provide buffer capacity. In accordance with the proton sponge hypothesis, the authors showed that the addition of polyhistidine greatly enhanced the level of transfection.<sup>26</sup> Similar evidence was provided by Midoux *et al.* who found that partially substituting PLL with histidyl residues increased transfection efficiency.<sup>27</sup>

At the same time evidence arose that pointed against the proton sponge effect. Funhoff *et al.* added an extra amine group with pKa 5 to pDMAEMA (poly(2-dimethylamino ethyl)-methacrylate) in order to increase the buffer capacity of the polymer. Surprisingly they found that these polymers exhibited lower transfection efficiencies than the original pDMAEMA. After addition of a membrane disruptive peptide, the transfection efficiency was restored, suggesting that the decrease in transfection was due to limited endosomal escape.<sup>28</sup> Forrest *et al.* generated PEI derivatives by acetylation of primary amines; a modification that resulted in a decreased buffer capacity. They observed a 21-fold increase in transfection efficiency compared to unmodified PEI. However, as pointed out by the authors it could not be excluded that increased transfection was the consequence of altered vector unpacking, endocytic trafficking or increased lipophilicity of the polymers.<sup>29</sup> This is indeed a point of crucial importance: polymer modifications might alter the carrier's performance at the level of IC barriers preceding or following endosomal escape and looking at the endpoint of transfection might not be the best approach to evaluate the proton sponge effect.

### **3.2 Acidification of endosomes**

Rather than by polymer modifications, others have challenged the validity of the proton sponge hypothesis by looking into endosomal acidification. The proton sponge hypothesis states that an intraluminal influx of protons (and consequently chloride ions and water) is needed to increase the osmotic pressure inside the endosome, eventually leading to the bursting of the endosome. Rehman *et al.* evaluated the necessity of endosomal acidification on the induction of endosomal escape by pre-incubating HeLa cells with Bafilomycin A1, which prevents endosome acidification by blocking the V-ATPase pump. Rather than looking at the final transfection efficiency, they used an assay that evaluated endosomal escape frequency directly *via* co-incorporation of fluorescently labeled oligonucleotides (ONs) into the polyplexes. Upon endosomal escape, the ONs spread towards the cytoplasm and eventually accumulate into the nucleus. The authors found that in control cells, treated with PEI polyplexes, virtually all cells showed ON accumulation inside the nucleus, indicative of endosomal escape, while in Bafilomycin A1-treated cells, the ONs remained entrapped within the endosomes.<sup>30</sup> Consequently, treatment with Bafilomycin A1 inhibited transfection efficiency of PEI polyplexes, an observation also reported by several others before.<sup>24,27,30-32</sup> These findings clearly illustrate that the endosomal acidification process is essential for PEI-mediated transfection, as proposed by the proton sponge hypothesis. In a second set of experiments, researchers evaluated the effect of buffering polymers on the actual pH inside the endosomes.

Several reports showed that endosomal acidification slows down after administration of buffering polymers, whereas the pH of endosomes containing a non-buffering polymer decreases more rapidly.<sup>22,24</sup>

These observations are contradicted by others, who found that buffering polymers are unable to increase endolysosomal pH, potentially disproving the proton sponge effect.<sup>33,34</sup> For instance, Godbey *et al.* measured lysosomal pH (using LysoSensor Yellow/Blue) 2.5 – 5 h after transfection with PEI and did not see lysosomal buffering. However, it should be noted that the authors also stated that pDNA/PEI polyplexes did not interact with lysosomes, stained with LysoTracker Red, which makes the conclusions rather confounding.<sup>35</sup> Further adding to the debate, the lack of colocalization with LysoTracker in microscopy images was proposed by several researchers to be a confirmation of the proton sponge hypothesis since the buffering effect of the polymer inhibits staining with acidotropic dyes such as LysoTracker.<sup>36,37</sup> Moreover, the successful colocalization between polymer and LysoTracker does not necessarily implicate that buffering polymers did not buffer the endosome. Indeed, an increased flux of protons into the endosome could allow acidification of the endosome once the buffering polymer is fully protonated. Thus, even when polymers do exert a buffering effect in endosomes, this is no guarantee that the eventual pH of the vesicle remains increased.<sup>33,38,39</sup>

### **3.3 Chloride accumulation and endosomal swelling**

According to the proton sponge hypothesis, chloride ions migrate towards the endosomal interior following the influx of protons, for reasons of charge neutralization. As such, the proton sponge hypothesis has been tested by evaluating the concentration of chloride ions inside the endosomes with and without buffering polymer. Sonawane *et al.* developed a fluorescent Cl<sup>-</sup> indicator that enabled the measurement of endosomal chloride concentrations. They found that the addition of Bafilomycin A1 not only inhibited acidification, but also hindered the increase in endosomal chloride concentration, providing evidence that the influx of protons in endosomes is indeed accompanied by an influx of chloride ions.<sup>40</sup> Next, they used this probe to examine the endosomal chloride concentration after administration of PLL and PEI. Results showed an enhanced chloride accumulation for PEI polyplexes (115 mM at 60min) as compared to PLL polyplexes (80 mM at 60min), providing direct evidence that these polymers provoke an influx of chloride ions.<sup>22</sup> The influx of chloride ions is believed to be accompanied by entry of water molecules, creating an osmotic pressure, which induces swelling and eventually endosomal rupture. This was investigated by Sonawane *et al.* via light microscopy who confirmed that PEI polyplexes induced a 140% increase of endosomal volume, whereas this was only 20% for PLL polyplexes.<sup>22</sup> Likewise, Merdan

*et al.* observed an increase in vesicle size after administration of PEI through confocal microscopy, which they attributed to osmotic swelling or fusion with other PEI-containing vesicles.<sup>31</sup>

In order to elucidate whether the osmotic stress, produced by the proton sponge effect, can by itself induce endosomal membrane rupture, Benjaminsen *et al.* measured lysosomal PEI concentrations and used these concentrations to calculate the critical size of the lysosomes at which they might rupture. Since they calculated that the majority ( $\pm 63\%$ ) of lysosomes needs to swell to a diameter above 1.6  $\mu\text{m}$  to let them burst, they concluded that only a small fraction of the lysosomes will burst because of osmotic swelling and that it is uncertain that this is the dominant effect of endosomal rupture. However, they also acknowledged that a very limited amount of bursts could already be sufficient to induce transfection.<sup>33</sup> Won *et al.* calculated the osmotic pressure which may rise in endosomal vesicles with a diameter of 100-150 nm upon lowering the pH of the endosome from 7.4 to 5.0. They found that the osmotic pressure, originating from a single polyplex that consists of 5 pDNA strands with 5000 base pairs, will expand the vesicle membrane by 2.3%. Since lipid vesicles are able to withstand surface expansion up to 2-5%, the authors claim that the osmotic pressure build-up is probably insufficient to cause endosome disruption. However, they do not exclude that it is likely to be a significant contributing factor to the eventual disruption of the endosomal membrane.<sup>41</sup> It must be noted that it is very well possible for endosomes to contain more than a single polyplex and that the amount of polymer in a polyplex may vary. These are two factors that can greatly influence the effective proton sponge capacity. As will be shown in **Chapter 3**, a third factor that should be reckoned with is endosomal size, a cell type-dependent property. Cell types that contain small endosomes would need to accumulate less polyplexes compared to cell types that have larger endosomes in order to induce efficient endosomal bursting via the proton sponge effect.

As discussed above, experimental evidence which supports a proton sponge effect to occur as a consequence of buffering polymers clearly exists. However, to which extent this mechanism is able to introduce endosomal escape is still a matter of debate. The above-mentioned mathematical models, that describe the osmotic swelling resulting from buffering polymers, make us believe that the osmotic effect alone is perhaps insufficient to induce endosomal bursting and hint towards the involvement of additional factors that contribute to effective endosomal escape.

## 4 BEYOND POLYMER BUFFER CAPACITY: ADDITIONAL FACTORS THAT INFLUENCE THE PROTON SPONGE HYPOTHESIS

### 4.1 Polymer swelling

In 1997, the expansion of the polymeric network was first added as an extension of the proton sponge hypothesis.<sup>15</sup> The ability of polymers to unfold into an extended conformation after protonation increases the volume and space taken up by the polymer, as can be seen from **Figure 2.3**.<sup>42</sup> Indeed, it has been shown that upon protonation of PEI, the polymer chain elongates due to electrostatic repulsion. This has been demonstrated by measuring the distance between two amine groups with varying protonation states. Singly protonated ethylenediamine displayed an average distance of 2.9 Å while for doubly protonated molecules, the average distance increased to around 3.5 Å.<sup>43</sup> Tang *et al.* first demonstrated that polymer expansion could indeed contribute to increased transfection. They used intact and fractured polyamidoamine dendrimers to vary the degree of flexibility and their ability to expand in response to a decreasing pH. A superior transfection efficiency was found after administration of fractured dendrimers with optimal flexibility compared to intact dendrimers with sterical constraints.<sup>44</sup> Based on these results, Szoka proposed to refer to the volumetric expansion of polymers upon protonation as the 'umbrella hypothesis'.<sup>42</sup> It must be noted, however, that a higher degree of vector unpacking in flexible polymers could provide an alternative explanation for the increased transfection instead of a better endosomal escape efficiency.

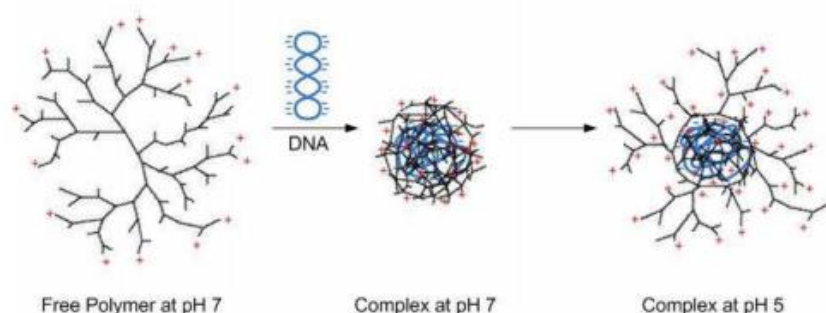


**Figure 2.3 Schematic representation of the umbrella hypothesis.** Cationic polymers condense negatively charged NAs into compact NMs. Upon acidification of the endosomes, amine groups of the polymer are protonated, leading to the elongation of the polymer chain due to electrostatic repulsion. The terminal branches of the polymer unfold from a collapsed state into an extended conformation. Image reprinted with permission of <sup>42</sup>. © 2012 American Chemical Society.

## 4.2 Membrane destabilization

Recently, it was determined *via* molecular dynamics simulations that elongated PEI chains can interact with the endosomal membrane, leading to the formation of hydrophilic pores in the lipid bilayer. These interactions can cause a local lipid bilayer destabilization, further contributing to the release of endosomal content.<sup>45</sup> Already in 2002, Thomas and Klibanov looked into the structure-activity relationship of various chemically modified PEIs and found that a moderate enhancement of the polymer's hydrophobicity increased transfection efficiency.<sup>25</sup> Rehman *et al.* showed *via* live-cell confocal microscopy that endosomal release does not lead to a complete lysis of the endosome but to a release that occurs from one particular region of the endosomal membrane, through which the cargo is jetted into the cytoplasm. They propose a model in which the protonation causes the highly charged polyplex to closely interact with the endosomal membrane. At this interaction site, a local (osmotic or mechanical) initial membrane destabilizing effect leads to rupture of the endosomal membrane due to an increase in membrane tension upon osmotic swelling of the endosome.<sup>30</sup> Additionally, Bieber *et al.* revealed membrane damage in PEI-containing vesicles through electron microscopic analysis, which they attributed to the proton sponge effect or a direct interaction of the polymer with the vesicular membrane.<sup>36</sup> Martens *et al.* agreed that the proton sponge effect is now thought to be assisted by an initial membrane destabilization induced by the cationic charge of the polymer, followed by further destabilization of the membrane as a consequence of the umbrella hypothesis.<sup>6</sup> The current view on proton-sponge based endosomal escape is schematically summarized in **Figure 2.4**.

However, as will be shown in **Chapter 3**, inducing membrane destabilization by interaction of the polymer with the endosomal membrane could also be counterproductive. We show that PEI polyplexes can induce leakiness of the endosomal membrane in a cell-type dependent manner. While ONs remained entrapped within the endosomes, small molecules such as water were able to cross the endosomal membrane and reach the cytoplasm. This was visualized by loading endosomes with calcein (as a model for small molecules such as water) and AF647-labeled ONs (cargo molecules). Confocal microscopy confirmed the release of quenched calcein (visualized as a change from punctate to diffuse fluorescent pattern) without the release of AF647-labeled ONs. Since endosomal escape, measured by accumulation of ONs in the nucleus, and transfection efficiency were markedly reduced in cell types in which this leakiness was observed, we hypothesized that endosomal membrane leakiness prevented effective build-up of osmotic pressure by PEI, rendering the proton sponge effect ineffective in leaky endosomes. This clearly indicates that the effectiveness of

proton sponge-based endosomal escape is not only cell type-dependent but also requires exactly the right interplay between osmotic forces and membrane destabilization.

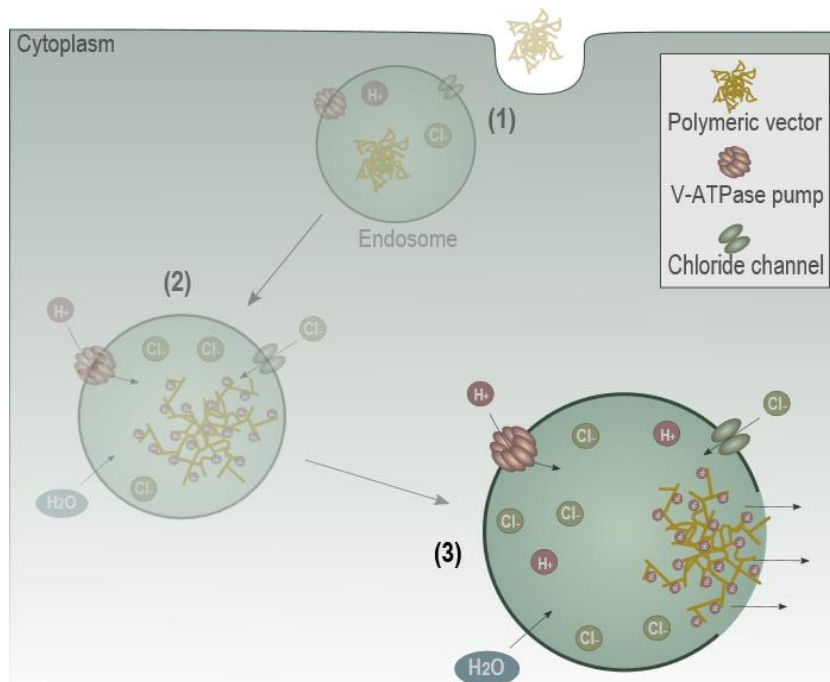


**Figure 2.4 State of the art representation of the proton sponge hypothesis.** Endosomal rupture through the proton sponge effect is nowadays considered to be due to a combination of osmotic forces arising from the buffer capacity of the polymer, polymer swelling due to internal charge repulsion upon protonation (as shown in **(1)** and **(2)**) and membrane destabilization because of the interaction between the protonated polymer and the endosomal membrane, as shown in **(3)**.

## 5 CONCLUSION

Altogether, these results illustrate that achieving effective endosomal escape by the use of proton sponge-based polymers depends on a delicate balance between osmotic pressure, polymer swelling and destabilization of the endosomal membrane. Moderate membrane destabilization due to polyplex interaction with the endosomal membrane likely leads to a locally weakened area where the membrane will rupture by the osmotic forces. It should be noted that most efforts to examine the efficiency of proton sponge based polymers were based on the evaluation of their transfection efficiency. It wasn't until recently that methods were developed to allow direct quantification of endosomal escape. An overview of these methods was presented in **Chapter 1**. Since we are now able to observe endosomal escape events, it should prove useful in the future to quantify endosomal escape efficiency itself, thereby eliminating interference of subsequent intracellular barriers.

## ACKNOWLEDGEMENTS

L. Vermeulen would like to acknowledge the financial support of the Agency for Innovation by Science and Technology in Belgium. Financial support by the Ghent University Special Research Fund and the Fund for Scientific Research Flanders (FWO, Belgium) is acknowledged with gratitude. This research was funded by the European Research Council (ERC) under the European Union's Horizon 2020 research and innovation program (grant agreement [648214]) and has received support from the Innovative Medicines Initiative Joint Undertaking under grant agreement n° 115363 resources of which are composed of financial contribution from the European Union's Seventh Framework Programme (FP7/2007-2013) and EFPIA companies' in kind contribution.

## REFERENCES

- (1) Guo, X.; Huang, L. Recent Advances in Non-Viral Vectors for Gene Delivery. *Acc Chem Res* **2012**, *45*, 971–979.
- (2) Ramamoorth, M. Non Viral Vectors in Gene Therapy- An Overview. *J. Clin. Diagnostic Res.* **2015**, *9*, 1–6.
- (3) Riley, M.; Vermerris, W. Recent Advances in Nanomaterials for Gene Delivery— A Review. *Nanomaterials* **2017**, *7*, 94.
- (4) Yin, H.; Kanasty, R. L.; Eltoukhy, A. A.; Vegas, A. J.; Dorkin, J. R.; Anderson, D. G. Non-Viral Vectors for Gene-Based Therapy. *Nat. Rev. Genet.* **2014**, *15*, 541–555.
- (5) Gottfried, L. F.; Dean, D. a. Extracellular and Intracellular Barriers to Non-Viral Gene Transfer. *Nov. Gene Ther. Approaches* **2013**, 75–88.
- (6) Martens, T. F.; Remaut, K.; Demeester, J.; De Smedt, S. C.; Braeckmans, K. Intracellular Delivery of Nanomaterials: How to Catch Endosomal Escape in the Act. *Nano Today*, **2014**, *9*, 344–364.
- (7) Gilleron, J.; Querbes, W.; Zeigerer, A.; Borodovsky, A.; Marsico, G.; Schubert, U.; Manygoats, K.; Seifert, S.; Andree, C.; Stöter, M.; *et al.* Image-Based Analysis of Lipid Nanoparticle-mediated siRNA Delivery, Intracellular Trafficking and Endosomal Escape. *Nat. Biotechnol.* **2013**, *31*, 638–646.
- (8) Shete, H. K.; Prabhu, R. H.; Patravale, V. B. Endosomal Escape: A Bottleneck in Intracellular Delivery. *J. Nanosci. Nanotechnol.* **2014**, *14*, 460–474.
- (9) Sahay, G.; Alakhova, D. Y.; Kabanov, A. V. Endocytosis of Nanomedicines. *J. Control. Release* **2010**, *145*, 182–195.
- (10) Canton, I.; Battaglia, G. Endocytosis at the Nanoscale. *Chem. Soc. Rev.* **2012**, *41*, 2718–2739.
- (11) Pangarkar, C.; Dinh, A. T.; Mitragotri, S. Endocytic Pathway Rapidly Delivers Internalized Molecules to Lysosomes: An Analysis of Vesicle Trafficking, Clustering and Mass Transfer. *J. Control. Release* **2012**, *162*, 76–83.
- (12) Selby, L. I.; Cortez-Jugo, C. M.; Such, G. K.; Johnston, A. P. R. Nanoescapology: Progress toward Understanding the Endosomal Escape of Polymeric Nanoparticles. *Wiley Interdiscip. Rev. Nanomedicine Nanobiotechnology* **2017**, *9*, 1-23.
- (13) Varkouhi, A. K.; Scholte, M.; Storm, G.; Haisma, H. J. Endosomal Escape Pathways for Delivery of Biologicals. *J. Control. Release* **2011**, *151*, 220–228.
- (14) Liang, W.; Lam, J. K. W. Endosomal Escape Pathways for Non-Viral Nucleic Acid Delivery Systems. In *Molecular Regulation of Endocytosis*; **2012**; pp. 429–456.
- (15) Behr, J. The Proton Sponge: A Trick to Enter Cells the Viruses Did Not Exploit. *Int. J. Chem.* **1997**, *2*, 34–36.
- (16) Lächelt, U.; Wagner, E. Nucleic Acid Therapeutics Using Polyplexes: A Journey

- of 50 Years (and Beyond). *Chem. Rev.* **2015**, *115*, 11043–11078.
- (17) De Smedt, S. C.; Demeester, J.; Hennink, W. E. Cationic Polymer Based Gene Delivery Systems. *Pharm. Res.* **2000**, *17*, 113–126.
- (18) Pack, D. W.; Hoffman, A. S.; Pun, S.; Stayton, P. S. Design and Development of Polymers for Gene Delivery. *Nat. Rev. Drug Discov.* **2005**, *4*, 581–593.
- (19) Haensler, J.; Szoka, F. C. Polyamidoamine Cascade Polymers Mediate Efficient Transfection of Cells in Culture. *Bioconjug. Chem.* **1993**, *4*, 372–379.
- (20) Behr, J. P.; Demeneix, B.; Loeffler, J. P.; Perez-Mutul, J. Efficient Gene Transfer into Mammalian Primary Endocrine Cells with Lipopolyamine-Coated DNA. *Proc. Natl. Acad. Sci. U. S. A.* **1989**, *86*, 6982–6986.
- (21) Boussif, O.; Lezoualc'h, F.; Zanta, M. A.; Mergny, M. D.; Scherman, D.; Demeneix, B.; Behr, J. P. A Versatile Vector for Gene and Oligonucleotide Transfer into Cells in Culture and in Vivo: Polyethylenimine. *Proc. Natl. Acad. Sci.* **1995**, *92*, 7297–7301.
- (22) Sonawane, N. D.; Szoka, F. C.; Verkman, A. S. Chloride Accumulation and Swelling in Endosomes Enhances DNA Transfer by Polyamine-DNA Polyplexes. *J. Biol. Chem.* **2003**, *278*, 44826–44831.
- (23) Singh, B.; Maharjan, S.; Park, T. E.; Jiang, T.; Kang, S. K.; Choi, Y. J.; Cho, C. S. Tuning the Buffering Capacity of Polyethylenimine with Glycerol Molecules for Efficient Gene Delivery: Staying in or out of the Endosomes. *Macromol. Biosci.* **2015**, *15*, 622–635.
- (24) Akinc, A.; Thomas, M.; Klibanov, A. M.; Langer, R. Exploring Polyethylenimine-Mediated DNA Transfection and the Proton Sponge Hypothesis. *J. Gene Med.* **2005**, *7*, 657–663.
- (25) Thomas, M.; Klibanov, A. M. Enhancing Polyethylenimine's Delivery of Plasmid DNA into Mammalian Cells. *Proc. Natl. Acad. Sci. U. S. A.* **2002**, *99*, 14640–14645.
- (26) Pack, D. W.; Putnam, D.; Langer, R. Design of Imidazole-Containing Endosomolytic Biopolymers for Gene Delivery. *Biotechnol. Bioeng.* **2000**, *67*, 217–223.
- (27) Midoux, P.; Monsigny, M. Efficient Gene Transfer by Histidylated Polylysine/PDNA Complexes. *Bioconjug. Chem.* **1999**, *10*, 406–411.
- (28) Funhoff, A. M.; van Nostrum, C. F.; Koning, G. A.; Schuurmans-Nieuwenbroek, N. M. E.; Crommelin, D. J. A.; Hennink, W. E. Endosomal Escape of Polymeric Gene Delivery Complexes Is Not Always Enhanced by Polymers Buffering at Low PH. *Biomacromolecules* **2004**, *5*, 32–39.
- (29) Forrest, M. L.; Meister, G. E.; Koerber, J. T.; Pack, D. W. Partial Acetylation of Polyethylenimine Enhances In Vitro Gene Delivery. *In Vitro* **2004**, *21*, 365–371.
- (30) Rehman, Z. U.; Hoekstra, D.; Zuhorn, I. S. Mechanism of Polyplex- and Lipoplex-Mediated Delivery of Nucleic Acids: Real-Time Visualization of Transient Membrane Destabilization without Endosomal Lysis. *ACS Nano* **2013**, *7*, 3767–3777.

- (31) Merdan, T.; Kunath, K.; Fischer, D.; Kopecek, J.; Kissel, T. Intracellular Processing of Poly ( Ethylene Imine )/ Ribozyme Complexes Can Be Observed in Living Cells by Using Confocal Laser Scanning Microscopy and Inhibitor Experiments. **2002**, *19*, 140–146.
- (32) Kichler, A.; Leborgne, C.; Coeytaux, E.; Danos, O. Polyethylenimine-Mediated Gene Delivery: A Mechanistic Study. *J. Gene Med.* **2001**, *3*, 135–144.
- (33) Benjaminsen, R. V; Matthebjerg, M. A.; Henriksen, J. R.; Moghimi, S. M.; Andresen, T. L. The Possible "Proton Sponge " Effect of Polyethylenimine (PEI) Does Not Include Change in Lysosomal PH. *Mol. Ther.* **2013**, *21*, 149–157.
- (34) Forrest, M. L.; Pack, D. W. On the Kinetics of Polyplex Endocytic Trafficking: Implications for Gene Delivery Vector Design. *Mol. Ther.* **2002**, *6*, 57–66.
- (35) Godbey, W. T.; Barry, M. A.; Saggau, P.; Wu, K. K.; Mikos, A. G. Poly ( Ethylenimine ) -Mediated Transfection : A New Paradigm for Gene Delivery. *Inc. J Biomed Master Res* **1999**, *51*, 321–328.
- (36) Bieber, T.; Meissner, W.; Kostin, S.; Niemann, A.; Elsasser, H. P. Intracellular Route and Transcriptional Competence of Polyethylenimine-DNA Complexes. *J. Control. Release* **2002**, *82*, 441–454.
- (37) Mo, R.; Sun, Q.; Li, N.; Zhang, C. Intracellular Delivery and Antitumor Effects of PH-Sensitive Liposomes Based on Zwitterionic Oligopeptide Lipids. *Biomaterials* **2013**, *34*, 2773–2786.
- (38) Richard, I.; Thibault, M.; De Crescenzo, G.; Buschmann, M. D.; Lavertu, M. Ionization Behavior of Chitosan and Chitosan-DNA Polyplexes Indicate That Chitosan Has a Similar Capability to Induce a Proton-Sponge Effect as PEI. *Biomacromolecules* **2013**, *14*, 1732–1740.
- (39) Neuberger, P.; Kichler, A. *Recent Developments in Nucleic Acid Delivery with Polyethylenimines*; Elsevier, **2014**; Vol. 88.
- (40) Sonawane, N. D.; Thiagarajah, J. R.; Verkman, A. S. Chloride Concentration in Endosomes Measured Using a Ratioable Fluorescent Cl<sup>-</sup> Indicator. Evidence for Chloride Accumulation during Acidification. *J. Biol. Chem.* **2002**, *277*, 5506–5513.
- (41) Won, Y. Y.; Sharma, R.; Konieczny, S. F. Missing Pieces in Understanding the Intracellular Trafficking of Polycation/DNA Complexes (Journal of Controlled Release (2009) 139: 2 (88-93)). *J. Control. Release* **2009**, *139*, 88–93.
- (42) Nguyen, J.; Szoka, F. C. Nucleic Acid Delivery: The Missing Pieces of the Puzzle? *Acc. Chem. Res.* **2012**, *45*, 1153–1162.
- (43) Ziebarth, J. D.; Wang, Y. Understanding the Protonation Behavior of Linear Polyethylenimine in Solutions through Monte Carlo Simulations. *Biomacromolecules* **2011**, *11*, 1–29.
- (44) Tang, M. X.; Redemann, C. T.; Szoka, F. C. In Vitro Gene Delivery by Degraded Polyamidoamine Dendrimers. *Bioconjug. Chem.* **1996**, *7*, 703–714.
- (45) Choudhury, C. K.; Kumar, A.; Roy, S. Characterization of Conformation and Interaction of Gene Delivery Vector Polyethylenimine with Phospholipid Bilayer

at Different Protonation State. *Biomacromolecules* **2013**, *14*, 3759–3768.

# Chapter 3

## Endosomal Size and Membrane Leakiness Influence Proton Sponge-Based Rupture of Endosomal Vesicles

**This chapter was published as:**

Vermeulen, L.M.P.<sup>1,2</sup>, Brans, T.<sup>1,2</sup>, Samal, S.K.<sup>1,2</sup>, Dubruel, P.<sup>3</sup>, Demeester, J.<sup>1</sup>, De Smedt, S.C.<sup>1</sup>, Remaut, K.<sup>1</sup>, Braeckmans, K.<sup>1,2</sup> Endosomal Size and Membrane Leakiness Influence Proton Sponge-Based Rupture of Endosomal Vesicles. *ACS Nano* **2018**, *12*, 2332-2345 **doi: 10.1021/acsnano.7b07583**

<sup>1</sup>Lab. General Biochemistry & Physical Pharmacy, Ghent University, Ottergemsesteenweg 460, Ghent, Belgium

<sup>2</sup>Centre for Nano- and Biophotonics, Ghent University, Ottergemsesteenweg 460, Ghent, Belgium

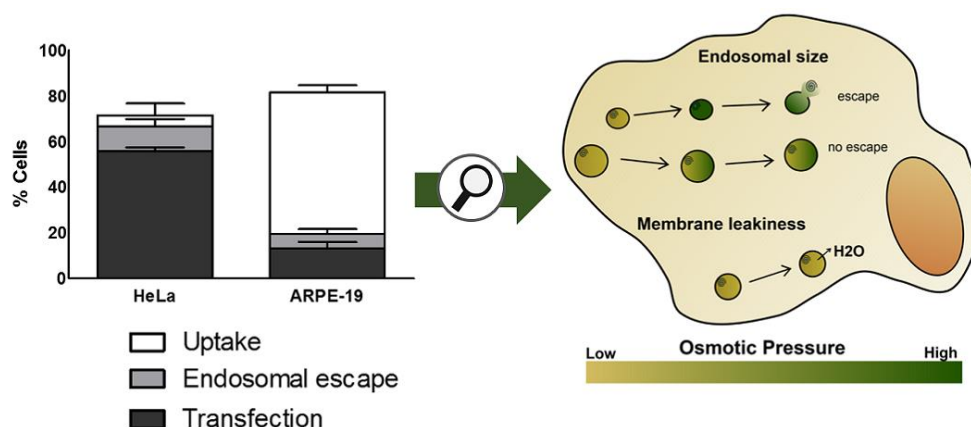
<sup>3</sup>Polymer Chemistry & Biomaterials Group, Ghent University, Krijgslaan 281, Ghent, Belgium

## TABLE OF CONTENTS

1	INTRODUCTION .....	90
2	MATERIALS AND METHODS .....	92
2.1	Materials.....	92
2.2	Cell culture.....	92
2.3	Purification of plasmids.....	92
2.4	Preparation of JetPEI/pDNA polyplexes .....	93
2.5	Characterization of JetPEI/pDNA polyplexes .....	93
2.6	Evaluation of transfection and uptake efficiency via flow cytometry .....	94
2.7	Cytotoxicity studies .....	94
2.8	Visualization and quantification of endosomal escape .....	95
2.9	Determination of pH, mobility, size, leakiness and number of endosomes .	95
2.10	Determining the amount of NH-containing monomers per JetPEI/pDNA polyplex.....	97
2.11	Statistical analysis .....	98
3	RESULTS.....	99
3.1	Characterization of JetPEI/pDNA polyplexes .....	99
3.2	Evaluation of transfection efficiency of JetPEI/pDNA polyplexes in HeLa and ARPE-19 cells .....	100
3.3	The role of endosomal escape.....	101
3.4	Exploring the influence of endosomal properties on endosomal escape .....	102
3.4.1	Influence of endosomal sequestration, pH and mobility.....	102
3.4.2	Influence of endosomal size .....	104
3.4.3	Influence of endosomal leakiness.....	108
3.4.4	The interplay between endosomal size and membrane leakiness.....	110
4	DISCUSSION .....	112
4.1	Endosomal sequestration, pH and mobility .....	112
4.2	Endosomal size.....	113
4.3	Endosomal leakiness .....	116
5	CONCLUSION .....	118

## ABSTRACT

In gene therapy, endosomal escape represents a major bottleneck since nanomedicines often remain entrapped inside endosomes and are trafficked towards the lysosomes for degradation. A detailed understanding of the endosomal barrier would be beneficial for developing rational strategies to improve transfection and endosomal escape. By visualizing individual endosomal escape events in live cells we obtain insight into mechanistic factors that influence proton sponge-based endosomal escape. In a comparative study, we found that HeLa cells treated with JetPEI/pDNA polyplexes have a 3.5-fold increased endosomal escape frequency compared to ARPE-19 cells. We found that endosomal size has a major impact on the escape capacity. The smaller HeLa endosomes are more easily ruptured by the proton sponge effect than the larger ARPE-19 endosomes, a finding supported by a mathematical model based on the underlying physical principles. Still, it remains intriguing that even in the small HeLa endosomes, less than 10% of the polyplex-containing endosomes show endosomal escape. Further experiments revealed that the membrane of polyplex-containing endosomes becomes leaky to small compounds, preventing effective build-up of osmotic pressure, which in turn prevents endosomal rupture. Analysis of H1299 and A549 cells revealed that endosomal size determines endosomal escape efficiency when cells have comparable membrane leakiness. However, at high levels of membrane leakiness build-up of osmotic pressure is no longer possible, regardless of endosomal size. Based on our findings that both endosomal size and membrane leakiness have a high impact on proton sponge-based endosomal rupture, we provide important clues towards further improvement of this escape strategy.



## 1 INTRODUCTION

In recent years, there has been an increasing interest in the cytosolic delivery of macromolecular drugs, which in many cases need to be delivered to intracellular (IC) targets to exert their intended function.<sup>1</sup> It is believed that using nanomedicines (NMs) for targeted delivery to IC compartments (cytosol, lysosomes, mitochondria, nucleus, *etc.*) holds great potential for precision therapeutics,<sup>2</sup> decreasing toxicity while maximizing therapeutic efficiency.<sup>1,3</sup> The biological barriers that NMs encounter during their mission to deliver therapeutic macromolecules to various IC destinations were reviewed in-depth in **Chapter 1**. Among those biological barriers, endosomal escape is considered to be a major bottleneck for efficient delivery. When NMs are unable to induce endosomal escape, endosomal acidification and fusion with lysosomes eventually leads to the degradation of the macromolecular therapeutic cargo.<sup>1,3-5</sup> As discussed in **Chapter 2**, several cationic polymers with an intrinsic endosomolytic activity are believed to escape the endosome *via* the so-called 'proton sponge effect', which is based on the osmotic rupture of endosomes due to extensive protonation of a buffering polymer followed by the influx of water molecules.<sup>6,7</sup> Recent findings indicate that next to osmotic swelling also membrane destabilization contributes to endosomal membrane rupture.<sup>4,8</sup> Yet, while the proton sponge mechanism has become a central paradigm for polymer-based carriers, it has recently been shown that per cell only a very limited number (as few as 1 up to 5) of internalized polyplexes effectively escape from the endosomes, rendering endosomal escape a crucial rate-limiting step for IC delivery of macromolecules.<sup>2,4,8-11</sup> It would be beneficial to understand why proton sponge-based endosomal escape is relatively inefficient, since enhancing the endosomal escape capacity of polyplexes could lower the dose that needs to be administered to obtain a certain transfection level, hence decreasing cytotoxicity that is often related to the use of cationic polymers.<sup>12</sup>

It has been reported that the clinical applicability of polyethylenimine (PEI), the gold standard for proton sponge-based delivery of nucleic acids (NAs), is limited due to its cytotoxicity. This is due to its cationic nature on the one hand, and non-biodegradability on the other hand.<sup>12,13</sup> Apart from decreasing cytotoxicity by increasing effectiveness (*e.g.* enhancing PEI's buffer capacity to increase its proton sponge effect as discussed in **Chapter 2**), a different strategy would be to chemically modify PEI to make it more biodegradable and decrease the polymer's intrinsic toxicity. According to Zhao *et al.*, combining PEI with the biocompatible chitosan while also introducing disulfide bonds that allow IC degradation of the copolymer would greatly decrease cytotoxicity while maintaining transfection efficiency.<sup>14</sup> In an attempt to implement this strategy, also we tried to synthesize chitosan-disulfide-conjugated low

molecular weight (LMW) PEI. A full report on the synthesis, characterization and evaluation of this copolymer can be found in **Addendum A**. Unfortunately, we found that the synthesized copolymer could not meet our requirements and we decided to use PEI itself to further study the proton sponge effect and in particular why it is relatively ineffective in the majority of endosomes.

Therefore, as a means to get further insight into the factors that contribute to effective proton sponge-based endosomal escape, we performed a detailed comparative study of the endosomal escape of JetPEI/pDNA polyplexes in two different cell lines, HeLa cells and ARPE-19 cells. While ARPE-19 cells internalize more polyplexes than HeLa cells, the level of transfection in HeLa cells is – surprisingly – much higher. We start by showing that this is linked to a higher frequency of endosomal escape events in HeLa cells as compared to ARPE-19 cells. As such, this marked difference between both cell types forms an interesting starting point for exploring intrinsic endosomal properties that affect endosomal escape efficiency. We study endosomal mobility, pH, size and membrane leakiness, leading to the conclusion that both endosomal size and membrane leakiness are very important factors that modulate effective endosomal escape. This finding is further tested on A549 and H1299 cells, which show low endosomal escape frequencies due to large endosomal size and extensive endosomal leakiness, respectively. Together, our work provides fundamental insights that can assist to ameliorate proton sponge-based endosomal release and thus transfection efficiency of gene polyplexes.

## **2 MATERIALS AND METHODS**

### **2.1 Materials**

DMEM/F-12, Opti-MEM, L-Glutamine, Penicillin-Streptomycin solution (5000 IU/ml penicillin and 5000 µg/ml streptomycin) (P/S), Fetal Bovine Serum (FBS), Trypan Blue, 0.25% Trypsin-EDTA and Dulbecco's phosphate-buffered saline 1x without Ca<sup>2+</sup>/Mg<sup>2+</sup> (DPBS-) were supplied by GibcoBRL (Merelbeke, Belgium). Hoechst 33342, YOYO-1 iodide, 10 kDa FITC dextrans and 10 kDa AF647 dextrans were purchased from Molecular Probes, Erembodegem, Belgium. Other reagents were purchased from Sigma-Aldrich (Bornem, Belgium) unless otherwise specified.

### **2.2 Cell culture**

HeLa cells (cervical adenocarcinoma cells, ATCC CCL-2) were cultured in Dulbecco's modified Eagle's medium supplemented with growth factor F12 (DMEM/F-12) supplemented with 10% FBS, 2 mM L-Glutamine and 100 µg/ml P/S. ARPE-19 cells (retinal pigment epithelial cells, ATCC CRL-2302) were cultured in Dulbecco's modified Eagle's medium supplemented with growth factor F12 (DMEM/F-12) supplemented with 10% FBS, 2 mM L-Glutamine and 50 µg/ml P/S. A549 cells (lung epithelial cells, ATCC CCL-185) were cultured in Dulbecco's modified Eagle's medium (DMEM) supplemented with 10% FBS, 2 mM L-Glutamine and 100 µg/ml P/S. H1299 cells (lung epithelial cells derived from metastatic lymph nodes, ATCC-CCL 5803) were cultured in Roswell Park Memorial Institute (RPMI) 1640 medium supplemented with 10% FBS, 2 mM L-Glutamine and 100 µg/ml P/S. Cells were incubated at 37°C in a humidified atmosphere containing 5% CO<sub>2</sub>. Cellular experiments were performed on cells with a passage number below 25.

### **2.3 Purification of plasmids**

pGL4.13 and gWIZ GFP (Promega, Leiden, The Netherlands) were amplified in transformed E. Coli bacteria and isolated from this bacteria suspension using a Qiafilter Plasmid Giga Kit (Qiagen, Venlo, The Netherlands). Concentration was determined on a NanoDrop 2000c (Thermo Fisher Scientific, Rockford, IL, USA) by UV absorption at 260 and 280 nm and adjusted to a final concentration of 1 µg/µl with HEPES buffer (20 mM, pH 7.2).

Labeling of pGL4.13 with YOYO-1 iodide (1 mM in DMSO) was performed by adding the dye to the pDNA mixture in a 1:10 ratio. This mixture was incubated in the dark for 4 h before purification by ethanol precipitation. To this end, 0.1 volume of 5 M NaCl and 2.5 volumes of ice-cold ethanol were added to 1 volume of the dye/pDNA suspension. This mixture was incubated at -80°C for 30 min before centrifugation for

30 min at 14000 g. The resulting pellet was washed with RNase - and DNase free 70% ethanol and centrifuged again for 10 min. Finally, the pellet was resuspended in fresh HEPES buffer (20 mM, pH 7.2) and the concentration was adjusted to 1 µg/µl after measurement on the NanoDrop 2000c.

#### **2.4 Preparation of JetPEI/pDNA polyplexes**

Polyplexes were prepared using commercially available JetPEI (Polyplus transfection, Leusden, The Netherlands). JetPEI/Nucleic Acid (NA) complexes were obtained by mixing the polymer solution with an equal volume of NA solution, which was composed of pDNA (gWIZ GFP or YOYO-1 labeled pGL4.13) and oligonucleotides (GAA-CTT-CAG-GGT-CAG-CTT-GTT, phosphorothioate linked, concentration 0.1 nmol/µg pDNA; AlexaFluor647 labeled (AF647 ONs) or unlabeled) (Eurogentec, Seraing, Belgium). N/P ratio of the polyplexes was calculated using the formula provided by the manufacturer (Equation 1). Next, the mixture was vortexed for 10 s at 2200 rpm and polyplexes were allowed to stabilize for 15 min before final dilution with HEPES buffer (20 mM, pH 7.2).

$$N/P\ ratio = \frac{7.5\ x\ \mu l\ of\ JetPEI}{3\ x\ \mu g\ of\ DNA} \quad (1)$$

#### **2.5 Characterization of JetPEI/pDNA polyplexes**

To evaluate complexation of NAs to the polymer, JetPEI/pDNA polyplexes (N/P ratio 1-8) were tested with gel electrophoresis. A 1% agarose gel was prepared by dissolving 1 g of agarose (UltraPure Agarose, Invitrogen, Erembodegem, Belgium) in 100 ml of 1 x Tris/Borate/EDTA (TBE) buffer after which GelRed (Biotium, Hayward, CA) was added for detection of NAs. 5 µl of Gel Loading Buffer (Ambion, Merelbeke, Belgium) was added per sample and a total volume of 25 µl was pipetted per lane. As a control, a 1 kb ladder (Bioron GmbH, Ludwigshafen, Germany), uncomplexed pDNA and uncomplexed AF647 ONs were taken along in the run. Gel electrophoresis was performed for 30 min at 100 V and a Kodak digital science camera (Kodak EDAS 120, Rochester, NY) was used to acquire an image of the gel under UV light (Bio-Rad UV transilluminator 2000, CA, USA).

For Dynamic Light Scattering measurements, JetPEI polyplexes were prepared as described above and were transferred to disposable folded capillary cells (Malvern, Worcestershire, UK) to determine hydrodynamic diameter, polydispersity index and zeta potential *via* the NanoZS Zetasizer (Malvern Instruments, Hoeilaart, Belgium).

## **2.6 Evaluation of transfection and uptake efficiency via flow cytometry**

Cells were seeded in 24 well plates at 50 000 cells per well and allowed to attach overnight. The next day, polyplexes containing gWIZ GFP and AF647 ONs (for transfection experiments) or YOYO-1 labeled pGL4.13 and unlabeled ONs (for uptake experiments) were prepared as described above. Cells were incubated with polyplexes in Opti-MEM for 15 min at 37°C after which they were washed and cultured for another 24 h (transfection) or 3 h (uptake). Particles, with N/P ratio 6, were applied in concentrations equal to 0.67 µg pDNA (NP 6 0.67) or 1.00 µg pDNA (NP 6 1) per 50 000 cells. For uptake studies, a negative control plate at 4°C was implemented and for all samples external YOYO-1 fluorescence was quenched by applying an ice-cold solution of Trypan Blue (½ diluted in DPBS-) after which the samples were prepared for flow cytometry analysis. For transfection studies, a negative control (using complexes prepared with Lipofectamine 2000 (Invitrogen, CA, USA) and pGL4.13) and a positive control (Lipofectamine and gWIZ GFP) were implemented.

To perform analysis by flow cytometry, cells were detached from the well plates using trypsin and transferred to flow cytometry tubes (BD Falcon, Radnor, USA). Next, cell suspensions were centrifuged at 300 g for 5 min (Bio-Rad DiaCent-12, DieMed GmbH, Cressier, Switzerland) and resuspended in flow buffer (DPBS- / 0.1 % Sodium Azide / 1% Bovine Serum Albumine). Finally, samples were vortexed at 2200 rpm for 10 s (YellowLine TTS2, IKA works, Wilmington, USA) and kept on ice. Flow cytometry was performed (FACS Calibur, BD Biosciences, Erembodegem, Belgium) and green fluorescence was measured on 10 000 events per sample (488 nm excitation with Argon laser and detection with a 530/30 nm bandpass filter). FlowJo software (Treestar Inc, Ashland, USA) was used for analysis.

## **2.7 Cytotoxicity studies**

Cells were seeded in 24 well plates at 50 000 cells per well and were allowed to attach overnight. The next day, polyplexes were prepared containing gWIZ GFP and AF647 ONs and cells were incubated with polyplexes for 15 min at 37°C in Opti-MEM. Next, cells were washed and incubated for an additional 3 h before addition of 3-(4,5-dimethyl-2-thiazolyl)-2,5-diphenyl-2H-tetrazolium bromide (MTT) solution (1 mg/ml in DPBS). After 3 h, the solution was removed and the newly formed purple formazan crystals were dissolved by addition of DMSO. The plates were covered in aluminum foil and placed on an orbital shaker (Rotamax 120, Heidolph, Germany) for 45 min at 1200 rpm. As a negative control, blank cells were fixed with a 4 % paraformaldehyde solution

to stop metabolic activity. UV absorbance was measured on a plate reader (Wallac Envision, Finland) at 590 nm (metabolic activity) and 690 nm (reference wavelength).

## **2.8 Visualization and quantification of endosomal escape**

Visualization and quantification of endosomal escape was performed based on a dequenching assay first published by Rehman *et al.*<sup>8</sup> To this end, red-labeled fluorescent oligonucleotides (AF647 ONs; 0,1 nmol per  $\mu\text{g}$  pDNA) were co-incorporated into the polyplexes. Upon endosomal escape, the labeled ONs will spread towards the cytoplasm, dequench (indicated by an intense burst of light) and finally accumulate into the nucleus. Cells were seeded in 35 mm CELLview microscopy dishes with glass bottom (Greiner Bio-One, Vilvoorde, Belgium) at a density of 150 000 cells in 1.5 ml. On day 3, cell nuclei were stained with Hoechst 33342 staining (1 mg/ml in  $\text{H}_2\text{O}$ ; 1000x diluted). Next, polyplexes containing gWIZ GFP and AF647 ONs were added to the cells in Opti-MEM and incubated for 15 min at 37°C. After washing the particles off, the cells were provided with full cell culture medium and were inserted into a stage top incubator (Tokai hit, Shizuoka-ken, Japan) to enable live-cell imaging at optimal environmental conditions (5%  $\text{CO}_2$ , 100% humidity and 37°C). Live-cell imaging was performed using a swept-field confocal (SFC) microscope (Nikon eclipse Ti, Japan) equipped with an MLC 400 B laser box (Agilent technologies, California, USA), SFC scan controller (Prairie Technologies, Middleton, USA), an iXon ultra EMCCD camera (Andor Technology, Belfast, UK) and NIS Elements software (Nikon, Japan). A Plan Apo VC 60x 1.4 NA oil immersion objective lens (Nikon, Japan), equipped with a lens heater (6 Watt temperature controller, Bioptechs, Butler, PA, USA), combined with an additional 1.7x magnification on the camera rendered a pixel size of 160 nm. A large image (8x8 frames) was taken every 30 s for a total period of 6 h using the perfect focus system to secure a good focus on the cells during the time of acquisition. Exposure time was set to 20 msec and a slit width of 35  $\mu\text{m}$  was selected. Movies were analyzed using ImageJ (FIJI) software.

## **2.9 Determination of pH, mobility, size, leakiness and number of endosomes**

### **Cell seeding**

*To evaluate the pH inside the endosomes:* Cells were seeded in glass bottom 96 well plates (Greiner Bio-One, Frickenhausen, Germany) with a density of 10 000 cells in a total volume of 100  $\mu\text{l}$ . On the day of imaging, cell nuclei were stained with Hoechst 33342 staining.

*For evaluating the number of polyplex-containing endosomes, endosomal mobility, endosomal size and endosomal leakiness:* Cells were seeded in 35mm CELLview microscopy dishes with glass bottom with a density of 150 000 cells in 1.5 ml. On the day of imaging, cell nuclei were stained with Hoechst 33342 staining.

### ***Image acquisition and processing***

*Counting the number of polyplex-containing endosomes:* To visualize cell boundaries, cells were incubated with 5  $\mu$ M calceinAM in Opti-MEM for 30 min at 37 °C before adding JetPEI polyplexes (containing AF647 ONs). After a 15 min incubation, polyplexes were removed by washing and cell culture medium was added. After 3 h, cells were imaged in the focal plane 2  $\mu$ m above the coverslip using a Nikon C1si confocal laser scanning microscope system equipped with a Plan Apo VC 60x 1.4 NA oil immersion objective lens (Nikon) and a pixel size of 160nm. Image processing was carried out using custom developed software (IPS in Matlab; details in **Table S1**) to determine the amount of polyplex-containing endosomes within the cell boundaries (**Figure S1**).

*Measuring endosomal pH:* Cells were incubated at 37°C for 45 min with 100  $\mu$ l of a mixture of 2 mg/ml 10 kDa FITC dextrans and 1 mg/ml 10 kDa AF647 dextrans in DPBS-. The ratio of fluorescence intensity in the green channel to fluorescence intensity in the red channel ( $I_{\text{FITC}}/I_{\text{AF647}}$ ) was determined as an indication of endosomal pH since  $I_{\text{FITC}}$  is dependent of pH and  $I_{\text{AF647}}$  is independent of pH.<sup>15</sup> After a washing step, the 96 well plate was placed on a spinning disk confocal (SDC) microscope (SFC scan controller, previously described in the swept field microscope set-up was replaced by a Yokogawa CSU-X confocal spinning disk device (Andor, Belfast, UK)) equipped with a Plan Apo VC 60x 1.4 NA oil immersion objective lens (Nikon, Japan) and an additional 1.5x magnification on the microscope to yield a pixel size of 156 nm. Exposure time was set to 20 msec and images were taken at several time points (5 min, 30 min, 1 h, 2 h, 3 h and 24 h) after the washing step. Endosomal contour determination was performed in Matlab (IPS; details in **Table S1**). FITC dextrans and AF647 dextrans were considered colocalized if their centers were separated less than the maximum of the respective mean radiuses. When colocalization on the endosome scale was observed,  $I_{\text{FITC}}/I_{\text{AF647}}$  ratio was determined. In order to link experimental ratio values to pH values, a calibration was performed next. Various buffers were prepared (pH 4.5 and 5.0 were citrate buffers, pH 5.5, 6.0, 6.5, 7.0 and 7.5 were 20 mM HEPES buffers) and mixed with FITC dextrans and AF647 dextrans. Calibration ratios were measured, a calibration curve was fitted in Matlab (**Figure S2**) and with the use of this calibration curve, the experimental  $I_{\text{FITC}}/I_{\text{AF647}}$  ratios were transformed into pH values.

*Measuring endosomal mobility:* JetPEI polyplexes were added to the cells and incubated at 37°C for 15 min. After washing the cells with Opti-MEM, the dish was placed inside the stage top incubator. Movies of 60 s with a frame rate of 5 frames per second were recorded using the SFC microscope (35 µm slit, exposure time 40 msec) with a pixel size of 107 nm. Videos were recorded on several time points after addition of the particles (30 min, 1 h, 2 h and 3 h). Matlab software (IPS; details in **Table S1**) was used to determine the contours of the endosomes and motion trajectories of individual endosomes were obtained *via* Matlab software (Supporting Information 'Image processing – mobility analysis in Matlab') and were used to calculate endosomal velocity.

*Determination of endosomal size:* After incubation with 2 mg/ml 10 kDa FITC dextrans for 45 min in 37°C, cells were washed and chased with cell culture medium for 3 h. Imaging was performed using the SDC with a pixel size of 92 nm. Next, contours of the FITC-containing endosomes were determined (IPS; details in **Table S1**) and a distribution of endosomal radiuses was generated.

*Evaluation of endosomal leakiness:* Cells were incubated with JetPEI polyplexes for 15 min at 37 °C. After washing off the polyplexes, endosomes were stained with calcein in self quenching concentration (3 mM) for 15 min. Cells were washed with Opti-MEM and incubated for another 3 h before confocal images were acquired using a Nikon C1si confocal laser scanning microscope system equipped with a Plan Apo VC 60x 1.4 NA oil immersion objective lens (Nikon) and a pixel size of 210 nm. Afterwards, cells were trypsinized and their diameter was measured, again *via* confocal microscopy. Finally, samples were prepared for analysis *via* flow cytometry.

## **2.10 Determining the amount of NH-containing monomers per**

### ***JetPEI/pDNA polyplex***

In order to determine the number of NH-containing monomers per JetPEI/pDNA polyplex, polyplexes with N/P 6, were prepared as described previously, containing gWIZ GFP and AF647 ONs, and diluted to 50 ml with HEPES (20 mM, pH 7.2). Next, polyplex concentration was measured *via* Nanoparticle Tracking Analysis using the NanoSight LM10 (Malvern, Worcestershire, UK). Measurements were recorded in quintuplet. Based on the theoretical number of pDNA and ON strands added during preparation of the polyplexes and the obtained polyplex concentration, it was possible to determine the average number of pDNA and ON strands per polyplex and thereby calculate the amount of NH-containing monomers per JetPEI/pDNA polyplex.

### **2.11 Statistical analysis**

All statistical analysis were performed using GraphPad software (La Jolla, CA, USA) and propagation of errors was applied when necessary. Number of asterisks in figures indicates statistical significance: \*\*\*  $p < 0.0001$ ; \*\*  $p < 0.01$ ; \*  $p < 0.05$ .

### 3 RESULTS

#### 3.1 Characterization of JetPEI/pDNA polyplexes

JetPEI/pDNA polyplexes were prepared from JetPEI and a mixture of pDNA and AlexaFluor 647 (AF647)-labeled oligonucleotides (ONs) at different N/P ratios (=charge ratio defined as Nitrogen/Phosphate ratio). Gel electrophoresis was performed to evaluate if pDNA and ONs are retained in the polyplexes. As can be seen in **Figure S3 A**, starting from N/P 4 both pDNA and ONs are efficiently complexed inside the polyplexes. Next, hydrodynamic diameter, polydispersity index (PdI) and zeta potential of particles with N/P 2, 4, 6 and 8 were measured with dynamic light scattering (**Figure S3 B-C**). JetPEI N/P 6 particles with a size of  $108.7 \pm 4.5$  nm (mean  $\pm$  stdev) and zeta potential of  $31.6 \pm 0.5$  mV (mean  $\pm$  stdev) were selected for further experiments.

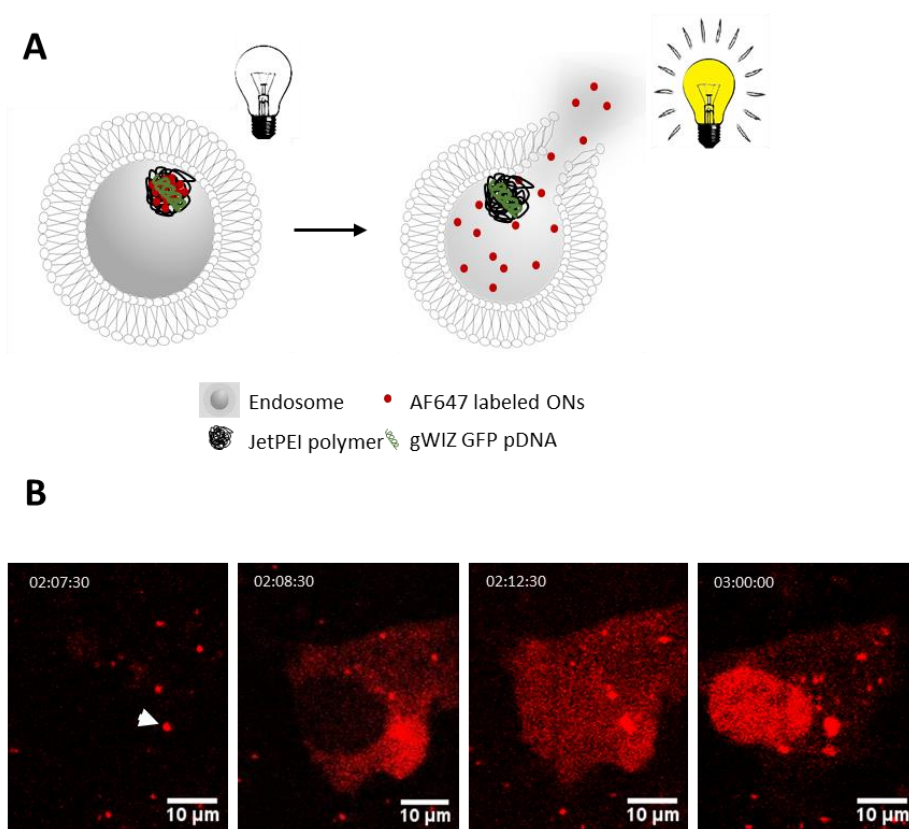


**Figure 3.1 Dequenching assay to evaluate endosomal escape efficiency of NMs. (A)** Schematic representation of the dequenching assay where the release of AF647 ONs visualizes the time point and place of endosomal bursts. **(B)** Microscopic images of an endosomal escape event. The arrow in the first frame indicates an endosome that contains quenched ONs. In the second frame this endosome has burst, as can be seen from a sudden increase in fluorescence intensity. In the third frame the released ONs spread into the cytoplasm and eventually accumulate into the nucleus (frame 4). Time is indicated in the left upper corner in hh:mm:ss after addition of the JetPEI/pDNA polyplexes.

The purpose of co-incorporating fluorescently labelled ONs into the JetPEI/pDNA complexes is to visualize and quantify endosomal escape according to a recently published dequenching assay.<sup>8,16</sup> When the polyplexes reside in the endosome, the fluorescence of these ONs is effectively quenched. Upon endosomal bursting, the labeled ONs escape from the endosome to the cytoplasm which can be seen as an intense burst of fluorescence, thus allowing to evaluate the number of endosomal escape events in time and space (**Figure 3.1 A**). A few minutes after endosomal escape, the ON fluorescence spreads towards the entire cytoplasm and eventually accumulates into the nucleus (**Figure 3.1 B**). The burst and subsequent accumulation in the nucleus provides a double confirmation that endosomal escape has happened. A live-cell movie recorded with a SFC microscope is provided (**Movie S1**; time indicated in hh:mm:ss) to illustrate this assay.

### **3.2 Evaluation of transfection efficiency of JetPEI/pDNA polyplexes in HeLa and ARPE-19 cells**

HeLa and ARPE-19 cells were transfected with JetPEI/pDNA N/P 6 polyplexes. The transfection efficiency based on GFP expression was quantified after 24 h *via* flow cytometry, showing a marked difference between both cell types. As apparent from both the percentage of GFP positive cells (**Figure 3.2 A**) as well as the median GFP fluorescence per transfected cell (**Figure 3.2 B**), HeLa cells were clearly much easier to transfect than ARPE-19 cells when exposed to the same concentration of JetPEI/pDNA polyplexes. This was irrespective of when polyplexes were applied in concentrations equal to 0.67 or 1.00  $\mu\text{g}$  pDNA per 50 000 cells. The difference in transfection efficiency is most obvious from **Figure 3.2 C**, which displays the average GFP content per cell over the entire population (*i.e.* including non-transfected cells). After 48h post transfection (the cell division time of ARPE-19 cells is 48h<sup>17</sup> versus 22h for HeLa cells<sup>18</sup>), the difference in transfection between HeLa cells and ARPE-19 cells was even more pronounced (**Figure S4**).

This much higher transfection efficiency in HeLa cells could not be explained by a difference in cytotoxicity, as MTT assay showed >80% viability for both cell types (**Figure 3.2 D**). Second, uptake experiments were carried out to see if a difference in polyplex uptake efficiency may be the cause. Uptake of JetPEI polyplexes was quantified *via* flow cytometry (**Figure 3.2 E**) and showed a significant increase in polyplex content in ARPE-19 cells vs HeLa cells. Since HeLa cells internalize less polyplexes, a difference in uptake clearly cannot account for the higher transfection efficiency.

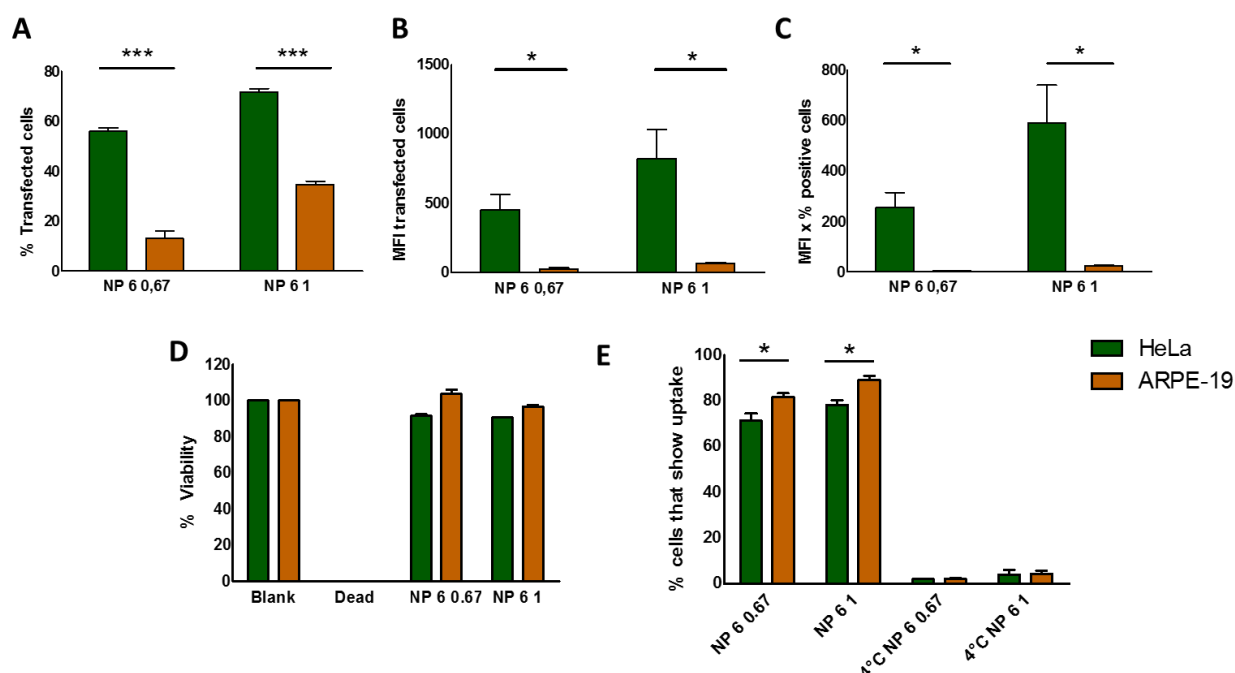


**Figure 3.2 Measuring transfection efficiency, cell viability and cellular uptake of JetPEI/pDNA polyplexes. (A)** The percentage of cells that are positive for GFP transfection. **(B)** The median GFP fluorescence intensity (MFI) of transfected cells. **(C)** MFI x the percentage of positive cells was calculated to display the average GFP content per cell over the entire population (including untransfected cells). **(D)** Cell viability was measured by means of an MTT test. **(E)** Polyplex uptake was quantified as percentage of positive cells. 4°C controls were included to show that membrane-attached polyplexes do not contribute to the measured signal thanks to Trypan Blue quenching. All graphs show mean  $\pm$  SEM; n=3. Significance was calculated using student t-tests (transfection, uptake) or one-way ANOVA with Dunnett's post-test (compare means to the value of 80% cell viability) (\*\*\*)  $p < 0.0001$ ; \*\*  $p < 0.01$ ; \*  $p < 0.05$ ).

### 3.3 The role of endosomal escape

In further pursuit of an explanation concerning the observed difference in transfection efficiency in HeLa vs ARPE-19 cells, we next investigated endosomal escape, which was visualized and quantified by time-lapse confocal microscopy as mentioned above. After a 15 min incubation with JetPEI/pDNA polyplexes, cells were imaged every 30 s for a total time of 6 h. Individual endosomal escape events were observed as sudden intense, localized bursts of light followed by translocation of the labelled ONs to the nucleus (see **Movie S2** (HeLa) and **Movie S3** (ARPE-19) both have time indication in hh:mm:ss). Therefore, the number of cells in which endosomal escape happened at least once could be quantified by counting the number of red fluorescent nuclei. Microscopy images at time point 3 h can be seen in **Figure 3.3 A** and illustrate that endosomal escape occurred in a much greater amount of HeLa than ARPE-19 cells. By analyzing a total of 1308 HeLa and 1052 ARPE-19 cells over time, it was shown that endosomal escape happened in  $3.42 \pm 0.40$  times more HeLa cells as compared to ARPE-19 cells (**Figure 3.3 B**). Furthermore, it became apparent that

endosomal escape predominantly occurred within the first three hours after addition of the polyplexes in both cell types. This marked difference points to the fact that endosomal escape efficiency plays an important role in the difference in transfection efficiency observed for both cell types.

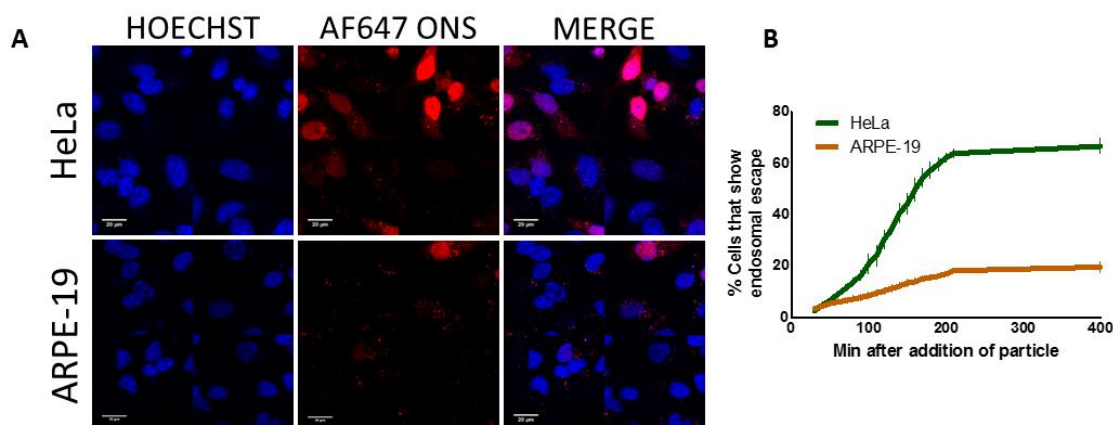


**Figure 3.3 Evaluating the role of endosomal escape. (A)** Representative confocal images as seen in the dequenching endosomal escape assay 3h after incubation with polyplexes. Hoechst nuclei can be seen in blue, while cells in which endosomal escape occurred show nuclear fluorescence in the red channel due to the release of AF647 ONs from the polyplexes. Scalebar represents 20 µm. **(B)** The percentage of cells with red nuclei in which endosomal escape has happened at least once are quantified in function of time. Values represent mean ± SEM and statistical analysis was carried out using a student t-test on a total of 1308 HeLa cells and 1052 ARPE-19 cells.

### 3.4 Exploring the influence of endosomal properties on endosomal escape

Considering the fact that HeLa cells actually internalized less polyplexes, the question arose as to why endosomal escape was that much more efficient in HeLa cells than in ARPE-19 cells. An answer to this question was sought by investigating the influence of several mechanistic endosomal properties on proton sponge-based endosomal escape.

#### 3.4.1 Influence of endosomal sequestration, pH and mobility

First, we investigated if perhaps polyplexes are sequestered at higher concentrations in HeLa endosomes, *e.g.* due to differences in cellular uptake and trafficking pathways. This could be of considerable importance since one could argue that a higher amount of polyplexes within an endosome increases the buffering capacity, making endosomal swelling and bursting more likely to happen. To answer this question we compared the number of polyplex-containing endosomes in both cell types *via* confocal microscopy. It turned out that HeLa cells had  $2.11 \pm 0.24$  times

more polyplex-containing endosomes per cell than ARPE-19 cells (**Figure 3.4 A**). Combined with the fact that HeLa cells internalized a smaller total amount of polyplexes than ARPE-19 cells (**Figure 3.2 E**), this means that the average number of polyplexes per endosome in HeLa cells is about 3 times less, as schematically presented in **Figure 3.4 B**. This points to the fact that the higher endosomal escape efficiency in HeLa cells did not simply arise from a higher polyplex load per endosome.

One could argue though that, since HeLa cells have about two times more polyplex-containing endosomes, endosomal escape is twice as likely to happen. To investigate this, we turned back to the endosomal escape movies and determined the number of individual endosomal escape events per cell. Multiple endosomal escape events can indeed happen within the same cell, as shown in **Figure 3.4 C** (arrows indicate places where individual escape events can be seen) and **Movie S4** (time indicated in hh:mm:ss). By image analysis an average of  $2.26 \pm 0.14$  burst events was found per HeLa cell, while for ARPE-19 cells this was only  $0.253 \pm 0.029$  (**Figure 3.4 D**). Taking into account that HeLa cells have 2 times more polyplex-containing endosomes per cell, it still means that endosomes in HeLa cells are intrinsically  $4.22 \pm 0.73$  times more likely to burst as compared to ARPE-19 cells (**Figure 3.4 E**). Clearly, other fundamental endosomal properties must play a role, warranting further investigation.

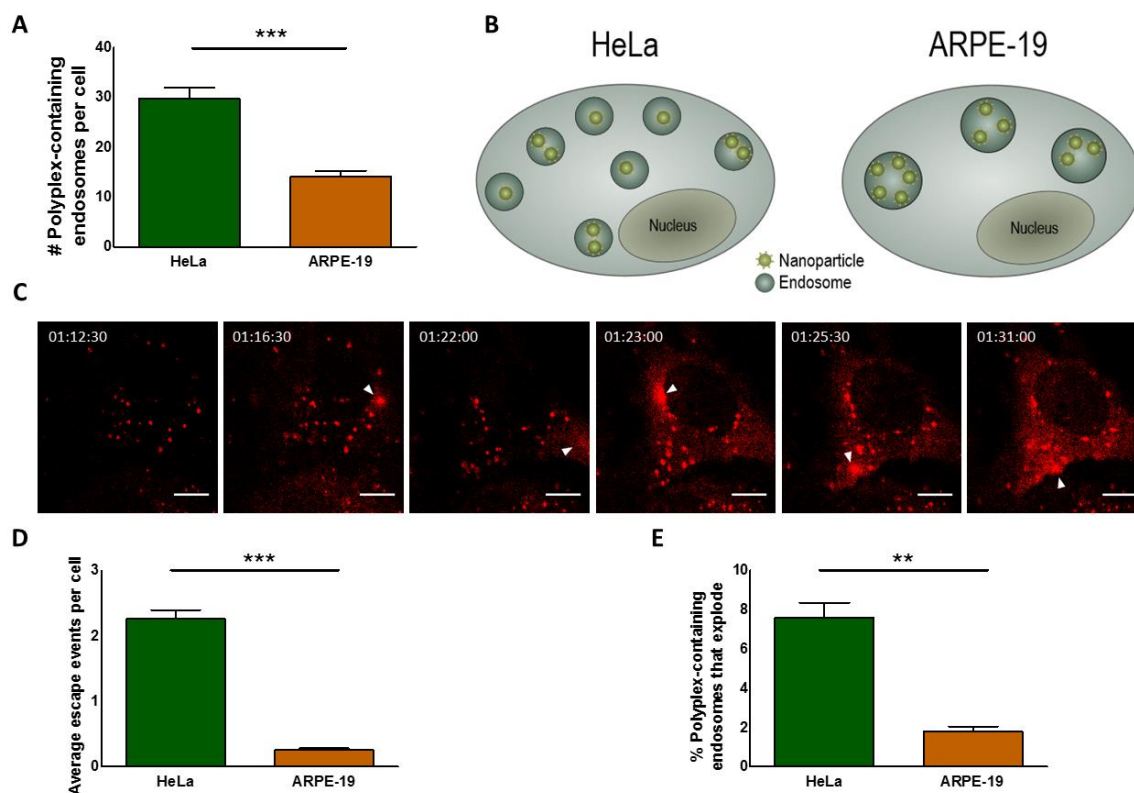


**Figure 3.4** Evaluation of the influence of polyplex content per endosome and total number of polyplex-containing endosomes on endosomal escape efficiency in HeLa vs

**ARPE-19 cells. (A)** The graph displays the number of polyplex-containing endosomes per cell that are visible 2  $\mu\text{m}$  above the cover slip in HeLa cells and ARPE-19 cells. Bars represent mean  $\pm$  SEM based on evaluation of 33 HeLa and 39 ARPE-19 cells. **(B)** Schematic presentation of the distribution of nanoparticles inside endosomes in HeLa vs ARPE-19 cells, indicating that the polyplex content per endosomes is lower in HeLa cells than in ARPE-19 cells. **(C)** Confocal images that demonstrate multiple endosomal escape events (white arrows) within one cell over time. Scale bar represents 10  $\mu\text{m}$ . **(D)** The average number of endosomal burst events per cell in a HeLa population vs ARPE-19 population is presented. Bars represent mean  $\pm$  SEM. **(E)** The graph displays the percentage of polyplex-containing endosomes that explode in HeLa cells vs ARPE-19 cells. Bars represent mean  $\pm$  SEM and are calculated using values displayed in Figure 3.4 A and Figure 3.4 D. Statistical analysis on all data was performed using student t-tests (\*\* $p < 0.0001$ ; \*\*  $p < 0.01$ ; \*  $p < 0.05$ ).

A decrease in pH is the driving factor of endosomal swelling in the proton sponge mechanism. As such it may be that endosomal acidification may be less pronounced in ARPE-19 cells which would lead to less endosomal swelling and bursting. Results in **Figure 3.5 A** show that ARPE-19 endosomes are actually slightly more acidic than HeLa endosomes, which shows that a difference in pH cannot explain the observed results. Another hypothesis could be that HeLa cells have higher endosomal mobility, which could result in increased shear stress, thus making bursting of swollen endosomes more likely. The instantaneous endosomal velocity (nm/s) of the endosomes was determined by Single Particle Tracking microscopy and is displayed in **Figure 3.5 B** and **Movie S5** (time indicated in mm:ss:ms). Based on these results, no obvious difference between the mobility of endosomes from HeLa cells and endosomes from ARPE-19 cells was observed.

### **3.4.2 Influence of endosomal size**

Next, we turned our attention to the potential role of endosomal size. Even though endosomes are close to the resolution limit of confocal microscopy, it could be noted that endosomes in ARPE-19 cells appeared bigger than those in HeLa cells. This can be readily appreciated in the confocal images of **Figure 3.5 C**, where endosomes were labeled by fluid phase uptake of 10 kDa FITC-dextran. By image processing, we determined the apparent endosomal size after initial incubation with 10 kDa FITC-dextran and subsequent chase with cell culture medium for 3 h. The endosomal size distribution of 783 HeLa and 1466 ARPE-19 endosomes is shown in **Figure 3.5 D**. Although these radii should not be considered to be absolutely correct given the optical resolution limit, still one can appreciate a relative shift to larger sizes of the ARPE-19 endosomes.

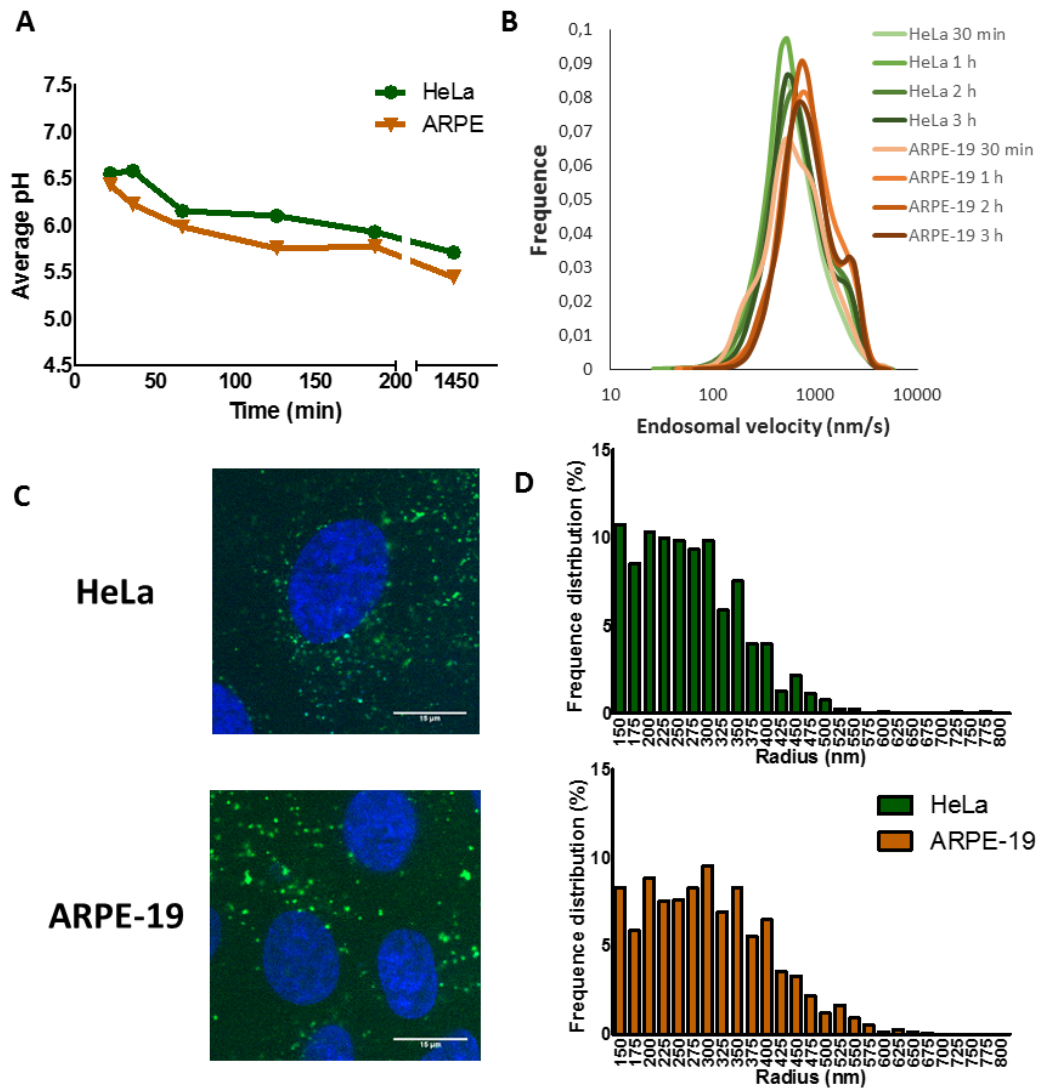


**Figure 3.5 Investigating the difference in pH, mobility and size between HeLa and ARPE-19 endosomes to evaluate their influence on the endosomal escape capacity exerted by JetPEI/pDNA polyplexes in these cell types. (A)** The average pH  $\pm$  SEM at several time points – as measured by confocal microscopy – is displayed for HeLa and ARPE-19 endosomes. Graph is based on the evaluation of 19667 HeLa endosomes and 14862 ARPE-19 endosomes. **(B)** Endosomal velocity – measured by single particle tracking – is depicted. Green lines represent distributions measured in HeLa cells, while orange distributions are measured in ARPE-19 cells. Graph is based on the evaluation of 14980 HeLa endosomes and 12383 ARPE-19 endosomes. **(C)** A representative confocal image of HeLa and ARPE-19 cells is shown to demonstrate the visual difference in endosomal size. Scale bar represents 15  $\mu$ m. **(D)** The size of 783 HeLa vs 1466 ARPE-19 endosomes was measured after incubation with FITC dextrans and subsequent chase with cell culture medium for 3h. Frequency distributions of endosomal radii show a shift to higher endosomal radii, indicating that ARPE-19 cells have more larger endosomes, as is also visually evident from **(C)**.

Understanding the influence of endosomal size on bursting of the endosome: a mathematical model

To examine the impact of endosomal size on endosomal escape efficiency *via* the proton sponge effect, a simple mathematical model is set up that describes the relation between endosomal size and the proton sponge hypothesis. We start from the assumption that a certain amount of polyplex is endocytosed and located inside an endosome of radius  $R_0$ . Under the proton sponge hypothesis, the buffering action of the polymer will cause an influx of  $\text{Cl}^-$  ions ( $\Delta N$ ). This in turn causes an influx of  $\text{H}_2\text{O}$  into the endosome, increasing endosomal size to  $R$ . Hereby, an osmotic pressure ( $P_{osm}$ ) is generated that is described by the “van ‘t Hoff formula” :

$$P_{osm} = \Delta C k_b T \quad (2)$$

with  $\Delta C = C_e - C_0$  the difference in chloride number concentration in an endosome with ( $C_e$ ) and without ( $C_0$ ) the polymer,  $k_b$  the Boltzmann constant and  $T$  the absolute temperature. Due to the surface tension  $\gamma$  of the endosomal membrane, endosomal swelling will, however, be counteracted by a pressure described by Laplace’s law:

$$P_{Lap} = \frac{2\gamma}{R} \quad (3)$$

When  $P_{osm}$  equals  $P_{Lap}$ , an equilibrium is reached, from which it follows that:

$$\Delta C = \frac{4\kappa\epsilon d}{k_b T R_0 (1 + \epsilon)} \quad (4)$$

in which the surface tension was rewritten as  $\gamma = 2\kappa\epsilon d$ , with  $\kappa$  Young’s elasticity modulus,  $d$  the thickness of the membrane and  $\epsilon = \Delta R/R_0$  the strain.<sup>19</sup> Equation (4) expresses the concentration difference in chloride ions that is needed to let the endosome with initial radius  $R_0$  swell to such an extent that the endosomal membrane experiences a strain  $\epsilon$ . If we finally rewrite  $\Delta C = \Delta N/V_0$ , and denoting  $\epsilon_{max}$  as the maximal strain supported by the membrane (*i.e.* the burst criterion), one finally finds:

$$\Delta N = \frac{16\pi\kappa d}{3k_b T} \cdot \frac{\epsilon_{max}}{1 + \epsilon_{max}} \cdot R_0^2 \quad (5)$$

Equation (5) shows that the number of protons or chloride ions needed to burst an endosome increases with the square of the endosomal radius, *i.e.* proportional to the endosome’s surface area. This gives a clear indication as to why endosomal escape in cells with bigger endosomes, as for the ARPE-19 cells, is intrinsically less likely to happen for a given amount of polymer.

### Putting the model to the test

In order to evaluate the plausibility of Equation (5), several constants used in the formula need to be defined. According to Li *et al.*<sup>20</sup> the elastic limit of phospholipid vesicles is around 5-10% increase in surface area, which can be translated into a burst criterion of 5% endosomal strain ( $\varepsilon_{max} = 0.05$ ; see Supporting Information 'Defining the burst criterion'). The elastic modulus  $\kappa$  of phospholipid vesicles is reported to be in the range of  $3 \cdot 10^7 - 8 \cdot 10^7 \frac{N}{m^2}$ <sup>19</sup> and the thickness of the membrane is set to  $4.1 \text{ nm}$ <sup>21</sup>. The absolute temperature in the cells corresponds to 310 K and  $k_b$  equals  $1.38 \cdot 10^{-23} \text{ JK}^{-1}$ . Based on this information, Equation (5) is plotted in **Figure 3.6** (dotted line as the upper limit ( $\kappa = 8 \cdot 10^7 \frac{N}{m^2}$ ) and solid line as the lower limit ( $\kappa = 3 \cdot 10^7 \frac{N}{m^2}$ )), showing the quadratic dependence of the endosomal chloride ion influx needed to burst the vesicle as a function of the endosomal radius. Selected values are also presented in Table 1. It is interesting to relate these numbers to the amount of polymer that is actually needed to burst an endosome of a given size. It should be noted that the effective buffering capacity of a JetPEI/pDNA polyplex is only 20% of the free polymer, due to the electrostatic interaction with pDNA and the electrostatic repulsion resulting from protonation of neighboring amine groups.<sup>22</sup> Based on this information, the number of NH-containing monomers that is needed to cause the required  $\text{Cl}^-$  influx for endosomal bursting can be calculated (**Table 3.1** and right y-axis of **Figure 3.6**).

As a final step, it is more meaningful to convert these values to the corresponding number of polyplexes. In order to achieve this conversion, we calculated that one polyplex contains on average  $1,9 \pm 0,2 \cdot 10^6$  NH-containing monomers (calculation in Supporting Information 'Converting NH-containing monomers to the amount of polyplexes'). Using this average, the number of polyplexes needed to burst an endosome with a given radius was determined and is displayed in **Table 3.1**.

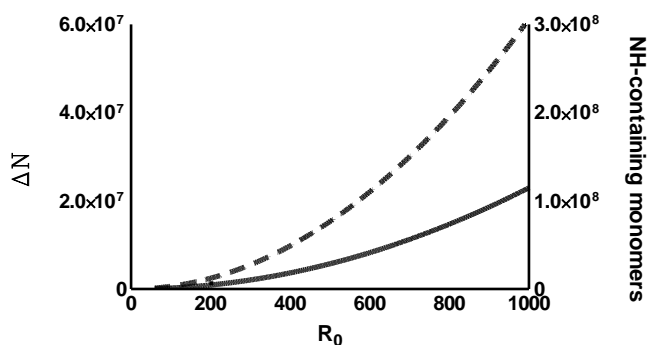


**Figure 3.6** Graph to illustrate the influence of endosomal radius ( $R_0$ ) on the amount of chloride ions ( $\Delta N$ ; left y-axis) or NH-containing monomers (right y-axis) needed to induce endosomal bursting (*cfr.* Equation (5) and values mentioned in the main text).

The dotted line represents the upper limit ( $\kappa = 8 \cdot 10^7 \frac{N}{m^2}$ ) while the solid line indicates the lower limit ( $\kappa = 3 \cdot 10^7 \frac{N}{m^2}$ ).

**Table 3.1 Overview of the number of chloride ions, NH-containing monomers and corresponding number of JetPEI/pDNA polyplexes needed to burst an endosome of a given radius.** Lower limit is calculated using  $\kappa = 3 \cdot 10^7 \frac{N}{m^2}$ ; upper limit is calculated using  $\kappa = 8 \cdot 10^7 \frac{N}{m^2}$ .

	<b>200 nm</b>	<b>400 nm</b>	<b>600 nm</b>
<b>Chloride influx</b> ( $\Delta N$ in ions)	9,2.10 <sup>5</sup> - 2,5.10 <sup>6</sup>	3,7.10 <sup>6</sup> - 9,8.10 <sup>6</sup>	8,3.10 <sup>6</sup> - 2,2.10 <sup>7</sup>
<b>NH-containing monomers</b>	4,6.10 <sup>6</sup> - 1,2.10 <sup>7</sup>	1,8.10 <sup>7</sup> - 4,9.10 <sup>7</sup>	4,1.10 <sup>7</sup> - 1,1.10 <sup>8</sup>
<b>Polyplexes</b>	2-7	8-28	19-62

The calculated amount of polyplexes are quite plausible, giving a good indication that Equation (5) provides a reasonable description of swelling and bursting of an endosome by the proton sponge mechanism. Since our results show that HeLa cells have smaller endosomes, they would need to accumulate less polyplexes to efficiently induce endosomal bursting *via* the proton sponge effect. In our opinion, having ruled out many other potential causes, this provides a plausible explanation as to why endosomal escape is more efficient in HeLa cells than in ARPE-19 cells.

### **3.4.3 Influence of endosomal leakiness**

While differences in endosomal size can explain the differences in transfection efficiency between HeLa and ARPE-19 cells, it remains quite intriguing why even in the smaller HeLa endosomes, endosomal escape happens in less than 10% of the total amount of polyplex-containing endosomes. This means that an astonishing >90% of the polyplexes do not contribute to the final biological effect. We reasoned that this may perhaps be the result of endosomal membrane leakiness, *i.e.* the loss of its semi-permeable property for small molecules such as chloride ions and water molecules, which would prevent the build-up of osmotic pressure. Such leakiness may in fact be induced by stress on the endosomal membrane due to the gradually increasing osmotic pressure combined with membrane destabilization due to interaction with the cationic polyplexes. To test this experimentally, calcein was incorporated into endosomes as a model for small molecules. Since it was used in self-quenching concentrations, a subtle leak in the endosomal membrane could be easily witnessed by the change from a punctate fluorescent pattern (endosomes) to a diffuse (dequenched) cytoplasmic fluorescence. The microscopy images in **Figure 3.7 A** confirm that for both HeLa and

ARPE-19 cells, calcein is released in virtually every cell that has taken up polyplexes, even in those that do not show release of AF647 labeled ONs. Control cells (incubated with calcein alone) did not show any cytoplasmic fluorescence apart from a punctuate endosomal pattern. Furthermore, a PEI dose curve was performed where cells were incubated with a decreasing concentration of polyplexes in order to evaluate the effect on endosomal leakiness. **Figure 3.7 B** shows the intensity of cytosolic calcein fluorescence after incubation with 1, 1/2, 1/5 and 1/10 dilutions of NPs, clearly indicating that calcein release is dependent on polyplex concentration, thus providing clear evidence that polyplex-containing endosomes do become more leaky to small molecules, which may hinder effective build-up of osmotic pressure and, therefore, endosomal escape.

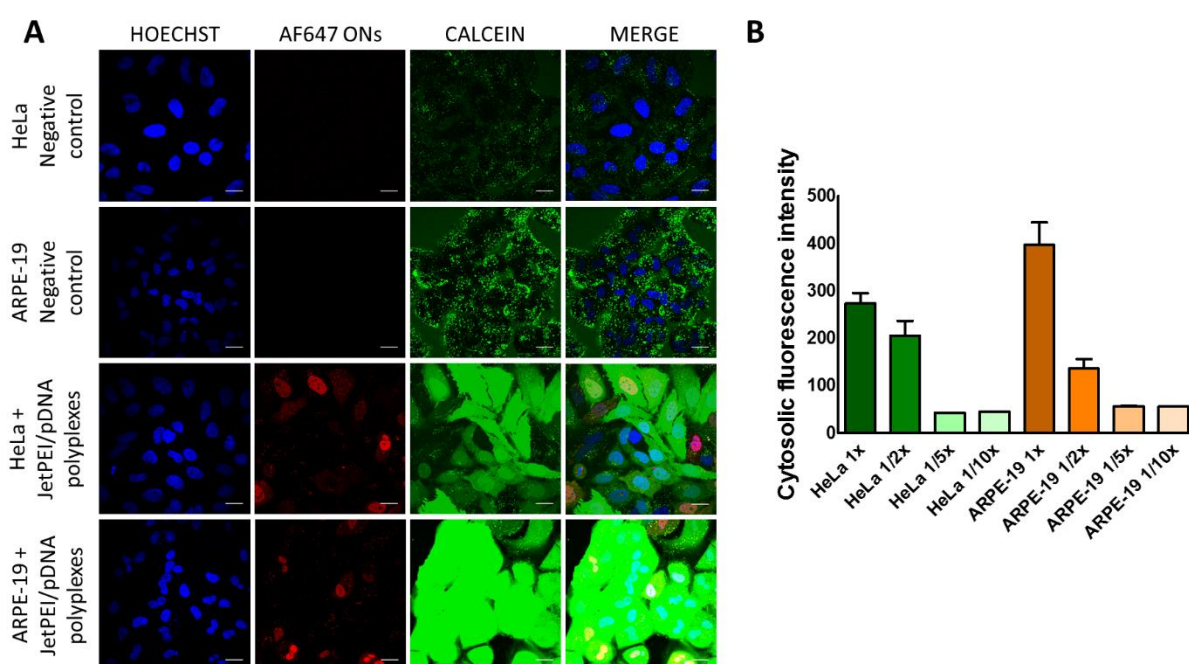


**Figure 3.7 Evaluation of endosomal leakiness induced by JetPEI/pDNA polyplexes. (A)** HeLa and ARPE-19 cells were incubated with polyplexes and calcein-AM at a self-quenching concentration of 3 mM. The first column shows nuclear staining with Hoechst. The second column shows AF647 fluorescence, where red nuclei indicate that endosomal escape of AF647 labeled ONs has happened. In the third column, the calcein fluorescence is displayed, where green cells indicate that calcein was able to escape endosomal confinement and leak to the cytoplasm. The last column depicts the merged images. First two rows represent the negative controls (cells incubated with calcein without addition of JetPEI/pDNA polyplexes). The last two rows show images of HeLa and ARPE-19 cells after incubation with both JetPEI/pDNA polyplexes and calcein. Scale bar represents 25  $\mu$ m. **(B)** The cytosolic fluorescence intensity of calcein was quantified from microscopy images after incubation with 1x, 1/2x, 1/5x and 1/10x dilutions of the original polyplex concentration, showing that endosomal membrane leakiness is a concentration dependent effect. Graph shows mean  $\pm$  SEM. In total, 319 HeLa cells and 312 ARPE-19 cells were measured.

### 3.4.4 The interplay between endosomal size and membrane leakiness

Our results point to endosomal size and membrane leakiness as important factors that determine proton sponge-based endosomal escape in a cell-dependent manner. HeLa cells and ARPE-19 cells are, however, very different cell types with very different cell division times. Therefore, to further corroborate our findings we included two additional cell lines, A549 and H1299, that have division times that match more closely to HeLa cells (A549 22h; H1299 20-23h; HeLa 22h). Both A549 and H1299 cells showed poor transfection efficiency after incubation with JetPEI/pDNA polyplexes, which again could not be attributed to cellular uptake or cytotoxicity (**Figure 3.8 A-C**; dashed lines indicate results for HeLa cells as a reference). Endosomal escape, however, was again found to be low as measured by ON translocation to the nucleus as before. Only  $11.37 \pm 0.44$  % and  $11.12 \pm 1.70$  % cells showed endosomal escape for A549 and H1299 cells respectively (**Figure 3.8 D**). Measuring the endosomal size as before, A549 cells have endosomes that are even larger than in ARPE-19 cells, while the endosomes of H1299 cells are even smaller than those of HeLa cells (**Figure 3.8 E** and **Figure S5**). Thus, while the presence of large endosomes provides an explanation for the low transfection results in A549 cells, it does not for the H1299 cells.

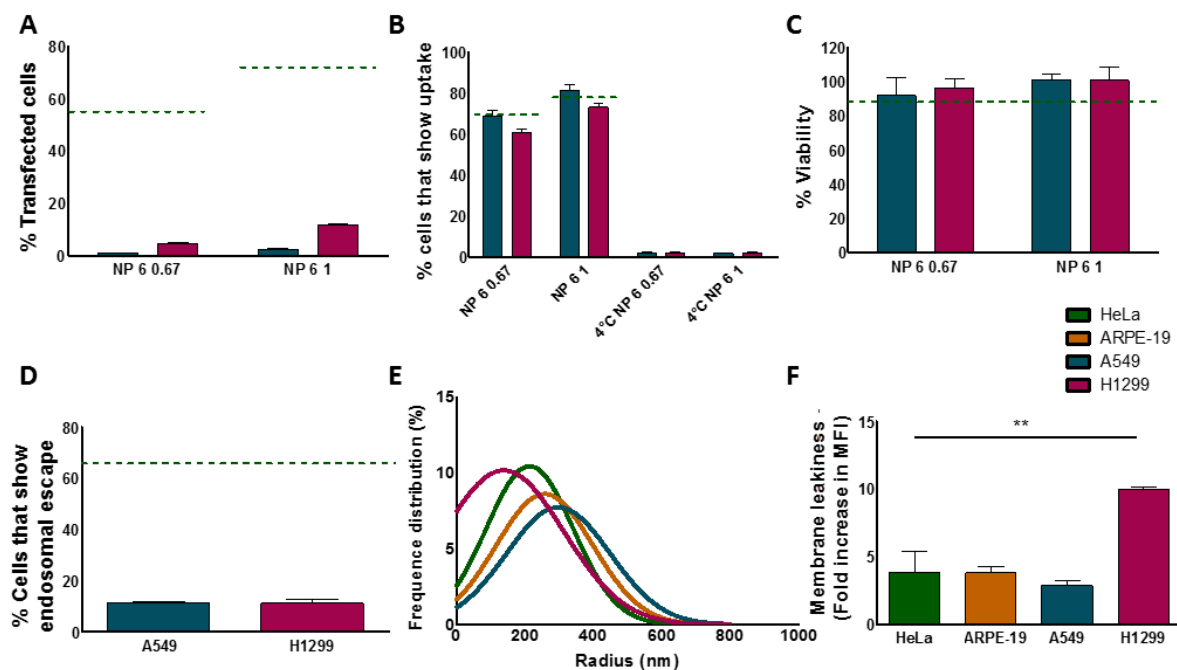


**Figure 3.8 Evaluation of A549 and H1299 cells. (A)** Transfection efficiency expressed as percentage of transfected cells. Graph shows mean  $\pm$  SEM;  $n=3$  **(B)** Polyplex uptake is shown as the percentage of cells that show uptake. Graph shows mean  $\pm$  SEM;  $n=2$ . **(C)** Toxicity was evaluated by means of an MTT test. Graph shows mean  $\pm$  SEM;  $n=2$ . **(D)** Endosomal escape was evaluated 6h after addition of polyplexes (NP 6 0.67 $\mu$ g pDNA) to the cells. Graph represents mean  $\pm$  SEM after evaluation of 713 A549 cells and 780 H1299 cells. For graphs **A-D** a dotted green line was added to compare the values with the reference value as measured on HeLa cells.

**(E)** The size of 1008 A549 and 942 H1299 endosomes was measured after incubation with FITC dextrans and subsequent chase with cell culture medium for 3h. A Gaussian fit was performed on the frequency distributions of endosomal radii from **figure S3** and were compared to the Gaussian fit performed for HeLa and ARPE-19 cells to show the variability in endosomal sizes. **(F)** Membrane leakiness evaluated by measuring calcein fluorescence *via* flow cytometry. Values were corrected for initial calcein uptake and cell volume. The fold increase of calcein fluorescence was calculated after incubation with JetPEI/pDNA NP 6 0.67 particles for 15min and subsequent chase for 3h vs calcein uptake without addition of particles. Graph shows mean  $\pm$  SEM; n=2.

Next we investigated endosomal leakiness induced by JetPEI/pDNA polyplexes with the calcein release assay in the four cell types (HeLa, ARPE-19, A549 and H1299) *via* flow cytometry. In order to be able to compare the membrane leakiness between cell lines, calcein fluorescence after addition of polyplexes was corrected for both initial calcein uptake and cell volume. Results are shown in **Figure 3.8 F** and indicate that HeLa, ARPE-19 and A549 have similar, rather low levels of membrane leakiness, indicating that endosomal leakiness is independent of endosomal size. On the other hand, H1299 endosomes showed markedly more endosomal membrane leakiness, which explains low endosomal escape efficiency in these cells in spite of their smaller endosomes. Based on these results, we can conclude that endosomal escape efficiency by the proton sponge mechanism depends on both endosomal leakiness and endosomal size, which is cell-type dependent. When membrane leakiness is comparable between cell lines (*e.g.* HeLa vs ARPE-19 vs A549) endosomal escape efficiency is correlated to endosomal size: when endosomal size increases, endosomal escape becomes less feasible. However, when vesicles exhibit extreme leakiness (*e.g.* H1299), even a small endosomal size will not induce high rates of endosomal escape since the vesicles are unable to sufficiently build up osmotic pressure.

## 4 DISCUSSION

Endosomal escape has been identified as one of the main bottlenecks in gene delivery<sup>2,4,9-11</sup> and the interest in this barrier has spiked in the last decade. This is reflected by the growing number of publications on this topic, which has increased 10x since 2000.<sup>23</sup> However, trial and error and empirical experimental approaches have predominantly driven the field of nanoparticle design. Recently, critical voices are emerging saying it is time to change course towards a more rational approach of nanoparticle design, taking into consideration the complex series of biological barriers.<sup>24</sup> It is now thought that an enhanced fundamental understanding of cell biology coupled with innovations in material science will be beneficial for the development of a new generation of synthetic carriers.<sup>9,25-27</sup>

In line with this view, we tried to get a better insight into the factors that influence proton sponge-based endosomal escape of polymer gene carriers, which was enabled by recent developments that made detection and visualization of this elusive event possible by high-end live-cell microscopy.<sup>2,10,28</sup> Our work was inspired by the observation that polyplexes induced a markedly higher transfection efficiency in HeLa cells as compared to ARPE-19 cells. Cellular experiments revealed that the difference in transfection was not based on a variation in toxicity or an increase in cellular uptake of the polyplexes in HeLa cells. On the contrary: uptake was even found to be higher in ARPE-19 cells than in HeLa cells. Next, using a specific dequenching assay in live-cell SDC and SFC microscopy, the endosomal escape capacity of JetPEI/pDNA polyplexes was evaluated directly.<sup>8</sup> With image processing, >1000 cells were analyzed, revealing that JetPEI/pDNA polyplexes induce on average about 9 times more endosomal escape events in HeLa cells as in ARPE-19 cells (**Figure 3.4 D**). This finding is illustrative of the current view that on the IC level endosomal escape is indeed one of the most prominent – and perhaps least understood – barriers to effective gene delivery.<sup>4,11,29</sup> Even though there are several barriers that still may play a role after the endosomal barrier (*e.g.* vector unpacking, nuclear uptake), transfection efficiency is clearly linked to the extent to which endosomal escape happens. We reckoned that this marked difference between both cell types would be an interesting starting point to find out more about the factors that govern proton sponge-based endosomal escape.

### 4.1 Endosomal sequestration, pH and mobility

If HeLa cells would internalize and sequester polyplexes to a higher extent than ARPE-19 cells, this could explain the higher endosomal escape frequency since it has been stated before that a critical threshold exists for polymers to mediate endosomal escape through the proton sponge effect.<sup>30,31</sup> However, our results indicated that the

number of polyplexes per endosome was actually lower in HeLa cells than in ARPE-19 cells since HeLa cells internalized less polyplexes (**Figure 3.2 E**) and distributed them over more endosomes (**Figure 3.4 A**) as illustrated in **Figure 3.4 B**. Furthermore, endosomal escape cannot be considered a game of chances since a doubling in number of endosomes cannot account for the 9 times increase in endosomal escape frequency. Next, since pH is a major determinant of the proton sponge hypothesis, it is obvious that it could have a significant impact on endosomal escape. pH measurements confirmed a rapid (<15 min) drop in intravesicular pH to 6.5, reaching an equilibrium at around pH 5.5 as expected.<sup>32-34</sup> However, the endosomal pH in ARPE-19 endosomes was found to be slightly lower than the pH in HeLa endosomes, so that differences regarding endosomal escape capacities could not be attributed to a difference in intrinsic pH value of the endosomes (**Figure 3.5 A**). Thereafter it was hypothesized that the mobility of endosomes could have an impact on endosomal escape frequencies in two different manners. First, the shear stress on the vesicle membrane caused by the migration of the endosomes through the cytoplasm could result in a destabilization of the endosomal membrane. Second, greater endosomal mobility could result in higher energy collisions with other cell organelles or the cytoskeleton, which could lead to endosomal bursting. Quantitative analysis of endosomal mobility by Single Particle Tracking microscopy did, however, not reveal clear differences between the two cell types. If anything, ARPE-19 cells showed a slightly increased mobility when compared to HeLa cells (**Figure 3.5 B**).

## **4.2 Endosomal size**

When inspecting the confocal microscopy images, a rather marked difference between both cell types was that ARPE-19 cells appeared to have larger endosomes than HeLa cells, which was confirmed by quantifying the endosomal size (**Figure 3.5 C-D**). We hypothesized that this might be an important parameter for proton sponge-based endosomal escape. In literature, some reports already indicated a possible relation between endosomal size and transfection efficiency. For instance, Lagache *et al.* developed a biophysical model to describe the escape of small nonenveloped viruses from endosomes triggered by low pH-mediated conformational changes of viral endosomolytic proteins. Their model showed that viral escape time should increase with endosomal size and decrease with the number of viral particles inside the endosome.<sup>35</sup> Barua and Rege found that treatment with tubacin, which acetylates tubulin of microtubules in the cytoplasm, abolished polyplex sequestration at the perinuclear recycling compartment/microtubule organizing center, thereby increasing transgene expression up to forty-fold. The authors hypothesized that distribution of polyplexes in smaller vesicles throughout the cytoplasm as opposed to aggregation at

a single large perinuclear region, could allow for greater endosomal escape, which in turn could enhance transfection.<sup>36</sup>

To better understand the relation between endosomal size and proton sponge-based endosomal escape, a simple mathematical model was introduced describing endosomal burst by the proton sponge effect, taking into account both osmotic pressure and the counteracting Laplace pressure. By balancing both opposing forces, we found that the endosomal chloride influx ( $\Delta N$ ) needed to induce endosomal rupture is proportional to the square of the (original) endosomal radius ( $R_0^2$ ). This can be easily appreciated as being the result of the combined influence of the proton sponge effect causing a change in volume (proportional to  $R_0^3$ ) and the counteracting influence of Laplace's law (proportional to  $\frac{1}{R_0}$ ). This simple mathematical model gives support to our hypothesis that large endosomes, as in ARPE-19 cells, are more difficult to burst: an endosome of double the size needs 4 times more polymer to burst. However, we would like to note that some factors were not considered while setting up this model. First there is the contribution by free polymer that is dissolved in the cell medium upon incubation with the polyplexes and that is endocytosed alongside the polyplexes. Indeed, upon preparation of polyplexes, not all polymer will be incorporated into the particles but a fraction remains free in solution.<sup>37</sup> As such there will be free polymer present in the lumen of the endosomes as well. However, this fraction of dissolved PEI polymer gives a negligible contribution to the osmotic pressure, as explained in Supporting Information ("Amount of NH-containing monomers per endosome from free PEI in solution"), and can be safely disregarded. The second factor that we did not consider is the fraction of free PEI polymer that is electrostatically attracted to the negatively charged cell membrane. Upon endocytosis of polyplexes, *i.e.* by invagination of the cell membrane, it seems likely that the inside of the endosomal membrane will be coated with a layer of membrane-attached polymer. While this fraction of membrane-associated polymer may significantly contribute to the osmotic pressure, it does not matter in our discussion on the role of endosomal size. Indeed, being proportional to the endosomal surface area it only gives a constant offset to the prefactor in Equation (5), but does not change the above considerations on larger endosomes requiring more polyplexes to induce endosomal escape. Finally, disassembly of pDNA from the polyplex could also increase the buffer capacity of the polymer as amines that were used to complex pDNA are now available again to buffer protons. However, we do not have indications to believe that polyplex disassembly happens faster or more efficiently in smaller endosomes than bigger ones. Together this does mean that the number of polyplexes in Table 1 needed to cause endosomal

bursting can slightly vary according to the amount of polymer that is attracted to the cell membrane and the disassembly of the polyplex in the endosomal lumen.

It should also be noted that endosomal size is only half the argument. Endosomal trafficking is a highly dynamic process where payloads can be transferred or accumulated during trafficking. As such it cannot be excluded that within a cell larger endosomes may burst if they contain a high polyplex content. For instance, an endosome of twice the size can theoretically contain 8 times as much polymer, which is more than the factor of 4 that is minimally needed to induce endosomal escape. Therefore, one should not expect that endosomal escape only happens in the smallest endosomes within a cell as trafficking plays a role as well. In any case, while the mathematical model presented in this paper is a simplified representation that only describes the equilibrium state, it does capture the essence that differences in endosomal size can play a decisive role in the inherent capacity of polymer carriers to induce endosomal escape and correlates with the fact that less endosomal escape is seen in ARPE-19 cells. Nevertheless, in future work it would be interesting to explore more extensive computational models of the proton sponge effect, such as the one by Freeman *et al.* for dendrimers that can give a detailed time-dependent description of the proton sponge effect.<sup>38</sup>

With the fundamental understanding of the endosomal barrier that follows from our results, it is tempting to contemplate on ways to boost endosomal release and transfection efficiency of non-viral gene therapeutics. Conceptually it would be interesting to find ways to introduce polyplexes in smaller endosomes, as these should rupture more efficiently than larger endosomes. One option could be to target an endosomal pathway where endosomes have a small intrinsic diameter. In this respect, one could consider using a ligand such as folic acid<sup>39</sup> or albumin<sup>40</sup> to target caveolae mediated endocytosis, since it has been reported that this pathway results in the formation of very small endosomes of 60-80 nm in diameter (compared to 120-150 nm after internalization *via* the classical route of clathrin-dependent endocytosis).<sup>41,42</sup> Several reports indeed show an increased transfection efficiency of caveolae-targeted polyplexes compared to unmodified polyplexes.<sup>39,43</sup> Moreover, even though PEI polyplexes are internalized through a combination of caveolae-mediated endocytosis and clathrin mediated endocytosis, it is stated in several papers that only inhibition of caveolae-mediated endocytosis drastically reduces transfection efficiency.<sup>39,44,45</sup> Together it seems that our size argument may explain, at least in part, why caveolin-mediated uptake offers better transfection of PEI polyplexes. Another concept could be to find ways to sequester more polyplexes in fewer endosomes. Ogris *et al.* found that large aggregates of PEI and pDNA (> 500 nm) were more efficient than small PEI/pDNA

polyplexes (80-150 nm), even though the large aggregates were internalized very slowly and to a low extent.<sup>46</sup> Furthermore, controlled aggregation of PEI/pDNA polyplexes at the cell membrane has been shown to induce an increased transfection efficiency *in vivo*, possibly due to elevated levels of cell binding and endosomal release.<sup>47</sup>

A third approach could be to interact with different endosomal proteins such as Rab GTPases, as they are known to be key regulatory factors for endocytosis and are involved in the formation, transport, tethering and fusion of vesicles.<sup>48</sup> Ganley *et al.* described the formation of late endosomes with decreased size and a reduction in the number of multilamellar and dense-tubule-containing late endosomes/lysosomes after siRNA mediated depletion of Rab9.<sup>49</sup> Endosomal morphology can also be influenced by manipulating Rab5 expression since Rab5 regulates membrane docking and fusion events in the early endocytic pathway. Rab5 inhibition is reported to induce a very small endocytic profile, while Rab5 stimulation leads to enlargement of early endosomes and a juxtranuclear localization.<sup>50,51</sup> Furthermore, inhibition or induction of proteins that affect Rab GTPases (*e.g.* Rin1, a Rab5-guanine exchange factor) or other endosomal proteins (*e.g.* Secretory carrier membrane protein 3) have been reported to influence endosomal size.<sup>52,53</sup> Given the complexity of biochemical processes performed in the cell, it is clear that the interaction of all these endosomal proteins makes it difficult to predict the downstream consequences when stimulating or inhibiting one protein. It is may very well be that manipulating protein expression will have many other (unwanted) effects besides reducing endosomal size. Of course, interfering with protein expression is more of theoretical consideration since it requires cell transfections which we are trying to optimize in the first place.

### **4.3 Endosomal leakiness**

It remains a flagrant observation that even in HeLa cells less than 10% of the polyplex-containing endosomes show escape at some point. We hypothesized that this may be due to leakiness of the endosomal membrane as the leakage of water and ions from the endosomal lumen to the cytoplasm results in the loss of osmotic pressure and thereby abolishes proton sponge-based endosomal rupture. Endosomal leakiness can be a result of small defects that arise in the endosomal membrane when pressure builds up upon osmotic swelling in combination with interaction of the protonated PEI chains with the endosomal lipid bilayer.<sup>54</sup> Co-incubation of PEI polyplexes with quenched calcein confirmed this hypothesis since both HeLa and ARPE-19 cells that had taken up PEI/pDNA polyplexes showed cytosolic calcein release in virtually every cell whereas calcein remained trapped in endosomes in the absence of polyplexes (**Figure 3.7**).

Li *et al.* investigated the elasticity of unilamellar dioleoylphosphatidic acid (DOPA) and DOPA-cholesterol (10-25 mol%) vesicles in KCl and sucrose solutions and found that neither the presence nor the concentration of cholesterol had a significant influence on elasticity. They showed that the elastic limit of examined vesicles remained relatively constant with an elastic limit of 3-5% in KCl solutions and 8-10 % in sucrose solutions.<sup>20</sup> Based on these findings, it seems unlikely that membrane composition alone would have a significant effect on endosomal escape frequency. It would therefore be very interesting to study the interaction of protonated PEI chains with different membrane compositions and its effect on membrane leakiness. In this respect, a paper was published very recently by Clark *et al.* who studied the interaction of PEI with endosomal lipids under osmotic stress using synthetic monolayers and vesicles.<sup>55</sup> Moreover, it would be fascinating not only to study the intercellular differences in membrane composition, but also intracellular differences such as different membrane composition resulting from different uptake pathways within the same cell type. This information could lead us towards identifying types of endosomes that are less likely to form these leaks, thereby giving proton sponge-based rupture a better chance at success.

## **5 CONCLUSION**

Taken together, our results point to the fact that both endosomal size and polyplex-induced membrane leakiness have a considerable impact on proton sponge-based endosomal escape. Based on rigorous analysis of four different cell types, we conclude that endosomal size largely determines endosomal escape efficiency when cells have comparable polyplex induced membrane leakiness. However, at high levels of membrane leakiness build-up of osmotic pressure is no longer possible, regardless of endosomal size. In future work, it is of interest to further investigate the reasons why endosomal membrane leakiness differs between cell types, and if endosomal escape efficiency can be increased by interfering with endosomal size and endosomal membrane leakiness.

## **ACKNOWLEDGEMENTS**

L. Vermeulen would like to acknowledge the financial support of the Agency for Innovation by Science and Technology in Belgium. Financial support by the Ghent University Special Research Fund and the Fund for Scientific Research Flanders (FWO, Belgium) is acknowledged with gratitude. This research was funded by the European Research Council (ERC) under the European Union's Horizon 2020 research and innovation program (grant agreement [648214]) and has received support from the Innovative Medicines Initiative Joint Undertaking under grant agreement n° 115363 resources of which are composed of financial contribution from the European Union's Seventh Framework Programme (FP7/2007-2013) and EFPIA companies' in kind contribution.

## REFERENCES

- (1) Jhaveri, A.; Torchilin, V. Intracellular Delivery of Nanocarriers and Targeting to Subcellular Organelles. *Expert Opin. Drug Deliv.* **2016**, *13*, 49–70.
- (2) Lönn, P.; Kacsinta, A. D.; Cui, X.-S.; Hamil, A. S.; Kaulich, M.; Gogoi, K.; Dowdy, S. F. Enhancing Endosomal Escape for Intracellular Delivery of Macromolecular Biologic Therapeutics. *Sci. Rep.* **2016**, *6*, 32301.
- (3) Rajendran, L.; Knölker, H.-J.; Simons, K. Subcellular Targeting Strategies for Drug Design and Delivery. *Nat. Rev. Drug Discov.* **2010**, *9*, 29–42.
- (4) Martens, T. F.; Remaut, K.; Demeester, J.; De Smedt, S. C.; Braeckmans, K. Intracellular Delivery of Nanomaterials: How to Catch Endosomal Escape in the Act. *Nano Today*, 2014, *9*, 344–364.
- (5) Pangarkar, C.; Dinh, A. T.; Mitragotri, S. Endocytic Pathway Rapidly Delivers Internalized Molecules to Lysosomes: An Analysis of Vesicle Trafficking, Clustering and Mass Transfer. *J. Control. Release* **2012**, *162*, 76–83.
- (6) Remaut, K.; Sanders, N. N.; De Geest, B. G.; Braeckmans, K.; Demeester, J.; De Smedt, S. C. Nucleic Acid Delivery: Where Material Sciences and Bio-Sciences Meet. *Mater. Sci. Eng. R Reports* **2007**, *58*, 117–161.
- (7) Pack, D. W.; Hoffman, A. S.; Pun, S.; Stayton, P. S. Design and Development of Polymers for Gene Delivery. *Nat. Rev. Drug Discov.* **2005**, *4*, 581–593.
- (8) Rehman, Z. U.; Hoekstra, D.; Zuhorn, I. S. Mechanism of Polyplex- and Lipoplex-Mediated Delivery of Nucleic Acids: Real-Time Visualization of Transient Membrane Destabilization without Endosomal Lysis. *ACS Nano* **2013**, *7*, 3767–3777.
- (9) Stewart, M. P.; Lorenz, A.; Dahlman, J.; Sahay, G. Challenges in Carrier-Mediated Intracellular Delivery: Moving beyond Endosomal Barriers. *Wiley Interdiscip. Rev. Nanomedicine Nanobiotechnology* **2016**, *8*, 465–478.
- (10) Gilleron, J.; Querbes, W.; Zeigerer, A.; Borodovsky, A.; Marsico, G.; Schubert, U.; Manygoats, K.; Seifert, S.; Andree, C.; Stöter, M.; *et al.* Image-Based Analysis of Lipid Nanoparticle-mediated siRNA Delivery, Intracellular Trafficking and Endosomal Escape. *Nat. Biotechnol.* **2013**, *31*, 638–646.
- (11) Shete, H. K.; Prabhu, R. H.; Patravale, V. B. Endosomal Escape: A Bottleneck in Intracellular Delivery. *J. Nanosci. Nanotechnol.* **2014**, *14*, 460–474.
- (12) Lv, H.; Zhang, S.; Wang, B.; Cui, S.; Yan, J. Toxicity of Cationic Lipids and Cationic Polymers in Gene Delivery. *J. Control. Release* **2006**, *114*, 100–109.
- (13) Taranejoo, S.; Chandrasekaran, R.; Cheng, W.; Hourigan, K. Bioreducible PEI-Functionalized Glycol Chitosan: A Novel Gene Vector with Reduced Cytotoxicity and Improved Transfection Efficiency. *Carbohydr. Polym.* **2016**, *153*, 160–168.
- (14) Zhao, X.; Li, Z.; Pan, H.; Liu, W.; Lv, M.; Leung, F.; Lu, W. W. Enhanced Gene Delivery by Chitosan-Disulfide-Conjugated LMW-PEI for Facilitating Osteogenic Differentiation. *Acta Biomater.* **2013**, *9*, 6694–6703.

- (15) Geisow, M. J. Fluorescein Conjugates as Indicators of Subcellular pH. A Critical Evaluation. *Exp. Cell Res.* **1984**, *150*, 29–35.
- (16) Wang, C.; de Jong, E.; Sjollem, K. A.; Zuhorn, I. S. Entry of PIP3-Containing Polyplexes into MDCK Epithelial Cells by Local Apical-Basal Polarity Reversal. *Sci. Rep.* **2016**, *6*, 21436.
- (17) Dean, B. .; Goddard, M. B. I.; Rein, D. H.; Stabila, P. F.; Tao, W. Arpe-19 as a Platform Cell Line for Encapsulated Cell-Based Delivery, 2004.
- (18) Posakony, J. W.; England, J. M.; Attardi, G. CYCLE GROWTH AND DIVISION DURING THE Conditions O F Cell Culture and. **1977**, *74*, 468–491.
- (19) Hallett, F. R.; Marsh, J.; Nickel, B. G.; Wood, J. M. Mechanical Properties of Vesicles. II. A Model for Osmotic Swelling and Lysis. *Biophys. J.* **1993**, *64*, 435–442.
- (20) Li, W.; Aurora, T. S.; Haines, T. H.; Cummins, H. Z. Elasticity of Synthetic Phospholipid Vesicles and Submitochondrial Particles during Osmotic Swelling. *Biochemistry* **1986**, *25*, 8220–8229.
- (21) Rutkowski, C. a; Williams, L. M.; Haines, T. H.; Cummins, H. Z. The Elasticity of Synthetic Phospholipid Vesicles Obtained by Photon Correlation Spectroscopy. *Biochemistry* **1991**, *30*, 5688–5696.
- (22) Ziebarth, J. D.; Wang, Y. Understanding the Protonation Behavior of Linear Polyethylenimine in Solutions through Monte Carlo Simulations. *Biomacromolecules* **2011**, *11*, 1–29.
- (23) Medline (PubMed) Trend <http://dan.corlan.net/medline-trend.html> (accessed Jan 4, 2017).
- (24) Blanco, E.; Shen, H.; Ferrari, M. Principles of Nanoparticle Design for Overcoming Biological Barriers to Drug Delivery. *Nat. Biotechnol.* **2015**, *33*, 941–951.
- (25) Yin, H.; Kanasty, R. L.; Eltoukhy, A. A.; Vegas, A. J.; Dorkin, J. R.; Anderson, D. G. Non-Viral Vectors for Gene-Based Therapy. *Nat. Rev. Genet.* **2014**, *15*, 541–555.
- (26) Bishop, C. J.; Kozielski, K. L.; Green, J. J. Exploring the Role of Polymer Structure on Intracellular Nucleic Acid Delivery via Polymeric Nanoparticles. *J. Control. Release* **2015**, *219*, 488–499.
- (27) Editorial. Time to Deliver. *Nat. Biotechnol.* **2014**, *32*, 961.
- (28) Wittrup, A.; Ai, A.; Liu, X.; Hamar, P.; Trifonova, R.; Charisse, K.; Manoharan, M.; Kirchhausen, T.; Lieberman, J. Visualizing Lipid-Formulated siRNA Release from Endosomes and Target Gene Knockdown. *Nat. Biotechnol.* **2015**, *33*, 870–876.
- (29) Varkouhi, A. K.; Scholte, M.; Storm, G.; Haisma, H. J. Endosomal Escape Pathways for Delivery of Biologicals. *J. Control. Release* **2011**, *151*, 220–228.
- (30) Kichler, A.; Leborgne, C.; Coeytaux, E.; Danos, O. Polyethylenimine-Mediated Gene Delivery: A Mechanistic Study. *J. Gene Med.* **2001**, *3*, 135–144.

- (31) Richard, I.; Thibault, M.; De Crescenzo, G.; Buschmann, M. D.; Lavertu, M. Ionization Behavior of Chitosan and Chitosan-DNA Polyplexes Indicate That Chitosan Has a Similar Capability to Induce a Proton-Sponge Effect as PEI. *Biomacromolecules* **2013**, *14*, 1732–1740.
- (32) Geisow, J.; Evans, W. H. pH in the Endosome - Measurement during Pinocytosis and Receptor-Mediated Endocytosis. *Cell* **1984**, *150*, 36–46.
- (33) Huotari, J.; Helenius, A. Endosome Maturation. *EMBO J.* **2011**, *30*, 3481–3500.
- (34) Wang, C.; Zhao, T.; Li, Y.; Huang, G.; White, M. A.; Gao, J. Investigation of Endosome and Lysosome Biology by Ultra pH-Sensitive Nanoprobes. *Adv. Drug Deliv. Rev.* **2017**, *113*, 87–96.
- (35) Lagache, T.; Danos, O.; Holcman, D. Modeling the Step of Endosomal Escape during Cell Infection by a Nonenveloped Virus. *Biophys. J.* **2012**, *102*, 980–989.
- (36) Barua, S.; Rege, K. The Influence of Mediators of Intracellular Trafficking on Transgene Expression Efficacy of Polymer-Plasmid DNA Complexes. *Biomaterials* **2010**, *31*, 5894–5902.
- (37) Benjaminsen, R. V.; Matthebjerg, M. A.; Henriksen, J. R.; Moghimi, S. M.; Andresen, T. L. The Possible "Proton Sponge " Effect of Polyethylenimine (PEI) Does Not Include Change in Lysosomal pH. *Mol. Ther.* **2013**, *21*, 149–157.
- (38) Freeman, E. C.; Weiland, L. M.; Meng, W. S. Modeling the Proton Sponge Hypothesis: Examining Proton Sponge Effectiveness for Enhancing Intracellular Gene Delivery through Multiscale Modeling. *J. Biomater. Sci. Polym. Ed.* **2013**, *24*, 398–416.
- (39) Gabrielson, N. P.; Pack, D. W. Efficient Polyethylenimine-Mediated Gene Delivery Proceeds via a Caveolar Pathway in HeLa Cells. *J. Control. Release* **2009**, *136*, 54–61.
- (40) Wang, Z.; Tiruppathi, C.; Minshall, R. D.; Malik, A. B. Size and Dynamics of Caveolae Studied Using Nanoparticles in Living Endothelial Cells. *ACS Nano* **2009**, *3*, 4110–4116.
- (41) Sahay, G.; Alakhova, D. Y.; Kabanov, A. V. Endocytosis of Nanomedicines. *J. Control. Release* **2010**, *145*, 182–195.
- (42) El-Sayed, A.; Harashima, H. Endocytosis of Gene Delivery Vectors: From Clathrin-Dependent to Lipid Raft-Mediated Endocytosis. *Mol. Ther.* **2013**, *21*, 1118–1130.
- (43) Cao, D.; Tian, S.; Huang, H.; Chen, J.; Pan, S. Divalent Folate Modification on PEG: An Effective Strategy for Improving the Cellular Uptake and Targetability of PEGylated Polyamidoamine – Polyethylenimine Copolymer. *Mol. Pharm.* **2015**, *12*, 240–252.
- (44) Rejman, J.; Bragonzi, A.; Conese, M. Role of Clathrin- and Caveolae-Mediated Endocytosis in Gene Transfer Mediated by Lipo- and Polyplexes. *Mol. Ther.* **2005**, *12*, 468–474.
- (45) Van Der Aa, M. A. E. M.; Huth, U. S.; Häfele, S. Y.; Schubert, R.; Oosting, R. S.; Mastrobattista, E.; Hennink, W. E.; Peschka-Süss, R.; Koning, G. A.;

- Crommelin, D. J. A. Cellular Uptake of Cationic Polymer-DNA Complexes via Caveolae Plays a Pivotal Role in Gene Transfection in COS-7 Cells. *Pharm. Res.* **2007**, *24*, 1590–1598.
- (46) Ogris, M.; Steinlein, P.; Carotta, S.; Brunner, S.; Wagner, E. DNA/polyethylenimine Transfection Particles: Influence of Ligands, Polymer Size, and PEGylation on Internalization and Gene Expression. *AAPS PharmSci* **2001**, *3*, 43–53.
- (47) Wightman, L.; Kircheis, R.; Rössler, V.; Garotta, S.; Ruzicka, R.; Kursa, M.; Wagner, E. Different Behavior of Branched and Linear Polyethylenimine for Gene Delivery in Vitro and in Vivo. *J. Gene Med.* **2001**, *3*, 362–372.
- (48) Hutagalung, A. H.; Novick, P. J. Role of Rab GTPases in Membrane Traffic and Cell Physiology. *Physiol. Rev.* **2011**, *91*, 119–149.
- (49) Ganley, I. G.; Carroll, K.; Bittova, L.; Pfeffer, S. Rab9 GTPase Regulates Late Endosome Size and Requires Effector Interaction for Its Stability. *Mol. Biol. Cell* **2004**, *15*, 5420–5430.
- (50) Nielsen, E.; Severin, F.; Backer, J. M.; Hyman, A. A.; Zerial, M. Rab5 Regulates Motility of Early Endosomes on Microtubules. *Nat. Cell Biol.* **1999**, *1*, 376–382.
- (51) Stenmark, H.; Parton, R. G.; Steele-Mortimer, O.; Lütcke, A.; Gruenberg, J.; Zerial, M. Inhibition of rab5 GTPase Activity Stimulates Membrane Fusion in Endocytosis. *EMBO J.* **1994**, *13*, 1287–1296.
- (52) Galvis, A.; Giambini, H.; Villasana, Z.; Barbieri, M. A. Functional Determinants of Ras Interference 1 Mutants Required for Their Inhibitory Activity on Endocytosis. *Exp. Cell Res.* **2009**, *315*, 820–835.
- (53) Thomas, P.; Wohlford, D.; Aoh, Q. L. SCAMP-3 Is a Novel Regulator of Endosomal Morphology and Composition. *Biochem. Biophys. Res. Commun.* **2016**, *478*, 1028–1034.
- (54) Choudhury, C. K.; Kumar, A.; Roy, S. Characterization of Conformation and Interaction of Gene Delivery Vector Polyethylenimine with Phospholipid Bilayer at Different Protonation State. *Biomacromolecules* **2013**, *14*, 3759–3768.
- (55) Clark, S. R.; Lee, K. Y.; Lee, H.; Khetan, J.; Kim, H. C.; Choi, Y. H.; Shin, K.; Won, Y.-Y. Determining the Effects of PEI Adsorption on the Permeability of DPPC/BMP Membranes under Osmotic Stress. *Acta Biomater.* **2018**, *65*, 317–326.

# SUPPORTING INFORMATION

## Chapter 3

### Endosomal Size and Membrane Leakiness Influence Proton Sponge-Based Rupture of Endosomal Vesicles

#### **SUPPORTING INFORMATION**

Supporting Information consists of 1 additional table, 5 additional figures, the derivation to define the burst criterion, the conversion of NH-containing monomers to the amount of polyplexes, the amount of NH-containing monomers per endosome due to free PEI in solution and information regarding image processing. Five supporting movies are also available. This material is available free of charge *via* the Internet at <http://pubs.acs.org>.

**Table S1** – image processing filters and parameters used in IPS (Custom developed Matlab software).

	Unsharp average filter	Median filter	Treshold (N=)
<b><i>Polyplex-containing endosomes</i></b>	Kernel size 21 Subtraction factor 1	Kernel size 5	2
<b><i>Endosomal pH</i></b>	Kernel size 21 Subtraction factor 1	Kernel size 3	2.5
<b><i>Endosomal mobility</i></b>	Kernel size 21 Subtraction factor 1	Kernel size 3	4.25
<b><i>Endosomal size</i></b>	Kernel size 21 Subtraction fraction 1	Kernel size 3	7.5

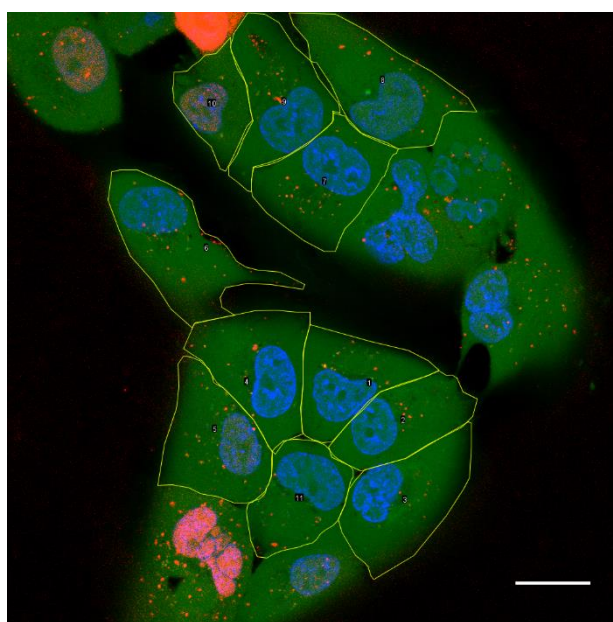


**Figure S1. Microscopy image to show the determination of the number of endosomes in cells** (ARPE-19 cells shown) after incubation with JetPEI/pDNA polyplexes for 15 min. Yellow lines represent cell boundaries determined by incubation with calceinAM. The nucleus is shown in blue, polyplex-containing endosomes are labeled in red and a red nucleus indicates the occurrence of an endosomal escape event. Scalebar represents 20  $\mu\text{m}$ .

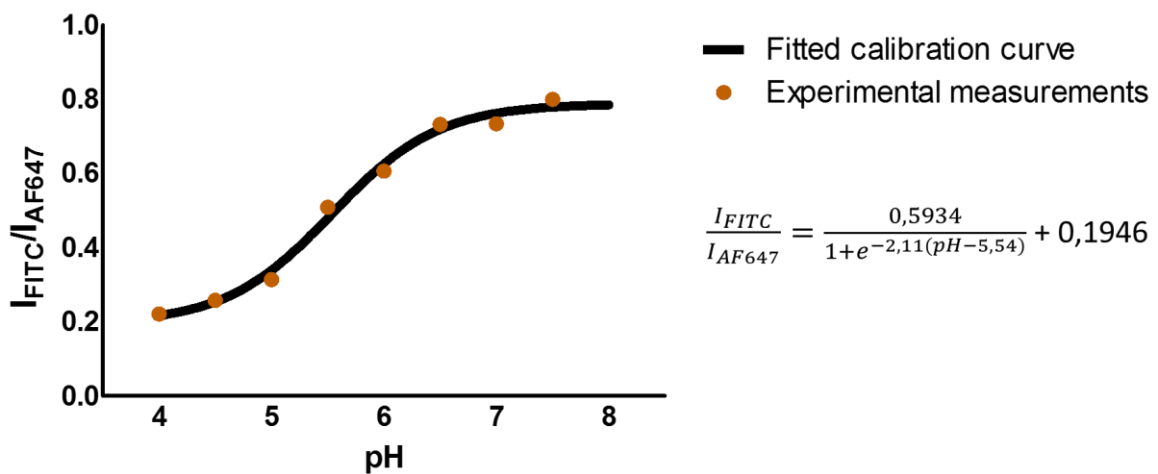


**Figure S2. Conversion of  $I_{FITC}/I_{AF647}$  values to pH values.** A calibration curve (black line; formula displayed) was fitted to a logistic function in Matlab based on experimental measurements of  $I_{FITC}/I_{AF647}$  in buffer solutions with various pH (orange dots).

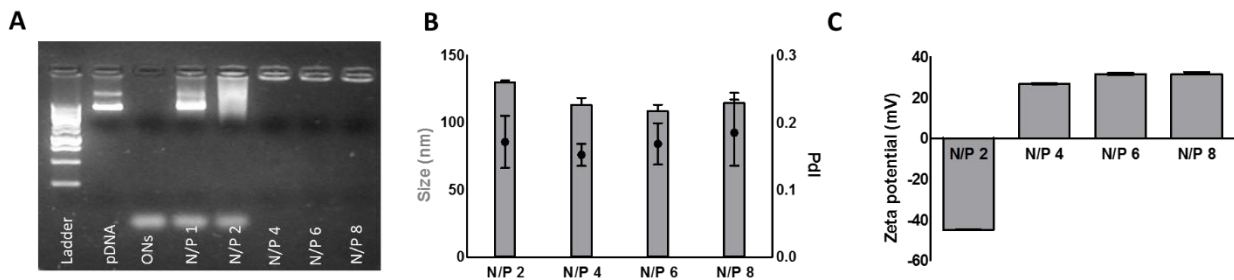


**Figure S3. Characterization of JetPEI/pDNA polyplexes in HEPES (20 mM, pH 7.2) buffer.** (A) Gel electrophoresis shows successful pDNA and ON complexation starting from an N/P ratio of 4. Further characterization by DLS reveals the size (B) (grey bars), PdI (black dots) and zeta potential (C) for different N/P ratios. Values are displayed as mean  $\pm$  stdev; n=3.

### JetPEI NP 6 0.67

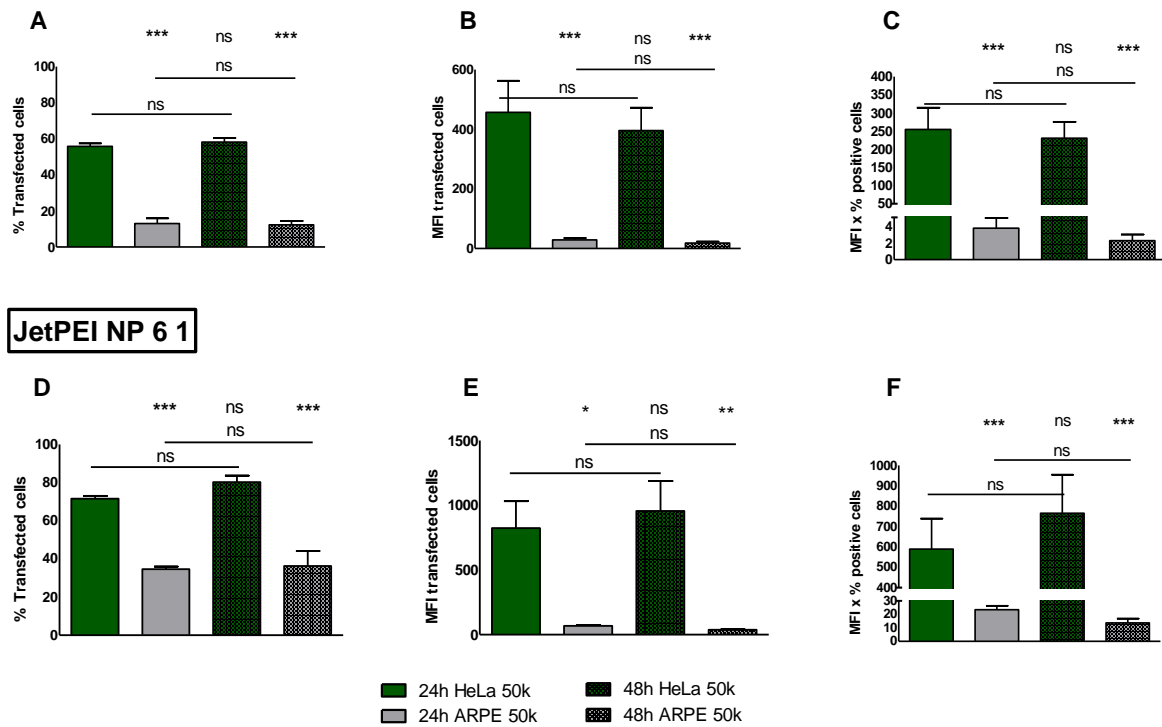


**Figure S4.** To investigate the influence of a different cell division time, read-out time for transfection (24h vs 48h) was varied. JetPEI/pDNA polyplexes with an N/P ratio of 6 (NP 6) were used in two different concentrations. Graph A-C show results for JetPEI/pDNA NP 6 polyplexes containing 0.67 µg gWIZ GFP pDNA per well, while graph D-F show results for JetPEI/pDNA NP 6 polyplexes containing 1 µg gWIZ GFP pDNA per well. Graph A and D display the percentage of transfected cells after incubation with the JetPEI/pDNA polyplexes. Graph B and E show the median fluorescence intensity (MFI) of the transfected cells. Graph C and F show MFI x percentage of GFP-positive cells as a measure for the average GFP content. Values represent mean ± SEM; n=3 and significance was calculated using ANOVA test with Bonferroni's post-test (\*\*\*) p < 0.0001; \*\* p < 0.01; \* p < 0.05).

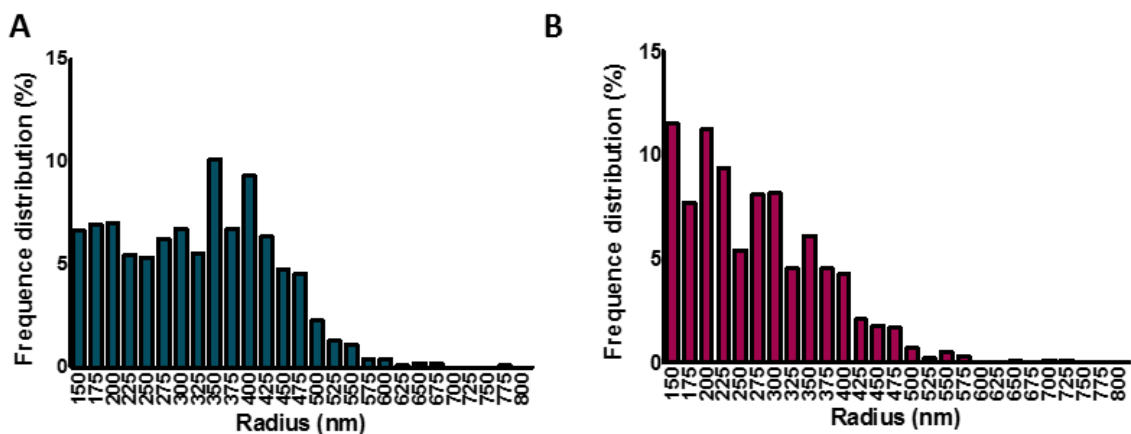


**Figure S5.** Determination of endosomal size in A549 vs H1299 cells. Graphs show the relative frequency distribution (%) of endosomal radii (in nm) for A549 cells (A) and H1299 cells (B). A total of 1008 A549 and 942 H1299 endosomes were measured.

## Defining the burst criterion

According to Li *et al.*<sup>1</sup> the elastic limit of phospholipid vesicles equals a 5-10% increase in surface area ( $S$ ). Assuming the maximal increase in surface area is set to 10%, the maximum stretch on the vesicle  $\frac{\Delta R}{R_0}$  can be calculated.

$$\Delta S = S_{final} - S_0 \quad (A)$$

The surface area of a sphere is given by

$$S = 4\pi R^2 \quad (B)$$

Equation B can now be substituted into equation A, giving

$$\Delta S = 4\pi(R_{final}^2 - R_0^2) = 0,1S_0$$

$$\Leftrightarrow 4\pi((R_0 + \Delta R)^2 - R_0^2) = 0,1S_0$$

$$\Leftrightarrow 4\pi(R_0^2 + 2R_0\Delta R + \Delta R^2 - R_0^2) = 0,1S_0$$

$$\Leftrightarrow 4\pi R_0^2 \left( 2 \frac{\Delta R}{R_0} + \left( \frac{\Delta R}{R_0} \right)^2 \right) = 0,1S_0$$

$$\Leftrightarrow \left( \frac{\Delta R}{R_0} \right)^2 + 2 \frac{\Delta R}{R_0} - 0,1 = 0$$

$$\frac{\Delta R}{R_0} = \varepsilon = \frac{-2 \pm 2\sqrt{1 + 0,1}}{2} \approx 0,05 \quad (C)$$

A 10% increase in surface area equals a 5% increase in endosomal strain and the burst criterion is thus defined as  $\varepsilon = 5\%$  increase.

## Converting NH-containing monomers to the amount of polyplexes

First, the theoretical number of pDNA and ON strands in the polyplex mixture is calculated. The molecular weight of gWIZ GFP pDNA is calculated to be 3.5 MDa (according to the formula provided by Thermofisher<sup>2</sup> knowing that gWIZ GFP pDNA contains 5757 basepairs<sup>3</sup>). Taking into account Avogadro's number, it is calculated that 2.68 µg gWIZ GFP pDNA (amount of pDNA used to prepare the polyplexes) contains  $4.58 \cdot 10^{11}$  pDNA strands. Similarly, the total number of ON strands used to prepare the polyplexes was calculated to be  $16.3 \cdot 10^{13}$ . Next, the amount of polyplexes was determined to be  $2.7 \cdot 10^{10} \pm 2.3 \cdot 10^9$  (Nanoparticle Tracking Analysis, NanoSight), leading to  $17.0 \pm 1.3$  pDNA strands per polyplex and  $6.02 \pm 0.47 \cdot 10^3$  ON strands per polyplex. Next, it is possible to calculate the amount of positive charges per polyplex ( $PC$ ; = NH-containing monomers) by multiplying the amount of negative charges per (pDNA or ON) strand ( $NC$ ) with the previously determined amount of pDNA or ON strands per polyplex ( $n$ ), and applying an N/P ratio of 6 (Equation D). One strand of gWIZ GFP pDNA contains  $11.5 \cdot 10^3$  negative charges, leading to  $11.7 \pm 0.9 \cdot 10^5$  positive charges per polyplex and one strand of ON contains 21 negative charges, leading to  $7.6 \pm 0.6 \cdot 10^5$  positive charges per polyplex.

$$PC = NC \times n \times N/P \quad (D)$$

These calculations lead to a total combined amount of  $1.9 \pm 0.2 \cdot 10^6$  positive charges (or NH-containing monomers) per JetPEI/pDNA N/P 6 polyplex, which can then be used to convert the number of NH-containing monomers needed to burst an endosome to the number of polyplexes needed to achieve this goal (**Table 3.1**).

## Amount of NH-containing monomers per endosome from free PEI in solution

### 1. Calculate the concentration of free PEI in solution

First, we need to calculate the total amount of NH containing monomers we added to the cells. As explained in the main text we do this as follows:

200  $\mu\text{l}$  particles contains 2  $\mu\text{g}$  gWIZ GFP pDNA (equivalent to  $3.44 \cdot 10^{11}$  pDNA strands) and 1.55  $\mu\text{g}$  ONs (equivalent to  $1.19 \cdot 10^{14}$  ON strands). Since 1 pDNA strand contains 11514 negative charges per strand and 1 ON strand contains 21 negative charges per strand, a total of  $6.46 \cdot 10^{15}$  negative charges are added to the cells. Since particles were prepared with an N/P ratio of 6, it was calculated that  **$3.88 \cdot 10^{16}$  NH-containing monomers** were added to the cells.

Under the assumption that at N/P ratios higher than 3, the excess PEI is free in solution<sup>4</sup>, we can state that half of these monomers ( $= 1.94 \cdot 10^{16}$  NH-containing monomers) are free in the total volume of cell culture medium added to the cells ( $= 1500 \mu\text{L}$ ), leading to a **final free PEI concentration of 20.75  $\mu\text{M}$  or  $1.29 \cdot 10^{13}$  monomers per  $\mu\text{L}$ .**

### 2. Determine amount of NH containing monomers per endosome due to free PEI

Next, we calculate the volume of endosomes with a given radius to evaluate the amount of free PEI they encapsulate during uptake:

Volume of endosome with radius 200 nm:

$$\frac{4}{3} \cdot \pi \cdot 200\text{nm}^3 = 3.35 \cdot 10^{-8} \text{ nL} \quad \rightarrow \text{this volume contains a total amount of } \underline{433 \text{ NH containing monomers}}$$

Volume of endosome with radius 400 nm:

$$\frac{4}{3} \cdot \pi \cdot 400\text{nm}^3 = 2.68 \cdot 10^{-7} \text{ nL} \quad \rightarrow \text{this volume contains a total amount of } \underline{3462 \text{ NH containing monomers}}$$

Volume of endosome with radius 600nm:

$$\frac{4}{3} \cdot \pi \cdot 600\text{nm}^3 = 9.04 \cdot 10^{-7} \text{ nL} \quad \rightarrow \text{this volume contains a total amount of } \underline{11677 \text{ NH-containing monomers}}$$

When we compare the amount of monomers that is taken up in the endosomes due to free PEI to the amount of endosomes that is needed to burst that endosome (**Table 3.1**), we come to the conclusion that the contribution of free PEI can be neglected.

## **Image processing – mobility analysis in Matlab**

Trackviewer was used to perform D analysis on recorded movies with max step size = 20, min track = 5 and missing steps = 0. Next, a MEM analysis was performed for every time point (30 min, 1 h, 2 h and 3 h) rendering a frequency distribution of the diffusion coefficients ( $D$ ) of the endosomes. Mean square displacement (MSD) was calculated from these diffusion coefficients using  $MSD = 4D\Delta t$  with  $\Delta t$  the time between frames.

## REFERENCES

- (1) Li, W.; Aurora, T. S.; Haines, T. H.; Cummins, H. Z. Elasticity of Synthetic Phospholipid Vesicles and Submitochondrial Particles during Osmotic Swelling. *Biochemistry* **1986**, *25*, 8220–8229.
- (2) ThermoFischer Scientific DNA and RNA Molecular Weights and Conversions <https://www.thermofisher.com/be/en/home/references/ambion-tech-support/rna-tools-and-calculators/dna-and-rna-molecular-weights-and-conversions.html> (accessed Jun 17, 2017).
- (3) Aldevron Products Page <http://www.aldevron.com/products/dnas/gwiz> (accessed Jun 17, 2017).
- (4) Benjaminsen, R. V; Matthebjerg, M. A.; Henriksen, J. R.; Moghimi, S. M.; Andresen, T. L. The Possible "Proton Sponge " Effect of Polyethylenimine (PEI) Does Not Include Change in Lysosomal pH. *Mol. Ther.* **2013**, *21*, 149–157.



# Chapter 4

## Photothermally Triggered Endosomal Escape and Its Influence on Transfection Efficiency of Gold-functionalized JetPEI/pDNA Nanoparticles

### **Manuscript in preparation**

Lotte M.P. Vermeulen<sup>1,2</sup>, Juan C. Fraire<sup>1,2</sup>, Ellen De Meester<sup>3</sup>, Sarah De Keulenaer<sup>3</sup>, Filip Van Nieuwerburgh<sup>3</sup>, Stefaan De Smedt<sup>1</sup>, Katrien Remaut<sup>1</sup>, Kevin Braeckmans.<sup>1,2</sup> Photothermally Triggered Endosomal Escape and Its Influence on Transfection Efficiency of Gold-functionalized JetPEI/pDNA Nanoparticles. *Int J Mol Sci*

<sup>1</sup>Lab. General Biochemistry & Physical Pharmacy, Ghent University, Ottergemsesteenweg 460, Ghent, Belgium

<sup>2</sup>Centre for Nano- and Biophotonics, Ghent University, Ottergemsesteenweg 460, Ghent, Belgium

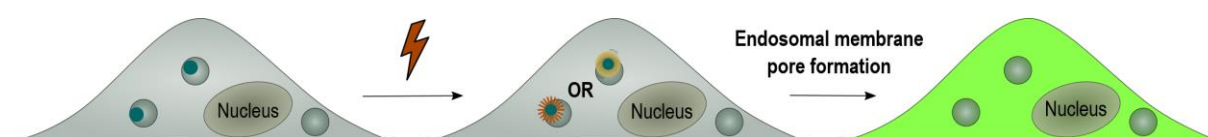
<sup>3</sup>Lab. Pharmaceutical Biotechnology, Ghent University, Ottergemsesteenweg 460, Ghent, Belgium

## TABLE OF CONTENTS

1	INTRODUCTION.....	136
2	MATERIALS AND METHODS.....	140
2.1	Materials.....	140
2.2	Synthesis and characterization of hyaluronic acid coated 10 nm gold nanoparticles.....	140
2.2.1	Synthesis of 10 nm gold nanoparticles.....	140
2.2.2	Functionalization with HA to form HA AuNP 10 nm .....	140
2.3	Preparation of plasmids .....	141
2.4	Preparation of Au functionalized JetPEI/pDNA complexes .....	141
2.5	Physicochemical characterization of JetPEI/pDNA/Au complexes .....	141
2.6	Cell culture.....	142
2.7	Generation and detection of JetPEI/pDNA/Au complex heating and vapour nanobubble (VNB) formation. ....	142
2.8	Evaluation of transfection efficiency and cytotoxicity .....	144
2.9	Flow cytometry .....	144
2.10	Evaluation of uptake efficiency.....	144
2.11	Visualization and quantification of endosomal escape .....	145
2.12	Determination of pDNA content via PicoGreen assay.....	145
3	RESULTS .....	146
3.1	Relation between cell division and transfection .....	146
3.2	Synthesis and characterization of JetPEI/pDNA/Au complexes .....	147
3.2.1	Characterization 10 nm AuNPs and HA coating .....	147
3.2.2	Characterization JetPEI/pDNA/Au complexes .....	148
3.3	Threshold determination for heating and VNB formation .....	149
3.4	Evaluation of uptake efficiency.....	151
3.5	Evaluation of transfection efficiency and cell viability .....	152
3.6	Evaluation of endosomal escape and pDNA breakdown .....	153
4	DISCUSSION.....	155
5	CONCLUSION.....	158

## ABSTRACT

Plasmonic nanoparticles (NPs) for drug delivery have attracted increasing interest over the last years. Their localized surface plasmon resonance causes photothermal effects upon laser irradiation, which allows to deliver drugs in a spatio-temporally controlled manner. In this chapter, we explore the use of AuNPs as carriers for pDNA in combination with pulsed laser irradiation to induce endosomal escape, which is currently considered to be one of the major bottlenecks in macromolecular drug delivery on the intracellular level. In particular we evaluate nanocomplexes composed of JetPEI/pDNA/AuNP which do not exhibit endosomal escape by themselves. After incubating HeLa cells with these complexes, we evaluated endosomal escape and transfection efficiency using low and high energy laser pulses. At low laser energy heat is produced by the nanocomplexes, while at higher laser energy explosive vapour nanobubbles (VNB) are formed. We investigated the ability of heat transfer and VNB formation to induce endosomal escape and we examine the integrity of pDNA cargo after inducing both photothermal effects. We conclude that JetPEI/pDNA/Au complexes are unable to induce meaningful transfection efficiencies because laser treatment renders the pDNA cargo dysfunctional.



## 1 INTRODUCTION

Apart from delivering nucleic acids (NAs) packaged by polymeric vectors as described in **Chapter 2** and **3**, gold nanoparticles (AuNPs) have attracted increasing interest as a promising new vehicle for gene therapy. The interest in AuNPs has been stimulated by their basic physical, chemical and optical properties.<sup>1</sup> First of all, the gold core is essentially inert and non-toxic.<sup>2</sup> Secondly, synthesis and surface modifications are fairly straightforward and allow the preparation of a variety of AuNPs that are able to bind macromolecular therapeutics (*e.g.* proteins, siRNA, pDNA, *etc.*).<sup>3</sup> Finally, their optical properties make it interesting to investigate the use of AuNPs for spatio-temporal controlled delivery of the cargo. AuNPs and other metal NPs (*e.g.* Ag<sup>4,5</sup>, Cu<sup>6</sup> and Al<sup>7</sup>) are known to have an enhanced optical absorption *via* Localized Surface Plasmon Resonance (LSPR). LSPR is a consequence of the interaction between the free electrons of the conduction band of a metal NP and an external oscillating electromagnetic field, as shown in **Figure 4.1 A**. An electromagnetic field – usually provided by laser light – forces free electrons in the NP to oscillate. These oscillating electrons are also referred to as localized surface plasmons. Depending on the NP composition, size and shape, resonant behavior of the plasmon oscillations occurs at a specific wavelength of the incident electromagnetic wave. At this resonant wavelength, the surface plasmon oscillations are maximal, which is what is referred to as LSPR. Light at and near the resonant wavelength will be absorbed by the NP. Small particles absorb shorter wavelengths, while the LSPR for bigger particles is red-shifted to longer wavelengths, resulting in a size dependent variety of colors as displayed in **Figure 4.1 B**.<sup>8-10</sup>

Due to the oscillations of the localized surface plasmons, a series of sequential energy transfer processes occur within the NP, which results in an increase of the NP temperature. In a matter of picoseconds, thermal equilibration inside the NP is reached, which is followed by heat transfer from the particle to the environment.<sup>11</sup> By using continuous wave laser irradiation or low intensity laser pulses, direct heat transfer can lead to a rise in temperature of the local surroundings by ten to several hundreds of degrees. On the other hand, the use of intense short laser pulses (<10 ns) causes an extremely rapid increase in the NP temperature of several hundreds to even thousand degrees. This is due to the fact that all light energy is delivered in a short time scale before the heat is able to diffuse into the environment, a phenomenon known as 'heat confinement'. Due to these very high AuNP temperatures, the water surrounding the NP quickly evaporates, leading to the formation of (laser-induced) vapour nanobubbles (VNB). The expansion and collapse of a VNB causes a high pressure shockwave without transferring heat to the environment since nearly all

incident laser energy is essentially converted into mechanical energy of the expanding VNB. The size of VNBs can be tuned from tens to several hundreds of nm by varying the laser intensity and the size of NPs.<sup>8</sup> Both heat transfer and VNB formation are depicted in **Figure 4.1 C**.

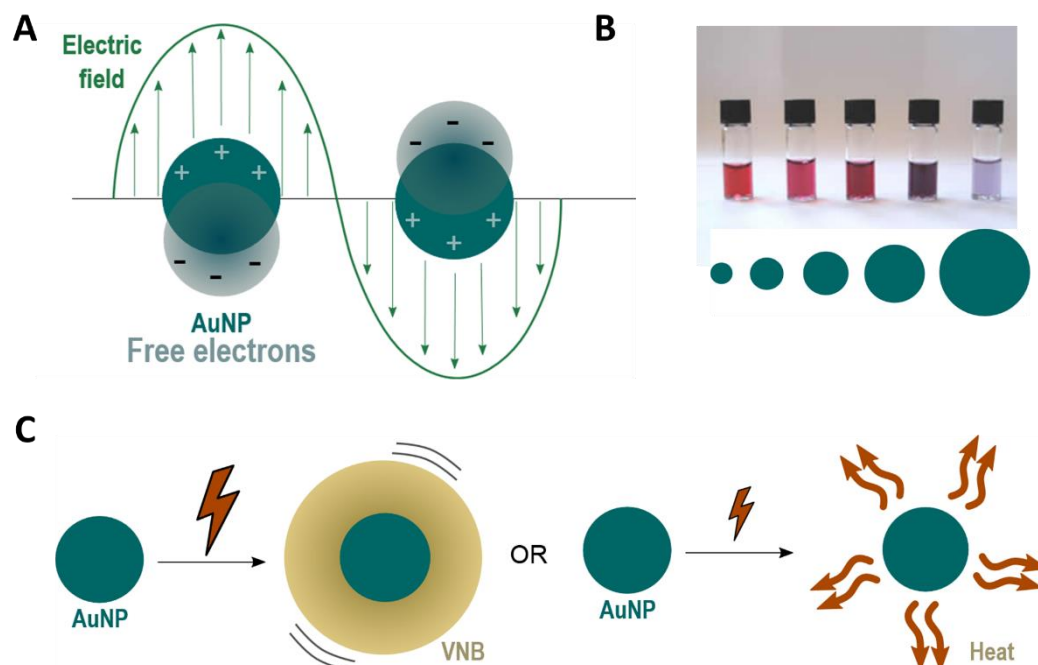


**Figure 4.1 (A)** Under the influence of an external oscillating electromagnetic field, usually provided by laser light, the free electrons of gold nanoparticles (AuNPs) start to oscillate. When the amplitude of this oscillation is maximal, this phenomenon is referred to as Localized Surface Plasmon Resonance (LSPR). **(B)** The LSPR of AuNPs and therefore the color of colloidal AuNP solutions depends on the size of the AuNP core. **(C)** Laser irradiation of AuNPs can lead to the formation of VNBs or heat transfer to the surrounding environment.

LSPR-induced photothermal heating can be used in photothermal therapies. Photothermal cancer therapy is one of the earliest studied applications, where plasmonic NPs act as a localized source of heat to damage and destroy cancer cells.<sup>1,9,11</sup> Later on, these light-triggered properties were employed for drug delivery purposes. Besides the delivery of chemical payloads<sup>12-14</sup>, currently there is an increasing interest in the use of light-triggered delivery of NAs for gene therapy where plasmonic NPs are used as NA nanocarriers. Plasmonic effects can be used for two purposes: (1) light-triggered release of the NA payload at the desired time and place, and (2) overcoming intracellular (IC) barriers. Both aspects will be discussed briefly.

For photothermal release of NA from plasmonic carriers, different strategies have been investigated to couple NAs to the surface of the NP, which can be subdivided into covalent vs non-covalent approaches.<sup>15</sup> When the NA is covalently attached to the gold surface, femtosecond laser pulses that break the covalent bond can be employed

in order to release the intact NA.<sup>16,17</sup> The second strategy consists of loading the NA onto a carrier molecule using weaker, non-covalent bonds that can be disrupted more easily using lower laser power densities. The carrier molecule should be covalently attached to the gold surface before loading the NA.<sup>15,18,19</sup>

Photothermal effects can also aid in tackling IC barriers that obstruct the way for efficient gene delivery (IC barriers *cf.* **Chapter 1**). In order to gain direct access to the cytosol (*i.e.* without the need to escape endosomes), NP-sensitized photoporation of the plasma membrane has been investigated.<sup>20</sup> Photoporation of the plasma membrane can be achieved by thermal membrane permeabilization through a local phase transition of the lipid bilayer in response to the heat transfer of the irradiated plasmonic NP to the environment. Alternatively, the generation of a VNB can cause mechanical membrane poration. After laser irradiation, exogenous compounds can diffuse through the pores into the cytoplasm (**Figure 4.2 A**).<sup>8,11</sup> While this has proven to work very well for compounds up to about 500 kDa, delivering larger molecules such as mRNA or pDNA through the plasma membrane has proven to be more difficult.<sup>20–22</sup> Presumably this is because the pores that are formed are too small to allow diffusion of large macromolecules such as pDNA. An alternative strategy is to allow cellular uptake of NA-loaded plasmonic NPs *via* endocytosis, followed by light-triggered endosomal escape, as depicted in **Figure 4.2 B**.<sup>23,24</sup> Plasmonic NPs have already been used successfully to induce light-triggered endosomal rupture and cytosolic delivery of several macromolecules such as proteins<sup>25–27</sup>, siRNA<sup>15,28,29</sup> and ONs<sup>15</sup>. However, to date, there has been no record of successful delivery of the larger range of NAs, such as pDNA, *via* light-triggered endosomal escape.

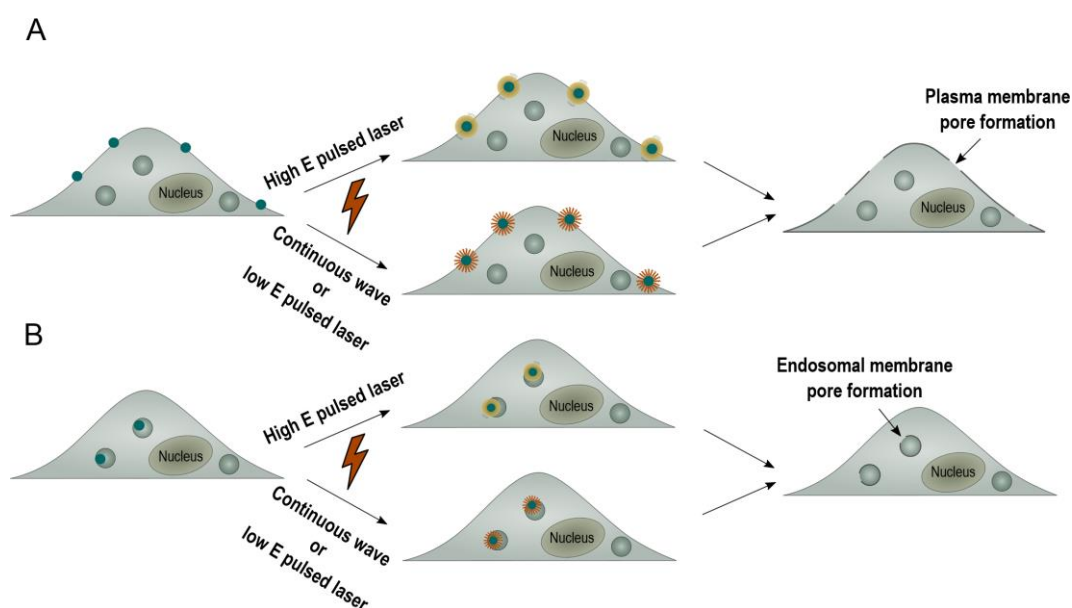


**Figure 4.2** The application of plasmonic NPs to overcome intracellular barriers. **(A)** NP-sensitized plasma membrane photoporation. Cells are incubated with plasmonic NPs to allow

attachment of the NPs to the plasma membrane. Next, laser irradiation causes the formation of VNBs (high energy pulsed laser) or heating (continuous wave or low energy pulsed laser). The generation of these plasmonic effects cause the formation of a pore in the plasma membrane, which allows entry of exogeneous compounds into the cell by diffusion. **(B)** Light-triggered endosomal escape. Plasmonic NPs are allowed to be taken up by the cell through endocytosis. Next, laser irradiation causes the formation of VNBs (high energy pulsed laser) or heating (continuous wave or low energy pulsed laser). The generation of these plasmonic effects cause the formation of a pore in the endosomal membrane, which allows release of endocytosed cargo.

Besides providing an efficient endosomal escape mechanism for pDNA delivery, light-triggered endosomal escape could also be a useful tool to perform fundamental investigations regarding the influence of the time and place of endosomal escape on transfection efficiency. In literature, it has been stated regularly that endosomal escape of pDNA close to the nucleus is thought to be beneficial for enhanced transfection efficiency, presumably because the DNA then would have a better chance for translocation into the nucleus.<sup>30</sup> However, initial experiments performed in our lab indicated that for JetPEI/pDNA complexes, successful transfection almost exclusively happens after cell division, independent when and where endosomal escape has happened. This suggests that the location of endosomal escape may not matter that much since during cell division the nuclear envelope is temporarily disassembled and the cytoplasm is mixed anyway. In order to further examine the relation between time and place of endosomal escape, cell division and transfection, we prepared JetPEI/pDNA/Au complexes in an attempt to induce spatio-temporally controlled light-triggered pDNA transfection of HeLa cells. In this chapter, we will evaluate the effect of heating vs VNB formation on endosomal escape efficiency, pDNA integrity and final transfection efficiency.

## 2 MATERIALS AND METHODS

### 2.1 Materials

DMEM/F-12, L-Glutamine, Penicillin-Streptomycin solution (5000 IU/ml penicillin and 5000 µg/ml streptomycin) (P/S), Fetal Bovine Serum (FBS), Opti-MEM, Trypan Blue, 0.25% Trypsin-EDTA and Dulbecco's phosphate-buffered saline 1x without Ca<sup>2+</sup>/Mg<sup>2+</sup> (DPBS-) were provided by GibcoBRL (Merelbeke, Belgium). YOYO-1 iodide, Hoechst 33342 and Quant-IT PicoGreen dsDNA Assay Kit were supplied by Molecular Probes (Erembodegem, Belgium). Other reagents were purchased from Sigma-Aldrich (Bornem, Belgium) unless otherwise specified.

### 2.2 Synthesis and characterization of hyaluronic acid coated 10 nm gold nanoparticles

#### 2.2.1 *Synthesis of 10 nm gold nanoparticles*

The synthesis of 10 nm gold nanoparticles (AuNPs) was performed using ascorbate as reducing agent. A typical synthesis consists in adding Au to give a final concentration of 0.2 mM HAuCl<sub>4</sub> with the addition of equimolar quantities of sodium ascorbate (final volume = 100 ml) under rapid stirring and let react for 30 min.

The characterization of AuNPs was performed combining UV/VIS spectroscopy, dynamic light scattering (DLS), transmission electron microscopy (TEM), and electrodynamic modeling using Mie theory. UV/VIS spectroscopy was performed on a NanoDrop 2000c spectrophotometer (Thermo Scientific, Rockford, IL, USA). DLS measurements were carried out using a Zetasizer Nano (Malvern, Worcestershire, UK) and disposable folded capillary cells (Malvern, Worcestershire, UK) to determine hydrodynamic diameter, polydispersity index and zeta potential. TEM images were obtained at the VIB-UGent Transmission Electron Microscopy-Core facility using a JEM 1400plus transmission electron microscope (JEOL, Tokyo, Japan) operating at 60 kV. Samples were prepared by adding one drop (~ 50 µl) of the samples colloidal solution onto formvar/C-coated hexagonal copper grids (EMS G200H-Cu) for 20 min and washed 5 times in double distilled water (ddiH<sub>2</sub>O). Finally, the size and concentration of AuNPs was estimated using the experimental extinction intensities at the maximum wavelength ( $\lambda_{\max} = 520$  nm), and Mie theory calculations<sup>31-33</sup> of the extinction cross section for spherical particles ( $\sigma_{\text{ext}}(520 \text{ nm}) = 5.2 \times 10^{-13} \text{ cm}^2/\text{NP}$ ).

#### 2.2.2 *Functionalization with HA to form HA AuNP 10 nm*

The synthesized NPs were immediately functionalized with hyaluronic acid (HA) to install a negative zeta potential, required for complexation with positively charged

JetPEI/pDNA complexes. Typically, functionalization with HA was performed by adding 6-10 mg of the polymer (all stock solutions of the synthesized AuNPs in pM concentration). Successful functionalization was confirmed by DLS zeta potential measurements, performed after centrifugation of the AuNPs to remove unbound HA.

### 2.3 Preparation of plasmids

gWIZ GFP (Promega, Leiden, The Netherlands) was amplified in transformed E. Coli bacteria and isolated from this bacteria suspension using a Qiafilter Plasmid Giga Kit (Qiagen, Venlo, The Netherlands). Concentration was determined on a NanoDrop 2000c (Thermo Fisher Scientific, Rockford, IL, USA) by UV absorption at 260 and 280 nm and adjusted to a final concentration of 1 µg/µl with HEPES buffer (20 mM, pH 7.2).

### 2.4 Preparation of Au functionalized JetPEI/pDNA complexes

JetPEI/pDNA polyplexes were prepared using commercially available JetPEI (Polyplus transfection, Leusden, The Netherlands). JetPEI/pDNA complexes were obtained by mixing the polymer solution with an equal volume of pDNA solution. N/P ratio of the polyplexes was calculated using the formula provided by the manufacturer (Equation 4.1). Next, the mixture was vortexed for 10 s at 2200 rpm and polyplexes were allowed to stabilize for 15 min.

$$N/P \text{ ratio} = \frac{7.5 \times \mu\text{l of JetPEI}}{3 \times \mu\text{g of DNA}} \quad (4.1)$$

Next, the required amount of HA coated 10nm AuNPs was centrifuged at 12 000 g for 10 min. The supernatant was removed and the pellet was resuspended in ddiH<sub>2</sub>O before mixing with JetPEI/pDNA complexes in equal volumes. The resultant mixture was allowed to stabilize for 30 min followed by final dilution with ddiH<sub>2</sub>O.

### 2.5 Physicochemical characterization of JetPEI/pDNA/Au complexes

To evaluate complexation of pDNA to the JetPEI/pDNA/Au complexes, gel electrophoresis was performed. The complexes were prepared as described above. A 1% agarose gel was prepared by dissolving 1 g of agarose (UltraPure Agarose, Invitrogen, Erembodegem, Belgium) in 100 ml of 1 x Tris/Borate/EDTA (TBE) buffer after which GelRed (Biotium, Hayward, CA, USA) was added in order to detect pDNA. 5 µl of Gel Loading Buffer (Ambion, Merelbeke, Belgium) was added to 20 µl of complexes and a total volume of 25 µl was pipetted in every lane. A 1 kb ladder (Bioron GmbH, Ludwigshafen, Germany) and uncomplexed pDNA were taken along as controls.

Gel electrophoresis was performed at 100 V for 30 min and a PhotoDoc-It Imaging system (UVP, CA, USA) was used to acquire an image of the gel under UV light (Bio-Rad UV transilluminator 2000, CA, USA).

Next, Dynamic Light Scattering measurements were performed on the NanoZS Zetasizer. The complexes were prepared as described above and were transferred to disposable folded capillary cells to determine hydrodynamic diameter, polydispersity index and zeta potential. The same complexes were used to measure the UV/VIS spectrum on a NanoDrop 2000c. Finally, the concentration of JetPEI/pDNA/Au complexes was measured *via* Nanoparticle Tracking Analysis using the NanoSight LM10 (Malvern, Worcestershire, UK). The measurements were performed in quintuplet.

## **2.6 Cell culture**

HeLa cells (cervical adenocarcinoma cells, ATCC CCL-2) were cultured in Dulbecco's modified Eagle's medium supplemented with growth factor F12 (DMEM/F-12) and enriched with 10% FBS, 2 mM L-Glutamine and 100 µg/ml P/S. Cells were cultured in a humidified atmosphere at 37°C and 5% CO<sub>2</sub>. Experiments were performed on cells with a passage number below 25.

## **2.7 Generation and detection of JetPEI/pDNA/Au complex heating and vapour nanobubble (VNB) formation.**

A homemade setup, according to the optical design in **Figure 4.3**, was used to generate and detect heating or VNB formation. The setup is built around an inverted TE2000 epi-fluorescence microscope (Nikon, Nikon BeLux, Brussels, Belgium) equipped with a Plan Fluor 10x 0.3 NA lens (Nikon, Japan). A pulsed laser with a pulse duration of ~7 ns was tuned at a wavelength of 561 nm with an Optical Parametric Oscillator (OPO) laser (Opolette™ HE 355 LD, OPOTEK Inc., CA, USA) and used to excite the localized surface plasmon resonance of the JetPEI/pDNA/Au complexes. The energy of the laser pulses was measured with an energy meter (J-25MB-HE&LE, Energy Max-USB/RS sensors, Coherent).

Detection of VNB formation was performed using dark-field microscopy as VNBs efficiently scatter light. Since VNBs typically have a very short lifetime (< 1 µs), the camera (EMCCD camera, Cascade II: 512, Photometrics, Tucson, USA) was synchronized with the pulsed laser using an electronic pulse generator (BNC575, Berkely Nucleonics Corporation, CA, USA). The pulse laser sends a Q-switch signal to trigger the pulse generator and the camera at a certain delay. In this way, dark-field images were taken before, during and after illumination. Dark-field microscopy was used to determine the fluence threshold for VNB formation and heating of

JetPEI/pDNA/Au complexes. To determine the thresholds in HeLa cells, cells were first seeded in 50 mm  $\gamma$ -irradiated glass bottom dishes (MatTek Corporation, MA, USA) at a density of 600 000 cells. Cells were allowed to attach overnight and the next day, complexes were added to the cells in Opti-MEM. After incubation at 37°C for 1 h, the cells were washed, full culture medium was added and dark-field microscopy was performed. In order to calculate the threshold for heating and VNB formation, dark-field images were analyzed using ImageJ and the number of VNBs was plotted in function of the laser fluence that was used.

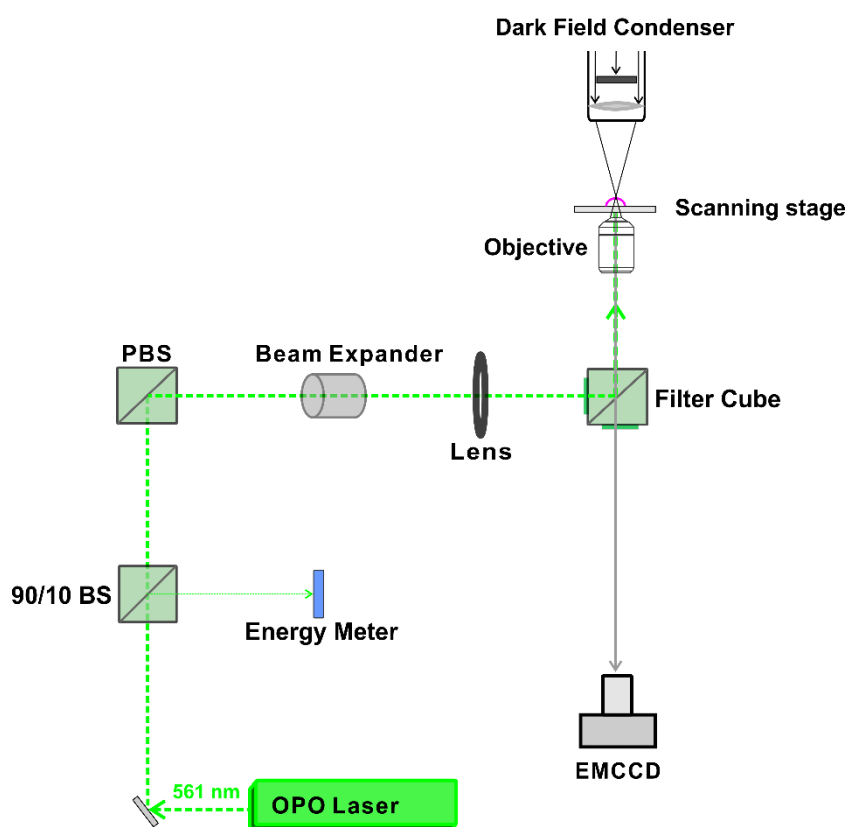


**Figure 4.3 Optical design for generation and detection of heating and VNB formation.** AOTF: acousto-optic tunable filter to control the power of the continuous wave laser. OPO laser: pulsed laser with  $\sim 7$  ns pulses equipped with an Optic Parametric Oscillator that allows to tune the wavelength from 410 to 2200 nm. 90/10 BS: laser beam splitter that reflects 10% and transmits 90% of the laser light. PBS: polarization beam splitter. Image adjusted with permission from <sup>20</sup> © American Chemical Society.

For scanning larger areas such as wells of a 96 well plate, we used an automatic Prior Proscan III stage (Prior scientific Ltd., Cambridge, UK) to scan the sample line by line with a scanning speed of 2.2 mm/s and a 150  $\mu\text{m}$  diameter laser beam with 20 Hz pulse frequency. The distance between subsequent lines was set to 110  $\mu\text{m}$  to ensure the illumination of all complexes present in the sample.

## **2.8 Evaluation of transfection efficiency and cytotoxicity**

HeLa cells were seeded in 96 well plates at 10 000 cells per well and were allowed to attach overnight. The next day, JetPEI/pDNA/Au complexes containing gWIZ GFP were prepared as described above. Cells were incubated with JetPEI/pDNA/Au complexes in Opti-MEM for 1 h at 37°C. Afterwards they were washed with Opti-MEM and full cell culture medium was added before laser treatment, as described above. After laser treatment, the cells were cultured for another 24 h before they were prepared for flow cytometry analysis. To examine transfection efficiency, expression of gWIZ GFP was measured in the green channel. For cytotoxicity evaluation, DAPI (ThermoFischer) was added to the flow buffer according to the manufacturer's instructions.

## **2.9 Flow cytometry**

To perform analysis by flow cytometry, cells were detached using trypsin and transferred to flow cytometry tubes (BD Falcon, Radnor, USA). Next, the cell suspensions were centrifuged at 300 g for 5 min (Bio-Rad DiaCent-12, DieMed GmbH, Cressier, Switzerland) and resuspended in flow buffer (DPBS-, 0.1% Sodium Azide, 1% Bovine Serum Albumine). Finally, samples were vortexed at 2200 rpm (YellowLine TTS2, IKA works, Wilmington, USA). Flow cytometry was performed on 10 000 events per sample (CytoFLEX™ Flow Cytometer, Beckman Coulter, Krefeld, Germany) or for a total duration of 120 s. gWIZ GFP fluorescence was detected with 525/40 nm bandpass filter after 488 nm excitation. DAPI fluorescence was detected with a 450/45 nm bandpass filter after 405 nm excitation. FlowJo software (Treestar Inc, Ashland, USA) was used to perform the analysis.

## **2.10 Evaluation of uptake efficiency**

Cells were seeded in 96 well plates with glass bottom (Greiner Bio-One, Frickenhausen, Germany) at a density of 10 000 cells per well and were allowed to attach overnight. The next day, cell nuclei were stained with Hoechst 33342 staining (1 mg/ml in H<sub>2</sub>O; 1000x diluted). JetPEI/pDNA/Au 5 pt complexes were prepared as described above. Cells were incubated with JetPEI/pDNA/Au 5pt complexes in Opti-MEM for 1 h at 37°C. After washing the particles off, the cells were provided with full cell culture medium and live-cell imaging was performed using a confocal laser scanning microscope (C1si, Nikon, Japan). A Plan Apo VS 60x 1.4 NA oil immersion objective lens (Nikon, Japan) was used to obtain a pixel size of 70 nm and AuNP were detected by the reflected laser light of the 561 nm laser. Image processing was performed using ImageJ (FIJI) software.

### **2.11 Visualization and quantification of endosomal escape**

Visualization and quantification of endosomal escape was performed based on the dequenching assay that was first published by Rehman *et al.*<sup>34</sup> Therefore, red-fluorescent oligonucleotides (AF647 ONs) were co-incorporated into the complexes. Cells were seeded in 96 well plates with glass bottom at a density of 10 000 cells per well and were allowed to attach overnight. Cell nuclei were stained with Hoechst 33342 staining (1 mg/ml in H<sub>2</sub>O; 1000x diluted). Next, AF647 ON-containing complexes were added to the cells in Opti-MEM and incubated for 1 h at 37°C. After washing off the complexes, the cells were provided with full cell culture medium and laser treatment was performed, as described above. After laser treatment, the cells were imaged using a spinning disk confocal (SDC) microscope (Nikon eclipse Ti, Japan) equipped with an MLC 400 B laser box (Agilent technologies, California, USA), a Yokogawa CSU-X confocal spinning disk device (Andor, Belfast, UK), an iXon ultra EMCCD camera (Andor Technology, Belfast, UK) and NIS Elements software (Nikon, Japan). A Plan Apo VC 60x 1.4 NA oil immersion objective lens (Nikon, Japan) was used to yield an image pixel size of 234 nm. Exposure time was set to 20 msec and the images were processed using ImageJ (FIJI).

### **2.12 Determination of pDNA content via PicoGreen assay**

JetPEI/pDNA/Au 5 pt complexes were prepared and underwent laser treatment, as described above. To the resulting samples (untreated, heat and VNB treated), dextran sulphate (50 mg/ml in PBS-) was added in order to release the complexed pDNA. Finally, the amount of pDNA in the samples was quantified using Quant-IT PicoGreen dsDNA Assay Kit according to the manufacturer's protocol. Fluorescent measurements of the assay were performed on a fluorescence microplate reader (Tecan, Mechelen, Belgium).

### 3 RESULTS

#### 3.1 Relation between cell division and transfection

In literature it has been suggested that pDNA should preferably escape from endosomes close to the nuclear envelope. This is under the assumption that pDNA can translocate across the nuclear envelope. If this is correct, it would mean that cells can express the pDNA without cell division (at which time the nuclear envelope is disassembled). To verify this hypothesis, we started by investigating the influence of cell division on transfection efficiency. Therefore, HeLa cells were incubated with JetPEI/pDNA NP 6 particles that had an average size of  $108.7 \pm 4.5$  nm (mean  $\pm$  stdev) and zeta potential of  $31.6 \pm 0.5$  mV (mean  $\pm$  stdev) (*cf.* **Chapter 3**). After an incubation of 15 min, the cells were washed and time-lapse confocal images were recorded in order to visualize endosomal escape, cell division and transfection. Endosomal escape was visualized by the nuclear accumulation of AF647-labeled ONs and transfection was visualized by the appearance of GFP. A total of 286 cells that showed endosomal escape were analyzed, of which the results are summarized in **Figure 4.4**. Two main categories were observed after endosomal escape: 55% of the cells showed cell division followed by transfection. 40% of the cells didn't divide and also failed to produce expression of GFP. The fraction of cells that divided after endosomal escape but did not show transfection was limited to 2% and only 3% showed transfection without prior cell division. These data clearly show that, in cells where endosomal escape has happened, there is a high ( $\pm 97\%$ ) chance for successful transfection after cell division while there is only a very limited ( $\pm 7\%$ ) chance for transfection without cell division. Further analysis revealed that the time between cell division and the start of transfection was only  $126 \pm 58$  min.

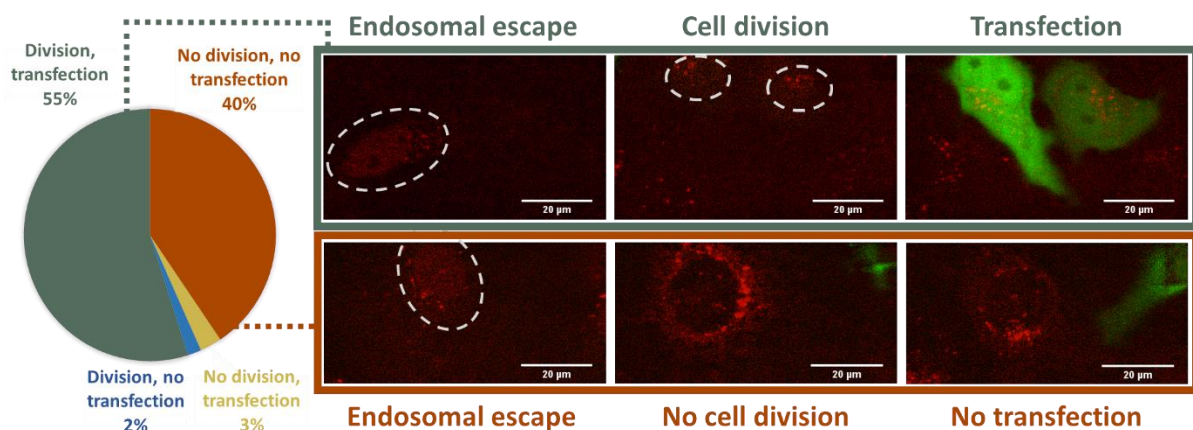


**Figure 4.4 The relation between cell division and transfection.** Analysis of 286 HeLa cells revealed two main categories: one where cell division is followed by transfection (55%; displayed in green) and one where neither cell division nor transfection was observed (40%; displayed in orange). The cells that did not show transfection after cell division and the cells that showed

transfection without cell division were limited to 2 and 3% respectively. Confocal images show an example of the two main categories. Scalebar represents 20  $\mu\text{m}$ .

These data clearly indicate that cell division and transfection efficiency are linked. Although it has been known for a long time that cell division is often necessary for transfection, several reports suggest that transfection efficiency would decrease when endosomal escape happens in the cell periphery vs in the perinuclear area of the cell.<sup>30,35</sup> This suggestion is mainly based upon the fact that pDNA has very limited ability to diffuse through the cytoplasm.<sup>36</sup> Thus, the closer pDNA is released to the nucleus, the more likely it is thought to be for the pDNA to reach the nuclear compartment. However, there is strong evidence that direct migration of pDNA through the nucleopores of the nuclear membrane is highly inefficient.<sup>37</sup> Combining this with the fact that the cytoplasmic and nuclear content are actively mixed during cell division<sup>37</sup>, it seems that the distance of an endosomal escape event to the nucleus may not be as relevant as it is sometimes claimed to be. In order to investigate this hypothesis more directly, we set out to develop photothermally triggered endosomal escape with AuNP based carriers, for which endosomal escape can be precisely controlled in time and space.

### **3.2 Synthesis and characterization of JetPEI/pDNA/Au complexes**

JetPEI/pDNA/Au complexes were prepared as a vehicle to combine both pDNA and AuNP into a single complex to induce photothermally triggered endosomal escape of pDNA. JetPEI/pDNA complexes with a positive charge and an N/P ratio of 4 are mixed with negatively charged hyaluronic acid (HA) coated AuNPs. Both AuNPs and JetPEI/pDNA/Au complexes were characterized to ensure the formation of stable, reproducible complexes.

#### **3.2.1 Characterization 10 nm AuNPs and HA coating**

First of all, 10 nm AuNPs were synthesized using ascorbate as reducing agent. In order to verify that the AuNPs have a core size of 10 nm, characterization of these particles was performed. TEM images were recorded and are shown in **Figure 4.5 A**. The core size of the NPs was determined *via* image processing using ImageJ and the result is displayed in **Figure 4.5 B**. Next, the UV/VIS spectrum of the synthesized AuNPs was measured and compared to simulated data of the extinction of a 10 nm AuNP according to the Mie theory (see **Figure 4.5 C**). Based on the obtained TEM frequency distribution and the excellent agreement between the experimental extinction spectrum to the simulated extinction cross-section spectrum, we conclude that the synthesized AuNPs have a core size of around 10 nm on average.

Functionalization of 10 nm AuNPs with HA was performed to allow complexation of the AuNPs to the positively charged JetPEI/pDNA complexes. Functionalization with HA was confirmed as the zeta potential of the AuNPs shifted from  $-14.7 \pm 0.5$  mV to  $-29.4 \pm 3.21$  mV (mean  $\pm$  stdev) after addition of HA and subsequent centrifugation to remove unbound HA.

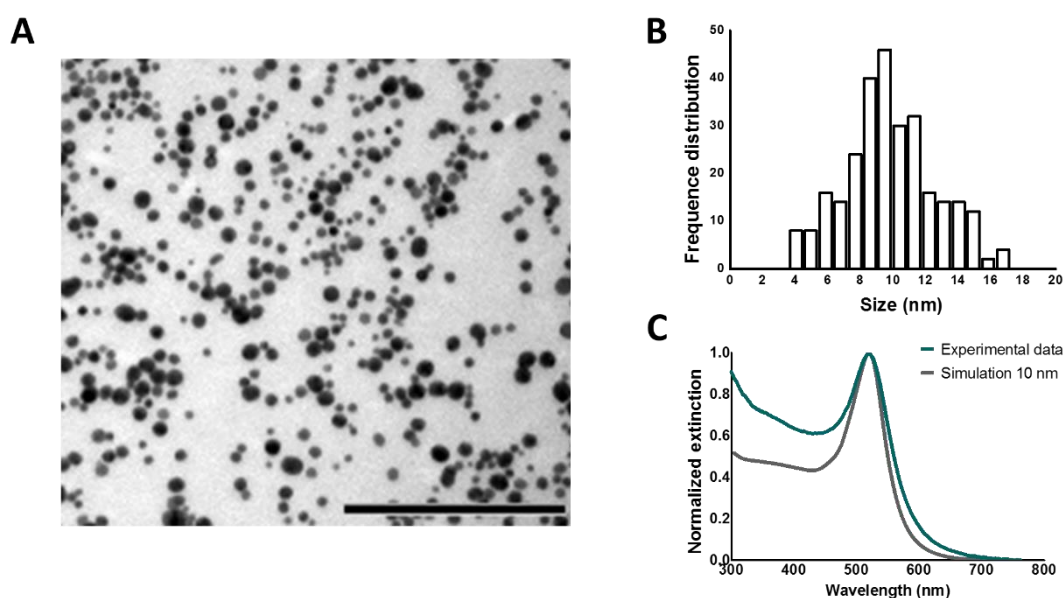


**Figure 4.5 Characterization 10 nm AuNPs.** (A) TEM image of unfunctionalized AuNPs. Scalebar represents 200 nm. (B) Frequency distribution of AuNP core size derived from TEM image in (A). (C) Normalized extinction of pristine AuNPs. The blue line represents the experimental data, as measured by UV/VIS spectrophotometry. The grey line represents the simulation of a 10 nm AuNP according to Mie theory.

### 3.2.2 Characterization JetPEI/pDNA/Au complexes

JetPEI/pDNA/Au complexes were prepared by mixing JetPEI/pDNA NP 4 polyplexes with 10 nm HA coated AuNPs. AuNPs were added after centrifugation in a range of concentrations: 0.5 pellets (0.5 pt;  $7.2 \times 10^{10}$  AuNPs), 1 pellet (1 pt;  $1.44 \times 10^{11}$  AuNPs), 5 pellets (5 pt;  $7.2 \times 10^{11}$  AuNPs) and 10 pellets (10 pt;  $1.44 \times 10^{12}$  AuNPs). Based on UV/VIS measurements, the concentration of AuNPs was calculated *via* the Lambert-Beer formula. The extinction coefficient used was provided by Mie theory calculations of 10 nm Au spheres ( $\sigma_{520\text{nm}} = 5.2 \times 10^{-13}$  cm<sup>2</sup>/NP). Next, gel electrophoresis was performed to evaluate if pDNA was retained inside the complexes. As can be seen from **Figure 4.6 A**, the addition of HA AuNPs did not interfere with the complexation of pDNA to JetPEI. Next, hydrodynamic diameter, polydispersity index (PdI) and zeta potential were determined using dynamic light scattering (DLS; **Figure 4.6 B-C**). Finally, UV/VIS spectra of these complexes were measured, as can be seen

in **Figure 4.6 D**. JetPEI/pDNA/Au 5 pt complexes were selected for further experiments since they were able to complex pDNA and had the smallest size ( $92.5 \pm 5.1$  nm  $n=3$ ) with a negative zeta potential ( $-27.7 \pm 0.5$  mV  $n=3$ ). UV/VIS spectra showed that the plasmon peak of this complex is situated around 530-570 nm, which is well suited to absorb the 561 nm laser light of the pulsed laser that will be used for inducing photothermal endosomal escape. Finally, using Nanoparticle Tracking Analysis, the concentration of the JetPEI/pDNA/Au pt 5 complexes was measured to be  $2.75 \times 10^{11} \pm 3.54 \times 10^{10}$  particles per ml.

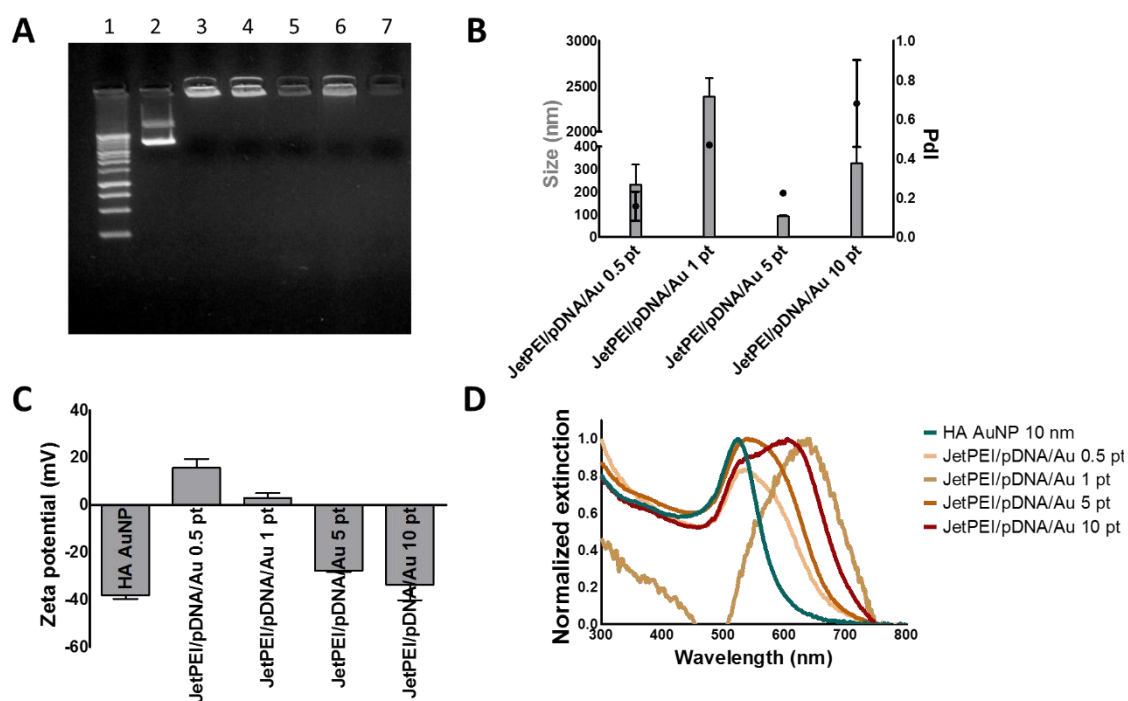


**Figure 4.6 Characterization of JetPEI/pDNA/Au complexes.** (A) Gel electrophoresis shows successful pDNA complexation for all JetPEI/pDNA/Au complexes. Lane 1 shows 1 kb ladder control. Lane 2 shows free pDNA. Lane 3 shows JetPEI/pDNA NP 4. Lane 4, 5, 6 and 7 show JetPEI/pDNA/Au with 0.5, 1, 5 and 10 pellets respectively. Further characterization of the complexes by DLS reveals (B) the size (grey bars), PdI (black dots) and (C) zeta potential. Values are displayed as mean  $\pm$  stdev;  $n = 2$ . (D) Normalized UV/VIS spectra of HA AuNPs (blue line) and JetPEI/pDNA/Au complexes (orange – red lines).

### 3.3 Threshold determination for heating and VNB formation

To be able to scan larger areas such as wells of a 96 well plate in a high-throughput way, we determine one laser fluence per sample that can be used to form VNBs (VNB threshold) and one laser fluence per sample that is used to induce heating (heating threshold). In order to determine the laser fluence threshold for heating and VNB formation, dark-field microscopy was performed since this method enables us to set up a graph to evaluate the effect of laser fluence on the formation of VNBs. As can

be seen in **Figure 4.7 A-C**, dark-field microscopy allows visualization of the AuNPs before, during and after VNB formation. In this way, the number of VNBs generated after a single pulse was counted and plotted against the used laser fluence, as measured by the energy meter in the setup. Afterwards, the VNB threshold is determined as the laser fluence where 90% of the VNBs are formed and the fluence for heating is selected at  $\frac{1}{4}$  of the VNB threshold, in accordance with published literature.<sup>20</sup> An example of the graph used to determine heating and VNB thresholds in buffer can be seen in **Figure 4.7 D**. The thresholds in HeLa cells were determined again *via* darkfield microscopy but this time after incubating HeLa cells with the diluted JetPEI/pDNA/Au 5 pt complexes for 1 h. JetPEI/pDNA/Au 5 pt complex dilutions in the range of 1/10 to 1/500 were evaluated and their respective VNB and heating thresholds in HeLa cells are displayed in **Figure 4.7 E**.

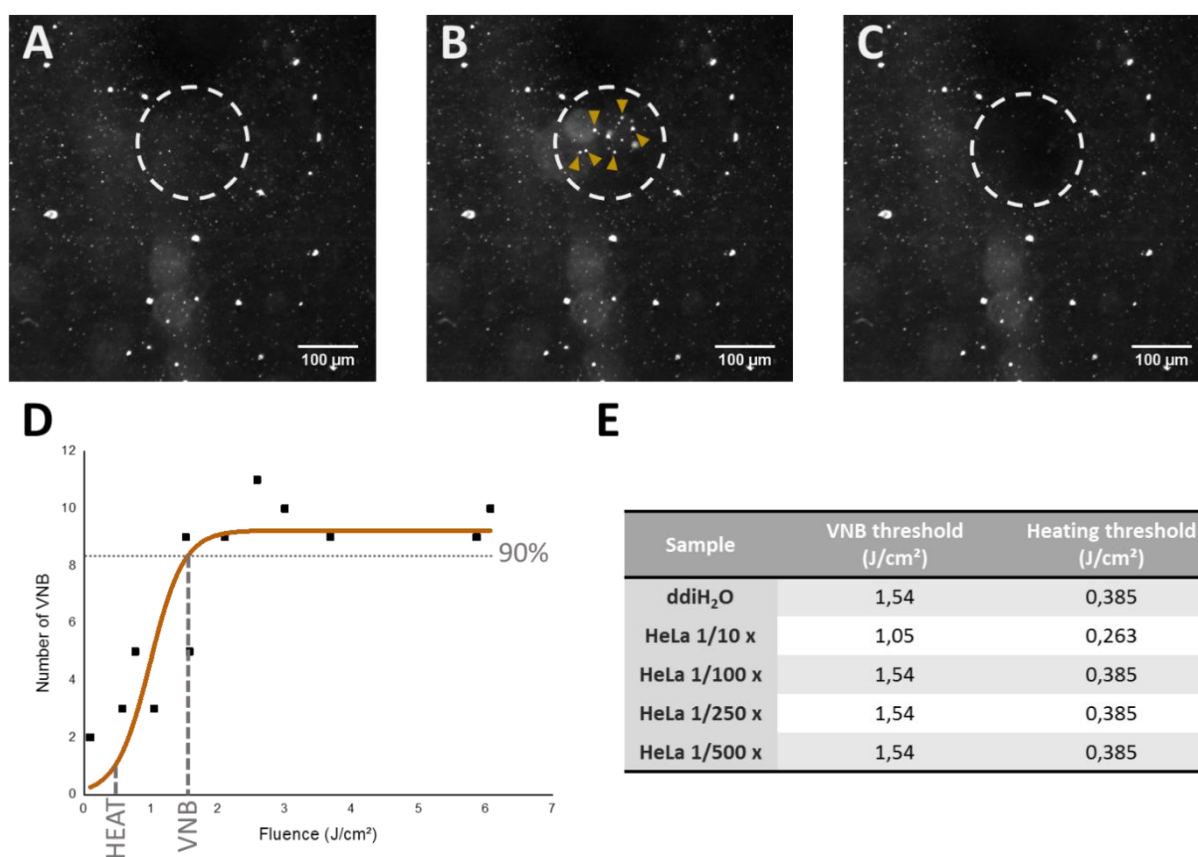


**Figure 4.7 Determination of heating and VNB threshold *via* dark-field microscopy.** (A) Dark-field microscopy image of JetPEI/pDNA/Au 5 pt complexes in ddiH<sub>2</sub>O. (B) Dark-field microscopy image upon VNB formation (VNBs indicated by yellow arrows). (C) Dark-field microscopy image after VNB formation. Scalebar on the images represents 100  $\mu\text{m}$ . (D) Graph shows the relation between the number of VNBs per cell and laser fluence. VNB threshold is calculated as the laser fluence needed to reach 90% of the maximum number of VNBs per cell. The fluence for heating is selected at  $\frac{1}{4}$  of the VNB threshold. (E) Table shows the threshold values for VNB formation and heating (in J/cm<sup>2</sup>) used for JetPEI/pDNA/Au pt 5 complexes in further experiments.

### 3.4 Evaluation of uptake efficiency

Uptake experiments were carried out using confocal microscopy to visualize the uptake of JetPEI/pDNA/Au 5 pt complexes in HeLa cells. A representative image of each dilution is presented in **Figure 4.8**. The blue channel shows nuclei that were stained with Hoechst and the orange channel shows the AuNP core, that could be visualized in confocal reflection mode using the 561 nm laser because of its high scattering properties. Confocal images show that HeLa cells are capable of incorporating JetPEI/pDNA/Au 5 pt complexes. It must be noted however, that the number of particles taken up after administration of a 1/500 dilution is very low, hinting that a further decrease in concentration likely would not be relevant.

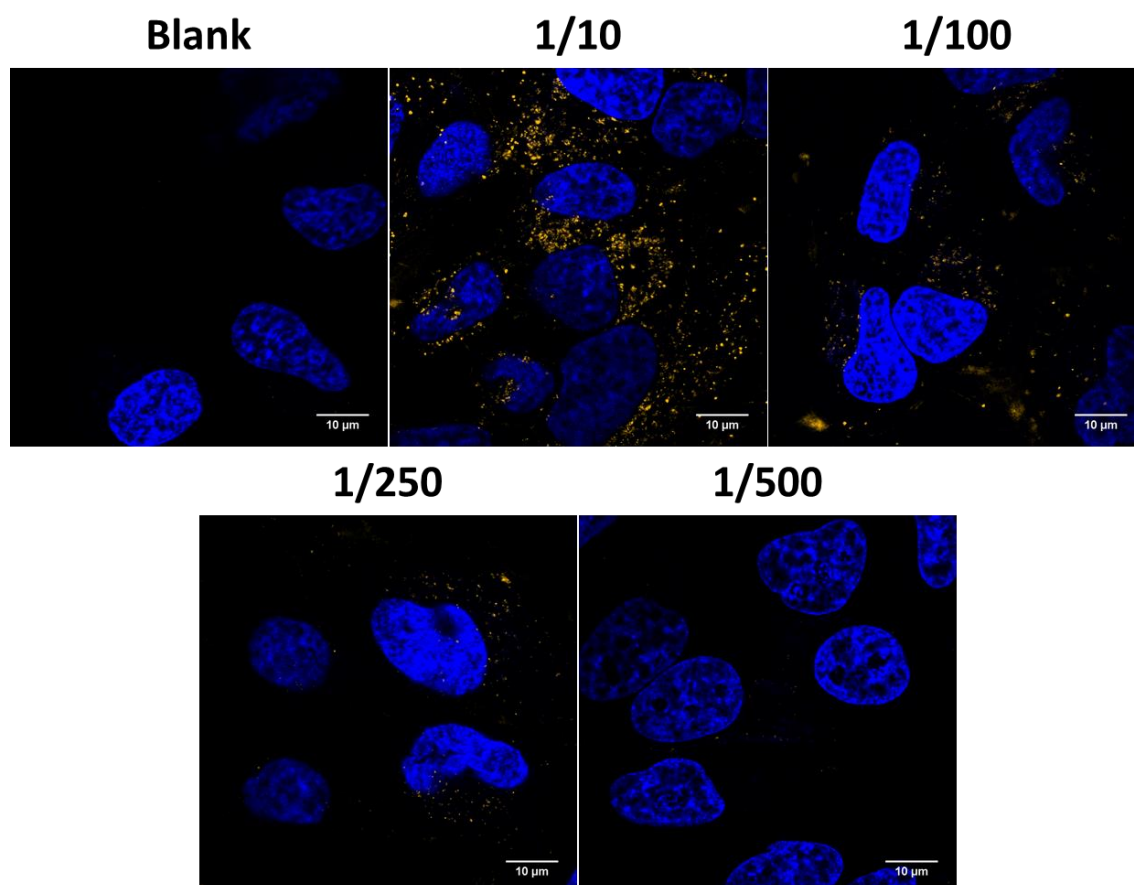


**Figure 4.8 Evaluation of the uptake of JetPEI/pDNA/Au complexes in HeLa cells.** Confocal microscopy images show nuclei stained with Hoechst in the blue channel and AuNP core in the orange channel. Scalebar represents 10 μm.

### 3.5 Evaluation of transfection efficiency and cell viability

In order to test the applicability of photothermally triggered endosomal escape of pDNA, transfection efficiencies and related cellular toxicity was evaluated. HeLa cells were incubated with JetPEI/pDNA/Au 5 pt complexes and the transfection efficiency based on GFP expression was evaluated after 24 h *via* flow cytometry. As shown in **Figure 4.9 A**, the complexes by themselves (*i.e.* without laser irradiation) showed no transfection at any of the concentrations tested, as expected. Cells irradiated with a low intensity laser pulse (heating regime) were not transfected either. At high laser pulse energy (VNB regime) a small fraction of the cells (3%) became transfected in case of the highest concentration of complexes. Cell viability was measured in parallel and showed acceptable cell viability (>70%) in the heating regime starting from a 1/100 dilution and in the VNB regime starting from a 1/250 dilution (see **Figure 4.9 B**). Unfortunately, no significant transfection was observed for those conditions. While unfortunately these complexes clearly are not suited for studying the relation between the location of endosomal escape and the resulting transfection efficiency, it is of fundamental interest to try to find out why transfections were unsuccessful as these insights might teach us how to improve future systems for light-triggered pDNA transfections.

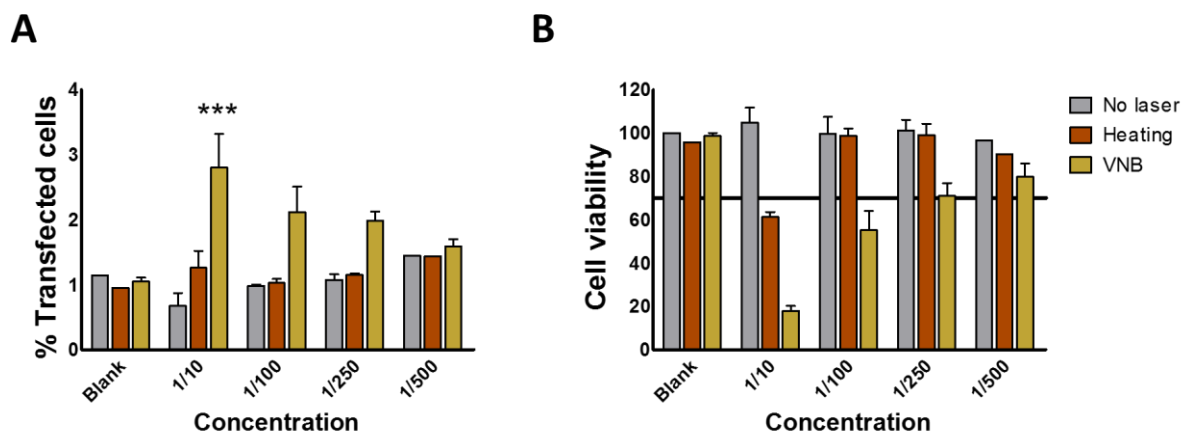


**Figure 4.9 Evaluating transfection efficiency and cell viability in HeLa cells. (A)** Graph shows the percentage of cells that are positive for GFP transfection. **(B)** Graph shows the percentage of cell viability as measured by DAPI staining. All graphs show mean  $\pm$  SEM;  $n=2$ . Significance was calculated using two-way ANOVA with Bonferroni post-test (compare means to blank) (\*\*\*)  $p < 0.0001$ ; \*\*  $p < 0.01$ ; \*  $p < 0.05$ ).

### 3.6 Evaluation of endosomal escape and pDNA breakdown

A first possible reason why transfections were unsuccessful is a lack of endosomal escape upon laser irradiation. Therefore, endosomal escape efficiency was investigated specifically by time-lapse confocal microscopy. As explained earlier in **Chapter 3**, this was achieved by incorporating fluorescently labeled oligonucleotides (AF647 ONs) into the complexes that dequench and accumulate into the nucleus upon endosomal release. After an incubation period of 1 h, the cells underwent laser treatment and were allowed to stabilize for 3 h. Next, cells were visualized by confocal microscopy and the number of red nuclei (indicative for endosomal escape) was counted. **Figure 4.10 A** shows confocal images of the 1/10 concentration and illustrate that for this concentration, endosomal escape occurred in nearly every cell. The percentage of cells that showed endosomal escape is displayed in **Figure 4.10 B** and indicates that the VNB regime is more efficient in inducing endosomal escape than the heating regime. We conclude that photothermally induced rupture of endosomes was successful, as evidenced by the release of fluorescent oligonucleotides.

Another reason why transfections were unsuccessful could be because the pDNA is damaged by the laser-induced photothermal effects. To investigate this, the effect of heating and VNB formation on the integrity of pDNA was studied separately. A dispersion of JetPEI/pDNA/Au 5 pt complexes in ddiH<sub>2</sub>O was irradiated with low (heat) or high (VNB) intensity laser pulses, and the amount of pDNA remaining after laser irradiation was measured by the use of a PicoGreen assay. PicoGreen becomes fluorescent upon DNA intercalation, which can only happen after it has been released from the complexes. Therefore, we added dextran sulphate to the complexes to release the remaining pDNA. The concentration of pDNA released from the complexes and measured by PicoGreen assay can be observed in **Figure 4.10 C**. In case of VNB treatment, it was noted that the remaining pDNA was only half the amount that was originally incorporated into the complexes. This drop indicates the degradation of a substantial amount of pDNA in such a way that PicoGreen is no longer able to intercalate with the remains. However, the detection of pDNA structure *via* PicoGreen assay does not necessarily mean that the remaining pDNA is intact and functional. Indeed, it could be possible that the pDNA is fragmented after laser treatment, still allowing intercalation but unable to produce transfection. To determine the functionality of the remaining pDNA after laser treatment, we are evaluating the transfection of HeLa cells with this remaining pDNA through electroporation. However, at the time of writing experiments were still ongoing.

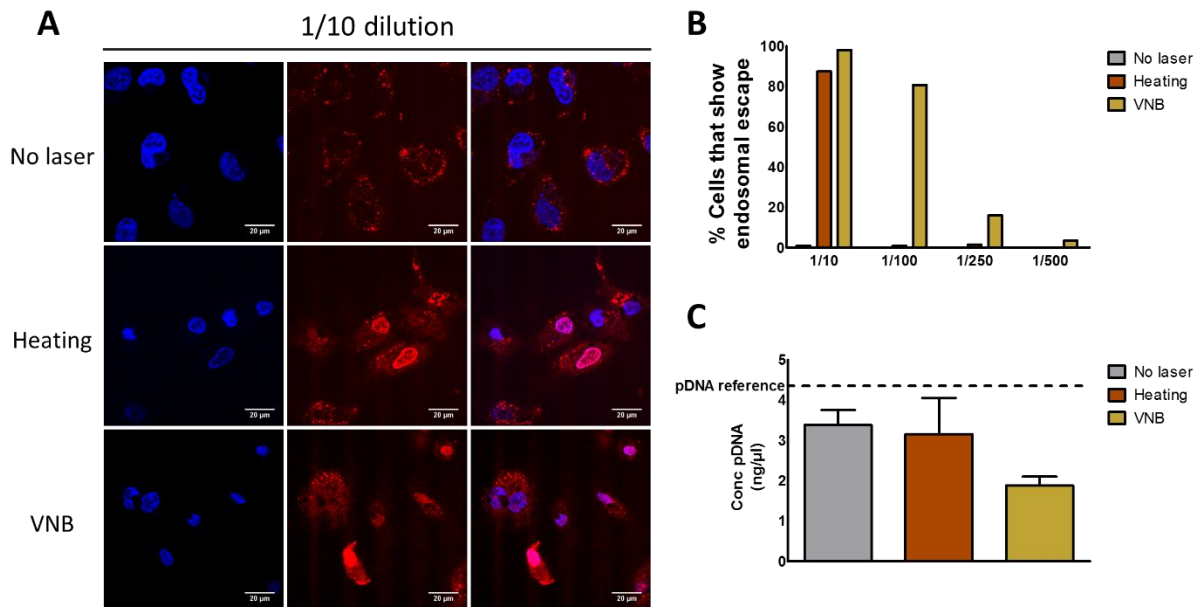


**Figure 4.10 Evaluation of endosomal escape and pDNA integrity.** **(A)** Confocal images show the result of the endosomal escape assay without laser treatment, after heating and after VNB formation of JetPEI/pDNA/Au pt 5 complexes in a 1/10 dilution. The scalebar represents 20  $\mu\text{m}$ . The left column shows nuclei after Hoechst staining; the middle column shows AF647 ONs; and the right column shows the merge. **(B)** Graph shows the percentage of cells that show endosomal escape for the different dilutions of JetPEI/pDNA/Au pt 5 complexes. A total of 888 cells were analyzed visually for accumulation of AF647 ONs in the nucleus. **(C)** The pDNA concentration was measured *via* PicoGreen assay after the addition of dextran sulphate. Graph shows mean  $\pm$  SEM; n=2

## 4 DISCUSSION

In recent years, the interest in AuNPs for drug delivery purposes has increased tremendously, not in the least because their optical properties could be used in order to obtain spatio-temporal controlled delivery of cargo. In this chapter, we aimed to use the plasmonic properties of AuNPs to induce light triggered rupture of the endosomal membrane after incubation of HeLa cells with JetPEI/pDNA/Au complexes. We examined if photothermal effects such as heating and VNB formation were able to induce endosomal release and transfect HeLa cells. After evaluation of JetPEI/pDNA/Au complexes prepared with different amounts of AuNPs, JetPEI/pDNA/Au 5 pt complexes were selected for further experiments since they showed a good size, zeta potential and UV/VIS extinction spectrum; and their uptake was confirmed *via* confocal microscopy. Unfortunately, we observed that neither heat transfer nor VNB formation were able to induce efficient transfection in HeLa cells.

In order to find out what is the cause of this inefficient transfection, we first studied endosomal escape through the use of the dequenching assay already reported in **Chapter 3**. Results showed that both heat transfer and VNB formation were able to induce endosomal rupture, with VNB being the most efficient of the two. We hypothesize that in order to induce endosomal escape *via* heating, a relatively high concentration of AuNPs is needed per endosome in order to heat up the endosomal lumen to a temperature that is high enough to induce thermal membrane destabilization. On the other hand, the mechanical force arising from the formation of already one VNB is likely sufficient to induce mechanical disruption of the endosomal membrane and thus release of endosomal content. Two side notes must be made on the use of the ON dequenching assay to evaluate endosomal escape. First of all, it should be kept in mind that the endosomal release of the small ONs might not be fully representative to evaluate endosomal escape of a much larger construct such as pDNA. While it shows that the endosomal membrane was permeabilized, it remains uncertain if larger pDNA molecules can escape from the endosomes. Especially in case of heat-induced permeabilization pores may be on the small side. Secondly, low concentrations of complexes had to be used to keep toxicity at an acceptable level. When using these low concentrations, visual confirmation of endosomal escape based on the ON dequenching assay after VNB formation became difficult. If the amount of AF647 ONs per endosome is not high enough to be detected, endosomal escape could remain invisible using this method, despite the fact that it may actually have happened. In order to confirm our hypothesis that one VNB is capable of disrupting the endosomal membrane, it would be useful to use a more sensitive assay to detect endosomal escape. Such an assay was proposed by Wittrup *et al.* (see **Chapter 1**) where they

used two different exposure settings in order to extend the dynamic range. Using long exposure times, weakly fluorescent signals that may remain unnoticed in the dequenching assay should become detectable.<sup>38</sup> Nevertheless, since in the 1/10 dilution the majority of cells show endosomal escape after VNB formation and after heat transfer, we conclude that the endosomal rupture is not the limiting factor for photothermally triggered transfection.

We next went on to evaluate the integrity of pDNA after inducing the photothermal effects. Mechanical or thermal stimuli may damage nucleic acids, rendering the pDNA ineffective even when it is able to reach the cytosol. Although photothermally triggered endosomal escape of siRNA has been performed successfully, pDNA offers an extra challenge because of its longer sequence. Therefore, we examined the pDNA content after VNB formation and heating regime *via* PicoGreen assay. We found that a large part of the cargo was degraded after VNB formation as PicoGreen was no longer able to intercalate. However, there was still a considerable amount of structural pDNA detected after heating and VNB regime. Since a PicoGreen assay only indicates the presence of pDNA structure, it does not provide any information regarding the integrity (and thus transfection potential) of the remaining pDNA. Therefore, in the future, we should evaluate the functionality of the DS released pDNA, *e.g.* by transfecting HeLa cells through electroporation with the pDNA collected from photothermally treated polyplexes or by determination of the molecular weight of the remaining cargo. Since a large part of the pDNA seems to be destroyed to such an extent that intercalation with PicoGreen is no longer possible, it is likely that the sequence of the remaining pDNA is no longer entirely intact either. If this should prove to be the case, one can consider designing a NP that better protects the pDNA against these photothermal effects or to co-incubate pDNA-containing polyplexes with endosome-disruptive AuNPs. One option would be to design a NP that has a gold core, surrounded by a stimuli-responsive polymer that allows the release of pDNA prior to photothermal laser treatment, as shown in **Figure 4.11**. Such stimuli-responsive polymers could be pH-responsive polymers that degrade upon endosomal acidification or thermo-sensitive polymers that degrade after an initial soft heating step. Another interesting point is that after VNB formation, AuNPs are known to be fragmented into smaller particles that are able to bind into the major groove of DNA, possibly hindering pDNA transcription.<sup>39</sup>

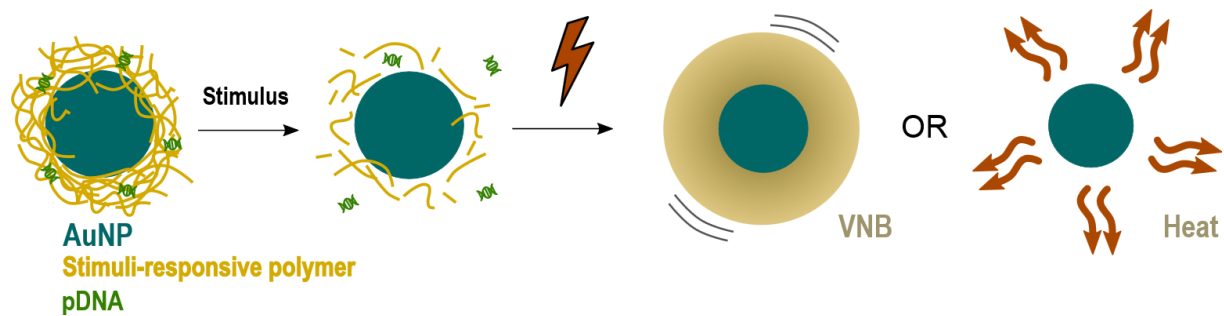


**Figure 4.11** Alternative NP design for cytosolic delivery of intact pDNA after endocytosis.

## **5 CONCLUSION**

Photothermally triggered endosomal escape of pDNA is a fascinating technique that could be used to obtain spatio-temporal control over the cytosolic delivery of pDNA. Besides its usefulness as a tool to acquire fundamental insights into the role of the place and time of endosomal escape for transfection efficiency, it would also be an excellent method to increase endosomal escape capacity of pDNA complexes. The results obtained in this chapter show that although this technique has been used before to induce endosomal escape of siRNA, the delivery of much larger pDNA poses some extra challenges. Unfortunately, we observed that neither the formation of VNBS nor the generation of heat were able to induce efficient transfection in HeLa cells. It is hypothesized that the main reason for this lack of transfection is that the laser treatment renders the pDNA dysfunctional. In the future, improvements to the design of the complex are needed to ensure endosomal release of intact pDNA.

## **ACKNOWLEDGEMENTS**

L. Vermeulen would like to acknowledge the financial support of the Agency for Innovation by Science and Technology in Belgium. Financial support by the Ghent University Special Research Fund and the Fund for Scientific Research Flanders (FWO, Belgium) is acknowledged with gratitude. This research was funded by the European Research Council (ERC) under the European Union's Horizon 2020 research and innovation program (grant agreement [648214]).

## REFERENCES

- (1) Pissuwan, D.; Niidome, T.; Cortie, M. B. The Forthcoming Applications of Gold Nanoparticles in Drug and Gene Delivery Systems. *J. Control. Release* **2011**, *149*, 65–71.
- (2) Sperling, R. A.; Gil, P. R.; Zhang, F.; Zanella, M.; Parak, W. J. Biological Applications of Gold Nanoparticles. *Chem. Soc. Rev.* **2008**, *37*, 1896–1908.
- (3) Ghosh, P.; Han, G.; De, M.; Kim, C. K.; Rotello, V. M. Gold Nanoparticles in Delivery Applications. *Adv. Drug Deliv. Rev.* **2008**, *60*, 1307–1315.
- (4) Cao, W.; Huang, T.; Xu, X.-H. N.; Elsayed-Ali, H. E. Localized Surface Plasmon Resonance of Single Silver Nanoparticles Studied by Dark-Field Optical Microscopy and Spectroscopy. *J. Appl. Phys.* **2011**, *109*, 034310.
- (5) Yan, L.; Yan, Y.; Xu, L.; Ma, R.; Jiang, F.; Xu, X. Large Range Localized Surface Plasmon Resonance of Ag Nanoparticles Films Dependent of Surface Morphology. *Appl. Surf. Sci.* **2016**, *367*, 563–568.
- (6) Chan, G. H.; Zhao, J.; Hicks, E. M.; Schatz, G. C.; Van Duyne, R. P. Plasmonic Properties of Copper Nanoparticles Fabricated by Nanosphere Lithography. *Nano Lett.* **2007**, *7*, 1947–1952.
- (7) Langhammer, C.; Schwind, M.; Kasemo, B.; Zoric, I. Localized Surface Plasmon Resonances in Aluminum Nanodisks. *Nano Lett.* **2008**, *8*, 1461–1471.
- (8) Xiong, R.; Samal, S. K.; Demeester, J.; Skirtach, A. G.; De Smedt, S. C.; Braeckmans, K. Laser-Assisted Photoporation: Fundamentals, Technological Advances and Applications. *Adv. Phys. X* **2016**, *1*, 596–620.
- (9) Qiu, J.; Wei, W. D. Surface Plasmon-Mediated Photothermal Chemistry. *J. Phys. Chem. C* **2014**, *118*, 20735–20749.
- (10) Kelly, K. L.; Coronado, E.; Zhao, L. L.; Schatz, G. C. The Optical Properties of Metal Nanoparticles: The Influence of Size, Shape, and Dielectric Environment. *J. Phys. Chem. B* **2003**, *107*, 668–677.
- (11) Boulais, E.; Lachaine, R.; Hatef, A.; Meunier, M. Plasmonics for Pulsed-Laser Cell Nanosurgery: Fundamentals and Applications. *J. Photochem. Photobiol. C Photochem. Rev.* **2013**, *17*, 26–49.
- (12) Sershen, S. R.; Westcott, S. L.; Halas, N. J.; West, J. L. Temperature-Sensitive Polymer-Nanoshell Composites for Photothermally Modulated Drug Delivery. *J. Biomed. Mater. Res.* **2000**, *51*, 293–298.
- (13) Radt, B.; Smith, T. A.; Caruso, F. Optically Addressable Nanostructured Capsules. *Adv. Mater.* **2004**, *16*, 2184–2189.
- (14) Kawano, T.; Niidome, Y.; Mori, T.; Katayama, Y.; Niidome, T. PNIPAM Gel-Coated Gold Nanorods for Targeted Delivery Responding to a Near-Infrared Laser. **2009**, 0–4.
- (15) Huschka, R.; Barhoumi, A.; Liu, Q.; Roth, J. A.; Ji, L.; Halas, N. J. Gene Silencing

- by Gold Nanoshell-Mediated Delivery and Laser-Triggered Release of Antisense Oligonucleotide and siRNA. *ACS Nano* **2012**, *6*, 7681–7691.
- (16) Jain, P. K.; Qian, W.; El-Sayed, M. A. Ultrafast Cooling of Photoexcited Electrons in Gold Nanoparticle-Thiolated DNA Conjugates Involves the Dissociation of the Gold-Thiol Bond. *J. Am. Chem. Soc.* **2006**, *128*, 2426–2433.
- (17) Wijaya, a; Schaffer, S.; Pallares, I.; Hamad-Schifferli, K. Selective Release of Multiple DNA Oligonucleotids from Gold Nanorods. *ACS Nano* **2008**, *3*, 80–86.
- (18) Barhoumi, A.; Huschka, R.; Bardhan, R.; Knight, M. W.; Halas, N. J. Light-Induced Release of DNA from Plasmon-Resonant Nanoparticles: Towards Light-Controlled Gene Therapy. *Chem. Phys. Lett.* **2009**, *482*, 171–179.
- (19) Huschka, R.; Neumann, O.; Barhoumi, A.; Halas, N. J. Visualizing Light-Triggered Release of Molecules inside Living Cells. *Nano Lett.* **2010**, *10*, 4117–4122.
- (20) Xiong, R.; Raemdonck, K.; Peynshaert, K.; Lentacker, I.; De Cock, I.; Demeester, J.; De Smedt, S. C.; Skirtach, A. G.; Braeckmans, K. Comparison of Gold Nanoparticle Mediated Photoporation: Vapor Nanobubbles Outperform Direct Heating for Delivering Macromolecules in Live Cells. *ACS Nano* **2014**, *8*, 6288–6296.
- (21) Schomaker, M.; Killian, D.; Willenbrock, S.; Heinemann, D.; Kalies, S.; Ngezahayo, A.; Nolte, I.; Ripken, T.; Junghanß, C.; Meyer, H.; *et al.* Biophysical Effects in Off-Resonant Gold Nanoparticle Mediated (GNOME) Laser Transfection of Cell Lines, Primary- and Stem Cells Using Fs Laser Pulses. *J. Biophotonics* **2015**, *8*, 646–658.
- (22) Kalies, S.; Birr, T.; Heinemann, D.; Schomaker, M.; Ripken, T.; Heisterkamp, A.; Meyer, H. Enhancement of Extracellular Molecule Uptake in Plasmonic Laser Perforation. *J. Biophotonics* **2014**, *7*, 474–482.
- (23) Lukianova-Hleb, E. Y.; Belyanin, A.; Kashinath, S.; Wu, X.; Lapotko, D. O. Plasmonic Nanobubble-Enhanced Endosomal Escape Processes for Selective and Guided Intracellular Delivery of Chemotherapy to Drug-Resistant Cancer Cells. *Biomaterials* **2012**, *33*, 1821–1826.
- (24) Krpetić, Ž.; Nativo, P.; Sée, V.; Prior, I. A.; Brust, M.; Volk, M. Inflicting Controlled Nonthermal Damage to Subcellular Structures by Laser-Activated Gold Nanoparticles. *Nano Lett.* **2010**, *10*, 4549–4554.
- (25) Carregal-Romero, S.; Ochs, M.; Rivera-Gil, P.; Ganas, C.; Pavlov, A. M.; Sukhorukov, G. B.; Parak, W. J. NIR-Light Triggered Delivery of Macromolecules into the Cytosol. *J. Control. Release* **2012**, *159*, 120–127.
- (26) Morales, D. P.; Braun, G. B.; Pallaoro, A.; Chen, R.; Huang, X.; Zasadzinski, J. A.; Reich, N. O. Targeted Intracellular Delivery of Proteins with Spatial and Temporal Control. *Mol. Pharm.* **2015**, *12*, 600–609.
- (27) Morales, D. P.; Wonderly, W. R.; Huang, X.; McAdams, M.; Chron, A. B.; Reich, N. O. Affinity-Based Assembly of Peptides on Plasmonic Nanoparticles Delivered Intracellularly with Light Activated Control. *Bioconjug. Chem.* **2017**, *28*, 1816–1820.

- (28) Huang, X.; Pallaoro, A.; Braun, G.; Morales, D.; Zasadzinski, J.; Reich, N. Modular Plasmonic Nanocarriers for Efficient and Targeted Delivery of Cancer-Therapeutic siRNA. *Nano Lett.* **2014**, *14*, 2046–2051.
- (29) Braun, G. B.; Pallaoro, A.; Wu, G.; Missirlis, D.; Zasadzinski, J. A.; Tirrell, M.; Reich, N. O. Laser-Activated Gene Silencing via Gold Nanoshell-siRNA Conjugates. *ACS Nano* **2009**, *3*, 2007–2015.
- (30) Forrest, M. L.; Pack, D. W. On the Kinetics of Polyplex Endocytic Trafficking: Implications for Gene Delivery Vector Design. *Mol. Ther.* **2002**, *6*, 57–66.
- (31) Encina, E. R.; Coronado, E. A. On the Far Field Optical Properties of Ag - Au Nanosphere Pairs. *J. Phys. Chem. C* **2010**, 16278–16284.
- (32) Encina, E. R.; Coronado, E. A. Plasmon Coupling in Silver Nanosphere Pairs. *J. Phys. Chem. C* **2010**, *114*, 3918–3923.
- (33) Encina, E. R.; Coronado, E. A. Near Field Enhancement in Ag Au Nanospheres Heterodimers. *J. Phys. Chem. C* **2011**, *115*, 15908–15914.
- (34) Rehman, Z. U.; Hoekstra, D.; Zuhorn, I. S. Mechanism of Polyplex- and Lipoplex-Mediated Delivery of Nucleic Acids: Real-Time Visualization of Transient Membrane Destabilization without Endosomal Lysis. *ACS Nano* **2013**, *7*, 3767–3777.
- (35) Nguyen, J.; Szoka, F. C. Nucleic Acid Delivery: The Missing Pieces of the Puzzle? *Acc. Chem. Res.* **2012**, *45*, 1153–1162.
- (36) Lukacs, G. L.; Haggie, P.; Seksek, O.; Lechardeur, D.; Freedman, N.; Verkman, A. S. Size-Dependent DNA Mobility in Cytoplasm and Nucleus. *J. Biol. Chem.* **2000**, *275*, 1625–1629.
- (37) Symens, N.; Soenen, S. J.; Rejman, J.; Braeckmans, K.; De Smedt, S. C.; Remaut, K. Intracellular Partitioning of Cell Organelles and Extraneous Nanoparticles during Mitosis. *Adv. Drug Deliv. Rev.* **2012**, *64*, 78–94.
- (38) Wittrup, A.; Ai, A.; Liu, X.; Hamar, P.; Trifonova, R.; Charisse, K.; Manoharan, M.; Kirchhausen, T.; Lieberman, J. Visualizing Lipid-Formulated siRNA Release from Endosomes and Target Gene Knockdown. *Nat. Biotechnol.* **2015**, *33*, 870–876.
- (39) Pan, Y.; Neuss, S.; Leifert, A.; Fischler, M.; Wen, F.; Simon, U.; Schmid, G.; Brandau, W.; Jahnen-Dechent, W. Size-Dependent Cytotoxicity of Gold Nanoparticles. *Small* **2007**, *3*, 1941–1949.



# Chapter 5

## Broader International Context, Relevance and Future Perspectives

Vermeulen, L.M.P.<sup>1,2</sup>, Braeckmans, K.<sup>1,2</sup>

<sup>1</sup>Lab. General Biochemistry & Physical Pharmacy, Ghent University, Ottergemsesteenweg 460, Ghent, Belgium

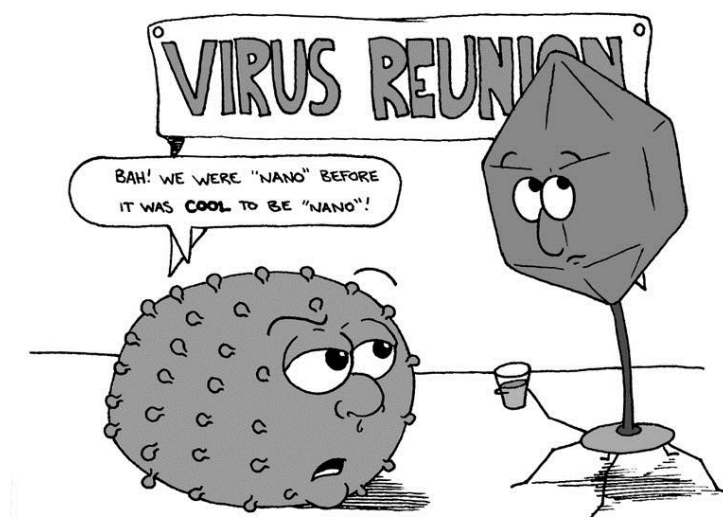
<sup>2</sup>Centre for Nano- and Biophotonics, Ghent University, Ottergemsesteenweg 460, Ghent, Belgium

## TABLE OF CONTENTS

1	THE CHALLENGES AND SUCCESSES OF GENE THERAPY .....	166
2	THE LIMITATIONS THAT HINDER PROGRESSION IN NON-VIRAL GENE THERAPY.....	168
2.1	The delivery problem.....	168
2.2	Trial and error without fundamental understanding .....	169
3	HOW DO WE PROCEED?.....	170
3.1	Studying biological barriers to gene therapy .....	170
3.2	Applying fundamental insights to nanomedicine design.....	172
3.3	The power of reporting negative results .....	173
4	CONCLUSION .....	174

## ABSTRACT

After providing a general overview of the intracellular barriers nanomedicines have to conquer, this thesis focused on the gathering of fundamental knowledge about the endosomal membrane as a barrier for gene therapy. We examined the influence of cellular and endosomal properties on the efficiency of proton sponge-based endosomal rupture. Next, we evaluated the feasibility of a new, gold-mediated mechanism for endosomal release of pDNA-containing PEI complexes. In this final chapter, we will discuss the broader international context of our work and its relevance to the field. We will start by providing a short overview of the key challenges encountered in the field of gene therapy and the progression that was achieved over the years. Next, we will discuss the limitations that are currently preventing nanomedicines to reach their full potential. We will focus on the need to obtain a more fundamental understanding of biological barriers while further directing our attention to the endosomal barrier.



## 1 THE CHALLENGES AND SUCCESSES OF GENE THERAPY

Since its first hypothesis nearly 5 decades ago, gene therapy has fascinated scientists as it offers the possibility to treat a disease at its genetic roots. Indeed, the introduction of genes into human cells to restore normal cellular function would be a very attractive addition to our therapeutic toolbox.<sup>1-3</sup> Although gene therapy seems elegantly simple in its concept, there are several **key challenges** that need to be overcome (see **Figure 5.1**). A first challenge regarding the use of gene therapeutics is the identification of genes for gene modulation and technologies for gene editing. Secondly, it soon became clear that the actual delivery of these gene therapeutics to their target cells is another major hurdle since it was observed that naked nucleic acids were no match to our bodies' defense mechanisms, specialized in fighting off foreign invaders. The third challenge is to deliver gene therapeutics without inducing unwanted side effects.<sup>4,5</sup>

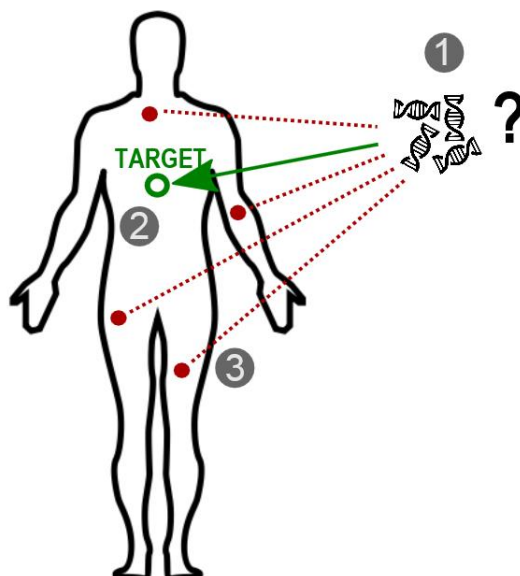


**Figure 5.1 Key challenges to gene therapy.** **1.** Identification of genes and technologies that are of therapeutic interest. **2.** Delivery of the gene therapeutic to its target, which is situated on the intracellular level. **3.** Avoid unwanted side effects for instance by reducing off-target delivery. (Human body and gene icon © The Noun Project)

Different types of delivery systems can be applied to deliver a gene to its target site. The first type of gene delivery vectors that attracted attention were the **viral vectors**. Encouraging results in preclinical disease models led to the initiation of the first gene therapy clinical trials in the early 1990s. However, serious therapy-related toxicities caused by the viral vector (*e.g.* inflammatory responses and malignancies due to insertional mutagenesis) were observed.<sup>3</sup> These setbacks fueled the search for alternative delivery strategies that would enable safer delivery of nucleic acids to their target. With this search came the rise of **nanomedicine** in the field of gene therapy.

Nanomedicine is the application of nanotechnology for health and medicine and includes the packaging of therapeutics in a single or a combination of materials of which cationic lipids, peptides, metals, synthetic polymers and polysaccharides are the most commonly applied.<sup>6</sup> It was long thought that nanomedicine would revolutionize the treatment of a variety of diseases because of their advantageous properties, as briefly mentioned in **Chapter 1**. It is true that since the approval of the first nanotherapeutic (Doxil in 1995), the clinical use of more than 50 other nanoparticle-based drugs was authorized by the U.S. Food and Drug Administration (FDA) and the European Medicines Agency (EMA).<sup>7</sup> Nevertheless, it must be noted that the majority of nanomedicines in clinical development are nanomedicines of previously approved small molecules and that the most frequently observed clinical benefit is a reduction in toxicity rather than an increase in efficacy.<sup>6</sup> Although non-viral vectors for gene therapy have entered clinical trials, they generally remain stuck in the early stages of evaluation (Phase I and II) as the majority of nanomedicines fail to pass Phase 3 clinical trials.<sup>8</sup> Meanwhile, the field of viral gene therapy underwent efforts to improve its safety profile and the majority of gene therapy clinical trials to date utilize viral vectors as delivery vehicles.<sup>9-11</sup> In fact, while the number of gene therapy products that have reached the market is still limited, it is interesting to note that until now all approved gene therapies make use of viral vectors (see **Table 5.1**).

**Table 5.1 Overview of currently approved gene therapies.**

	<b>Vector</b>	<b>Indication</b>	<b>Target cell</b>	<b>Approved</b>	<b>Ref</b>
<b>Glybera</b>	AAV*	Lipoprotein lipase deficiency	<i>In vivo:</i> Muscle cells	2012 (EMA) <sup>1</sup>	12
<b>Strimvelis</b>	Lentivirus	Adenosine deaminase deficiency	<i>Ex vivo:</i> CD34+ autologous stem cells	2016 (EMA)	12
<b>Kymriah</b>	Lentivirus	B-cell precursor acute lymphoblastic leukemia	<i>Ex vivo:</i> Autologous T cells	2017 (FDA)	13,14
<b>Yescarta</b>	Retrovirus	Large B-cell lymphoma	<i>Ex vivo:</i> Autologous T cells	2017 (FDA)	13,14
<b>Luxturna</b>	AAV*	Biallelic RPE65 mutation-associated retinal dystrophy	<i>In vivo:</i> Retinal cells	2017 (FDA)	13,14

\* Adeno-associated virus

<sup>1</sup> Marketing authorization has expired following the marketing-authorization holder's decision not to apply for renewal

However, despite the successes obtained in viral gene therapy, the uncertainty of triggering immune responses, the risk of gene mis-insertion, problems with large-scale production and the difficulty of packaging large nucleic acids are issues that remain unresolved.<sup>8</sup> Since non-viral vectors may provide several advantages with regard to safety profile, cost-effective manufacturing, *etc.* they remain an attractive area of research.

## 2 THE LIMITATIONS THAT HINDER PROGRESSION IN NON-VIRAL GENE THERAPY

Although non-viral strategies would be advantageous on many levels, their development represents a significant challenge. Indeed, despite many years of intensive research exploring the use of nanotechnology for gene therapy, this approach has not met the expectations so far. With no approved non-viral gene therapeutics until now and only a limited amount of nanomedicines currently in clinical trials, it becomes evident that nanotherapeutics for gene delivery are lagging behind their viral counterparts. In this section we will discuss why non-viral gene therapy lacks efficiency and what are the factors that hinder progression of the field.

### 2.1 The delivery problem

Whereas viruses have evolved to deliver their genetic content efficiently to mammalian cells, the main reason for the limited efficacy of nanomedicines in gene therapy is their inability to deliver sufficient amounts of nucleic acid cargo to the target.<sup>9</sup> Consequently, this lack in efficiency requires the administration of large amounts of carrier material, causing toxicity. Unfortunately, this delivery problem is a grave one and is situated on various levels. As overviewed and discussed in **Chapter 1**, the delivery vector must first overcome several **extracellular barriers** that could lead to cargo degradation, rapid clearance or immobilization of the nanomedicines, rendering them ineffective. Furthermore, the vectors should avoid nonspecific distribution and accumulate at the targeted tissue in a sufficiently high dose. The severity of this extracellular part of the delivery problem becomes clear when evaluating the amount of nanoparticles that actually reach their target tissue. In 2016, Wilhelm *et al.* conducted a multivariate analysis of the literature of the last 10 years and found that only 0.7% of the administered nanoparticle dose was delivered to a solid tumor *in vivo*. This shows without any doubt that our inability to deliver nanomedicines to the target tissue/cell presents a major limitation.<sup>15</sup>

Sadly, successful delivery of nanomedicines to the target tissue/cell would not guarantee the triumph of non-viral gene therapy since their molecular target is located in the intracellular environment. Indeed, even on the cellular level there are various barriers that obstruct the road to efficient gene delivery. In **Chapter 1**, an extensive overview of the different **intracellular barriers** is provided together with the role they play in preventing efficient transfection by nanomedicines. We have discussed the plasma membrane, exocytosis, endosomal confinement, autophagy, vector unpacking, cytoplasmic degradation and nuclear translocation as prominent intracellular barriers. Of those, **endosomal escape** appears to be a particularly difficult bottleneck for

nanomedicines. For polyplexes, for instance, it has been reported that as few as 1 to 5 internalized particles have the capacity to effectively escape endosomal confinement.<sup>16</sup> Also for lipid nanoparticles, Wittrup *et al.* found that merely 7% of the particle-containing endosomes were able to efficiently release siRNA into the cytosol. Likewise, Gilleron *et al.* measured release efficiencies of siRNA from lipid nanoparticles to be as low as 1-2% of the administered cargo.<sup>17,18</sup> In accordance with these findings, we demonstrated in **Chapter 3** that the percentage of JetPEI/pDNA polyplex-containing endosomes that show proton sponge-based endosomal escape is limited to 2% in ARPE-19 cells and 8% in HeLa cells. It confirms the current view that on the intracellular level, endosomal escape is one of the most prominent barriers for effective gene therapy.

Furthermore, our study also illustrates that there can be **intercellular variation** of the endosomal barrier. This intercellular variation was further corroborated by the inclusion of A549 and H1299 cells, which also showed low endosomal escape efficiencies after incubation with the same JetPEI/pDNA polyplexes. Indeed, we discovered that intercellular variations in endosomal size and endosomal membrane leakiness have a considerable impact on proton sponge-based endosomal escape. Since variations in cellular properties influence the effectiveness of nanomedicines, it is of crucial importance to determine the right cell type/animal model when conducting experiments, as will be discussed later in this chapter. In line with this view, there is a need to perform fundamental investigations to unravel intercellular variations.

## **2.2 Trial and error without fundamental understanding**

Unfortunately however, **fundamental research** on intracellular barriers and intercellular variations regarding these barriers is rather limited, giving us little chance to gain mechanistic insights that could unlock the development of a next generation of delivery systems. The paucity of fundamental studies may be explained by a long period characterized by testing all kinds of nanomedicines in a **trial and error** approach, hoping that sooner or later the formula to success would emerge.<sup>19,20</sup> It must be said however, that a trial and error approach may be valuable, especially when combined with high-throughput screening techniques, but typically these efforts come at the expense of solid attempts to investigate and understand the underlying biological mechanisms. Furthermore, if a formulation works *in vitro*, researchers are usually eager to test it *in vivo* as quickly as possible. If a formulation does not work, the prevailing view is to not waste any more time on the formulation but rather switch to the next candidate. If this line of thinking goes on too long without success, we are setting sail not only towards failure but towards failure without learning from it.

### 3 HOW DO WE PROCEED?

The lack of therapeutic efficiency is a direct consequence of the nanomedicines' inability to overcome the complex series of biological barriers. Site-specific accumulation of nanotherapeutics will remain a distant reality unless nanocarrier design takes into account the numerous biological barriers a nanomedicine encounters upon administration. Therefore, an enhanced understanding of the interaction between nanomedicines and these barriers would continue to enable the development of a new generation of rationally-designed nanocarriers capable of overcoming the many hurdles for efficient delivery of nucleic acids to their molecular target.<sup>21</sup>

#### 3.1 Studying biological barriers to gene therapy

In order to achieve an enhanced understanding, it is of crucial importance to be able to visualize and reliably quantify **nanoparticle-barrier interactions**. Based on this necessity, **Chapter 1** provides an overview of the entire toolbox that is currently available to study a variety of intracellular barriers. We focused on quantitative methods since it is important to know to what extent nanomedicines are able to cross biological barriers. We feel that systematic reviews of methodologies to investigate nanomedicine-barrier interactions are necessary to increase awareness about the ever-expanding toolbox that is at our disposition. In **Chapter 3**, we used one of these assays to study the interaction between JetPEI/pDNA polyplexes and the endosomal barrier by quantifying the number of endosomal escape events. Although there long has been a lack of papers that evaluate the endosomal barrier directly, the recent development of several endosomal escape assay allows researchers nowadays to analyze the interaction between particles and this peculiar barrier.<sup>16,18,22-24</sup>

Besides visualization and quantification, it is equally important to invest in the development of new tools that empower us to gather fundamental information. In line with this view, in **Chapter 4** we aimed at developing light-triggered endosomal escape of pDNA in order to achieve a spatio-temporally controlled system that could be used to perform fundamental investigations regarding the influence of cell division and time and place of endosomal escape on transfection efficiency. Unfortunately however, this approach did not prove to be successful as the transfection potential of the pDNA was completely diminished, likely because of breakdown of the pDNA. If photothermal effects by AuNPs would indeed have a harmful effect on the pDNA, it would be useful in the future to try to find other nanoparticle designs that better protect the pDNA against photothermal damage. One example would be to induce release of electrostatically bound pDNA from a polymer coated-gold core by allowing degradation of the polymer. When the pDNA is successfully released from the gold, laser irradiation

can be applied to induce endosomal escape *e.g. via* VNB formation. Polymers that could be used include pH-responsive polymers that degrade upon acidification of the endosomal compartment or thermo-sensitive polymers that require an initial 'soft' heating step.<sup>25</sup>

Finally, it is also important to take into account that the interaction between nanomedicines and their barriers is highly dependent on the cell type studied. As seen in **Chapter 3**, cellular properties such as endosomal size and membrane leakiness can differ between cell types, causing a substantial difference in the ability of a nanomedicine to overcome the endosomal barrier. This **intercellular variation** is not only manifested at the level of the endosomal barrier, but also applies to other barriers (*e.g.* endosomal uptake and nuclear uptake).<sup>26</sup> With the increased awareness of intercellular variation, researchers started to experiment on primary cells instead of using immortalized cell lines, as these should be more representative to the clinic.<sup>27</sup> To be even more representative to *in vivo* environments, the development of 3D models tries to bridge the *in vitro* – *in vivo* gap by offering a tissue-mimicking environment while still allowing to control experimental conditions and performing analysis with conventional techniques.<sup>28-30</sup> Although this thesis focuses on the gathering of fundamental information on the *in vitro* level, there is also a need to obtain insights into biological mechanisms on all other levels of research. Careful characterization of the delivery barriers on different levels could help us to choose (or develop) the right models in order to correlate the effects observed *in vitro* to the response observed *in vivo*. Furthermore, it could aid to resolve the discrepancy between animal models and humans – a problem that is until now one of the leading responsibilities for failure of many compounds in clinical trials.

### 3.2 Applying fundamental insights to nanomedicine design

Expanding our fundamental knowledge might benefit the nano delivery community in several ways. First of all, an increased understanding could shed new light on previously poorly understood experimental outcomes, thereby even allowing to connect data that initially seemed contradictory. Secondly, fundamental knowledge could be applied to nanomedicine design in order to increase the particle's chance at successfully overcoming the biological barriers. A nice example with regard to the endosomal barrier and the proton sponge hypothesis is provided in this thesis. In **Chapter 2**, we reflected on the conflicting reports that have been published on the proton sponge hypothesis over the years. By including the overlooked factor of endosomal membrane destabilization we provide an important missing piece of the puzzle to more completely understand the proton sponge hypothesis. Next, the proton sponge effect was further investigated on a fundamental level in **Chapter 3**, where we observed that endosomal size and membrane leakiness had a considerable impact on the ability of the proton sponge effect to induce endosomal escape. Since smaller endosomes would need to accumulate less polyplexes to efficiently induce endosomal bursting *via* the proton sponge effect, this fundamental information could be used to incorporate innovative features into the design of nanomedicines. Conceptually, it would be interesting to find ways to introduce polyplexes into small endosomes; or to sequester more polyplexes in fewer endosomes (*e.g.* by controlled aggregation at the cell surface). Another fascinating observation was that endosomal leakiness – the leakage of water and ions from the endosomal lumen to the cytoplasm – could result in the loss of osmotic pressure, thereby abolishing proton sponge-based endosomal rupture. Although we showed the leakage of calcein as a model compound for small molecules, it would be interesting to confirm and quantify this phenomenon further. For instance, it would be intriguing to identify which type of endosomes are most likely to be leaky and to investigate why endosomes in some cells are more resistant to leakiness as compared to others. Since this leakiness is presumed to be the consequence of a combination of osmotic swelling and interaction with cationic polymer chains, one hypothesis could be that a difference in lipid composition between endosomal membranes causes inter- and intracellular differences in endosomal leakiness. An attractive idea would be to design nanomedicines that target specific endosomal pathways that have non-leaky endosomes. Or to come up with complementary strategies to modulate cells so that their endosomes are more resistant to leaking.

### 3.3 The power of reporting negative results

*“Failure is the opportunity to begin again, only this time more intelligently.”* – Henry Ford

Despite their potential, negative results are frequently downgraded to the trash bins as the academic community has developed a culture that supports publication of positive results, thereby leaving ‘failed’ attempts in the dust.<sup>31</sup> However, finding out why a nanoformulation fails is equally valuable as understanding why a nanoformulation is successful, as this failure could be used as a stepping stone towards success.<sup>32</sup> First of all, by thoroughly investigating why a nanoparticle is inefficient, we can gather information on what we can do to change the formulation in order to make it work. In this thesis, we encountered a lack of transfection after administration of nanoparticles both in **Chapter 3** and in **Chapter 4**. By revealing the underlying cause of failure, we were able to gather new insights that could be applied in the future to rationally re-design nanomedicines to increase their chance at success. Secondly, since science is a collaborative discipline, we should report negative findings so our colleagues do not waste their time and resources repeating our findings.<sup>31-33</sup> In order to reduce the publication bias towards positive outcomes, the World Health Organisation (WHO) recently called upon researchers to publish the results of all clinical trials – including negative findings.<sup>34</sup> Furthermore, new journals and initiatives are trying to balance the literature by encouraging to publish negative results.<sup>31-33</sup> It is however important to note that manuscripts covering negative results should be based on well-designed experiments according to the same standards of scientific rigor and excellence. A mere statement that “a certain formulation does not work, but we don’t know why” has little informative value indeed.

## **4 CONCLUSION**

Non-viral vectors still hold great potential for the delivery of gene therapeutics, mainly because of their advantages in terms of safety, packaging of nucleic acids, *etc.* However, in order to become as successful as their viral counterparts, continued efforts will be required to boost their efficiency. The design of nanomedicines for gene therapy should take into account the complex series of biological barriers a particle encounters in order to deliver its cargo to the target. An increased fundamental knowledge of the interaction of nanomedicines with these barriers and of the biology of these barriers should enable the rational design of a new generation of non-viral gene therapeutics, capable of reaching their full potential.

## REFERENCES

- (1) Macpherson, J. L.; Rasko, J. E. J. Clinical Potential of Gene Therapy: Towards Meeting the Demand. *Intern. Med. J.* **2014**, *44*, 224–233.
- (2) Naldini, L. Gene Therapy Returns to Centre Stage. *Nature* **2015**, *526*, 351–360.
- (3) Dunbar, C. E.; High, K. A.; Joung, J. K.; Kohn, D. B.; Ozawa, K.; Sadelain, M. Gene Therapy Comes of Age. *Science (80-. )*. **2018**, 359.
- (4) Das, S. K.; Menezes, M. E.; Bhatia, S.; Wang, X.-Y.; Emdad, L.; Sarkar, D.; Fisher, P. B. Gene Therapies for Cancer: Strategies, Challenges and Successes. *J Cell Physiol* **2015**, *230*, 259–271.
- (5) Verma, I. M.; Somia, N. Gene Therapy - Promises, Problems and Prospects. *Nature* **1997**, *389*, 239–242.
- (6) Caster, J. M.; Patel, A. N.; Zhang, T.; Wang, A. Investigational Nanomedicines in 2016: A Review of Nanotherapeutics Currently Undergoing Clinical Trials. *Wiley Interdiscip. Rev. Nanomedicine Nanobiotechnology* **2017**, *9*.
- (7) Bobo, D.; Robinson, K. J.; Islam, J.; Thurecht, K. J.; Corrie, S. R. Nanoparticle-Based Medicines: A Review of FDA-Approved Materials and Clinical Trials to Date. *Pharm. Res.* **2016**, *33*, 2373–2387.
- (8) Foldvari, M.; Chen, D. W.; Nafissi, N.; Calderon, D.; Narsineni, L.; Rafiee, A. Non-Viral Gene Therapy: Gains and Challenges of Non-Invasive Administration Methods. *J. Control. Release* **2016**, *240*, 165–190.
- (9) Yin, H.; Kanasty, R. L.; Eltoukhy, A. A.; Vegas, A. J.; Dorkin, J. R.; Anderson, D. G. Non-Viral Vectors for Gene-Based Therapy. *Nat. Rev. Genet.* **2014**, *15*, 541–555.
- (10) Hanna, E.; Rémuzat, C.; Auquier, P.; Toumi, M. Gene Therapies Development: Slow Progress and Promising Prospect. *J. Mark. Access Heal. Policy* **2017**, *5*, 1265293.
- (11) Won, Y. Y.; Sharma, R.; Konieczny, S. F. Missing Pieces in Understanding the Intracellular Trafficking of Polycation/DNA Complexes (Journal of Controlled Release (2009) 139: 2 (88-93)). *J. Control. Release* **2009**, *139*, 88–93.
- (12) European Medicines Agency  
[http://www.ema.europa.eu/ema/index.jsp?curl=pages/medicines/landing/epar\\_search.jsp&mid=WC0b01ac058001d124](http://www.ema.europa.eu/ema/index.jsp?curl=pages/medicines/landing/epar_search.jsp&mid=WC0b01ac058001d124) (accessed Apr 25, 2018).
- (13) FDA News Release  
<https://www.fda.gov/NewsEvents/Newsroom/PressAnnouncements/ucm589467.htm> (accessed Apr 25, 2018).
- (14) Hamers, L. Approval of Gene Therapies for Two Blood Cancers Led to An “Explosion of Interest” in 2017. *ScienceNews*. December 2017, p. 29.
- (15) Wilhelm, S.; Tavares, A. J.; Dai, Q.; Ohta, S.; Audet, J.; Dvorak, H. F.; Chan, W. C. W.; Chatterley, A.; Group, W. Analysis of Nanoparticle Delivery to Tumours. *Nat. Rev. Mater.* **2016**, *1*, 1–138.
- (16) Rehman, Z. U.; Hoekstra, D.; Zuhorn, I. S. Mechanism of Polyplex- and Lipoplex-Mediated Delivery of Nucleic Acids: Real-Time Visualization of Transient Membrane Destabilization without Endosomal Lysis. *ACS Nano* **2013**, *7*, 3767–3777.

- (17) Gilleron, J.; Querbes, W.; Zeigerer, A.; Borodovsky, A.; Marsico, G.; Schubert, U.; Manygoats, K.; Seifert, S.; Andree, C.; Stöter, M.; *et al.* Image-Based Analysis of Lipid Nanoparticle-mediated siRNA Delivery, Intracellular Trafficking and Endosomal Escape. *Nat. Biotechnol.* **2013**, *31*, 638–646.
- (18) Wittrup, A.; Ai, A.; Liu, X.; Hamar, P.; Trifonova, R.; Charisse, K.; Manoharan, M.; Kirchhausen, T.; Lieberman, J. Visualizing Lipid-Formulated siRNA Release from Endosomes and Target Gene Knockdown. *Nat. Biotechnol.* **2015**, *33*, 870–876.
- (19) Stewart, M. P.; Lorenz, A.; Dahlman, J.; Sahay, G. Challenges in Carrier-Mediated Intracellular Delivery: Moving beyond Endosomal Barriers. *Wiley Interdiscip. Rev. Nanomedicine Nanobiotechnology* **2016**, *8*, 465–478.
- (20) Nguyen, J.; Szoka, F. C. Nucleic Acid Delivery: The Missing Pieces of the Puzzle? *Acc. Chem. Res.* **2012**, *45*, 1153–1162.
- (21) Blanco, E.; Shen, H.; Ferrari, M. Principles of Nanoparticle Design for Overcoming Biological Barriers to Drug Delivery. *Nat. Biotechnol.* **2015**, *33*, 941–951.
- (22) Lönn, P.; Kacsinta, A. D.; Cui, X.-S.; Hamil, A. S.; Kaulich, M.; Gogoi, K.; Dowdy, S. F. Enhancing Endosomal Escape for Intracellular Delivery of Macromolecular Biologic Therapeutics. *Sci. Rep.* **2016**, *6*, 32301.
- (23) Selby, L. I.; Cortez-Jugo, C. M.; Such, G. K.; Johnston, A. P. R. Nanoescapology: Progress toward Understanding the Endosomal Escape of Polymeric Nanoparticles. *Wiley Interdiscip. Rev. Nanomedicine Nanobiotechnology* **2017**, *9*, 1–23.
- (24) Martens, T. F.; Remaut, K.; Demeester, J.; De Smedt, S. C.; Braeckmans, K. Intracellular Delivery of Nanomaterials: How to Catch Endosomal Escape in the Act. *Nano Today*, **2014**, *9*, 344–364.
- (25) Crucho, C. I. C. Stimuli-Responsive Polymeric Nanoparticles for Nanomedicine. *ChemMedChem* **2015**, *10*, 24–38.
- (26) Voigt, J.; Christensen, J.; Shastri, V. P. Differential Uptake of Nanoparticles by Endothelial Cells through Polyelectrolytes with Affinity for Caveolae. *Proc. Natl. Acad. Sci.* **2014**, *111*, 2942–2947.
- (27) Kaur, G.; Dufour, J. M. Cell Lines: Valuable Tools or Useless Artifacts. *Spermatogenesis* **2012**, *2*, 1–5.
- (28) Alemany-Ribes, M.; Semino, C. E. Bioengineering 3D Environments for Cancer Models. *Adv. Drug Deliv. Rev.* **2014**, *79*, 40–49.
- (29) Bhatia, S. N.; Ingber, D. E. Microfluidic Organs-on-Chips. *Nat. Biotechnol.* **2014**, *32*, 760–772.
- (30) Costa, E. C.; Moreira, A. F.; de Melo-Diogo, D.; Gaspar, V. M.; Carvalho, M. P.; Correia, I. J. 3D Tumor Spheroids: An Overview on the Tools and Techniques Used for Their Analysis. *Biotechnol. Adv.* **2016**, *34*, 1427–1441.
- (31) Goodchild van Hilten, L. Why It's Time to Publish Research "Failures" Publishing Bias Favors Positive Results; Now There's a Movement to Change That. *Elsevier Connect* **2015**, 1–6.
- (32) Weintraub, P. G. The Importance of Publishing Negative Results. *J. Insect Sci.* **2016**, *16*, 109.
- (33) Thompson, J. T. Negative Results Matter: Why Can't We Improve the Treatment

of Proliferative Vitreoretinopathy? *Ophthalmology* **2017**, *124*, 753–754.  
(34) <http://www.who.int/ictrp/results/reporting/en/> (Accessed May 11, 2018)



# Addendum A

## Synthesis and Evaluation of Chitosan-disulfide-conjugated LMW-PEI as a Non-viral Vector for Gene Delivery

**This addendum contains unpublished data**

Lotte M.P. Vermeulen<sup>1,2</sup>, Sangram K. Samal<sup>1,2</sup>, Juan C. Fraire<sup>1,2</sup>, Peter Dubruel<sup>3</sup>, Katrien Remaut<sup>1</sup>, Kevin Braeckmans<sup>1,2</sup>

<sup>1</sup>Lab. General Biochemistry & Physical Pharmacy, Ghent University, Ottergemsesteenweg 460, Ghent, Belgium

<sup>2</sup>Centre for Nano- and Biophotonics, Ghent University, Ottergemsesteenweg 460, Ghent, Belgium

<sup>3</sup>Polymer Chemistry & Biomaterials Group, Ghent University, Ghent, Belgium

## TABLE OF CONTENTS

1	INTRODUCTION .....	181
2	MATERIALS AND METHODS .....	183
2.1	Materials.....	183
2.2	Synthesis of chitosan-disulfide-conjugated LMW-PEI.....	183
2.3	Characterization of chitosan-disulfide-conjugated LMW-PEI .....	184
2.4	Purification of plasmids.....	185
2.5	Preparation of complexes.....	186
2.6	Physicochemical characterization of complexes .....	186
2.7	Cell culture.....	186
2.8	Evaluation of transfection efficiency .....	186
2.9	Flow cytometry .....	187
2.10	Cytotoxicity studies .....	187
3	RESULTS.....	188
3.1	Synthesis and characterization of chitosan-disulfide-conjugated LMW-PEI .....	188
3.2	Characterization of pDNA/chitosan-S-S-PEI complexes .....	192
3.3	Transfection efficiency of pDNA/chitosan-S-S-PEI complexes in HeLa cells .....	193
3.4	Cytotoxicity of pDNA/chitosan-S-S-PEI complexes.....	194
4	DISCUSSION .....	196
5	CONCLUSION .....	198

## 1 INTRODUCTION

As mentioned in **Chapter 1**, the development of safe and effective gene carriers has proven to be quite difficult.<sup>1,2</sup> Among the non-viral vectors, polyethylenimine (PEI) is considered the gold standard. Due to its proton sponge effect, which was discussed elaborately in **Chapter 2**, PEI displays good transfection efficiency in a variety of cells. However, its toxicity, mainly induced by its cationic nature and non-biodegradability, severely limits its use in clinical applications.<sup>3,4</sup> Reducing the intrinsic cellular toxicity of PEI has been an important research topic in the last years. A first strategy is to combine PEI with a more biocompatible polymer, such as chitosan that has been widely investigated because of its biocompatibility and low cytotoxicity. However, the main drawback of chitosan is that it is unable to provide efficient transfection.<sup>5,6</sup> Hence, combining PEI and chitosan into a copolymer has proven to be a valuable strategy to increase transfection efficiency compared to chitosan, while decreasing the cytotoxicity attributed to PEI.<sup>7,8</sup> A second strategy to reduce the toxicity of PEI consists in the conversion of low molecular weight (LMW) PEI into high molecular weight (HMW) PEI through the use of biodegradable linkers. In this way, the transfection efficiency is preserved (property of HMW PEI) while cellular toxicity decreases (property of LMW PEI).<sup>9-11</sup> Different approaches have been proposed to establish intracellular (IC) degradation of cationic polymers. Among them, pH and redox potential are the most commonly investigated triggers.<sup>12</sup> The benefit of redox potential over pH is that the breakdown of the polymer is induced only when the polyplex reaches a reductive environment, such as the cytosol or the nucleus. Therefore, release of the cargo can only be triggered after endosomal escape; whereas pH-triggered release could already occur inside the acidifying endosome, rendering the cargo more susceptible to degradation.<sup>9</sup> An often used reduction sensitive bond is the disulfide bond. Within the reductive IC environment, a high concentration of glutathione is present which is able to cleave the disulfide bond, thereby degrading the polymer.<sup>13</sup> IC biodegradability should not only lower the polymer's toxicity, it could also facilitate pDNA dissociation, potentially rendering the polymer even more effective.<sup>14</sup>

As briefly mentioned in **Chapter 3**, in the very beginning of this PhD project we tried to synthesize chitosan-disulfide-conjugated LMW-PEI. Although the outcome was not as expected, in this Addendum we report on the synthesis and characterization of this copolymer. Chitosan-disulfide-conjugated LMW-PEI was prepared *via* combining two commonly used strategies: copolymerization of PEI with biocompatible chitosan and the introduction of disulfide bonds that will allow IC degradation of the copolymer. This way, we wanted to create a polymer that is as efficient as PEI, but shows less cellular toxicity. First, chitosan and PEI were thiolated separately by the addition of 2-

iminothiolane. Afterwards, the thiolated polymers were left to form disulfide linkages in the presence of oxygen. Using this disulfide-conjugated copolymer, polyplexes were prepared through electrostatic interaction between the copolymers and the pDNA. Finally, transfection efficiency and toxicity were evaluated in HeLa cells as a reference cell line.

## 2 MATERIALS AND METHODS

### 2.1 Materials

DMEM/F-12, L-Glutamine, Penicillin-Streptomycin solution (5000 IU/ml penicillin and 5000 µg/ml streptomycin) (P/S), Fetal Bovine Serum (FBS), OptiMEM, Dulbecco's phosphate-buffered saline 1x without Ca<sup>2+</sup> and Mg<sup>2+</sup> (DPBS-), Trypan Blue and 0.25% Trypsin-EDTA were purchased from GibcoBRL (Merelbeke, Belgium). YOYO-1 iodide was supplied by Molecular Probes (Erembodegem, Belgium). Na<sub>2</sub>HPO<sub>4</sub>, NaH<sub>2</sub>PO<sub>4</sub> and EDTA were purchased from Merck (Darmstadt, Germany). Other reagents were obtained from Sigma-Aldrich (Bornem, Belgium) unless otherwise specified.

### 2.2 Synthesis of chitosan-disulfide-conjugated LMW-PEI

**Thiolated chitosan** | 1000 mg of chitosan LMW (50 – 190 kDa; 75-85% deacetylated) was dissolved in 100 ml 1% acetic acid on a magnetic stirrer. Next, the pH of the solution was adjusted to 6.5 using 0.5 M NaOH and the solution was flushed for 1 h with nitrogen. 30 min after the addition of 100 mg 2-iminothiolane, the pH was increased to pH 7 using 0.5 M NaOH. Chitosan was left to react with 2-iminothiolane for 24 h on a magnetic stirrer under nitrogen atmosphere. The resultant chitosan-SH solution was then purified by dialysis (MW cutoff 500-1000 Da) to remove unreacted 2-iminothiolane. Dialysis medium was 5 mM HCl for the first day, which was decreased to 2 mM on the second day and eventually replaced by deionized water on the third day. A portion of this solution (needed for characterization of chitosan-SH) was flushed with nitrogen, put in the freezer overnight and freeze-dried (LyoBeta 25™ Telstar, Terrassa, Spain) for 36-48 h. The freeze-dried polymers were kept at -20°C.

**Thiolated PEI** | bPEI (1.8 kDa; 50wt%) was dissolved in DPBS- to make PEI<sub>1</sub> (2% v/v) and PEI<sub>2</sub> (10% v/v). Both solutions were flushed for 1 h with nitrogen before addition of 2-iminothiolane (11 mg per 50 ml PEI<sub>1</sub> and 55 mg per 50 ml PEI<sub>2</sub>). PEI was left to react with 2-iminothiolane for 24 h on a magnetic stirrer under nitrogen atmosphere. The PEI-SH solutions were purified by dialysis (MW cutoff 100-500 Da) against deionized water for 3 days to remove unreacted 2-iminothiolane. A portion of this solution (needed for characterization of the PEI-SH) was flushed with nitrogen, put in the freezer overnight and freeze-dried for 36-48 h. The freeze-dried polymers were kept at -20°C.

**Chitosan-disulfide-conjugated LMW-PEI** | Chitosan-disulfide-conjugated LMW-PEI (Chitosan-S-S-PEI) was prepared by oxidation of thiols on PEI and chitosan to form a disulfide linkage. Copolymers were prepared by adding PEI-SH to chitosan-SH in appropriate volumes. Three different copolymer solutions were prepared,

according to **Table I**. The solutions are left to react for 24 h in the presence of oxygen. Next, dialysis (MW cutoff 10 000 Da) was performed for 24 h against deionized water in order to remove unreacted PEI-SH. Finally, copolymer solutions were freeze-dried and kept at -20°C.

**Table I Composition of prepared copolymers**

<b>Copolymers</b>	<i>Chitosan-SH (ml)</i>	<i>PEI<sub>1</sub>-SH (ml)</i>	<i>PEI<sub>2</sub>-SH (ml)</i>
<b>1</b> <i>Chitosan-S-S-PEI<sub>1</sub> 1:1</i>	30	30	-
<b>2</b> <i>Chitosan-S-S-PEI<sub>2</sub> 1:1</i>	30	-	30
<b>3</b> <i>Chitosan-S-S-PEI<sub>2</sub> 0.5:1</i>	15	-	30

## 2.3 Characterization of chitosan-disulfide-conjugated LMW-PEI

### **Nuclear Magnetic Resonance (NMR)**

Proton Nuclear Magnetic Resonance (<sup>1</sup>H NMR) was used to evaluate the chemical composition of thiolated polymers and copolymers. 10 mg PEI<sub>1</sub>-SH, PEI<sub>2</sub>-SH, Chit-S-S-PEI<sub>1</sub> 1:1, Chit-S-S-PEI<sub>2</sub> 1:1 and Chit-S-S-PEI<sub>2</sub> 0.5:1 was dissolved in 1 ml D<sub>2</sub>O (Arcos, Geel, Belgium). PEI (1.8 kDa; 50wt%) was dried to remove water before 10 mg of dry PEI was dissolved in 1 ml D<sub>2</sub>O. 10 mg chitosan LMW and chitosan-SH was dissolved in 1 ml 1% DCI (Acros, Geel, Belgium). All samples were measured using a Varian Mercury 300 spectrometer (Palo Alto, CA, USA) at 25°C and a spin of 20 Hz. Data were processed using ACD/Spectrum software. Chemical shifts are given in parts per million (δ), relative to the residual solvent signals, in the case of deuterated water: δ = 4.79 for <sup>1</sup>H.

### **Infrared (IR) Spectroscopy**

IR spectroscopy was also used to examine the thiolation and copolymerization of the polymers. To this end, samples were measured on a Nicolet iS50 spectrometer (ThermoScientific, The Netherlands) equipped with a Specas Golden Gate Diamond ATR (Specac, Orpington, UK). For every sample, 32 scans were measured at a resolution of 4 cm<sup>-1</sup>.

### **Ellman's Assay**

Ellman's Assay was used to estimate the thiol content of the polymers by comparing experimental samples to a standard curve of thiol-containing compounds (e.g. cysteine). Standard solutions were prepared as described in **Table II** in order to generate this standard curve. Reaction buffer was a 0.1 M sodium phosphate buffer at pH 8 that contained 1 mM EDTA. Next, test solutions of the thiolated polymers and the

copolymers were prepared in deionized water in a concentration of 10 mg/ml. Ellman's reagent solution was prepared by dissolving 4 mg of Ellman's reagent (5,5-dithio-bis-(2-nitrobenzoic acid)); DTNB; Thermo Fisher Scientific, Rockford, IL, USA) in 1 ml of reaction buffer. Preparation of the samples was carried out as follows: 2.5 ml reaction buffer and 50  $\mu$ l of Ellman's reagent solution was added to 250  $\mu$ l of test- or standard solution. The samples were mixed and incubated for 15 min at room temperature. Finally, the absorbance of the samples was measured at 412 nm using the Nanodrop 2000c. The values, obtained from the standard solutions, were used to generate a standard curve. From this curve, experimental sample concentrations were determined.

**Table II Preparation of standard solutions in Ellman's assay.**

<i>Standard</i>	<i>Reaction buffer (ml)</i>	<i>Amount of Cysteine</i>	<i>Final concentration</i>
<i>A</i>	100	26.34 mg	1.50 mM
<i>B</i>	5	25 ml of Standard A	1.25 mM
<i>C</i>	10	20 ml of Standard A	1.00 mM
<i>D</i>	15	15 ml of Standard A	0.75 mM
<i>E</i>	20	10 ml of Standard A	0.50 mM
<i>F</i>	25	5 ml of Standard A	0.25 mM
<i>G</i>	30	0 ml	0 mM (Blank)

### **Buffer capacity**

The buffer capacity of the copolymers was measured by acid-base titration with HCl. PEI was used as a reference compound. Polymers were dissolved in 10 ml 150 mM NaCl solution to a concentration of 1 mg/ml and pH was brought to 11 with 0.1 M NaOH as starting point. Solutions were titrated with 0.1 M HCl in steps of 20  $\mu$ l until they reached pH 3. Solutions were placed on a magnetic stirrer and pH was measured using a pH meter (Consort C831, Belgium). As a blank, titration of a 150 mM NaCl solution was performed.

## **2.4 Purification of plasmids**

gWIZ GFP (Promega, Leiden, The Netherlands) was amplified in transformed E. Coli bacteria and isolated from the bacteria suspension with a Qiafilter Plasmid Giga Kit (Qiagen, Venlo, The Netherlands). Using UV absorption at 260 and 280 nm, concentration and purity of the pDNA was determined on a NanoDrop 2000c (Thermo Fischer Scientific, Rockford, IL, USA). Finally, the plasmids were suspended at a concentration of 1  $\mu$ g/ $\mu$ l with HEPES buffer (20 mM, pH 7.2) and stored at -20°C.

## **2.5 Preparation of complexes**

Using the three synthesized copolymers, complexes with pDNA were prepared. Chitosan-S-S-PEI/pDNA complexes were obtained by mixing the copolymer solution with an equal volume of pDNA solution in a given w/w ratio. Next, the mixture was vortexed for 10 s at 2200 rpm and polyplexes were allowed to stabilize for 15 min at room temperature before final dilution with HEPES buffer (20 mM, pH 7.2).

## **2.6 Physicochemical characterization of complexes**

In order to examine the complexation of pDNA to the copolymers, copolymer/pDNA complexes were tested with gel electrophoresis. A 1% agarose gel was prepared by dissolving 1 g of agarose (UltraPure Agarose, Invitrogen, Erembodegem, Belgium) in 100 ml of 1 x Tris/Borate/EDTA (TBE) buffer. Next, 4  $\mu$ l GelRed (Biotium, Hayward, CA) was added to detect the pDNA. To all the samples, 5  $\mu$ l of Gel Loading Buffer (Ambion, Merelbeke, Belgium) was added and a total volume of 25  $\mu$ l was pipetted per lane. A 1 kb ladder (Bioron GmbH, Ludwigshafen, Germany) and uncomplexed pDNA were taken along in the run as controls. Gel electrophoresis was performed for 30 min at 100 V. A Kodak digital science camera (Kodak EDAS 120, Rochester, NY) was used to image the gel under UV light (Bio-Rad UV transilluminator 2000, California, USA).

To evaluate the hydrodynamic size, polydispersity index and zeta potential of the complexes, polyplexes were prepared as described above and transferred to disposable folded capillary cells (Malvern, Worcestershire, UK). Dynamic Light Scattering measurements were performed using the NanoZS Zetasizer (Malvern Instruments, Hoeilaart, Belgium).

## **2.7 Cell culture**

HeLa cells (cervical adenocarcinoma cells, ATCC CCL-2) were cultured in Dulbecco's modified Eagle's medium supplemented with growth factor F12 (DMEM/F-12) and enriched with 10% FBS, 2 mM L-Glutamine and 100  $\mu$ g/ml P/S. Cells were cultured in a humidified atmosphere at 37°C and 5% CO<sub>2</sub>. Experiments were performed on cells with a passage number below 25.

## **2.8 Evaluation of transfection efficiency**

HeLa cells were seeded in 24 well plates at 50 000 cells per well and allowed to attach overnight. The next day, copolymer complexes containing gWIZ GFP were prepared as described above. Cells were incubated with complexes in Opti-MEM for 2 or 24 h after which they are washed and cultured to a total time of 24 or 48 h. A

negative control using pGL4.13 with Lipofectamine 2000 (Invitrogen, CA, USA) and a positive control (JetPEI/gWIZ GFP NP 6, prepared as described in **Chapter 3**) were implemented. Expression of GFP was examined using flow cytometry.

## **2.9 Flow cytometry**

To perform analysis by flow cytometry, cells were detached using trypsin and transferred to flow cytometry tubes (BD Falcon, Radnor, USA). Next, the cell suspensions were centrifuged at 300 g for 5 min (Bio-Rad DiaCent-12, DieMed GmbH, Cressier, Switzerland) and resuspended in flow buffer (DPBS-, 0.1% Sodium Azide, 1% Bovine Serum Albumine). Finally, samples were vortexed at 2200 rpm (YellowLine TTS2, IKA works, Wilmington, USA) and kept on ice. Flow cytometry was performed on 10 000 events per sample (FACS Calibur, BD Biosciences, Erembodegem, Belgium) and green fluorescence was measured (488 nm excitation with Argon laser and detection with 530/30 nm bandpass filter). FlowJo software (Treestar Inc, Ashland, USA) was used to perform the analysis.

## **2.10 Cytotoxicity studies**

HeLa cells were seeded in 24 well plates at 50 000 cells per well and were allowed to attach overnight. The next day, complexes with copolymers were prepared containing gWIZ GFP, as described above. Cells were incubated with the complexes for 2 h at 37°C in Opti-MEM before addition of 3-(4,5-dimethyl-2-tiazolyl)-2,5-diphenyl-2H-tetrazolium bromide (MTT) solution (1 mg/ml in DPBS-). After 3 h incubation at 37°C, the solution was removed and the newly formed purple formazan was dissolved by adding DMSO. Next, the plates were covered in aluminum foil and placed on an orbital shaker (Rotamax 120, Heidolph, Germany) for 45 min at 1200 rpm. As a negative control, the metabolic activity of cells that did not receive complexes was stopped using 4 % paraformaldehyde. Finally, UV absorbance was measured on a plate reader (Wallac Envision, Finland) at 590 nm to measure metabolic activity and at 690 nm to measure the background.

### 3 RESULTS

#### 3.1 Synthesis and characterization of chitosan-disulfide-conjugated LMW-PEI

In chitosan-disulfide-conjugated LMW-PEI, chitosan and PEI (structures shown in **Figure I**) are coupled *via* a disulfide bond. In order to be able to form this bond, the individual polymers should be thiolated. Thiolation of chitosan (to form chitosan-SH) and PEI (to form PEI-SH) was performed by the addition of 2-iminothiolane, as described before. In short, 2-iminothiolane was used to react with the primary amines of chitosan and PEI in order to yield a thiol group and an amidine moiety. By converting primary amines into amidines, the possibility to create positive charges in the copolymer was maintained.<sup>9,15</sup> Next, the reduced free thiol-containing chitosan and LMW PEI underwent oxidation at room temperature in the presence of oxygen in order to form a disulfide bond, as depicted in **Figure II**. Different copolymers were prepared by varying the ratio of chitosan to LMW-PEI.

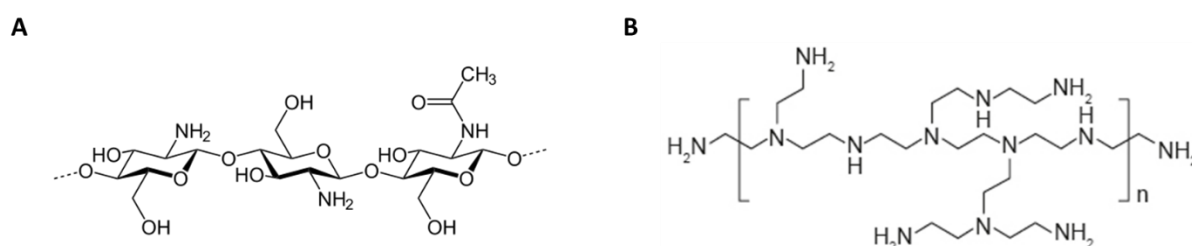


**Figure I** Chemical structures of (A) chitosan and (B) branched PEI

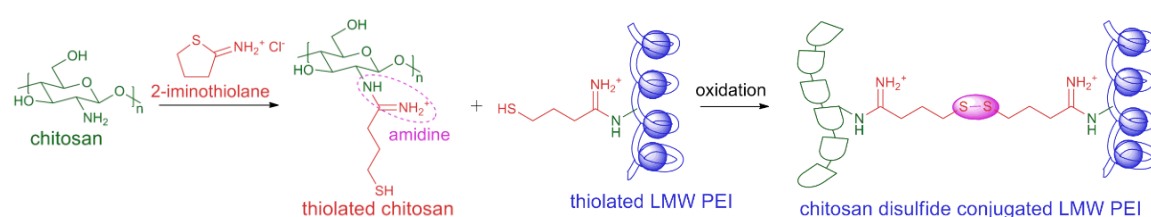


**Figure II** Strategy for the synthesis of chitosan-disulfide-conjugated LMW-PEI. Chitosan and PEI are thiolated by the addition of 2-iminothiolane and afterwards left to oxidize to form disulfide bonds, rendering chitosan-disulfide-conjugated LMW-PEI.

The molecular structure of thiolated polymers and chitosan-disulfide-conjugated LMW-PEI copolymers was first characterized by ATR-FTIR spectroscopy. Chitosan FTIR spectrum (**Figure III A**) showed a strong band in the region of  $3320\text{ cm}^{-1}$  attributed to NH and OH stretching and a peak at  $2870\text{ cm}^{-1}$  resulting from aliphatic CH stretching. The band at  $1640\text{ cm}^{-1}$  was attributed to C=O stretching vibration (amide I), the one at  $1590\text{ cm}^{-1}$  to NH bending (amide II) and the sharp peak

at  $1375\text{ cm}^{-1}$  to  $\text{CH}_3$  deformations (amide III). The bands at  $1060\text{ cm}^{-1}$  and at  $1025\text{ cm}^{-1}$  correspond to C-O stretching vibration. These bands, together with the band at  $1150\text{ cm}^{-1}$  corresponding to the asymmetric stretching of the C-O-C bridge were characteristics of chitosan's saccharide structure.<sup>16-18</sup>

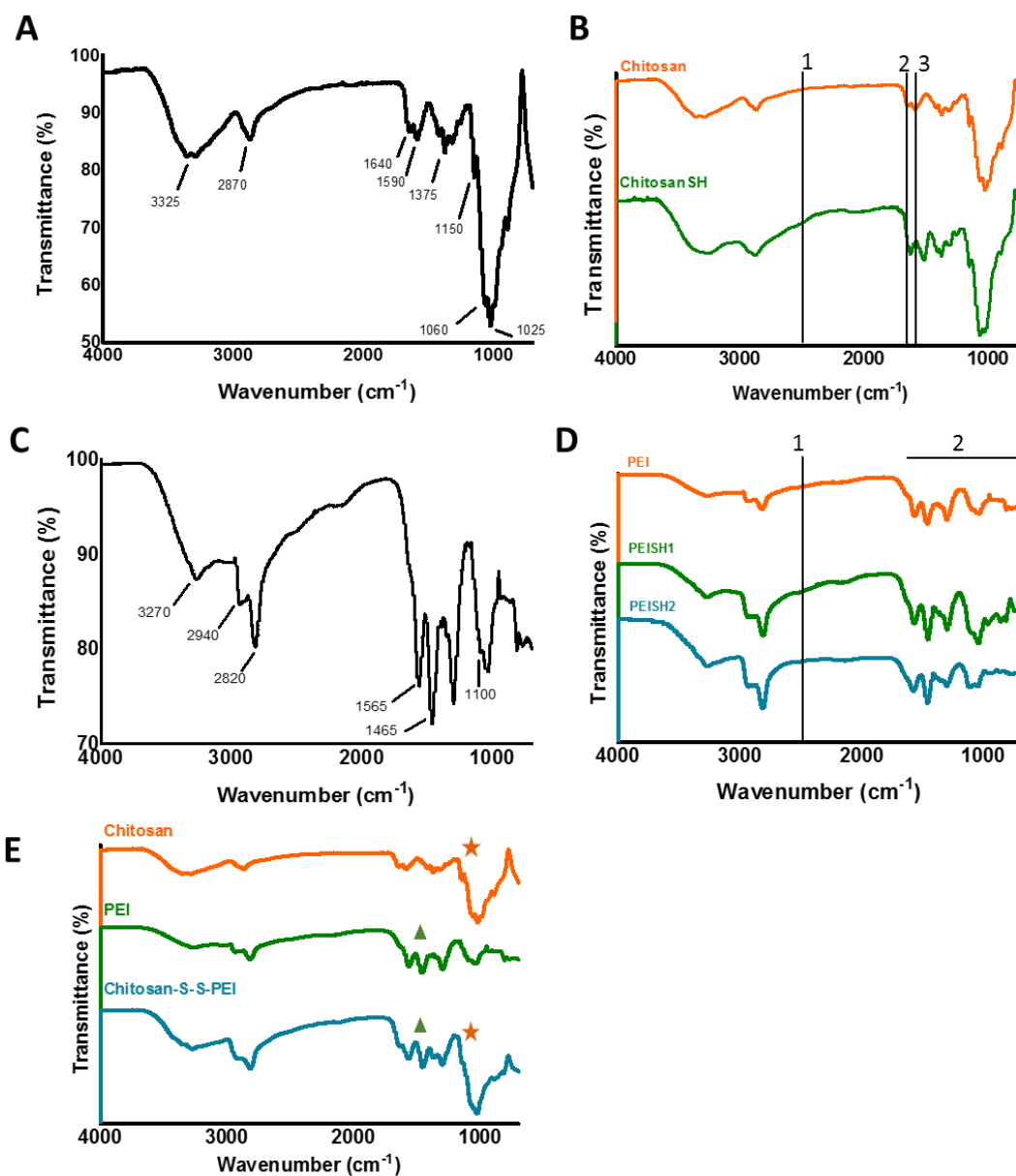


**Figure III Fourier Transform Infrared (FTIR) characterization of polymers, thiolated polymers and copolymers.** (A) FTIR spectrum of chitosan polymer. Wavenumbers (in  $\text{cm}^{-1}$ ) are provided of the characteristic bands. (B) FTIR spectrum of thiolated chitosan (ChitosanSH) compared to reference spectrum of chitosan. Differences due to thiolation are indicated with vertical lines where line 1 indicates the formation of a shoulder around  $2470\text{ cm}^{-1}$ , line 2 the shift in amide I band from  $1640$  to  $1625\text{ cm}^{-1}$  and line 3 the shift in amide II band from  $1590$  to  $1520\text{ cm}^{-1}$ . (C) FTIR spectrum of PEI polymer. Wavenumbers (in  $\text{cm}^{-1}$ ) are shown to indicate the characteristic bands. (D) Spectra of thiolated PEIs vs reference spectrum (PEI). Differences due to thiolation are situated at line 1, where there is a small increase in the shoulder at  $2490\text{ cm}^{-1}$  and small changes in the fingerprint region of PEI (2). (E) FTIR spectrum of chitosan-S-S-PEI<sub>2</sub> 1:1 was compared to the reference spectra of chitosan and PEI. The spectrum of chitosan-

S-S-PEI<sub>2</sub> 1:1 is representative for the spectra of all copolymers prepared and clearly indicated the involvement of bands that are related to the structure of PEI ( $\Delta$ ) as well as to the structure of chitosan (\*).

Thiolation of chitosan (**Figure III B**) shifted the amide I band from 1644  $\text{cm}^{-1}$  to 1625  $\text{cm}^{-1}$  and the amide II band from 1590  $\text{cm}^{-1}$  to 1520  $\text{cm}^{-1}$ , confirming the conjugation of 2-iminothiolane on the polymer backbone. Indeed, amidine stretching bands are typically observed between 1685-1580  $\text{cm}^{-1}$  and 1540-1515  $\text{cm}^{-1}$ .<sup>19</sup> Furthermore, a small shoulder appeared around 2470  $\text{cm}^{-1}$  which is attributed to SH vibrations.<sup>20,21</sup> The FTIR spectrum of PEI (**Figure III C**) shows following characteristic bands: a band at 3270  $\text{cm}^{-1}$  attributed to NH stretch vibration and bands at 2940  $\text{cm}^{-1}$  and 2820  $\text{cm}^{-1}$  resulting from asymmetrical and symmetrical vibration of CH<sub>2</sub> respectively. The peak at 1465  $\text{cm}^{-1}$  corresponds to CH<sub>2</sub> bending. The band at 1565  $\text{cm}^{-1}$  corresponds to N-H bend vibration and C-N stretch vibration can be seen in the band at 1100  $\text{cm}^{-1}$ .<sup>22</sup> Thiolation of PEI (**Figure III D**) was more difficult to confirm. Only small changes in the fingerprint region of PEI and a small increase in the shoulder around 2490  $\text{cm}^{-1}$  were observed, which points to the addition of SH-containing moieties to the PEI structure.<sup>12</sup> The FTIR spectrum of the copolymer is shown in **Figure III E** and clearly shows bands that are related to the structure of PEI (indicated with triangle) combined with bands that are related to the saccharide structure of chitosan (indicated with star), thereby confirming successful copolymerization.

<sup>1</sup>H NMR was also used to confirm copolymerization. In the <sup>1</sup>H NMR spectrum of chitosan, represented in **Figure IV A**, peaks that confirm the presence of a glucosamide moiety were observed at  $\delta=4.59$ ,  $\delta=3.00$  and  $\delta=3.50-3.80$ . Finally, the acetyl protons cause a peak at  $\delta=1.87$ .<sup>23,24</sup> PEI showed three characteristic peaks from the methylene protons in PEI centered at  $\delta=2.53$ ,  $\delta=2.60$  and  $\delta=2.67$ , as can be seen in **Figure IV B**.<sup>9,25</sup> The spectrum of the copolymer is shown in **Figure IV C** and displays peaks in the 2-3 ppm region, which can be attributed to the protons in PEI, and in the 3-4 ppm region, which can be ascribed to the protons in chitosan. Furthermore, the appearance of a new peak around 1.8 ppm could indicate the presence of thiolated structures.<sup>19</sup>

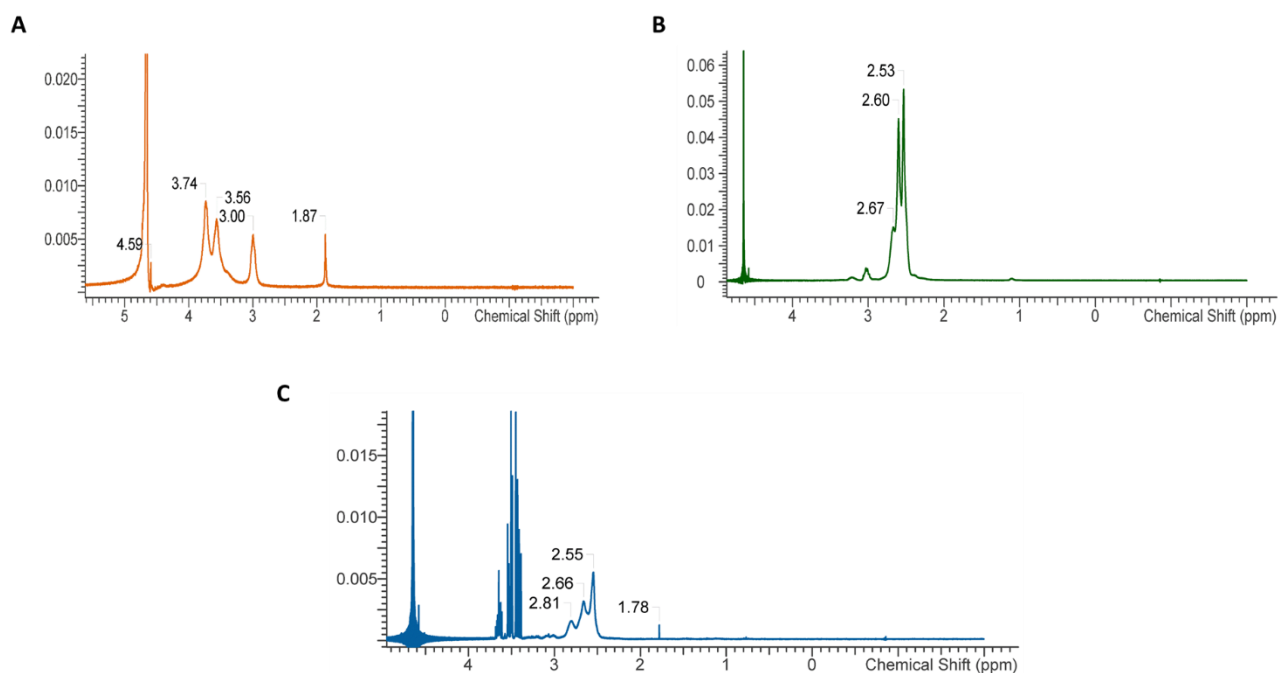


**Figure IV <sup>1</sup>H NMR spectra of polymers and copolymer.** (A) <sup>1</sup>H NMR spectrum of chitosan shows characteristic peaks that confirm the presence of a glucosamide moiety. (B) <sup>1</sup>H NMR spectrum of PEI displays the characteristic peaks between 2-3 ppm. (C) <sup>1</sup>H NMR spectrum of chitosan-S-S-PEI<sub>2</sub> 1:1 is shown and is representative for the spectra of all copolymers. The copolymer spectrum shows peaks that indicate the presence of both PEI (2-3 ppm) and chitosan (3-4 ppm).

Next, the thiol content of thiolated polymers and copolymers was measured using Ellman's assay. In this assay, Ellman's reagent is allowed to react with free sulfhydryl groups to yield a mixed disulfide and 2-nitro-5-thiobenzoic acid (TNB), a yellow-colored product that allows spectrophotometric detection at 412 nm. First, a standard curve was generated using known concentrations of cysteine, a thiol-containing compound. Next, the absorbance of experimental samples was measured and the concentration of thiol groups was determined based on the generated standard curve. **Figure V A** shows the standard curve with interpolated sample values. Thiolated chitosan, thiolated PEI<sub>1</sub> and thiolated PEI<sub>2</sub> show a free thiol concentration of 0.301, 1.014 and 1.027 mM respectively. The copolymers show a free thiol concentration of 0.166, 0.240 and 0.272 mM for chitosan-S-S-PEI<sub>1</sub> 1:1, chitosan-S-S-PEI<sub>2</sub> 1:1 and chitosan-S-S-PEI<sub>2</sub> 0.5:1 respectively. The reduced thiol content in the copolymers indicated that free thiols of the thiolated polymers were used to form disulfide bonds.

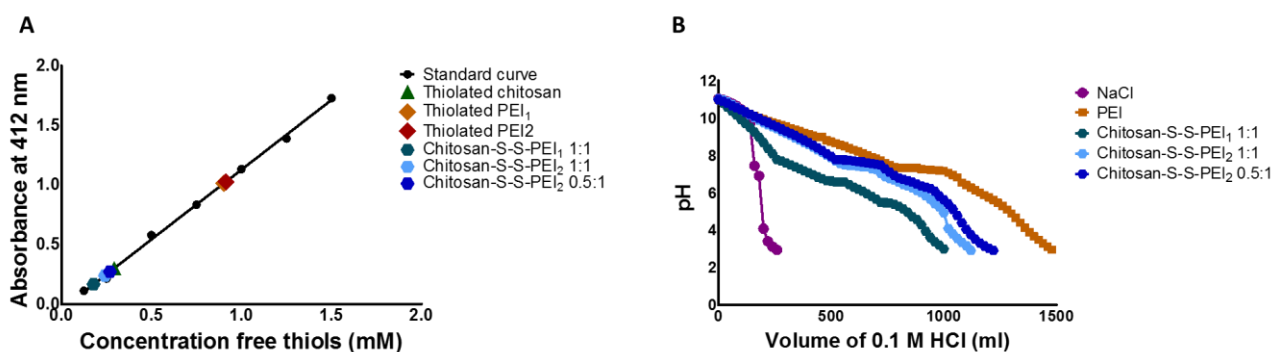


**Figure V (A)** Concentration of free thiols (mM) measured *via* spectrophotometry after reaction with Ellman's reagent. Black dots (measurements) and black line (linear regression) represent the standard solutions. Experimental samples were interpolated to this standard curve. **(B)** The buffer capacity of the copolymers was estimated upon titration with 0.1 M HCl and compared to the buffer capacity of PEI as a reference polymer and NaCl 150 mM as a blank.

Finally, the buffering effect of the chitosan-S-S-PEI copolymers was measured since this is assumed to facilitate endosomal escape through the proton sponge effect, as explained in **Chapter 2**. The buffer capacity of the copolymers should span from pH 5 to 7.4, the pH range from extracellular environment to the lower pH values of lysosomes. The buffering capacity of the copolymers was measured by acid-base titration with 0.1 M HCl after increasing the initial pH to 11 with NaOH (**Figure V B**). Since PEI is well-known for its proton sponge effect, a solution of 1 mg/ml PEI was used as a reference. Results showed that the buffer capacity increased when the portion of PEI incorporated in the copolymer increased.

### 3.2 Characterization of pDNA/chitosan-S-S-PEI complexes

A prerequisite for efficient gene delivery is the condensation of pDNA into nano-sized complexes. Chitosan-S-S-PEI/pDNA complexes were prepared in different weight ratios, as explained in section 2.5. Gel electrophoresis was performed to examine if pDNA was retained in the complexes. **Figure VI A** shows that starting from a weight ratio (pDNA:copolymer) of 1:1.6, 1:0.92 and 1:0.92 the pDNA was efficiently complexed inside chitosan-S-S-PEI<sub>1</sub> 1:1, chitosan-S-S-PEI<sub>2</sub> 1:1 and chitosan-S-S-PEI<sub>2</sub> 0.5:1 respectively. Next, hydrodynamic diameter, polydispersity index (PdI) and zeta potential were measured *via* dynamic light scattering. Results are displayed in **Figure VI B** and indicated that these initial w:w ratios caused massive aggregation. An increase in copolymer fraction was needed to obtain an acceptable size and zeta potential. Stable complexes were measured at w:w ratio of 1:2.6 for chitosan-S-S-PEI<sub>1</sub> 1:1, 1:1.6 for chitosan-S-S-PEI<sub>2</sub> 1:1 and 1:1.4 for chitosan-S-S-PEI<sub>2</sub> 0.5:1. The copolymers illustrate a stronger pDNA-binding ability with the increment of PEI portion.

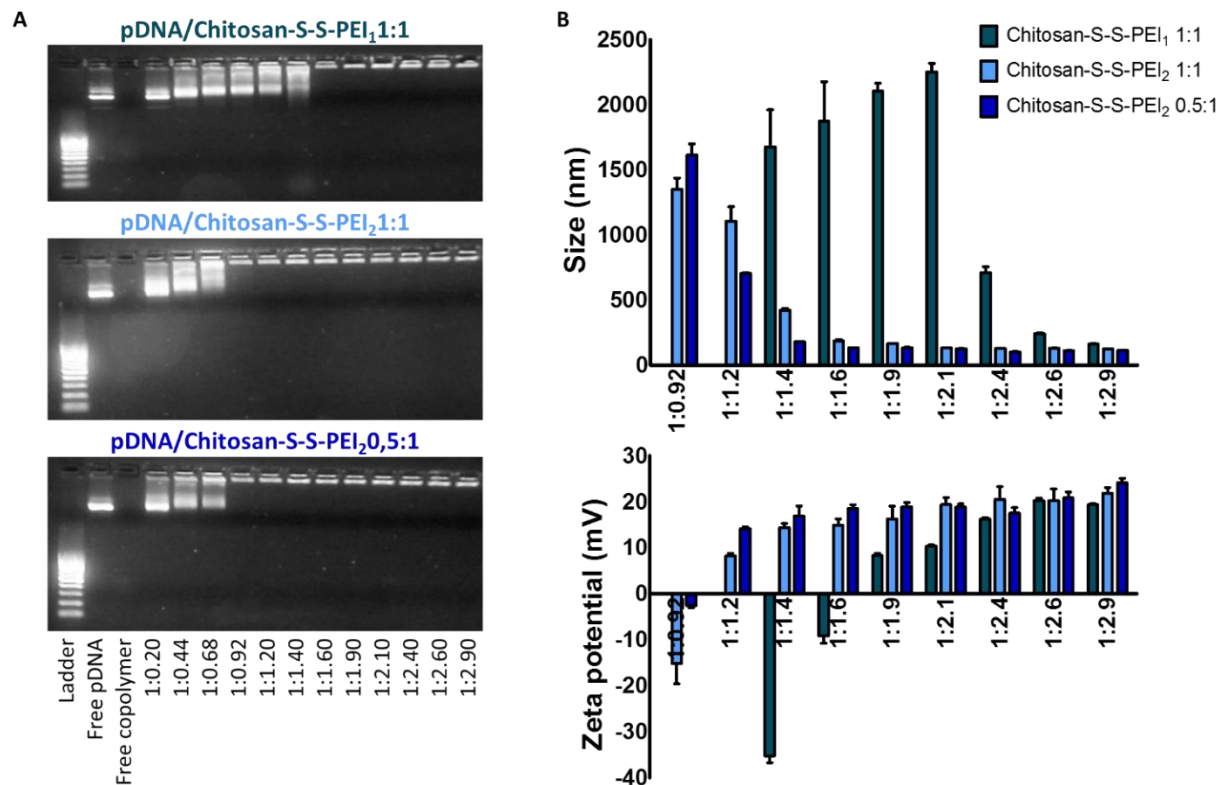


**Figure VI Characterization of pDNA/copolymer complexes. (A)** Gel electrophoresis shows successful complexation of pDNA starting from a ratio of 1:1.60 for chitosan-S-S-PEI<sub>1</sub> 1:1 and a ratio of 1:0.92 for both chitosan-S-S-PEI<sub>2</sub> 1:1 and chitosan-S-S-PEI<sub>2</sub> 0.5:1. **(B)** Dynamic light scattering measurements were performed to measure the size (in nm) and the zeta potential (in mV) of the prepared complexes. Graph shows mean  $\pm$  SD for three technical replicates.

### 3.3 Transfection efficiency of pDNA/chitosan-S-S-PEI complexes in HeLa cells

Gene transfer efficiency of pDNA/copolymer complexes was investigated in HeLa cells using the reporter gene GFP. Transfection efficiency was quantified *via* flow cytometry and the percentage of transfected cells is displayed in **Figure VII**. HeLa cells were first incubated with pDNA/copolymer complexes in w/w ratios that formed positively charged nanoparticles that retained pDNA. After an incubation of 2 h, transfection efficiency was determined at 24 h. These complexes did not exhibit transfection efficiency that was significantly higher than the negative control, as can be seen in **Figure VII A**. Therefore, the w/w ratio of the complexes was further increased to 1:10, 1:20 and 1:50. Complexes remained incubated for 2 h but transfection efficiency was now determined after 48 h (**Figure VII B**). Although a slight increase was achieved, transfection efficiencies still remained very low with less than 2.5% transfected cells for the highest w/w ratios. As a next strategy, copolymer solutions were brought to pH 5-6 in order to obtain complete dissolution of the copolymers. Afterwards, solutions were diluted with PBS- before complexation with

pDNA. These complexes were incubated for 24 h and transfection efficiency, determined after 48 h, is displayed in **Figure VII C**. An important raise in efficiency was observed, especially with chitosan-S-S-PEI<sub>2</sub> 0.5:1, which reached as high as 40% transfected cells in a w/w ratio of 1:50. Nevertheless, the purpose to reach comparable transfection efficiency as PEI ( $\pm$  80%) was clearly not achieved.

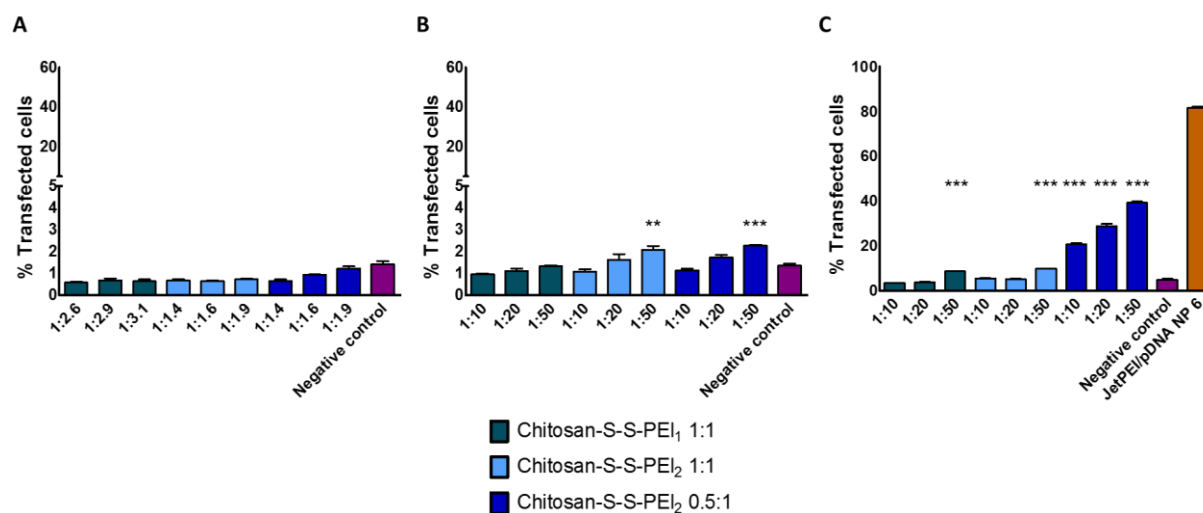


**Figure VII Transfection efficiency of pDNA/chitosan-S-S-PEI complexes in HeLa cells.** (A) Graph shows percentage transfected cells after incubation with pDNA/copolymer complexes for 2 h followed by incubation with full medium for 22 h. (B) Graph shows percentage transfected cells after incubation with pDNA/copolymer complexes for 2 h followed by incubation with full medium for 46 h. (C) Copolymer solutions were brought to pH 5-6 with 1 M HCl in order to achieve complete dissolution before formation of the complexes. Graph shows percentage transfected cells after incubation with pDNA/copolymer complexes for 24 h followed by incubation with full medium for 24 h. All graphs show mean  $\pm$  SEM for 3 technical replicates and significance was calculated *via* one-way ANOVA with Dunnett’s post-test (compare samples to negative control) (\*\*\*)  $p < 0.0001$ ; \*\*  $p < 0.01$ ; \*  $p < 0.05$ ).

### 3.4 Cytotoxicity of pDNA/chitosan-S-S-PEI complexes

The cytotoxicity of chitosan-S-S-PEI/pDNA complexes on HeLa cells was determined *via* an MTT assay. Only the cellular toxicity of complexes that were used in **Figure VII C** was measured since it was the only transfection experiment where considerable efficiency was reached. Cytotoxicity was measured after 24 h of incubation on HeLa cells and was compared to the cytotoxicity of JetPEI/pDNA NP 6 complexes as a reference. **Figure VIII** shows that JetPEI/pDNA NP 6 complexes exhibited considerable cytotoxicity (cell viability < 65%). However, the pDNA/chitosan-S-S-PEI<sub>2</sub> 0.5:1 complex in a w/w ratio of 1:50, that demonstrated the highest transfection efficiency, provoked even more cellular toxicity with a cell viability of < 35%.

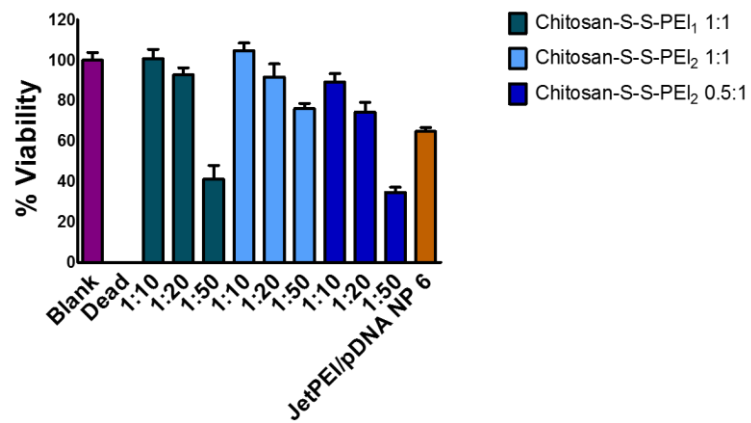


**Figure VIII Evaluation of cellular toxicity of pDNA/chitosan-S-S-PEI complexes on HeLa cells.** Graph shows the percentage of viability, measured by MTT assay, after 24 h of incubation with complexes. Graph shows mean ± SEM for three technical replicates.

## 4 DISCUSSION

Chitosan-disulfide-conjugated LMW-PEI has been synthesized before in the lab of Zhao and coworkers in order to deliver reporter genes of luciferase and GFP to COS-1 cells, 293T cells and HepG2 cells. Furthermore, the most successful copolymer was used to deliver the bone morphogenetic protein gene in vitro for osteogenic differentiation. Using the copolymer, they achieved transfection efficiencies that surpassed efficiencies reached with PEI.<sup>17</sup> However, in our hands, the preparation and effectiveness of chitosan-S-S-PEI copolymer was not that straightforward nor successful. The most successful copolymer tested was chitosan-S-S-PEI<sub>2</sub> 0.5:1, which reached a (rather disappointing) transfection efficiency of  $\pm$  40% when applied in a 1/50 w/w ratio (see **Figure VII C**). Unfortunately, when applied in this concentration, it also exerted a high toxicity, with less than 35% cell viability (see **Figure VIII**). It is clear that the copolymer synthesized here was unable to live up to its predetermined theoretical features: to be less cytotoxic than PEI but at least equally efficient. In this discussion, several reasons are postulated to explain the limited success of the prepared copolymers. Also, suggestions are made to improve the obtained results.

A first issue that would clarify the failure of the copolymers is the uncertainty concerning their successful synthesis. While thiolation of chitosan was nicely confirmed by FTIR (see **Figure III B**), validating thiolation of PEI seemed more troublesome as only small changes in the spectrum of PEI were observed upon thiolation (see **Figure III D**). On the other hand, coupling of chitosan and PEI was nicely confirmed using FTIR as the copolymer's spectrum clearly showed peaks that were correlated to the structure of PEI and peaks that were attributed to the structure of chitosan. Additional enforcement of copolymer formation could have been obtained through the identification of a band characteristic of disulfide bonds. This bond has been reported in literature to be visible in FTIR spectra around 500-800 cm<sup>-1</sup> but was not observed in the copolymer spectrum (see **Figure III E**). It must be noted however that literature states that this band should be very weak and that we didn't measure below 700 cm<sup>-1</sup> because of high noise in this region.<sup>19,23</sup> Finally, further confirmation of successful coupling of chitosan and PEI was provided by <sup>1</sup>H NMR as the spectrum showed peaks characteristic of both chitosan and PEI (see **Figure IV**). Although thiolation of PEI was difficult to confirm, the formation of the copolymer seemed successful, as indicated by the presence of characteristic peaks of both chitosan and PEI in both FTIR and <sup>1</sup>H NMR spectra.

The stability of thiolated polymers and copolymers is a second issue that should be mentioned. Ellman's assay did confirm thiolation of chitosan, although thiolation seemed rather inefficient. Thiolation of chitosan with 2-iminothiolane is a sensitive

process since working at a pH that is too low causes low reactivity of 2-iminothiolane while working at a pH that is too high causes low solubility of chitosan, leading to limited access of 2-iminothiolane to the primary amine groups.<sup>15</sup> We chose to perform thiolation of chitosan at an intermediate pH of 6.5-7. At this pH chitosan was indeed not fully solubilized and 2-iminothiolane reactivity might have been reduced as it is advised to use it between pH 7-10.<sup>26</sup> On the other hand, thiolation of PEI seemed very successful, which is attributed to the higher amine density, good solubility of the polymer and good reactivity of 2-iminothiolane at basic pH.<sup>17</sup> We observed that the thiolated polymers had the tendency to form gels upon dissolution due to crosslinking, a phenomenon that has been associated before with high thiolation degrees.<sup>9</sup> While this was not the case for the copolymers which proved to be well soluble in water, a couple of weeks after synthesis the formation of a gel-like structure was again observed when solubilizing the copolymers, causing concerns regarding the stability of thiolated polymers and copolymers.

What would be further possible to improve the results we obtained with the copolymer? First of all, further insurance of successful copolymerization could be provided by determination of the average molecular weight of the polymer *via* static light scattering, a well-established analytical method to determine the MW of polymers. Moreover, linkage *via* disulfide bonds could be confirmed by mimicking the thiol-rich environment of the cytosol, *e.g.* by using dithiothreitol (DDT) as a reducing agent. When the copolymer is treated with DDT, the MW should decrease because of degradation of the disulfide bond, thereby indicating the reducible property of the copolymer.<sup>9,17</sup> Besides an additional confirmation of copolymerization, cytotoxicity remains an issue to be tackled. In order to find out what causes the high toxicity of the copolymer, it would be advisable to measure the intrinsic cellular toxicity of chitosan, bPEI 1.8 kDa and thiolated variants. This way, it would be possible to determine if the observed toxicity was caused by the copolymerization, by the thiolation of the polymers or by the starting polymers itself. In a further attempt to decrease the toxicity, it might prove useful to prolong dialysis to remove any impurities.

## 5 CONCLUSION

In order to combine the biocompatibility of chitosan with the gene delivery ability of PEI, the two polymers were combined by the introduction of a disulfide bond. Chitosan-disulfide-conjugated LMW-PEI was synthesized by thiolation of chitosan and PEI with 2-iminothiolane followed by oxidation in air. Structural characterization of the copolymers was performed using FTIR and  $^1\text{H}$  NMR. Furthermore, Ellman's assay was used to assess the thiol content of both thiolated polymers and copolymers. As a final step, cell viability and transfection efficiency in HeLa cells was evaluated. Unfortunately, none of the copolymers could meet our demands as they showed high cellular toxicity and low transfection efficiency. Chitosan-S-S-PEI<sub>2</sub> 0.5:1 was the most "successful" copolymer, with a transfection efficiency of around 40% and a cell viability of 35%. Due to these disappointing results the chitosan-disulfide-conjugated LMW-PEI was abandoned and it was decided to continue working with unmodified PEI in the rest of the PhD project to study fundamental properties of the proton sponge effect.

## ACKNOWLEDGEMENTS

L. Vermeulen would like to acknowledge the financial support of the Agency for Innovation by Science and Technology in Belgium. Prof. B. De Spiegeleer and Dr. N. Bracke are acknowledged for helping to obtain the FTIR spectra. We would also like to thank Dr. M. Dash for her help during the initial phases of this project.

## REFERENCES

- (1) Naldini, L. Gene Therapy Returns to Centre Stage. *Nature* **2015**, *526*, 351–360.
- (2) Kumar, S. R.; Markusic, D. M.; Biswas, M.; High, K. A.; Herzog, R. W. Clinical Development of Gene Therapy: Results and Lessons from Recent Successes. *Mol. Ther. - Methods Clin. Dev.* **2016**, *3*, 16034.
- (3) Taranejoo, S.; Chandrasekaran, R.; Cheng, W.; Hourigan, K. Bioreducible PEI-Functionalized Glycol Chitosan: A Novel Gene Vector with Reduced Cytotoxicity and Improved Transfection Efficiency. *Carbohydr. Polym.* **2016**, *153*, 160–168.
- (4) Lv, H.; Zhang, S.; Wang, B.; Cui, S.; Yan, J. Toxicity of Cationic Lipids and Cationic Polymers in Gene Delivery. *J. Control. Release* **2006**, *114*, 100–109.
- (5) Mao, S.; Sun, W.; Kissel, T. Chitosan-Based Formulations for Delivery of DNA and siRNA. *Adv. Drug Deliv. Rev.* **2010**, *62*, 12–27.
- (6) Tong, H.; Qin, S.; Fernandes, J. C.; Li, L.; Dai, K.; Zhang, X. Progress and Prospects of Chitosan and Its Derivatives as Non-Viral Gene Vectors in Gene Therapy. *Curr Gene Ther* **2009**, *9*, 495–502.
- (7) Wong, K.; Sun, G.; Zhang, X.; Dai, H.; Liu, Y.; He, C.; Leong, K. W. PEI-G-Chitosan, a Novel Gene Delivery System With Transfection Efficiency Comparable to Polyethylenimine In Vitro and After Liver Administration In Vivo. *Bioconjug. Chem.* **2006**, *17*, 152–158.
- (8) Chen, H.; Cui, S.; Zhao, Y.; Zhang, C.; Zhang, S.; Peng, X. Grafting Chitosan With Polyethylenimine in an Ionic Liquid for Efficient Gene Delivery. *PLoS One* **2015**, *10*, 1–17.
- (9) Kang, H. C.; Kang, H. J.; Bae, Y. H. A Reducible Polycationic Gene Vector Derived from Thiolated Low Molecular Weight Branched Polyethyleneimine Linked by 2-Iminoethanol. *Biomaterials* **2011**, *32*, 1193–1203.
- (10) Gosselin, M. A.; Guo, W.; Lee, R. J. Efficient Gene Transfer Using Reversibly Cross-Linked Low Molecular Weight Polyethylenimine. *Bioconjug. Chem.* **2001**, *12*, 989–994.
- (11) Forrest, M. L.; Koerber, J. T.; Pack, D. W. A Degradable Polyethylenimine Derivative with Low Toxicity for Highly Efficient Gene Delivery. *Bioconjug. Chem.* **2003**, *14*, 934–940.
- (12) Nia, A. H.; Eshghi, H.; Abnous, K.; Ramezani, M. The Intracellular Delivery of Plasmid DNA Using Cationic Reducible Carbon Nanotube — Disulfide Conjugates of Polyethylenimine. *Eur. J. Pharm. Sci.* **2017**, *100*, 176–186.
- (13) Schafer, F. Q.; Buettner, G. R. Redox Environment of the Cell As Viewed Through the Redox State of the Glutathione Disulfide/Glutathione Couple. *Free Radic. Biol. Med.* **2001**, *30*, 1191–1212.
- (14) Namvar, A.; Bolhassani, A.; Khairkhah, N.; Motevalli, F. Physicochemical Properties of Polymers: An Important System to Overcome the Cell Barriers in Gene Transfection. *Biopolymers* **2015**, *103*, 363–375.
- (15) Bernkop-Schnürch, A.; Hornof, M.; Zoidl, T. Thiolated Polymers - Thiomers: Synthesis and in Vitro Evaluation of Chitosan-2-Iminoethanol Conjugates. *Int. J. Pharm.* **2003**, *260*, 229–237.
- (16) Ramya, R.; Sudha, P. .; Mahalakshmi, D. . Preparation and Characterization of Chitosan Binary Blend. *Int. J. Sci. Res. Publ.* **2012**, *2*, 1–9.

- (17) Zhao, X.; Li, Z.; Pan, H.; Liu, W.; Lv, M.; Leung, F.; Lu, W. W. Enhanced Gene Delivery by Chitosan-Disulfide-Conjugated LMW-PEI for Facilitating Osteogenic Differentiation. *Acta Biomater.* **2013**, *9*, 6694–6703.
- (18) Queiroz, M. F.; Melo, K. R. T.; Sabry, D. A.; Sasaki, G. L.; Rocha, H. A. O. Does the Use of Chitosan Contribute to Oxalate Kidney Stone Formation? *Mar. Drugs* **2015**, *13*, 141–158.
- (19) Pretsch, E.; Bühlmann, P.; Badertscher, M. *Structure Determination of Organic Compounds*; 4th Editio.; 2009.
- (20) Sakloetsakun, D.; Perera, G.; Hombach, J.; Millotti, G.; Bernkop-Schnürch, A. The Impact of Vehicles on the Mucoadhesive Properties of Orally Administrated Nanoparticles: A Case Study with Chitosan-4-Thiobutylamidine Conjugate. *AAPS PharmSciTech* **2010**, *11*, 1185–1192.
- (21) Davidovich-Pinhas, M.; Danin-Poleg, Y.; Kashi, Y.; Bianco-Peled, H. Modified Chitosan: A Step toward Improving the Properties of Antibacterial Food Packages. *Food Packag. Shelf Life* **2014**, *1*, 160–169.
- (22) Yang, T.; Hussain, A.; Bai, S.; Khalil, I. A.; Harashima, H.; Ahsan, F. Positively Charged Polyethylenimines Enhance Nasal Absorption of the Negatively Charged Drug, Low Molecular Weight Heparin. *J. Control. Release* **2006**, *115*, 289–297.
- (23) Esquivel, R.; Juárez, J.; Almada, M.; Ibarra, J.; Valdez, M. A. Synthesis and Characterization of New Thiolated Chitosan Nanoparticles Obtained by Ionic Gelation Method. *Int. J. Polym. Sci.* **2015**, *2015*.
- (24) Weinhold, M. X.; Sauvageau, J. C. M.; Keddig, N.; Matzke, M.; Tartsch, B.; Grunwald, I.; Kübel, C.; Jastorff, B.; Thöming, J. Strategy to Improve the Characterization of Chitosan for Sustainable Biomedical Applications: SAR Guided Multi-Dimensional Analysis. *Green Chem.* **2009**, *11*, 498.
- (25) Wang, Y. Q.; Su, J.; Wu, F.; Lu, P.; Yuan, L. F.; Yuan, W. E.; Sheng, J.; Jin, T. Biscarbamate Cross-Linked Polyethylenimine Derivative with Low Molecular Weight, Low Cytotoxicity, and High Efficiency for Gene Delivery. *Int. J. Nanomedicine* **2012**, *7*, 693–704.
- (26) Sigma-Aldrich. 2-Iminothiolane hydrochloride  
<https://www.sigmaaldrich.com/catalog/product/sigma/i6256?lang=en&region=BE> (accessed Mar 27, 2018).

## Summary and conclusions

The delivery of genes of therapeutic relevance to their correct molecular target requires overcoming a complex series of barriers. Since naked nucleic acids are no match to our bodies' defense mechanisms, delivery vectors are being developed to guide these therapeutic genes across a myriad of hindrances. In the last decades, non-viral vectors have emerged as promising carrier systems as they possess several desirable traits such as ease of production, ability to carry large payloads, increased safety profile compared to viral alternatives, *etc.* Despite their many advantages, non-viral vectors (a.k.a. nanoparticles) – unfortunately – seem to lack therapeutic efficiency. In order to reach sufficient efficiency, scientists worldwide believe that nanoparticle design needs to take into account the numerous biological barriers a nanomedicine encounter after administration. However, the rational design of nanomedicines depends on our fundamental knowledge about these barriers and especially how nanomedicines interact with them. The design of a new generation of non-viral gene therapeutics, based on fundamental knowledge regarding the biological barriers, could bring about the long-awaited success of 'nano' in gene therapy.

In **Chapter 1** we start by providing an overview of the different biological barriers a nanomedicine encounters upon administration. After shortly discussing the extracellular barriers, an extensive overview of the intracellular barriers is provided. The plasma membrane, exocytosis, endosomal release, autophagy, vector unpacking, cytoplasmic degradation and nuclear uptake are all prominent intracellular barriers that prevent effective delivery *via* non-viral gene therapeutics. After discussing the physiology of the different barriers and why they pose a hindrance to gene delivery, we focus on methodologies (both well-known as state-of-the-art) that allow visualization and quantification of nanoparticle-barrier interactions. These assays and techniques should enable the scientific community to gain a better fundamental understanding of the delivery barriers to non-viral gene therapy.

Of these intracellular delivery barriers, endosomal escape is considered to be one of the major hurdles in gene therapy. After endocytic uptake, it is well-known that the majority of nanomedicines remain entrapped inside the endosomal compartment. Upon endosomal maturation, the nanomedicines become prone to degradation by lysosomal enzymes, apart from the fact that the endosomal membrane prevents translocation of the nucleic acid cargo into the cytosol. A commonly used strategy to overcome the endosomal barrier is the use of cationic polymeric vectors that are thought to induce osmotic endosomal bursting through the proton sponge effect. In

**Chapter 2** we review the conflicting reports that have been published on this subject. The debate about the validity of the proton sponge hypothesis has divided the scientific community for more than 2 decades. By systematically analyzing the individual reports and including recent findings on additional factors that contribute to the proton sponge hypothesis, we come to the conclusion that the various reports are not that conflicting after all. With this we hope to arrive at a consensus that the endosomal escape capacity of proton sponge-based polymers depends on a delicate balance between osmotic forces, polymer swelling and membrane destabilization.

In **Chapter 3** we set out to gain a deeper understanding of the mechanistic factors that govern effective proton sponge-based endosomal escape. Therefore, we perform a detailed comparative study of the endosomal escape capacity of JetPEI/pDNA polyplexes in HeLa cells vs ARPE-19 cells. We observed that JetPEI/pDNA polyplexes were able to induce higher levels of transfection in HeLa cells than in ARPE-19 cells, which we could attribute to an increased endosomal escape frequency in HeLa cells. After evaluation of several endosomal properties, we found that both endosomal size and endosomal membrane leakiness can have a considerable impact on proton sponge-mediated endosomal escape. Larger endosomes require a higher number of polyplexes to create an osmotic pressure that is sufficiently high to induce endosomal bursting. Membrane leakiness – the loss of its semi-permeable property for small molecules – prevents the build-up of osmotic pressure inside the endosome, thereby abolishing proton sponge-based endosomal rupture. The importance of these intercellular variations was confirmed with additional experiments on A549 and H1299 cells. We conclude that the effectivity of proton sponge-based endosomal escape is very much cell-dependent, with the endosomal size and endosomal membrane leakiness being two important factors that have been largely overlooked until now. When cells have comparable endosomal membrane leakiness, endosomal size will play a determining role. However, at high levels of leakiness, build-up of the osmotic pressure is no longer possible, regardless of endosomal size.

In **Chapter 4** we investigate the application of plasmonic nanoparticles coupled with laser irradiation to induce photothermally-triggered endosomal escape of pDNA. Besides the opportunity to overcome one of the most prominent intracellular barriers in gene therapy, this strategy would allow to obtain spatio-temporal control over the cytosolic delivery of pDNA, rendering it a suitable tool to conduct fundamental studies regarding the endosomal barrier. In particular, we examined the potential of JetPEI/pDNA/Au complexes to induce endosomal escape of functional pDNA in HeLa cells after irradiation in a heating regime (low laser energy) or after the formation of explosive vapour nanobubbles (high laser energy). Unfortunately, we observed that

although both regimes could induce endosomal rupture, they nevertheless failed to generate efficient transfection in HeLa cells. We believe this is primarily due to dysfunctionality of the pDNA after being subject to the aforementioned photothermal effects. Other nanoparticle designs should be considered that provide better protection to the pDNA upon laser irradiation.

Finally, **Chapter 5** discusses the broader international context of the work in this thesis and its relevance to the field. We started by giving a general overview of the key challenges and successes of gene therapy. As the development of efficient non-viral vectors poses a significant challenge, we discuss some factors that hinder the progression of nanomedicines in the field of gene therapy. The main reason for the inefficiency of non-viral gene therapeutics is a their inability to overcome one or more biological barriers. We propose that fundamental studies, focused on the properties of these biological barriers and the interaction of nanomedicines with these barriers, could lead to renewed insights that could enable the development of more effective rationally-designed nanomedicines for gene therapy.



## Samenvatting en conclusies

Het afleveren van therapeutisch relevante genen aan hun correcte moleculaire target veronderstelt de overwinning op een complexe serie van biologische barrières. Vermits naakte nucleïnezuren niet opgewassen zijn tegen de verdedigingsmechanismen van ons lichaam worden afleveringsvectoren ontwikkeld die de therapeutische genen doorheen een waaier van hindernissen moeten leiden. Gedurende de laatste decennia zijn de niet-virale vectoren naar voor getreden als beloftevolle carriers omwille van verscheidene aantrekkelijke eigenschappen zoals onder meer het gemak van productie, de mogelijkheid om grote nucleïnezuren te verpakken en hun verhoogde veiligheid in vergelijking met virale vectoren. Ondanks hun vele voordelen lijken niet-virale vectoren (ook wel nanopartikels genoemd) helaas therapeutische efficiëntie te missen. Om voldoende efficiëntie te bereiken geloven wetenschappers wereldwijd dat men bij het ontwerpen van nanomedicijnen rekening moet houden met de verschillende biologische barrières die het nanomedicijn zal tegenkomen wanneer het toegediend wordt. Het rationeel ontwerpen van nanopartikels hangt echter af van onze fundamentele kennis over de verschillende barrières én over de interactie tussen nanomedicijnen en deze barrières. Het ontwerpen van een nieuwe generatie aan niet-virale genterapieën, gebaseerd op fundamentele kennis over de biologische barrières zou kunnen leiden tot het langverwachte succes van het noveld binnen de genterapie.

In **Hoofdstuk 1** starten we met het geven van een overzicht van de verschillende biologische barrières die nanomedicijnen kunnen tegenkomen wanneer ze worden toegediend. Na een korte bespreking van de extracellulaire barrières geven we een uitgebreide uiteenzetting van de verscheidene intracellulaire barrières. We behandelen de plasmamembraan, exocytose, endosomale ontsnapping, autofagie, het uitpakken van vectoren, afbraak in het cytoplasma en opname in de kern als prominente intracellulaire barrières die efficiënte aflevering door gebruik van niet-virale vectoren verhinderen. We nemen eerst de fysiologie van de barrières door en bespreken waarom ze een hindernis vormen voor de aflevering van genen. Vervolgens focussen we op het geven van een overzicht van zowel welgekende als vernieuwende methodes die toelaten de interactie tussen nanomedicijnen en hun barrières te visualiseren en te kwantificeren. Deze assays en technieken zouden wetenschappers in staat kunnen stellen om de fundamentele kennis bij te schaven en diepgaand begrip te verwerven in verband met de afleveringsbarrières voor niet-virale genterapie.

Van de vele intracellulaire belemmeringen wordt de ontsnapping uit endosomen beschouwd als een van de belangrijkste hindernissen in gentherapie. Het is algemeen bekend dat na endocytische opname de meerderheid van de nanomedicijnen gevangen blijft in het endosomale compartiment. Terwijl deze endosomen matureren, worden de nanomedicijnen vatbaar voor degradatie door lysosomale enzymen en wordt hun lokalisering naar het cytosol belemmerd. Een frequent gebruikte strategie om de endosomale membraan te overmeesteren is het gebruik van kationische polymeren waarvan men veronderstelt dat zij het endosoom laten barsten via het zogenoemde proton spons mechanisme. In **Hoofdstuk 2** bespreken we de tegenstrijdige rapporten die gedurende de jaren over dit onderwerp gepubliceerd zijn. Het debat over de feitelijkheid van deze hypothese heeft de wetenschappelijke gemeenschap al meer dan 20 jaar in verdeeldheid gebracht. Door de individuele rapporten systematisch te analyseren en te koppelen aan recente bevindingen in verband met aanvullende factoren voor de proton spons hypothese, komen we tot de conclusie dat deze bevindingen toch niet zo tegensprekend zijn als eerst gedacht. We hopen op deze manier de consensus te bereiken dat de endosomale ontsnappingscapaciteit van proton spons-gebaseerde polymeren afhankelijk is van een delicate balans tussen osmotische krachten, zwelling van het polymeer en destabilisatie van de endosomale membraan.

In **Hoofdstuk 3** hopen we meer inzicht te krijgen in de mechanistische factoren die invloed hebben op de effectieve capaciteit van proton spons-gebaseerde polymeren om te ontsnappen uit het endosoom. Hiertoe voeren we een gedetailleerde vergelijkende studie uit van de endosomale ontsnappingscapaciteit van JetPEI/pDNA polyplexen in HeLa cellen vs ARPE-19 cellen. We hebben waargenomen dat JetPEI/pDNA polyplexen hogere transfectielevels konden bereiken in HeLa cellen dan in ARPE-19 cellen, hetgeen kon toegeschreven worden aan een verhoogde endosomale ontsnapping uit HeLa cellen. Na de evaluatie van verschillende endosomale eigenschappen stelden we vast dat zowel de grootte van de endosomen als de mate waarin de endosomale membraan vatbaar is voor lekken een aanzienlijke invloed kunnen hebben op proton spons-gemedieerde endosomale ontsnapping. Grotere endosomen hebben een groter aantal polyplexen nodig om een voldoende hoge osmotische druk te creëren om het endosoom te laten barsten. Lekkage van de endosomale membraan en het bijhorende verlies van de semi-permeabele eigenschap van de membraan voor kleine moleculen doet de opbouw van osmotische druk in het endosoom teniet, waardoor de ruptuur van het endosoom niet verwezenlijkt kan worden. Het belang van deze intercellulaire variaties werd bevestigd door aanvullend onderzoek in A549 en H1299 cellen. We concluderen dat de effectiviteit van proton spons-gebaseerde endosomale ontsnapping erg onderhevig is aan intercellulaire

variatie als gevolg van endosomale grootte en lekkage van de endosomale membraan. Deze twee belangrijke factoren werden tot nu toe grotendeels over het hoofd gezien. Wanneer cellen een vergelijkbare lekkage van de endosomal membraan vertonen, zal de grootte van de endosomen een doorslaggevende rol spelen. Echter, bij hoge niveaus van lekkage zal de opbouw van de osmotische druk niet langer mogelijk zijn, ongeacht de endosomale grootte.

In **Hoofdstuk 4** onderzoeken we het gebruik van plasmonische nanopartikels, gekoppeld aan laserbestraling, om op fothermische wijze endosomale ontsnapping van pDNA te verwezenlijken. Naast de mogelijkheid die deze techniek geeft om een van de meest prominente intracellulaire barrières voor gentherapie te overwinnen, zou deze strategie ook mogelijk maken om de cytosolische afgifte van pDNA te controleren in ruimte en tijd. Hierdoor zou het een geschikt hulpmiddel kunnen vormen voor het uitvoeren van fundamentele studies met betrekking tot de endosomale barrière. In het bijzonder onderzochten we het potentieel van JetPEI/pDNA/Au complexen om endosomale ontsnapping van functioneel pDNA in HeLa cellen te induceren na bestraling in een verwarmingsregime (gebruik makende van lage laserenergie) of na de vorming van explosieve waterdamp nanobubbels (gebruik makende van hoge laserenergie). Ongeacht het feit dat beide regimes endosomale rupturen veroorzaakten, waren ze niet in staat efficiënte transfectie te genereren in HeLa cellen. We vermoeden dat de oorzaak hiervan het niet correct functioneren van het pDNA is na blootstelling aan voorgenoemde fothermale effecten. Andere nanopartikels die een betere bescherming van het pDNA kunnen garanderen na laserbehandeling zouden moeten overwogen worden.

Om af te sluiten bespreken we in **Hoofdstuk 5** de bredere internationale context van het werk in dit proefschrift en zijn relevantie binnen het vakgebied. We beginnen met een algemeen overzicht van de meest belangrijke uitdagingen en successen in gentherapie. Aangezien de ontwikkeling van efficiënte niet-virale vectoren een aanzienlijke uitdaging vormt, bespreken we vervolgens enkele factoren die de progressie van nanomedicijnen op het gebied van gentherapie belemmeren. De belangrijkste hindernis voor niet-virale vectoren is het overwinnen van een of meer biologische barrières. We stellen voor dat fundamentele studies, gericht op het verschaffen van inzicht in de biologische eigenschappen van deze barrières en in de interactie tussen nanomedicijnen en de barrières, zouden kunnen leiden tot vernieuwende opvattingen. Deze opvattingen zouden op hun beurt de rationele ontwikkeling van effectievere nanomedicijnen kunnen bewerkstelligen die de afleveringsbarrières voor niet-virale gentherapie zouden kunnen overwinnen.



## CURRICULUM VITAE

### PERSONALIA

Name	Vermeulen
First names	Lotte Mariette Prosper
Nationality	Belgian
Date of birth	29/03/1990
Place of birth	Lokeren
Private address	Pieter Tackstraat 9 9160 Lokeren
Telephone	+32 (0)472 440 230
Professional address	Laboratory for General Biochemistry and Physical Pharmacy Faculty of Pharmaceutical Sciences, Ghent University Ottergemsesteenweg 460 9000 Ghent, Belgium
E-mail	<a href="mailto:LotteM.Vermeulen@UGent.be">LotteM.Vermeulen@UGent.be</a> <a href="mailto:Vermeulen-lotte@hotmail.com">Vermeulen-lotte@hotmail.com</a>
Website	<a href="http://www.biofys.ugent.be">www.biofys.ugent.be</a> <a href="https://www.linkedin.com/in/lotte-vermeulen-7b2893116/">https://www.linkedin.com/in/lotte-vermeulen-7b2893116/</a>

### EDUCATION

June 2013	Master in Drug Development (Magna cum laude) Ghent University, Ghent, Belgium
	<b>Master thesis:</b> "Obtaining chitosan microspheres on superhydrophobic surfaces for controlled release of 5 fluorouracil" under supervision of Prof. dr. Carmen Alvarez Lorenzo and Prof. dr. Angel Concheiro; University of Santiago de Compostela (Spain) and Prof. dr. Stefaan De Smedt; laboratory of General Biochemistry and Physical Pharmacy; Ghent University (Belgium).
June 2011	Bachelor of Science in Pharmaceutical Sciences (Cum laude) Ghent University, Ghent, Belgium
June 2008	Latin & Sciences Sint-Lodewijkcollege Lokeren, Belgium

## LANGUAGES

Dutch	Native language
English	Full professional proficiency
French	Limited proficiency
German	Elementary proficiency
Spanish	Elementary proficiency

## INTERNATIONAL PEER REVIEWED PUBLICATIONS

### Accepted

Colzani, B., Speranza, G., Dorati, R., Conti, B., Modena, T., Bruni, G., Zagato, E., **Vermeulen, L.**, Dakwar, G.R., Braeckmans, K., Genta, I. Design of smart GE11-PLGA/PEG-PLGA blend nanoparticulate platforms for parenteral administration of hydrophilic macromolecular drugs: synthesis, preparation and in vitro/ex vivo characterization. *Int. J. Pharm.* **2016**, *511*, 1112-1123 (IF<sub>2016</sub> **3.65**)

Zagato, E., **Vermeulen, L.M.P.**, Dewitte, H., Van Imschoot, G., Vandenbroucke, R.E., Demeester, J., De Smedt, S.C., Neyts, K., Remaut, K., Braeckmans, K. Quantifying the Average Number of Nucleic Acid Therapeutics per Nanocarrier by Single Particle Tracking Microscopy. *Mol Pharm.* **2018**, *15*, 1142-1149 (IF<sub>2016</sub> **4.44**)

**Vermeulen, L.M.P.**, Brans, T., Samal, S.K., Dubruel, P., Demeester, J., De Smedt, S.C., Remaut, K., Braeckmans, K. Endosomal Size and Membrane Leakiness Influence Proton Sponge-Based Rupture of Endosomal Vesicles. *ACS Nano*. **2018**, *12*, 2332-2345 (IF<sub>2016</sub> **13.94**)

### Under review

**Vermeulen, L.M.P.**, Brans, T., De Smedt, S.C., Remaut, K., Braeckmans, K. Methodologies to Investigate Intracellular Barriers for Nucleic Acid Delivery in Non-viral Gene Therapy. Minor revisions requested *Nano Today* May 2018 (IF<sub>2016</sub> **17.48**)

**Vermeulen, L.M.P.**, De Smedt, S.C., Remaut, K., Braeckmans, K. The Proton Sponge Hypothesis: Fable or Fact? Submitted to *Eur J Pharm and Biopharm* April 2018 (IF<sub>2016</sub> **4.16**)

### In preparation

**Vermeulen, L.M.P.**, Fraire, J.C., Remaut, K., Braeckmans, K. Photothermally Triggered Endosomal Escape and Its Influence on Transfection Efficiency of Gold-functionalized JetPEI/pDNA Nanoparticles. Invited by *Int J Mol Sci* (IF<sub>2016</sub> **3.23**)

Fraire, J.C., Liu, J., Raes, L., **Vermeulen, L.M.P.**, Brans, T., De Keulenaer, S., Van Nieuwerburgh, F., De Rycke, R., Raemdonck, K., De Smedt, S.C., Braeckmans, K. Comparison of Heating- and Vapour Nanobubble-Mediated Endosomal Escape of siRNA for Light-Triggered Gene Silencing.

## NATIONAL AND INTERNATIONAL CONFERENCES WITH ORAL PRESENTATION

- 2017 European Workshop on Particulate Systems, **Copenhagen, Denmark**  
*Effect of cellular properties on endosomal escape efficiency*
- COMPACT F2F and Plenum meeting, **Saarbrücken, Germany**  
*Effect of cellular properties on endosomal escape efficiency*
- COMPACT F2F and Plenum meeting, **Paris, France**  
*Endosomal Size and Membrane Leakiness Influence Proton Sponge-Based Rupture of Endosomal Vesicles*
- 2016 Meeting of the Belgian-Dutch Biopharmaceutical Society, **Utrecht, The Netherlands**  
*Influence of cellular properties on endosomal escape efficiency*
- COMPACT F2F Meeting, **Cardiff, UK** (presentation via skype)  
*Visualization of endosomal escape and further understanding the endosomal barrier*
- COMPACT F2F Meeting, **Stevenage, UK**  
*IC trafficking of DARPin constructs and endosomal escape*
- 2015 COMPACT F2F Meeting, **Brussels, Belgium**  
*IC trafficking and visualization of endosomal escape*
- Forum of Pharmaceutical Sciences, **Blankenberge, Belgium**  
*Unraveling the intracellular processing of non-viral gene carriers*
- 2014 COMPACT F2F Meeting, **Stockholm, Sweden.**  
*Intracellular trafficking of drug delivery systems*

## NATIONAL AND INTERNATIONAL CONFERENCES WITH POSTER PRESENTATION

- 2017 f-TALES, **Ghent, Belgium**  
*Endosomal Size and Membrane Leakiness Influence Proton Sponge-Based Endosomal Escape*
- RBSM Annual Meeting – From pictures to numbers, **Antwerp, Belgium**  
*Endosomal Size and Membrane Leakiness Influence Proton Sponge-Based Endosomal Escape*

- 2016 European Symposium on Controlled Drug Delivery (ESCDD),  
**Egmond aan Zee, The Netherlands**  
*Understanding the Endosomal Barrier – A Case Study with JetPEI*
- COMPACT Consortium meeting, **Stevenage, UK**  
*Visualizing Endosomal Escape – A Case Study with PEI*
- 2015 Meeting of the Belgian-Dutch Biopharmaceutical Society,  
**Leuven, Belgium**  
*Live-cell Imaging to Unravel Intracellular Processing and Endosomal Escape of Gene Complexes*
- Crossing Biological Barriers, **Dresden, Germany**  
*Relation Between Trafficking Pathway and Endosomal Escape*
- COMPACT Plenum Meeting, **Ludwigshafen, Germany**  
*Relation Between Trafficking Pathway and Endosomal Escape*
- 2014 Meeting of the Belgian-Dutch Biopharmaceutical Society,  
**Vlaardingen, The Netherlands**  
*Relation Between Trafficking Pathway and Endosomal Escape*
- COMPACT Consortium Meeting, **Stevenage, UK**  
*Intracellular Trafficking and Endosomal Escape of DDS*

## AWARDS AND GRANTS

- 2017 Best Oral Presentation Award at EWPS in Copenhagen, Denmark
- 2013-2017 Faculty travel grants for attending conferences and workshops
- 2014-2017 IWT PhD fellowship

## COURSES

- 2017 Project Management (Ghent University)
- 2016 Computer Optimized Microscopy (University of Barcelona)
- 2015 Effective Scientific Communication (Ghent University)
- Summer School in Advanced Light Microscopy (VIB, Zwijnaarde)

## **TEACHING ACTIVITIES**

2014-2017	Supervision of 2 students during their Master's research project
2014-2017	Supervision of 1 honours programme student
2013-2016	Tutor Problem-based learning 2 <sup>nd</sup> Bachelor Unraveling the biochemistry of DNA
2013-2016	Tutor and lab instructor for the Pharmaceutical Bachelor Thesis

